SYNTHESIS, CHARACTERISATION AND ANTI-CORROSION BEHAVIOUR OF NiO-CNTs-SnO_2 NANOCOMPOSITES COATINGS ON AISI 1020 STEEL

BY

KAREEM, Aduagba Ganiyu
PhD/SEET/2016/873

DEPARTMENT OF MECHANICAL ENGINEERING
FEDERAL UNIVERSITY OF TECHNOLOGY, MINNA

OCTOBER, 2021

ABSTRACT

In this study, synthesised NiO-CNTs-SnO_2 nanocomposites based coatings were applied on AISI 1020 steel samples to prevent corrosion. NiO-SnO_2 based nanocomposites were obtained via combination of green-impregnation and sonochemical methods followed by incorporation of CNTs at different ratios. The influence of process parameters on the synthesis of NiO and SnO_2 nanoparticles such as; solution pH, precursor concentration, and synthesis temperature on particle size were investigated via surface response methodology (RSM) using the Box-Behnken method. The synthesised nanocomposites were characterised with the aid of High resolution scanning electron microscopy (HRSEM), Energy Dispersive Spectroscopy (EDS), X-ray Diffraction (XRD), High Resolution Transmission Electron Microscope (HRTEM) and Selective Area Diffraction Spectroscopy (SAED) and X-ray Photoelectron Spectroscopy. Subsequently, NiO-SnO_2, NiO-CNTs, SnO_2-CNTs and NiO-CNTs-SnO_2, were dip-coated on the surface of AISI 1020 steel coupons. The corrosion performance of the (NiO-SnO_2, NiO-CNTs, SnO_2-CNTs) and NiO-CNTs-SnO_2, coatings in soil environment as corrosive media were investigated by Gravimetry, Potentiodynamic Polarization (PDP) and Electrochemical Impedance Spectroscopy methods (EIS). HRSEM analysis showed that the obtained NiO-CNTS-SnO_2 nanocomposites were aggregated, with combined spherical, tubular and cubic structures with an average crystalline size of 25 nm. Energy Dispersive Spectroscopy (EDS) analysis revealed the presence of Sn, Ni, C and O as major elements in the nanocomposites. The XRD analysis of as-synthesised nanocomposites revealed the formation of crystallinity bunsenite, graphite and cassiterite phases belonging to NiO, CNTs and SnO_2 respectively. The X-ray Photoelectron Spectroscopy (XPS) analysis of the nanocomposites revealed the formation of Nickel Oxycarbide-Tin alloy responsible for the improved anti-corrosion properties of the developed nanomaterial. Gravimetry analysis showed its lowest corrosion rate at 8.76E-08 mpy for a coupon coated and buried with NiO-CNTs-SnO_2 composite in the ratio (1:1:2) and a Protection Efficiency of 92.61% after 12 months of reweighing. The PDP showed that NiO-CNTs-SO_2, in the ratio (1:1:2), had excellent corrosion resistance behavior with lowest corrosion current of 0.0064 $\mu A/cm^2$ and Protection Efficiency of 93.30% while the charge transfer resistance, Rct of 6.244 $K\Omega \cdot cm^2$ and Protection Efficiency of 93.90% were established with the same NiO-CNTs-SnO_2 composite coating of the same ratio (1:1:2) for EIS measurement against the corrosion of AISI 1020 steel substrate. The corrosion rate was also found decreased from 0.0335 to 0.0022 mpy showing evidence of a slow rate of uniform corrosion and better Protection Efficiency of the steel substrate. HRSEM/Cross-Sectional analysis of steel coated with NiO-CNTs-SnO_2 (1:1:2) buried in the soil revealed successful protection of the steel coupon. XRD analysis also showed non-destruction of the diffraction peaks of NiO, CNTs and SnO_2, respectively. This study demonstrated NiO-CNTs-SnO_2 based coatings in the mixing ratio 1:1:2, as the most effective material to protect the steel coupon.

TABLE OF CONTENTS

LIST OF TABLES

LIST OF FIGURES

Figure **Page**

LIST OF PLATES

Plate **Page**

LIST OF APPENDICIES

Appendix **Page**

ABBREVIATIONS, GLOSSARIES AND SYMBOLS

$Fe(OH)_3$	Iron (III) Oxide Hydroxide
Fe_3O_4	Magnetite
$FeCl_3$	Iron (III) Chloride
Ag	Silver
AgCl	Silver Chloride
AISI	American Iron and Steel Institute
Ar	Argon
BET	Brunanuer Emmett Teller
C_2H_2	Acetylene
CCVD	Catalytic Chemical Vapour Deposition
CE	Counter Electrode
Cl^-	Chloride ion
CNTs	Carbon Nanotubes
CPE	Coating Protection Efficieny
CPEa	Capacitance of the Coating Layer contant Phase Element
CPEdl	Double Layer Contant Phase Element's Capacitance
CPR	Corrosion Penetration Rate
Cu	Copper
CVD	Chemical Vapour Deposition
DWCNT	Double-walled Carbon Nanotube
E_{corr}	Corrosion Potential
EDS	Energy Dispersive X-ray Spectroscopy
EDX	Energy Dispersive X-ray
EDX	Energy Dispersive X-ray Spectroscopy
EIS	Electrochemical Impedance Spectroscopy

Fe	Iron
$Fe(OH)_2$	Iron Hydroxide
Fe_2O_3	Iron (III) Oxide (Hematite)
FeO(OH)	Iron (III) Oxide Hydroxide
FTIR	Fourier Transformed Infrared Radiation
FTIR	Fourier Transform Infrared Spectroscopy
FUT	Federa University of Technology
FWHM	Full Width at Half Maximum
h	Hours
H_2SO_4	Sulfuric Acid
HNO_3	Nitric Acid
HRSEM	High Resolution Sanning Electron Microscopy
HRTEM	High Resolution Transmission Electron Microscopy
I_{corr}	Current Density
MC	Moisture Content
Min	Minute
mL/min	Millilitre per Minute
MWCNT	Multiwalled Carbon Nanotubes
N_2	Nitrogen
NaCl	Sodium Chloride
Ni	Nickel
NiO	Nickel Oxide
NiO-CNTs	Nickel Oxide-Carbon Nanotubes
NiO-CNTs-SnO_2	Nickel Oxide-Carbon Nanotubes-Tin Oxide
NiO-SnO_2	Nickel Oxide-Tin Oxide

nm	Nanometre
NPs	Nanoparticles
OCP	Open Circuit Potential
Pb	Lead
PDP	Potentiodynamic Polarization
PE	Protection Efficiency
PEG	Polyethylene Glycol
R_c	Coating Resistance
Rct	Charge Transfer Resistance
RE	Reference Electrode
Rsol	Solution Resistance
SAED	Selected Area Electron Diffraction
SnO_2	Tin Oxide
SnO_2-CNTs	Tin Oxide-Carbon Nanotubes
SO_4^{2-}	Sulphate Ion
SWCNT	Single-walled Carbon Nanotube
USA	United States of America
WE	Working Electrode
wt.%	Weight Percentage
XPS	X-Ray Photoelectron Spectroscopy
XRD	X-Ray Diffraction
Zn	Zinc
n	Homogeneity Constant
α-FeOOH	Goethite
γ-FeOOH	Lepidocrocite

λ	Wavelength
θ	Diffraction Angle in Radians
β	Full Width at Half Maximum
d	d-spacing in Angstrom

CHAPTER ONE

1.0 INTRODUCTION

1.1 Background to the Study

Steel is an engineering material widely used in the area of manufacturing, construction, defense, medical and transportation, to mention but a few. However, the corrosion of steel via chemical and electrochemical reaction with its service environment compromises the material integrity and aesthetic value (Herrera *et al*., 2020). In addition, corrosion of steel may take varying forms such as uniform corrosion, and galvanic corrosion, pitting corrosion, crevice corrosion, under-deposit corrosion, dealloying. Others include stress corrosion cracking, corrosion fatigue, erosion corrosion and microbially influenced corrosion (Kokilaramani *et al.*, 2021).

The harmful impacts of metallic corrosion are in multifolds on the economy, including the safety hazard and conservation of resources. Economically, the losses due to corrosion are enormous and most visible in iron pipes, ships, tanks, bridges, among others. The failure of equipment might be proven fatal for human life and replacing corroded metals is not only expensive, but also hazardous and put a burden on landfills (Abdeen *et al*., 2019). Moreso, the act of constantly replacing metals depletes natural resources. Hence, corrosion has negative impact on economy of any nation and needs to be addressed for sustainability (Kausar, 2019).

It is a general belief that corrosion is a universal enemy that should be accepted as a process that is inevitable. As products and production processes become more complex and the penalties for corrosion failures have become more expensive and increased awareness has been generated. Moreover, an average of 10 percent of the total metal output in the world is estimated to be lost in corrosion (Fayomi *et al*., 2019). This affects the economy of a nation and her assets: infrastructures, transportation, utilities,

nuclear and military facilities, and production and manufacturing plants. According to the National Association of Corrosion Engineers (NACE), corrosion costs globally accounted for about 3.4% of the global Gross Domestic Product as at 2013, which amounts to $2.5 trillion US dollars which is about 5 times of the GDP of Nigeria with $508 billion dollars (Popoola *et al*., 2017). According to NACE with current day technology, about a third of the costs incurred by corrosion can be saved, and there are various methods that help implement corrosion control (Akpoborie *et al*., 2021). The harmful effects of corrosion can be felt on society in both direct and indirect ways. Direct ways being that it affects how long we use our possession and indirect being that incurred costs obtained by manufacturers through corrosion are passed to consumers. Corrosion costs are partly related to attempts to give an attractive look to engineering equipment, structures and designs. Partly because of the direct replacement and maintenance costs and concurrent losses due to interruption to plant operation and additional costs associated with the use of expensive materials and other preventive measures. Generally, corrosion of steels in acidic aqueous solution is prevalent in many industries wherein acid is used in processes such as acid pickling, industrial acid cleaning, acid descaling and oil well acidizing (Farag, 2020). One of the most effective and economical approach to improve surface ability of material to withstand high surface stress and harsh environments is by creating surface layers that would possess a high level of corrosion and wear resistance (Abakay *et al.,* 2017).

Several methods (such as inhibitor, cathodic protection, appropriate material selection and design) have been employed to prevent and/or control corrosion in metals (Wei *et al*., 2020). While operational maintenance of cathodic protection might be sometimes uneasy due to the period inspection of the control system. The appropriate material selection on the other hand requires economic factor and application of inhibitors

sometimes affect the quality of product the material is meant to transport (Khan *et al.,* 2015).

One of these methods that standout and is considered acceptable in practice is isolation of the metals from the corrosive environment via coating. Metals and alloy, ceramics, polymers and their complex composites have deposited on mild steel for corrosion prevention, though having limitation such as, durability (Abdeen *et al*., 2019). Metal sage, weaken and deteriorate and eventually their useful life ends within a short period of time.

In contrast, the introduction of nanoparticles into organic polymers and the likes offers an effective way to improve the substrate properties such as electrical conductivity, mechanical properties, thermal stability, flame retardancy, and resistance to chemical reagents (Coetzee *et al*., 2020). Moreover, composite coating with nanoparticles also improved properties which simple steel and metal plating do not have. Such properties include corrosion resistance, wear resistance and stronger adhesive bond between the coating and substrate. Studies have shown the incorporation of a carbon-based coating material in electroplating; good hardness improved the thermal conductivity of the metallic substrate (Ai *et al.,* 2020). Furthermore, coatings with carbon-based nanomaterials improve wear resistance, hardness and lower frictional coefficient (Abdeen *et al*., 2019).

Nanoparticles are of great interest to the material scientist due to their extremely small size and large surface to volume ratio, responsible for improved both chemical and physical properties (These properties include mechanical, biological and catalytic activity, thermal and electrical conductivity, optical absorption and melting point) compared to bulk of the same chemical composition (Khan *et al*., 2017). It can therefore

be said that properties embedded in the materials produced at nanometer scale cannot be variously compared with the few properties realized at bulk state. In addition, the incorporation of carbon nanotubes in the coating matrix improved both tribological behavior, thermal conductivity and corrosion resistance of the material. Studies have shown that NiO-SnO_2 coatings possess a non-crystalline amorphous structure, thus exhibit excellent protection for mining, chemical equipment and structural components when used in the highly corrosive environments encountered in the oil and gas industries (Jeevanandam, 2018). Therefore, when applied to steel surfaces, NiO-SnO_2 coated CNTs will provide effective corrosion protection by creating a physical barrier that minimizes contact between the metallic substrate and aggressive environments.

This study focused on the synthesis of NiO-SnO_2-CNTs nanocomposites via combination of green-chemical vapour deposition and impregnation methods. This was followed by characterisation of the nanocomposites in terms of microstructure, elemental composition, morphology, mineralogical phases using different analytical techniques. Subsequently the synthesised nanomaterials were applied as a coating. The anti-wear and corrosion behavior of NiO-SnO_2-CNTs coating were further investigated.

1.2 Statement of the Research Problem

Premature and unpredictable failure of buried metals due to its exposure to physicochemical properties of the soils which is attributed to changes of the environment and season has contributed to loss of lives, properties and contamination of environment and products (Quej-Ake *et al*., 2015; Prasannakumar *et al*., 2020).

Most of the synthetic coatings used as barrier between metallic substrates and their surroundings are highly toxic, hazardous and easily dispersed into the environment due to poor adhesion of these coating materials onto the surface of metallic substrate (Zheng

et al., 2017).

Various methods have been employed to protect buried steel from corrosion, which includes the use of inhibitors, impressed current, sacrificial anodes and coatings, but corrosion damage in steel remains a very serious problematic due to climatic change and the time of exposure (Quej-Ake *et al.,* 2015; Zhan *et al.,* 2017).

Large utilization of nanoparticles in metal coating is susceptible to the formation of defects such as, cracks during micro hardness testing, which results in premature failure of the composites. Which is due to high colloidal instability and agglomeration of nanomaterials at higher concentration that affects evenly distribution and adhesion of the nanoparticles onto the surface of metallic substrate.

Corrosion protection efficiency of doping and co-doping of coaters on activated carbon or polymer is low due to poor water repellent ability of the matrics.

1.3 Aim and Objectives of the Study

The aim of this research work is to synthesis, characterise and investigate the anti-corrosion behaviour of NiO-SnO_2-CNTs nanocomposites on AISI 1020 steel. The aim was achieved through the following objectives; which are to:

The aim of this research is to synthesis, characterise and investigate the anti-corrosion behaviour of NiO-SnO_2-CNTs nanocomposites on AISI 1020 steel. The aim was achieved through the following objectives; which were to:

i. synthesise nickel oxide, and tin oxide nanoparticles using response surface methodology via Box-Behnken method;

ii. produce carbon nanotubes (CNTs) via catalytic chemical vapour deposition method on Fe-Ni/Kaolin catalyst;

iii. prepare NiO-CNTs, SnO_2-CNTs, NiO-SnO_2, and NiO-SnO_2-CNTs composites via wet impregnation/sonochemical methods involving variation of the amount of NiO, CNTs and SnO_2;

iv. characterise NiO, SnO_2, CNTs and their composites forms for their morphology, particle size, elemental composition and mineralogical phases using High resolution Scanning Electron Microscopy (HRSEM), Energy dispersive spectroscopy (EDS) and X-ray Diffraction (XRD) respectively.

v. apply the developed NiO, SnO_2, CNTs, NiO-CNTs, SnO_2-CNTs, NiO-SnO_2, and NiO-SnO_2-CNTs nanocomposites on the surface of the AISI 1020 steel as nanocoatings;

vi. determine some physico-chemical parameters in the soil where the metals were buried; and

vii. evaluate the corrosion coating efficiency of the prepared nanoparticles and nanocomposites on the AISI 1020 Steel via weight loss (WL) and potentiodynamic polarization (PDP) and electrochemical impedance spectroscopy (EIS) methods.

1.4 Justification of the Study

Researchers have found that the incorporation of nanoparticles into a coating has become an alternative way to further improve the corrosion resistance and mechanical properties of the existing surface coating to keep up with the rapidly changing needs of certain special applications (Tudela *et al.,* 2014; Aliyu & Srivastava, 2020). Immobilisation of nanoparticles on CNTs matrices provides an excellent barricade against the ingress of corrosive ions, reduces agglomeration of the nanoparticles and

release of the nanoparticles into the environment (Chhetri *et al*., 2019). High thermal and mechanical properties with excellent water repellant properties of CNTs favoured its choice as the matrices for anchoring the nanoparticles for coating of metallic substrate. Green synthesis of nanoparticles reduces metal precursors and also serve as capping agents for the nanoparticles produced. Fine sizes of the particle used in this nanocoating will help in filling the spaces and blocking the corrosive elements from diffusing into the steel substrate. This will in turn protect steel product, eliminate hazardous effect on human health and environment.

Consequently, the synergistic integration or incorporating of NiO-CNTs-SnO_2 nanocomposites on the surface of steel substrate via dip deposition technique would offer inhibition, barrier and hydrophobic action with active protection, which represents an effective and reliable potential development strategy to obtain longtime durable coating that enhance their performance in different fields. Therefore, there is a strive to make use of environmentally friendly, non-toxic /less toxic, nanocoating material that is capable of withstanding harsh climatic change and offer superior passivation over steel in an extended period of time.

1.5 Scope of the Study

The scope of this work is limited to development of NiO-SnO_2-CNTs nanocomposite as a coating material for prevention of AISI 1020 steel against corrosion in a soil environment.

CHAPTER TWO

2.0 LITERATURE REVIEW

2.1 Green Synthesis

Green synthesis involves the fabrication of micro and nano-scaled inorganic materials using naturally occurring biomolecules or microorganisms and plant extract as reducing agent. It involves the use of microorganisms and plant extracts for synthesis. It is considered to be a bottom-up approach and it involves oxidation-reduction (redox) processes where metallic compounds are usually reduced into their respective nanoparticles because of microbial enzymes activity or the plant phytochemicals with antioxidant or reducing properties (Lefojane *et al*., 2020). There are three important factors that should be considered in the application of this method and they include the choice of (a) the solvent medium used, (b) reducing agent and (c) a nontoxic material for the stabilization of the nanoparticles (Usman *et al*., 2019).

In plant-mediated synthesis of NiO and SnO_2 nanoparticles extract of different parts of plants is used as a reducing agent, while in some other cases rather than using the extract either whole plant is applied on a metal substrate or an entire part of plant is soaked in metal solution.

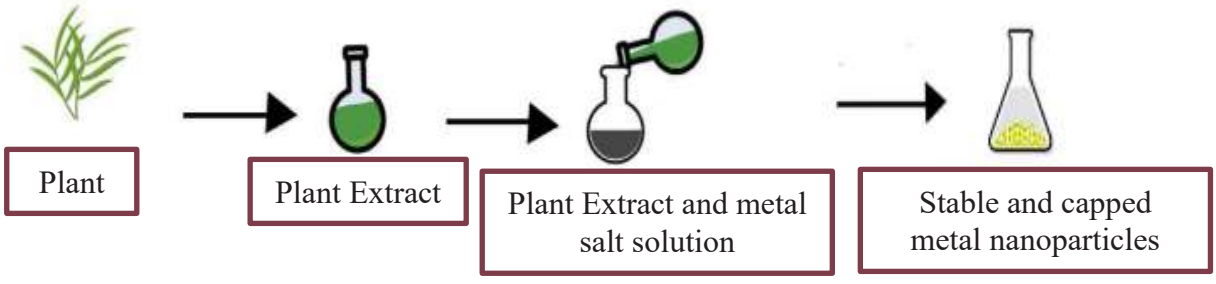

Figure 2.1: Pictorial Representation of Plant Mediated Synthesis of Metal and Metal Oxide Nanoparticles

Here, in situ reduction of metal ions occurs and their morphology can also be controlled

as porous parts of plants also act as bio-template as shown in Figure 2.1 (Singh *et al*.**,** 2020). Some naturally occurring biomolecules such as glucose, sucrose, or plant secretions may also work as good reducing agent and stabilizing agents and thus are used to fabricate NiO and SnO_2 nanoparticles (Suresh *et al*., 2020).

2.1.1 Green synthesis of NiO and SnO_2 nanoparticles

Nanoparticles (NPs) can be synthesised either by breaking down bulk materials into smaller dimensions or by joining up atoms, molecules or clusters. While the former is known as the Top down approach, the latter is referred to as the Bottom up method as illustrated in Figure 2.2 (Kumar & Kumbhat, 2016).

In the Top-down approach, a precursor material is broken down to get the nanosized particles. Top-down methods for the synthesis of nanomaterials include the following, Solid phase techniques namely, milling (mechanical and mechanochemical), Etching, Electro-explosion, Sputtering, Laser ablation, Lithography, Aresol-based techniques (electrospraying and flame pyrolsis) and Liquid-phase techniques (electrospinning) methods (Salem & Fouda, 2021).

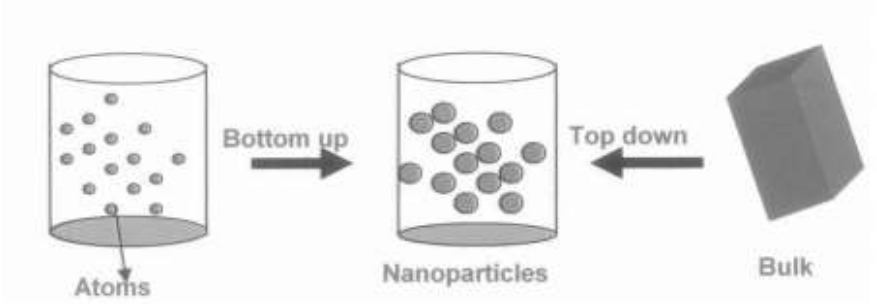

Figure 2.2: Schematic Representation of Bottom–up and Top–down Technique (Eugene *et al*., 2017)

The main disadvantage of the Top-down approach is the imperfection of the surface structure. For instance, the nanoparticles produced by the attrition may possess

relatively broad size distribution and various particle shape or geometry. In addition, they may contain significant amount of impurities (Natalia *et al*., 2015). In the Bottom-up approach, the individual atoms and molecules are placed or self assembled precisely where they are needed. Here the molecules or atomic building blocks fit together to produce nanoparticles. Bottom-up approaches have become more favorable and popular in the synthesis of nanoparticles and they involve vapor-phase techniques such as: Deposition techniques (thermal chemical vapor deposition, plasma-enhanced chemical depositon, and plasma arching), Chemical vapor condensation (molecular beam epitaxy and sputtered plasma processing), Solution-phase techniques (chemical reduction, precipitation, sol- gel, solvothermal synthesis and sonochemical synthesis) and Self assembly techniques (biological templating) (Salem & Fouda, 2021). Some of the commonest synthesis methods for the synthesis of NiO and SnO_2 nanoparticles via the bottom-up and top-down are discussed briefly in Sections 2.1.2 to 2.1.8.

2.1.2 Mechanical ball milling techniques

Mechanical alloying produces nanostructured NiO or SnO_2 nanomaterials by the structural disintegration of coarse-grained structures of its precursor salts due to severe plastic deformation. As a solid-state synthetic method, it is usually performed using ball milling equipment that is generally divided into low energy and high energy category based on the value of the induced mechanical energy to the powder mixture (Natalia *et al*., 2015). Mechanical alloying consists of repeated welding, fracturing and rewelding of powder particles in a dry high-energy ball mill until the composition of the resultant powder corresponds to the percentages of the respective constituents in the initial charge (De-Oliveira, 2020). In this process, mixtures of elemental or pre-alloyed powders are subjected to grinding under a protective atmosphere in equipment capable of high-energy compressive impact forces such as attrition mills, vibrating ball mills and shaker

mills. It has been shown that nanometer-sized grains can be obtained in almost any material after sufficient milling time.

2.1.3 Mechanochemical method

This technique involves coupling of mechanical and chemical phenomena on a molecular scale and includes mechanical breakage and chemical behavior of mechanically stressed solids such as, stress-corrosion cracking or enhanced oxidation (Jamkhande *et al.,* 2019). Mechanochemical synthesis differs from standard ball milling in that, in the standard ball milling process under inert atmosphere results in a moderate reduction of powder particle size and eventually the formation of nanosized grains within micron-sized particles. However, the mechanochemical method involves the initiation of a solid-state displacement reaction during the ball milling process which can result nanosized particles (down to ~5 nm in size) embedded within larger by-product phase particles (Munnings *et al*., 2014).

2.1.4 Etching techniques

This is traditionally the process of using strong acid or mordant (a corrosive liquid) to cut into the unprotected parts of a metal surface to create a design in the metal. In the modern approach of micro fabrication, different etching methods are used and these are the wet chemical etching and dry etching (Schoolcraft & Garrison, 1991). Wet etching is a material removal process that uses liquid chemicals or etchants to remove materials from a wafer. While in dry etching, it involves the removal of material, typically a masked pattern of semiconductor material. This is achieved by exposing the material to a bombardment of ions (usually a plasma of reactive gases such as fluorocarbons, oxygen, chlorine, boron trichloride; sometimes with addition of nitrogen, argon, helium and other gases) that dislodge portions of the material from the exposed surface (Eugene *et al*., 2017)**.**

2.1.5 Ionic sputtering

This is a process whereby particles are ejected from a solid target material due to bombardment of the target by energetic particles particularly, in the laboratory as gas ions. This can happen when the kinetic energy of the incoming particles is much higher than conventional thermal energies. Instead of using heat to eject material from a source, they can be bombarded with high-speed particles. The momentum transfer from the particles to the surface atoms can impart enough energy to allow the surface atoms to escape. Once ejected, these atoms (or molecules) can travel to a substrate and deposit as a film. Therefore, in sputtering, the target material and the substrate are placed in a vacuum chamber. A voltage is applied between them so that the target is the cathode and the substrate is attached to the anode (Govindrao *et al*, 2019).

2.1.6 Chemical vapor synthesis

Two major methods that make up these synthesis approach are (a) chemical vapor condensation (CVC) and (b) Chemical Vapor deposition (CVD). They have tremendous flexibility in producing a wide range of materials and can take advantage of the huge database of precursor chemistries that have been developed for the production of nanoparticles.

2.1.6.1 Chemical vapor condensation (CVC)

In chemical vapor condensation, vapor phase components are brought into a hot-wall reactor under conditions that favor nucleation of particles in the vapor phase rather than deposition of a film on the wall, which occurs in Chemical Vapor deposition (CVD). The precursors can be solid, liquid or gas at ambient conditions, but are delivered to the reactor as a vapor (from a bubbler or sublimation source, as necessary according to Cao (2016). Chemical Vapor Condensation (CVC) process was developed in Germany in 1994 (Rajput, 2015). When a mixture of gas reactants is delivered into a reaction

chamber, the chemical reactions among the gas molecules are induced by an input of energy such as resistant heating, laser, and plasma. Chlorides are the popular reactants for the formation of oxides because of their generally low vaporization temperature and low cost. A typical reaction for the synthesis of SnO_2 from $SnCl_4$ precursor is represented in Equation 2.1 (Ayuk *et al*., 2017).

$$SnCl_4(g) + 2H_2O\ (g) \rightarrow SnO_2(s) + 4HCl\ (g) \qquad (2.1)$$

2.1.6.2 Chemical vapor deposition (CVD)

Chemical Vapor Deposition (CVD) is a process in which a thin solid film is deposited on a heated surface via a chemical reaction from the vapor or gas phase. There are different types CVDs and they include thermal CVD, plasma CVD, laser CVD, photo-laser CVD, metal-organic chemical vapor deposition (MOCVD) to mention a few (Rajput, 2015: Suk *et al*., 2021).

A schematic diagram of a CVD is displayed in Figure 2.3.

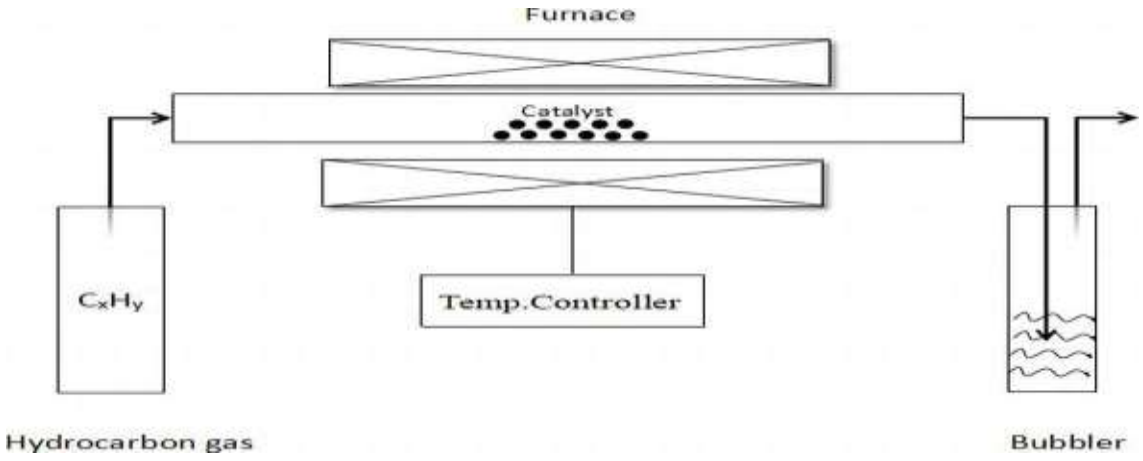

Figure 2.3: Schematic Diagram of CVD Reactor (Wang *et al.*, 2019)

Commonly used gaseous carbon sources include methane, acetylene, ethylene, carbon monoxide, benzene, toluene, and short chain alcohols (Saputri *et al*., 2020). The energy source is used to "crack" the molecule into reactive atomic carbon. The carbon then diffuses towards the substrate, which is heated and coated with a catalyst such as, Ni, Fe, Co, and Ru where it will form CNTs. Carbon nanotubes are formed if the proper parameters are maintained such as temperature and gas flow rates. Excellent alignment with positional control on a nanometre scale can be achieved using CVD. Control over the diameter as well as the growth rate of the nanotubes can also be maintained. If an appropriate metal is used, the catalyst can preferably grow SWCNTs rather than MWCNTs. The reaction temperature for synthesis of nanotubes by CVD is generally within 600-900 ^{o}C. The basic physicochemical steps in an overall CVD reaction involves four (4) or five (5) steps (Anthony and Michael, 2009; Wang *et al.,* 2019). These steps are; evaporation and transport of precursors in the bulk gas flow region into the reactor. Followed by gas phase reactions of precursors in the reaction zone to produce reactive intermediates and gaseous by-products, mass transport of reactants to the substrate surface, adsorption of the reactants on the substrate surface and surface diffusion to growth sites, nucleation and surface chemical reactions leading to film formation (Saputri *et al*., 2020).

Jamkhande *et al*. (2019) investigated the direct growth of multiwalled nanotubes (MWCNTs) on metal catalyst particles via thermal chemical vapor deposition (T.CVD) in the presence of zirconium hydride (ZrH_2) and aluminum nanoparticles. The effects of different parameters such as gas flow rates, metal catalyst systems, and temperature on the quality and quantity of the obtained MWCNTs were investigated and some interesting results were obtained. It was found that at moderate temperatures, MWCNTs growth rate on iron-based (Fe) catalyst was much more than that on nickel (Ni) and

cobalt (Co) particles. Transmission electron microscopy (TEM) results and TGA analysis revealed that metal nanoparticles as the nucleation sites come from the fragmentation of catalyst surfaces and the application of relatively small amounts of ZrH_2 significantly enhances this mechanism. Besides, crystalline structure of MWCNTs was performed by Raman spectroscopy, X-ray diffraction (XRD) and selected area electron diffraction (SAED) technique. This method shows great promise for achieving the goal of mass-production due to its high quality and yield; simplicity, and ease of scale-up.

2.1.7 Chemical precipitation

A precipitate is a solid that forms out of solution and a common example is that of the mixing of two clear solutions such as, silver nitrate ($AgNO_3$) and sodium chloride (NaCl). A chemical precipitation process consists of three main steps: chemical reaction, nucleation and crystal growth. Chemical precipitation is generally not a controlled process in terms of reaction kinetics and the solid phase nucleation and growth processes. Therefore, solids obtained by chemical precipitation have a wide particle size distribution plus uncontrolled particle morphology, along with agglomeration (Rajput, 2015; Sharma *et al*., 2017). In this strategy, the size is controlled by arrested precipitation technique. Thus, this is achieved by basic synthesising and studying the nanomaterial in situ i.e. in the same liquid medium avoiding the physical changes and aggregation of tiny crystallites. Thermal coagulation and Oswald ripening are controlled by double layer repulsion of crystallites using non-aqueous solvents at lower temperatures for the synthesis (Rajput, 2015; Rane *et al*., 2018). The synthesis involved reaction between constituent materials in suitable solvent. The synthesis added to the parent solution before precipitation reaction while a surfactant is used to maintain separation between the particles formed (Ashik *et al*., 2018). Thus, formed nanocrystals

are separated by centrifugation, washed and vacuum dried. Bahari *et al*. (2008) successfully prepared NiO nanopowder by chemical precipitation method, using nickel nitrate hexahydrate and sodium hydroxide as raw materials. The majority of obtained NiO nanopowders had an average particle size less than 50 nm in all cases. The main materials used were nickel nitrate hexahydrate ($Ni(NO_3)_2.6H_2O$), sodium hydroxide (NaOH), polyvinilpyrolidone (PVP, MW = 65000), polyethylene glycol (PEG, MW = 15000), and cetyltrimethyl ammonium bromide (CTAB). The main reactions that occured during the experimental procedure can be written in Equations 2.2 to 2.6.

$$2NaOH_{(s)} \rightarrow 2Na^{+}_{(aq)} + 2OH^{-}_{(aq)} \quad (2.2)$$

$$Ni(NO_3)_2.6H_2O \rightarrow Ni^{2+}_{(aq)} + 2NO^{-}_{3(aq)} + 6H_2O_{(l)} \quad (2.3)$$

$$Ni^{2+}_{(aq)} + 2OH^{-}_{(aq)} + XH_2O_{(aq)} \rightarrow Ni(OH)_2.XH_2O_{(s)} \quad (2.4)$$

$$Ni(OH)_2.XH_2O_{(s)} \rightarrow Ni(OH)_{2(s)} + XH_2O_{(g)} \quad (2.5)$$

$$Ni(OH)_{2(s)} \rightarrow NiO_{(s)} + XH_2O_{(g)} \quad (2.6)$$

2.1.8 Sol–gel synthesis

Sol–gel processing is also a promising method for the preparation of nano dimensional materials. It is most commonly used technique for the preparation of bulk nanomaterial of Metal Oxides (Parashar *et al*., 2020). The reaction product of the sol–gel synthesis could be either colloidal powders or films. One of the advantages of this method is the ability to control the microstructure of final product by controlling chemical reaction parameters. It involves the evolution of networks through the formation of colloidal suspension (sol) and gelatin or a network in continuous liquid phase (gel). The precursor for synthesising these colloids could be either inorganic salts or organic compounds known as metal alkoxides and aloxysilanes. The most widely used are tetramethoxysilane (TMOS), and tetraethoxysilanes (TEOS) which form silica gels. The

sol gel process involves initially a homogeneous solution of one or more selected alkoxides. These are organic precursors for silica, alumina, titania, zirconia, among others (Ashik *et al*., 2018). A catalyst is used to start reaction and control pH. Sol-gel formation occurs in four stages;

i. Hydrolysis.
ii. Condensation.
iii. Growth of particles and
iv. Agglomeration of particles.

According to Umbreen and Bushra, (2013) Nanoparticles of nickel Oxide has been synthesised by sol-gel method. In the first step, nano sols were prepared by dissolving metal salt in suitable Solvent. On condensation, nano sols were converted into nanostructured gel of nickle oxide nanoparticles was found to be 8.78 nm.

2.2 Review of Literature on Synthesis and Coating Application of Nanoparticles

Raj *et al*. (2014) assessed the effect of Ag doped SnO_2 nanoparticles on the corrosion inhibition of mild steel in 1 N H_2SO_4 solution by Potentiodynamic Polarization and Electrochemical Impedance Spectroscopy studies. The Ag and SnO_2 nanoparticles were prepared by green synthesis using *Cleistanthus collinus* methanolic extract. Results revealed that 60% SnO_2 nanoparticles in Ag exhibited the best corrosion inhibition for the mild steel in 1 N sulphuric acid solution, while the polarization curves revealed a mixed-type suppression of both anodic and cathodic processes and EIS study indicated two-time constants. They concluded that Ag doped SnO_2 nanocomposites acted as a mixed type inhibitor on mild steel after modification of the surface of substrate, forming a protective stable barrier coating against sulphuric acid environment. This was, attributed to the double layer charging and adsorption of the inhibitor.

Fayomi *et al*. (2015) in their research investigated the microstructural, mechanical and anti-corrosion properties of nanocomposite Zn–Al coating containing SnO_2 nanoparticles prepared from sulphates electrolyte by electrodeposition on mild steel substrate. The morphologies of the coating were analysed using SEM/EDS, AFM, Raman and X-ray diffraction techniques. The anticorrosion behaviour of the coating prepared with different concentrations of SnO_2 (7 and 13 g/L) and potential of (0.3 and 0.5 V) were examined in 3.65% NaCl solution using linear polarization techniques. The wear and hardness properties of the coatings were performed under accelerated reciprocating dry sliding wear tests and diamond micro-hardness tester respectively. Results obtained from the study showed that the incorporation of SnO_2 in the plating bath was responsible for the increase in corrosion resistance and mechanical properties of Zn–Al–SnO_2 composite coatings. While the SEM images showed a homogeneous grain structure and fine morphology of the coatings. The researchers concluded that the hardness values improved with the amount of the SnO_2 embedded into the Zn–Al metal deposit and effective deposition parameters.

Kartal *et al*. (2016) synthesised Nickel/multiwalled carbon nanotube (MWCNT) composite coatings that were deposited by pulse electrocodeposition method from a Watt's type electrolyte. The electrodeposited Ni matrix coatings were characterised by scanning electron microscopy, Raman spectroscopy and X-ray diffraction analysis for surface morphology, functional groups and crystal phases respectively. The influence of peak current density on the particle codeposition and distribution, the surface morphology, microstructure, microhardness and wear resistance of nanocomposite coatings were studied. Findings by the authors revealed that by reinforcing Ni matrix with MWCNTs, grain size of nickel matrix was decreased from 42 to 30.6 nm, which

resulted in an improved microhardness. More so, they observed that the effect of increasing current density on grain size beyond 3 A dm^{-2} is negligible and wear resistance significantly improved depending on MWCNT reinforcement at current density up to 3 A dm^{-2}. Therefore, the process parameters belonging to 3 A dm^{-2} and MWCNT concentration of 4 g L^{-1}were detected as optimum variables to develop fine structure and effective mechanical properties. In conclusion, they reported that Ni matrix with MWCNTs composite coatings can be assessed as good future candidates for high wear resistant microelectromechanical systems applications.

Research was conducted by Shajudheen *et al*. (2017) carried out a study on the comparison of anticorrosion studies of titanium dioxide and nickel oxide thin films fabricated by spray coating technique. According to the authors,' titanium and nickel oxide nanoparticles for the study were synthesised by chemical precipitation method, and coated on steel substrate (304L SS) using spray coating technique. The corrosion resistance of 304L SS substrates spray coated with nanostructured titanium dioxide (TiO_2) and Nickel oxide (NiO) in 3.5% NaCl was studied using Tafel polarization curve and electrochemical impedance spectra. Results revealed that the polarization curves of coated 304L SS substrates exhibited positive shift in corrosion potential with respect to that of bare. While the Nyquist plot of the coated films confirmed that, the coatings have improved the corrosion resistance of 304L SS substrate. They reported that the variation of impedance with frequency of the coated 304L SS before and after salt spray test showed that NiO and TiO_2 films are quite stable in salt environment, as there was little change in the surface morphology and surface roughness of films after corrosion test and this further confirmed the films stability in corrosive environment. Hence, the absence of cracks in AFM images of films subjected to load showed that the films were quite tough. They concluded that the non-existence of rust in coated substrate exposed

to salt environment (5% NaCl at 30°C) for 390 hr confirmed that the films could act as anticorrosive coating for 304L SS substrate in adverse salt environment.

Abdulrahaman *et al*. (2017) investigated the mechanical properties and corrosion behavior of mild steel coated with carbon nanotubes at different coating conditions. Multi-walled carbon nanotubes (MWCNTs) for the study were synthesised via the conventional chemical vapour deposition method using bimetallic Fe–Ni catalyst supported on kaolin, with acetylene gas as a carbon source. HRSEM/HRTEM analysis of the purified carbon materials revealed significant reduction in the diameters of the purified MWCNT bundles from 50 to 2 nm attributed to the ultrasonication assisted dispersion with surfactant (gum arabic) employed in purification process. The authors reported that as coating temperature and holding time increased, the coating thickness reduced. The mechanical properties (tensile strength, yield strength, hardness value) of the coated steel samples increased with increase in coating temperature and holding time. Comparing the different coating conditions, coated mild steels at the temperature of 950°C for 90 min holding time exhibited high hardness, yield strength and tensile strength values compared to others. They concluded that the corrosion current and corrosion rate of the coated mild steel samples decreased with increase in holding time and coating temperature.

Deepa *et al*. (2017) synthesised copper oxide and nickel oxide-copper oxide (NiO-CuO) nanoparticles were by co-precipitation method in aqueous solution using sodium hydroxide as precipitating agent and cetyl trimethyl ammonium bromide (CTAB) as a surfactant. The particles were characterised by XRD, SEM, EDS and FTIR analysis. Afterwards, the prepared metal oxide nanoparticles were employed for the fabrication of zinc-composite coating on mild steel by electroplating, while their corrosion behaviour was investigated by Tafel and Electrochemical impedance spectroscopy in corrosive

media of 3.5% NaCl solution. The XRD results showed smaller crystallite size of NiO-CuO nanocomposites compared to CuO nanoparticles. SEM image of CuO nanoparticles showed small spindle shaped like structure and the spherical shaped morphology was observed in NiO-CuO nanoparticles. The EDS analysis showed that the prepared nanoparticles were free of impurities, FTIR spectra revealed the presence of –OH group in the nanoparticles. The aurthors reported that from Tafel and electrochemical impedance spectroscopy studies, the as-synthesised Zn-NiO-CuO nanocomposite showed better anticorrosive property compared to Zn-CuO and pure Zn coating, as confirmed by by OCP measurements.

Deepa and Venkatesha (2018) synthesised Ni doped SnO_2 nanoparticles used as a composite additive for Zn-coating. The synthesis was carried out by the combustion method using citric acid as a fuel. Zn-Ni doped SnO_2 composite coating was deposited on mild steel by an electroplating technique; surface characterisation and elemental analysis of the coated samples were examined by X-ray diffraction spectroscopy (XRD), scanning electron microscopic images (SEM) and energy dispersive spectroscopy (EDAX). The surface morphology of Zn-Ni doped SnO_2 composite before and after corrosion showed a more compact surface structure with respect to the pure Zn-coat. The corrosion resistance property of the Zn-Ni doped SnO_2 composite coating was studied by Tafel polarization and electrochemical impedance spectroscopy and afterwards, the authors concluded that the presence of the Ni doped SnO_2 in Zn-coating increased the corrosion resistance property of Zn-deposit as compared to pure Zn-deposit.

Wang *et al*. (2018) evaluated the electrochemical behavior of nano-ZrO_2 particles in the co-deposition process. They used Electro-crystallization mechanism, electrodeposition parameters of composite coatings, Cyclic voltammetry (CV), Chronoamperometry

(CA), and Electrochemical Impedance Spectroscopy (EIS) techniques to offer a favorable reference for the electrochemical studies in an acidic amino sulfonate bath, and calculated kinetic parameters by fitting the experimental curves. The results of (CV) suggested that the co-deposition of nano-ZrO_2 particles and matrix metal caused the initial deposition potential of Ni^{2+} and Co^{2+} to shift to more positive values (−0.80 V vs SCE), while the nano-ZrO_2 inhibited the reduction of H^+ and decreased the cathodic polarization in co-deposition. The electro-crystallization of Ni-Co and Ni-Co-ZrO_2 sedimentary layer were governed by the Scharifker–Hill instantaneous nucleation model, and the nucleation rate of composite coatings was higher at potentials ranging from (−1.10 to −1.15 V), and nano-ZrO_2 absorbed on an electrode surface promoted the nucleation/growth of Ni^{2+} and Co^{2+}. However, nano-ZrO_2 particles hindered the nucleation/growth of Ni^{2+} and Co^{2+} at (−1.20 and −1.25 V vs. SCE); the calculated results were consistent with the theoretical analysis of experimental curves. The EIS test showed that the nano-ZrO_2 particles did not significantly affect the electric double-layer capacitance at the interface; nevertheless, the charge transfer resistance reduced significantly. They concluded that the addition of the nano-ZrO_2nanoparticles in the bath promoted the preferred orientation of the sedimentary layer shift to the (111) plane, moreover, the dense and smooth surface morphology of the composite coatings could be seen in the SEM images.

2.3 Design of Experiment

Design of experiment is a methodology for systematically applying statistics to scientific experiments. DOE was carried out in this research using Response Surface Methodology (RSM).

2.3.1 Response surface methodology (RSM)

RSM method is suitable for fitting a quadratic surface and it helps to optimize the process parameters with a minimum number of experiments, as well as to analyze the interaction among process parameters (Chelladurai *et al*., 2019). RSM is a collection of mathematical and statistical techniques useful for developing the empirical model building, improving and optimizing processes parameter and it can also be used to find the interaction of several factors (Montgomery, 2014; Chelladurai *et al*., 2020). RSM is a statistical method that uses quantitative data from the related experiment to determine regression model and to optimize a response (output variable) which is influenced by several independent variables (input variables). In order to optimize these important process parameters with the aim of minimizing the number of experimental runs, methods such as the Response Surface Methodology (RSM) have been applied (Ba-Abbad *et al*., 2013; Chelladurai & Arthanari, 2018). Such statistical method is used to evaluate the relationship between the multiple independent variables in order to determine the optimum conditions required to produce the desired size of nanoparticles (Chelladurai *et al*., 2020). The optimization process by RSM includes three main steps: (a) selection and implementation of the appropriate experimental design, (b) estimation of all the coefficients of the model from the developed mathematical model using analysis of variance (ANOVA), (c) validation of the final model by prediction and experimental runs of the process response (Senthilkumar *et al*., 2013; Das & Dewanjee *et al*., 2018).

2.3.2 Orthogonal array Box–Behnken design (BBD)

The Box–Behnken design is a second-order technique based on three-level factorial design for three factors and more with selected points from a system arrangement (Beg & Akhter, 2021). This design has two different forms to present the three factors graphs:

(a) cube that contains the central and the middle points of the edges and (b) Three interlocking 2^2 factorial designs with central point as shown in Figure 2.4.

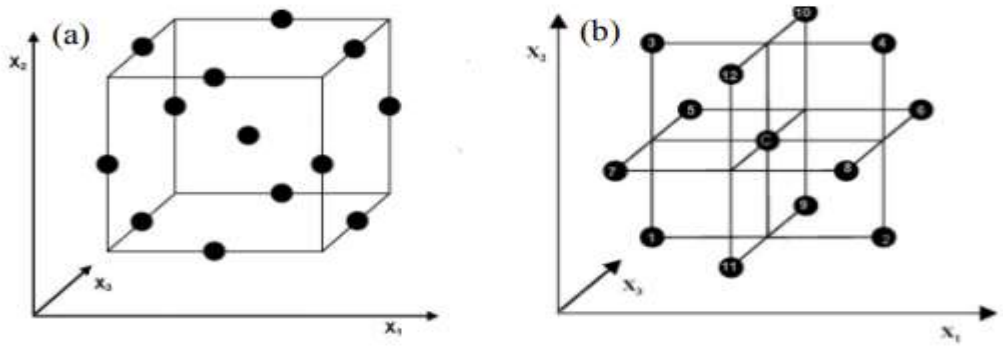

Figure 2.4: Forms of Box–Behnken Design (a) Cube (b) Three Interlocking 2^2 Factorial Design (Alaoui *et al*., 2015)

The number of experimental runs required (N) is calculated by N=2k (k-1) + C, where the number of factors is k and the centre point is C. The main advantage of this design is that it can reduce the number of runs and can be used for a large number of factors in one process. To improve the performance of the Box–Behnken Design, the three levels of the factors should be adjusted as −1 (lower), 0 (medial) and +1 (higher) (Alaoui *et al*., 2015; Beg & Akhter, 2021).

The advantages of Box-Behnken design compared to other surface design is that it is more efficient where the efficiency of one experimental design is defined as the number of coefficients in the estimated model divided by the number of experiments (Ait-Amir *et al*., 2020). However, Box-Behnken design does not contain combinations at highest or lowest levels of all selected process factors (Alaoui *et al*., 2015). Minitab ® software (Stat Ease Inc., Version 19.0) based on the Box–Behnken design was applied to optimize NiO and SnO_2 NPs synthesis following the quadratic polynomial in Equation 2.7.

$$Y = \beta_0 + \sum_{i=j}^{k} \beta_i X_i + \sum_{i=j}^{k} \beta_{ii} X_i^2 + \sum_{i=1} \sum_{j=i+1} \beta_{ij} X_i X_j + \varepsilon \qquad (2.7)$$

where Y is the predicted response (target of study), $\beta_i$are the coefficients of the linear

terms, $\beta_{ii}$are coefficients of the quadratic terms, $\beta_{ij}$are coefficients of the interaction factors, X_i and X_j indicated the independent variables and ε is the random error. The mathematical relationship between the three factors X_1, X_2 and X_3 with their coefficients represented by a second order calculation in Equation 2.8.

$$Y = \beta_0 + \beta_1 X_1 + \beta_2 X_2 + \beta_3 X_3 + \beta_{11} X_1^2 + \beta_{22} X_2^2 + \beta_{33} X_3^2 + \beta_{12} X_1 X_2 + \beta_{13} X_1 X_3 + \beta_{23} X_2 X_3 \quad (2.8)$$

2.4 Model Fitting and Statistical Analysis

ANOVA (Analysis of variance) was used for graphical analyses of the data to define the interaction between the process variables and the responses to estimate the statistical parameters. Minitab 19 has been used for the regression analysis of experimental data, to plot the response surfaces, and contour plot at the optimized condition. The statistical significance was checked by the F-test in the same program. The accuracy of the fitted polynomial model was determined by the coefficient of R^2. The significant model terms were evaluated by the probability value (P-value) at 95% confidence interval.

2.5 Carbon Nanotubes

Elemental carbon belongs to Sp^2 hybridization, which enhance its ability to form different structures. Carbon nanotube is an allotrope of carbon discovered over two decades ago by Ijima in 1991 while carrying out an analysis on helical arrangement of carbon atom on seamless coaxial cylinders (Gupta *et al*., 2019). It was also believed that nanotubes have been earlier discovered by Radushkevich and Lukyanovich (1952) based on TEM images of some nanosized carbon filaments. Nanotube is a tubular carbon structure made up of several tens of graphitic shells with an adjacent shell separation of ~0.34 nm, diameters of ~1 nm and high length/diameter ratio. Recently, carbon nanotube (CNTs) appears to be the leading material with high demand for diverse applications (Rahman *et al*., 2019). Structurally, carbon exist as diamond,

graphite, amorphous carbon, fullerenes, carbon fibers, carbon onions, carbon spheres or balls, carbon nanotubes which emanate from the unique ability of carbon to forms sp, sp^2 and sp^3 configurations (Eatemadi *et al.,* 2014; Baig *et al*., 2021).

2.5.1 Properties of carbon nanotubes

The unique properties of carbon nanotubes (CNTs) are classified as mechanical, chemical, electrical and discussed as follows:

2.5.1.1 Mechanical properties

Carbon nanotubes are known to exhibit high stiffness and axial strength due to formation of carbon–carbon sp^2 bonding existing between their molecules. The stiffness of CNTs is comparable to that of diamond and possesses an estimated tensile strength of 200 GPa, which is one hundred times higher than the value displayed by steel while weighing six times less (Kumar and Yoshinori, 2010). Practically, CNTs has a very high Young's modulus equivalent to that of graphite (1.4 TPa). In addition, it was established that the structure of CNTs is not easily affected by change in pressure. These properties make them suitable for reinforced composites and nanoelectromechanical systems. In contrast, the Young's modulus and tensile strength of high-strength steel is around 200 GPa, and 1-2 GPa respectively (Zhang *et al.,* 2005).

2.5.1.2 Electrical properties

CNTs can either be electrically conductive or semi-conductive, depending on their diameter, leading to nanoscale wires and electrical components due one-dimension character and electronic structure of graphite (Venkataraman *et al*., 2019). These one-dimensional fibres possess electrical conductivity as high as that of copper and thermal conductivity as high as diamond. Conversely, CNTs have low electrical resistance, which could be as a result of electron collision resulting to defect in crystal structure of

the carbon materials. This collision normally deflect electron from its path way and as such electron can either move forward or backward in 1-D structure indicating a low resistance (Marx & Barth, 2010: Sonia & Nazmu, 2018). CNTs has a high current density of 10^9 A/cm^2 that has allowed its usage in cathode ray tube emitting high rate of electrons hitting the target with minimum energy input (Kuwana *et al*., 2005). Thus, replacing the old giant cathode which required high supply of energy via magnetic or electric field, CNTs could therefore be regarded as the best electron field-emitters. Electronic computer could also be produced when nanotube is joined end to end together to form diode (Sonia & Nazmu, 2018).

2.5.1.3 Thermal properties

CNTs exhibit dual thermal properties and can act as good conductor along the tube and sometimes laterally act as insulator. The thermal conductivity of CNTs doubles that of diamond (Kuwana *et al*., 2005). It was established that carbon nanotubes can transmit up to 6000 W/mK at room temperature (Hone *et al*., 2002; Kuwana *et al*., 2005). Whereas, Copper can only transmit 385 W/mK, which was the best-known material with good thermal conductivity. Recent studies revealed that CNTs are more stable to oxidation and reactive than activated carbon. Therefore, CNTs are in the forefront of today's research as coating material due to their superior properties such as high resistance to acid/basic media and high surface area/porosity respectively (Marx & Barth, 2010).

2.5.2 Type of carbon nanotubes

There are two main types of carbon nanotubes that have high structural perfection and are discussed as follow:

2.5.2.1 Single walled carbon nanotubes (SWCNT)

Single walled nanotubes (SWCNT) consist of a single graphite sheet seamlessly wrapped into a cylindrical tube with a diameter ranging from 1-2 nm (Ajayan *et al*., 2000). The length of SWNTs are in micrometer range (Eatemadi *et al.,* 2014). A SWCNT could exhibit as chiral, zigzag or armchair depending on integer values representations (Das *et al.*, 2014). SWCNTs can be arranged to form hexagonal crystal-like configuration as shown in Figure 2.5.

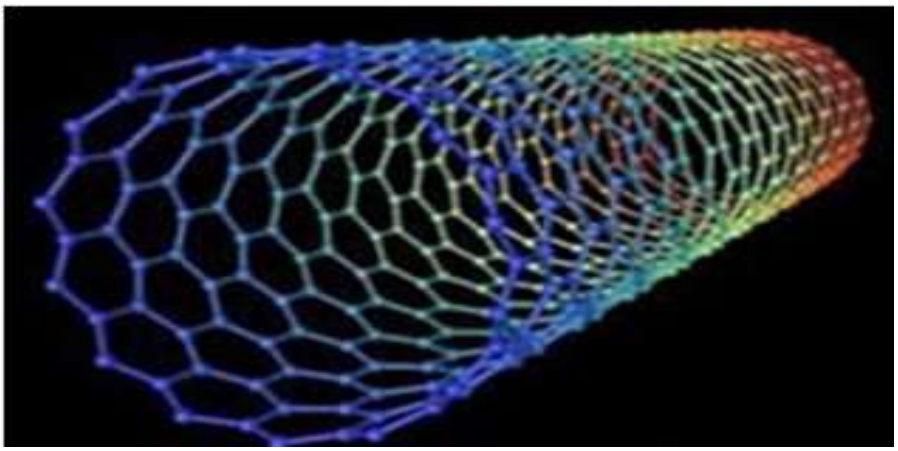

Figure 2.5: Structure of Single Walled Carbon Nanotube (Sonia and Nazmul, 2018)

2.5.2.2 Multi-walled carbon nanotubes (MWCNTs) and structures

Multiwalled nanotubes (MWCNT) consist of concentric array nested like rings of a tree trunk which can be in form of scroll multilayer, coaxial polygonised or coaxial cylinder curve nanotubes depending on interlayer's structural folding (Das *et al.*, 2014). The inner diameter of MWCNTs ranges from 0.4 nm up to a few nanometers while outer diameter varies from 2 nm to 30 nm depending on the number of graphene sheet. In addition, the tips of MWCNT often has a closed dome shape capped with half-fullerene molecules (pentagonal defects), and axial size differs from 1μm to a few centimetre as shown in Figure 2.6. The roll end half-fullerene molecules allow the closure of the tube at both ends (Eatemadi *et al.,* 2014).

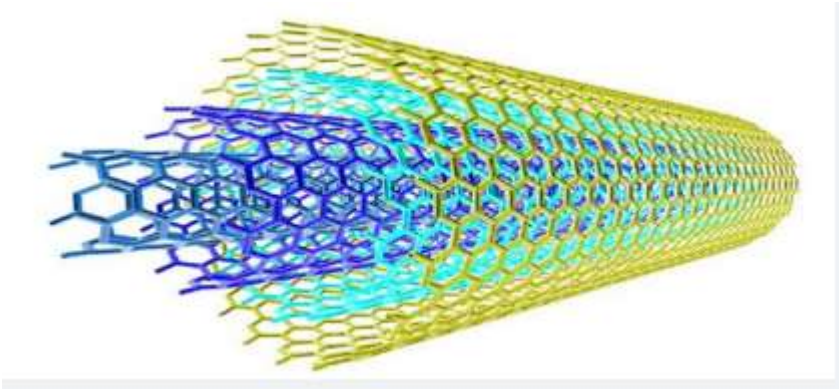

Figure 2.6: Structure of Multi Wall Carbon Nanotube (Sonia and Nazmul, 2018)

2.5.3 Synthesis of carbon nanotubes

Carbon nanotubes can be prepared through arc discharge (Shahid *et al.,* 2013), laser ablation, catalytic chemical vapor deposition (Angulakshmi, 2015), and closed systems (for instance in an autoclave or sealed quartz tube) under pressure (Hintsho *et al.,* 2015). The CVD techniques can be classified into floating catalyst process, gas phase process and the substrate (support) CVD process that employ the use of a thermally stable material to support metal particles that are responsible for the molecular decomposition of carbon source to form the CNTs. It is worthy to mention that CVD is the most popularly used techniques for synthesis of CNTs in large scale, owing to the fact that it allows the use of different substrates and enables the growth of CNTs in low cost to form carbon material (Angulakshmi *et al.,* 2015).

2.5.3.1 Chemical vapor deposition

Chemical vapor deposition (CVD) is a versatile process in which gas-phase molecules are decomposed to reactive species, leading to film or particle growth, CVD processes can be used to deposit a wide range of conducting, semiconducting, and insulating materials. A recent thrust of CVD techniques has been the controlled fabrication of nanomaterials in porous hosts including zeolite nano channels (Li *et al*., 2004). The

experimental setup used for the preparation of the carbon nanomaterials is schematically shown in Figure 2.7. The reactor is made of 550 mm long quartz tube of 35 mm inner diameter with provisions of inlet of reactants and outlet of spent vapours. The reactor is placed in a tubular electrical furnace. The substrates are placed in pyrolysis zone of the horizontal quartz reactor.

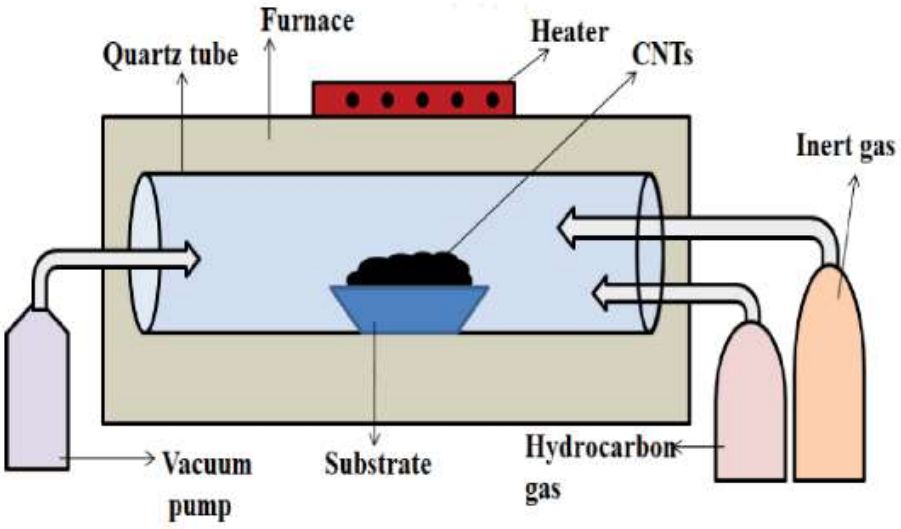

Figure 2.7: Schematic Diagram of Experimental Set Up used for the Preparation of CNTs by CVD (Jagadeesan *et al*., 2020)

Hydrocarbons were most frequently used as carbon sources for the production of CNTs by the CVD method at ambient pressure, however, there have been few articles published concerning the analysis and relative efficiency of different hydrocarbon sources for CNTs synthesis via the CVD process (Danafar *et al*., 2009). Two advantages of CVD methods are the ability to controllably create films of widely varying stoichiometry and to uniformly deposit thin films of materials, even onto non-uniform shapes.

During CVD, a gas phase carbon rich molecule (C_2H_2) is pyrolysed in the presence of a transition metal catalyst (Fe, Mo, Cu, Co) at high temperatures (800–1000°C) Though hydrocarbons do offer some disadvantages, as they are mostly hazardous and can form

polyaromatic by-products during a CVD synthesis process (Dunens *et al*., 2009).

There are many different types of CVD such as catalytic chemical vapor deposition (CCVD) either thermal (Vander Wal *et al*., 2003) or plasma enhanced (PE) oxygen assisted CVD (Iijima, 1993), water assisted CVD (He *et al*., 2010), microwave plasma (MPECVD) (Vander Wal *et al*., 2003) radiofrequency CVD (RF-CVD), or hot-filament (HFCVD) (Dervishi *et al*., 2009).

Among the synthesis methods of carbon nanotubes, the catalytic chemical vapour deposition (CCVD) is currently the standard technique and the most commonly used, due to its versatility in the growth morphology control of the carbon nanostructures by monitoring the reaction conditions (catalysts, temperature, composition and flow rate of the carrier gas, and hydrocarbons). It is considered as the most promising method for large-scale production of carbon nanostructures (Zhao *et al.,* 2006).

Catalytic chemical vapour deposition uses transition metals such as Fe, Co, Ni and Cr as active catalyst to catalyze the formation of carbon nanomaterials on the surface of suitable substrates using appropriate carbon source. In fact, catalytic activities of a metal-support system depend on a variety of factors ranging from the size and dispersion of the metal catalyst to chemical composition of vapour as well as on the crystalline phase of the support materials itself. Several studies have been focused on the control of MWCNTs growth by the introduction of monometallic and bimetallic catalyst nanoparticles, using carrier gas, in to the reaction chamber under decomposition of ethylene, methane, ethane and solid carbon (Vander Wal *et al*., 2003). In bimetallic systems, the introduction of another highly active metal species (such as nickel) may increase the activity and stability of the iron-based catalyst (Dervishi *et al*., 2009). Each production process has its limitation in respect to purity and cost as summarized in

Table 2.1.

Table 2.1: Comparison of Different Techniques used in the Synthesis of Carbon Nanotubes (Bose *et al*., 2010; Angulakshmi *et al.,* 2015)

Technique	Carbon impurities	Purity of carbon	Space time
Arc discharge	High	High	Low
Laser ablation	High	High	Low
CCVD/CVD	Low	High	High

The metals widely utilized for the synthesis of CNTs are iron (Fe), cobalt (Co) and nickel (Ni), Molybdenum (Mo) as well as the alloys of these metals. The choice of these metallic nanoparticles is based on the fact that carbon is easily decomposed at high temperature on these nanoparticles, thus influencing high carbon diffusion rate (Kumar and Yoshinori, 2010). The synthesis of carbon nanotubes also required support material where metals are usually dispersed and carbon source (methane, ethane, acetylene and agricultural products). The support materials utilized in the CVD method plays a significant role in improving the catalyst performance.

2.6 Nano-Formulation Coating Technique, Advantages and their Short Comings as Alternatives to Corrosion Inhibitors

Nanocoatings can be obtained by three general deposition methods, as shown in Figure 2.8 mechanical, physical, and chemical deposition according to Wunderlich (2014). Mechanical deposition is the cheapest, and can be achieved through spray, paint, spin-coating, or dip-coating.

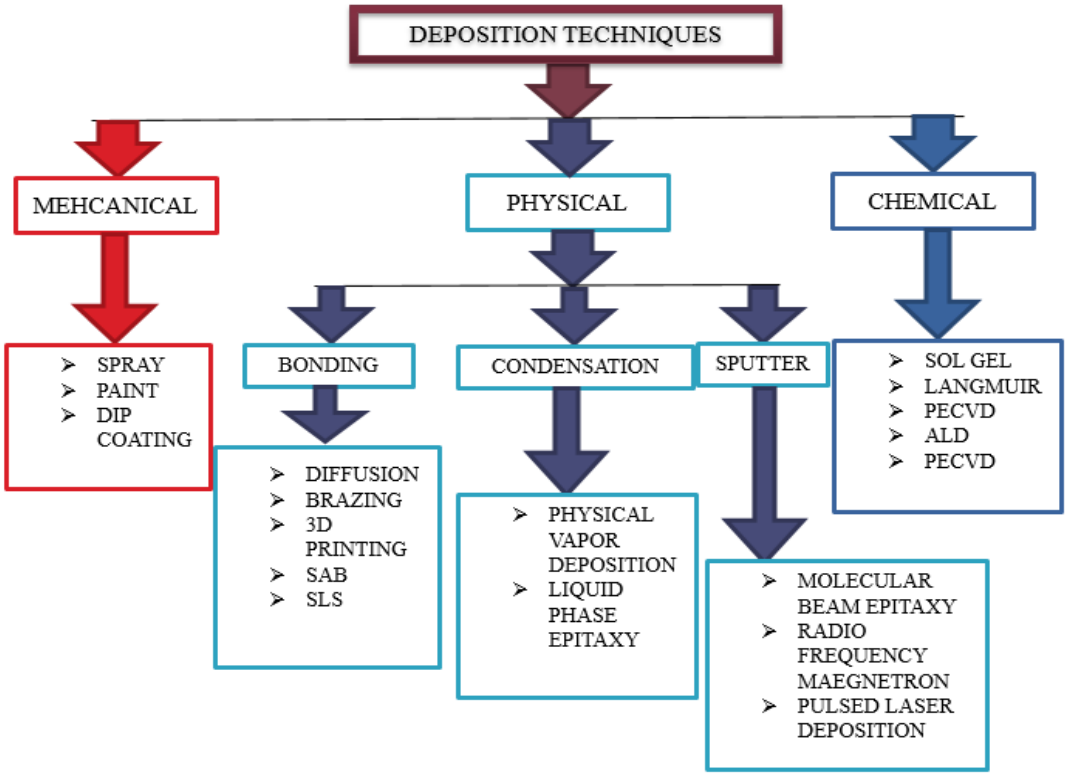

Figure 2.8: Nanocoating Techniques (Wunderlich, 2014)

2.6.1 Mechanical deposition

In the dip-coating process, the uncoated sample is immersed in a liquid and then withdrawn with a well-defined withdrawal speed at controlled temperature and atmospheric conditions. During the process, the environmental conditions (atmosphere and temperature) control the solvent evaporation from the diluted solution. During this stage, a densification of the solution occurs, leading eventually to a gelation phenomenon, favored by the presence of solid filler, with the formation of a compact and homogeneous film well adherent to the substrate. The thickness of the coating is mainly defined by the picking speed, the filler content, and the viscosity of the liquid (Brinker *et al*., 1991). The adhesion with the substrate is guaranteed choosing a suitable binder matrix able to interact both to filler and substrate surface in order to offer high adhesion and cohesion of the constituted composite coating.

2.6.2 Physical deposition

Physical deposition can be done by either bonding, condensation, or sputtering.

2.6.2.1 Physical diffusion bonding

In physical diffusion bonding, a moderate pressure and temperature are applied, while in brazing bonding, lubricants are added under higher temperatures. Bonding with surface-activated bonding (SAB) is performed at low temperatures and pressures for cleaned and atomically flat-polished surfaces. Moreover, selective laser sintering (SLS) is a three-dimensional (3D) printing technique in which a material is built layer-by-layer with the new manufacturing technology, additive manufacturing.

2.6.2.2 Physical deposition condensation

The second method of physical bonding is condensation. It is usually performed at vacuum as in physical vapour deposition (PVD), whereas it might be performed at regular pressure conditions, such as in liquid phase epitaxy (LPE).

2.6.2.3 Physical deposition sputtering

Sputtering techniques are usually more expensive as they have lower growth rates, yet they produce perfect epitaxial growth with strong bonds. Sputtering is conducted with either molecular beam epitaxy (MBE), radio frequency (RF) magnetron, or pulsed laser deposition (PLD).

2.6.3 Physical deposition chemical

Finally, chemical bonding techniques are usually cheaper, but requires expensive precursors, such as in Langmuir, sol-gel, and atomic layer deposition (ALD). Plasma-enhanced magneto optical chemical vapour deposition works at specified substrate temperature, pressure, and power (Wunderlich, 2014).

Each of the above-mentioned techniques of thin film deposition on the surface of the substrate affect the uniformity and surface properties such as strength, fracture toughness, and ductility (Agarwala *et al*., 2006). Each technique has its own advantages and disadvantages, and choosing the matching technique should be done while studying all of the processing elements. As in the case with conventional coatings, the technique should be applied with the optimized conditions in order to achieve the best surface coverage of the nanocoating in terms of uniformity, smoothness, adhesion, and crack-free surfaces. For instance, dip coating which was employed in this has been known to be inexpensive and can coat complex shapes, but it might suffer from thermal expansion mismatch and require high sintering temperatures. Pulsed laser deposition and hot pressing can produce dense and uniform coatings, but they have the same disadvantages as dip-coating. Some techniques might produce an amorphous structure due to the rapid cooling, as in thermal spraying and sputter-coating. Sol-gel is a preferred technique, as it has low pressing temperatures and it is a relatively cheap coating; however, it requires expensive raw materials, and needs a controlled processing atmosphere (Hamdy, 2010). Hence, more studies should be conducted to optimize the conditions and processing steps of different nanocoating techniques, as multi-step technologies are not attractive in the industrial market.

However, nanocoatings might not function as protective surfaces in some circumstances.

However, a nanocoating is an effective physical barrier at high-temperature applications, as the high density of their grain boundaries provide fast diffusion paths of passivated ions and better adhesion of the protective oxide layer to the substrate's surface (Gao & Li, 2004). Yet, the higher grain boundary fraction provides more anodic sites, which makes the surface more susceptible to corrosion attack. Moreover,

nanocoatings form a defensive structure by incorporating in the vacancies, dislocations, and grain/interphase boundaries. These features have the advantage of forming a more effective passivation layer, as the diffusion of passivating ions will be faster. On the other hand, the agglomeration of these nanosized materials might happen due to the accelerated diffusion of aggressive ions, which causes non-uniform surfaces and increases the possibility of active sites formation, thus decreasing corrosion resistance (Saji, 2012). Such a contradiction urges the need to study the corrosion behaviour of each nanocoating, while taking into consideration all of the surrounding conditions that are involved. Up until now, the wear/scratch resistance and corrosion behaviour of nanocoated surfaces is still under investigation; more research needs to be performed in this area.

2.6.4 Corrosion inhibitors

Corrosion inhibitors are chemical compounds which, when added in small quantities, reduce or completely prevent the corrosion process (Rajendran, 2012). Inorganic compounds like chromate, phosphates, molybdates, and a variety of the organic compounds containing heteroatoms which includes nitrogen, sulphur, and oxygen are being investigated as corrosion inhibitors. Nevertheless, the toxicity of inorganic corrosion inhibitors to the environment has prompted the search for green corrosion inhibitors as they are biodegradable, renewable, and free from toxic compounds (Saji, 2010). Most organic inhibitors contain at least one functional group. The strength of adsorption of organic inhibitors relies on the charge of this group rather on the heteroatom present in the organic molecule. The structure of the rest of the molecule influences the charge density on the functional group (Yaro *et al*., 2013). Most common organic inhibitors belonging to different chemical families such as fatty amides (Olivares *et al*., 2006), pyridines (Noor, 2009), imidazolines (Olivares-Xiometl *et al*.,

2009), other 1,3-azoles (Popova *et al*., 2007) and polymers have showed excellent performance as corrosion inhibitors (Tallman *et al*., 2002). The practical application of many of those inhibitors poses risk for environmental protection standards, cost and toxicity. Thus, there is a strong need to develop efficient and environmentally friendly corrosion inhibitors.

2.6.5 Nanocoating techniques

Nanocoating has one component that is in the nanoscale. Due to the very fine sizes of the particles used in this nanocoating, filling the spaces and blocking the corrosive elements from diffusing into the surface of the substrate will be more efficient. In addition, the high density of the nanocoatings' grain boundaries provide better adhesion properties, which will increase the lifetime of the coating. Nanocoatings provide superior mechanical and electronic properties, which make them stronger, harder (Rahmani *et al*., 2015), and have better resistance to environments with corrosion and wear (Schuh *et al*., 2003). Nanocoating technology has influenced the development of paints greatly with the addition of properties such as self-healing (Sriraman *et al*., 2012), self-cleaning (Andreatta *et al*., 2007), and high scratch and wear resistance (Wang *et al*., 2016). It also enabled the availability of replacements for chromium toxic coating (Hibbard *et al*., 2001; Ma *et al*., 2016). In the same manner, smart nanocoatings greatly benefit in reducing corrosion and biofouling effects. They are developed to respond to external stimulus such as pH, humidity, heat, stress, coating distortion, and electromagnetic radiation, by releasing controlled amounts of inhibitors in order to repair and cure defects and damages (McGee *et al*., 2012).

One of the widely used cost-effective methods for corrosion protection of metallic substrates is to apply surface engineering coatings and nanocoatings (Davis, 2001). In recent years, the research and development of environmentally friendly alternatives to

chromate-based coatings, due to their high toxic and carcinogenic limits, was widely investigated (Li *et al*., 2017). In this context, several developments have been made in the use of nanocomposite coatings that offer a synergistic action of active inhibition and corrosion barrier (Montemor, 2014). The barrier properties of a nanocoating can slow down the diffusion rate of the aggressive electrolyte towards the metal substrate. However, the presence of local defects or damage on the coating surface may allow an easier penetration of the aggressive species towards the metal interface, strongly limiting its durability (Zheng *et al*., 2017).

Consequently, the synergistic integration of the barrier action with active protection, through the addition of green inhibitors represents an effective and reliable potential development strategy to obtain longtime durable coatings (Tavandashti *et al*., 2016). Several classes of inhibitors were assessed in order to obtain chromate free and environmentally friendly active coatings. In such a context, transition and rare earth metals ions demonstrated a multi-functional corrosion protection action acting effectively to inhibit localized corrosion phenomena in ferrous and non-ferrous alloys (Yasakau *et al*., 2006; Forsyth & Hinton, 2014). However, the approach to introduce the inhibitory species within the coating matrix, although simple and cost-effective, is not an efficient solution due to the required high content of the species and the possible interaction with the film matrix that leads to an immediate or progressive loss of its barrier effect over time (Garcia-Heras *et al*., 2004). Often, the corrosion inhibitors added to the coating suffers of undesirable rapid leakage, which leads to its fast decrease over time, depleting its potential effective self-healing action (Khramov *et al*., 2005). Furthermore, the usage of the corrosion inhibitor involves the presence of a zone of discontinuity, where it is entrapped in the cross-linked structure of the coating that act as hosting material, which can significantly damage its integrity (Shchukin *et al*., 2006).

In order to limit such issues, an alternative strategy is to inoculate the inhibitor inside micro-nano-carriers obtaining a composite filler constituted by an inert reservoir activated by an inhibitory species placed inside it (Nesterova *et al*., 2012; Grigoriev *et al*., 2017). Indeed, in literature the use of inhibitors containers was investigated in order to offer a suitable mechanical and structural stability of the coating optimizing the interaction with the hosting matrix and, at the same time, to control the inhibitor release during time offering a selective self-healing action only in real corroding conditions (García *et al*., 2011).

2.7 Characterisation of Nanomaterials

Characterisation of nanomaterials can be achieved using different techniques such as scanning X- ray Diffraction (XRD), High Resolution Electron Microscopy (HRSEM), and Energy Dispersive X-ray (EDX).

2.7.1 X-Ray diffraction

XRD is a multidisciplinary analytical technique which produces diffraction patterns of a sample by bombarding it with X-rays to obtain the mineral phase identity and crystal structure. X-rays are produced when a fast-moving electron is slowed down rapidly and has a wavelength range of 0.06 - 125 Å in the electromagnetic radiation spectrum. Hence, X-rays are good probes for determining atomic arrangements of crystallographic materials because of their short wavelength. X-rays that are diffracted during XRD analysis give information about the crystallinity of the sample such as single crystalline, polycrystalline, microcrystalline or amorphous (Kotsedi, 2010). When a structure has a repeat distance similar to the incident wavelength when waves interfere with it, the event that occurs is known as diffraction. The interference can either be constructive or destructive because of the scattering of the incoming wave fronts by the structure (Cummiings, 2012). This technique uses Bragg's law Equation 2.9 to determine atomic

spacing in the crystal.

$$n\lambda = 2dsin\theta \quad (2.9)$$

whereλ is wavelength of the X-ray in nm, θ the incident angle in degrees, and d is the spacing of the reflecting atomic planes.

2.7.2 High resolution scanning electron microscopy (HRSEM) and energy dispersive spectroscopy (EDS)

HRSEM is one of the useful imaging techniques that uses a beam of electrons to form high magnification images or can be applied for chemical composition characterisation. Tungsten and Lanthanum hexaboride filaments are mostly used as electron source; the cathode is heated to produce electrons which have energy of a few hundred to 40 keV. These electron sources (W and LB_6) have high melting points and relatively low work functions, hence they are commonly used. The electron beam produced is accelerated by the applied voltage towards the anode, passes the anode via a magnetic lens system through an aperture into the vacuum chamber to the surface of the specimen. Image formation is dependent on the produced signals from the electron beam and electron interaction with the specimen. The signals obtained from the interaction of electrons are categorized into elastic and inelastic interaction.

The deflection of electrons by the outer shell electron or atomic nucleus of a specimen results in elastic scattering. Backscattered electrons (BSE) are incident electrons that are elastically scattered through an angle greater than 90^o and are very useful for imaging the sample. However, inelastic electrons are generated as a result of interaction of incident electrons with electrons and atoms of the specimen. Secondary electrons (SE) are caused by the excitation of the specimen electrons during ionization of the specimen atoms; these electrons have energy that is less than 50 eV and are used to form an

image. There are several other signals produced due to the electron-specimen interaction. Elements emit their characteristic X-ray line spectra when a specimen is irradiated by photons or charged particles with sufficient energy. All elements have unique spectral line energies and emit X-rays at their own characteristic lines. These spectral line energies are used for qualitative analysis and their intensities for quantitative analysis, this is the principle employed in the Energy Dispersive Spectroscopy (EDS) that is often coupled with the HRSEM equipment. The X-rays emitted are named according to where the electron was emitted e.g. if the X-rays are emitted by electron filling the innermost shell (K shell) then they are called 'K lines'. For heavier elements, K lines require a huge amount of energy for an electron to be emitted Hence, L and M lines are usually observed on the EDS spectra. (EDS) spectrometer allows for the determination of the elemental compositions of the nanomaterials (Khorrami & lofti, 2013).

2.7.3 High resolution transmission electron microscopy

High Resolution Transmission Electron Microscopy (HRTEM) is a technique used to determine the microstructures, sidewalls, inner and outer diameters, lengths, and impurities/defects presents on the sample. This process used 300KV of energy to accelerate beam of electrons that impinged a sample material (Khorrami & Lofti, 2013).

The interactions produced backscattered electrons which are transformed into an image by electromagnetic lens (Reimer, 1998). The size of the images provides magnified view of the sample materials and the element present in it. Both TEM and SEM techniques can be couple with an energy dispersive X-ray (EDX) spectrometer, which enhance the determination of elemental composition of the samples (Khorrami & Lofti, 2013).

2.8 Corrosion of Metal

Corrosion of metal is fundamentally an electrochemical process where an anodic metal loses its ions through donation of electrons to its immediate environment. The electrons absorbed at the cathode may react with oxygen in the atmosphere. In order to maintain charge neutrality, the total rate of anodic reaction should be equal to the total rate of cathodic reaction especially when no external voltage was applied (Sreeya, 2009).

When a metal is placed in an electrolyte with ions, a dynamic equilibrium is achieved: $M^{n+} + ne^{-} = M$ andat equilibrium, potential difference between the metal and the electrolyte usually occurred and gave rise to Nernest equation (Sreeya, 2009) as shown in Equation 2.10.

$$E = E_0 + \frac{RT}{nF} . ln(M^{n+}) \quad (2.10)$$

Here E_0 is the standard potential (when metals are placed in an increasing order, the standard potential list forms the electrochemical series), R is the universal gas constant (8.314 $J.mole^{-1}.K^{-1}$), T is temperature (in K), F is Faraday's constant (96,490 $C.mole^{-1}$) and M1 is the concentration of metallic ionic species in the electrolyte at equilibrium.

When two metals of different potentials are connected together (for instance by an external wire) current flows to reduce the potential difference between them. It is important to note that the corrosion process involves three parts as shown in Figure 2.9. The anode, which is corroded, the cathode where electrons are absorbed (a reduction process) and the external path through which electrons flow. All three must be present in order for the corrosion to occur. This is true for any redox reaction as shown in Equation 2.11.

$$Ox + ne- = Rdt \quad (2.11)$$

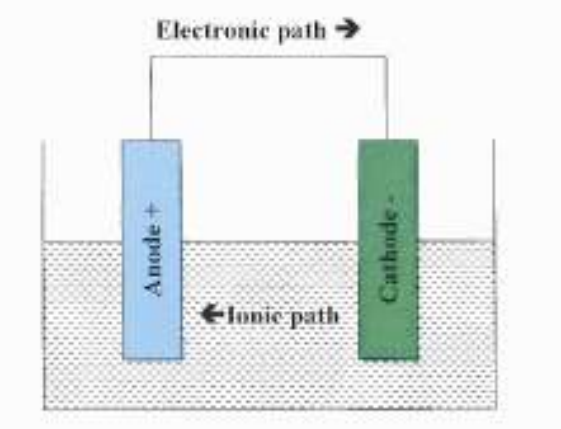

Figure 2.9: Electrochemical Cell (Sreeya, 2009)

where Ox is the oxidant and Rdt is the reductant. The applied potential is given by the corresponding Nernest equation as presented in Equation 2.12.

$$E = -0.440 - \frac{RT}{2F}\ln\left(\frac{[Fe^{2+}]}{[Fe]}\right) \quad (2.12)$$

Callister, (2012) classified corrosion damage into five main types:

Uniform attack - This includes the commonly occurring rusting. The initial rate of attack is usually higher than the final rate. Hence, the duration of exposure should also be mentioned. Other examples of uniform attack are tarnishing of silver, fogging of nickel and high temperature oxidation of metals. Corrosion rate isa measurement of the material lost depth per unit time (also called penetration rate). In SI units, corrosion rate is measured in millimetres per year (mm/yr). For example, ordinary steel corrodes at nearly 0.01270 mm/yr.

Pitting- This is a localized attack where rate of corrosion is higher at some points compared to the entire metal surface. If the area of attack is relatively small, then the pits formed are said to be deep. If the area of attack is wide and not so deep, it is said to be a shallow pit. Depth of pitting is expressed using a pitting factor, which is the ratio of the deepest penetration to the average pit depth. If the factor is 1 then the pitting is

uniform. Pitting typically occurs in iron buried in soil, steel immersed in seawater, copper and brass condenser tubes (Khan *et al.,* 2015).

Dezincification and Parting - Dezincification occurs with zinc alloys where the zinc corrodes preferentially. This reduces the metal's tensile strength and ductility. Parting is similar to dezincification where one or more components corrode preferentially and leave a porous residue of the metal behind. This occurs more in noble metals alloys such as gold-copper and gold-silver (Wei *et al.,* 2009).

Intergranular corrosion - This is a localized corrosion at grain boundaries of a metal resulting to loss of strength and ductility. This includes improperly heat treated 18-8 stainless steel or duralumin type alloys. The attack is rapid and catastrophic.

Cracking - When a metal subjected to constant tensile stress cracks in a corrosive environment, the failure is called stress corrosion cracking. Almost all structural materials are subjected to stress corrosion cracking. For instance, carbon and low alloy steels, brass, stainless steel, titanium alloys, nickel alloys and many others (Prabakaran *et al.,* 2016).

2.9 History of Corrosion Prevention for Iron and Steel

Corrosion is an induced damage on oil and gas metallic structures as a result of interaction with their environment. Corrosion is a natural process that cannot be totally prevented, but it can be minimized or controlled by proper selection of materials, design, use of anti-corrosive chemicals (inhibitors), coating, cathodic protection, and control of technological parameters (Groysman, 2017). Application of protective coating is one of the most common corrosion controls to enhance the life span of pipeline. Various types of coatings such as metallic, ceramic and polymer coatings have been investigated in a quest to find durable coatings to resist electrochemical decay of iron and steel in industrial applications (Ammar *et al*., 2018).

There are three main types of coatings for corrosion prevention: Metallic coatings, inorganic coatings and organic coatings. Metallic coating was further classified as noble and sacrificial with galvanization being the most popular sacrificial metal coatings. (Dubois, 1913; Sudrabin & Marks, 1952; Fujimoto & Tsuchiya, 2007).

Galvanization of iron and steel existed dated back to 18th century. In 1741 French chemist Melouin attempted to coat iron with zinc by a dipping process (Nowicka-Nowak *et al*., 2018). Another form of corrosion prevention is the utilization of organic coatings developed by Norman A. Dubois in 1913.

The authors conducted a study on corrosion of iron and steel with intent to discuss the essential properties for paint. He pointed out that there were several possible reasons for iron and steel to corrode and most paint were relatively impervious to corroding gases like carbon dioxide, oxygen and moisture. (Chigondo & Chigondo, 2016). In 1952, Sudrabin and Marks proposed cathodic protection for steel immersed in water as a combination of metal protective coating and maintaining a current to prevent corrosion at the vinyl coating flaws. In 2000, Alan MacDiarmid shared the Nobel Prize in chemistry for his work on organic conducting polymers. He demonstrated anodic protection of steel with polyaniline. Fujimoto and Tsuchiya (2007) used the semiconducting property of conducting polymers to prevent corrosion of iron-based alloys. Inorganic coatings include vitreous enamel coating and Portland cement coatings. These coatings have been in use since the beginning of the 19th century however, inorganic based coatings are susceptible to damage by mechanical and thermal shock.

Currently, there have been considerable advancements on the prevention of corrosion using nanomaterials. Unlike bulk materials, the particles of nano materials are so small

that electrons are not free to move about and due to these restrictions, the particles react differently with some usual properties (Siavash *et al.,* 2019).

2.10 Application of Steel for Underground Storage Tank

Steel is a material commonly used as underground storage tanks (USTs) due to its acceptable mechanical properties, availability and relatively low cost (Abdulrahman *et al.,* 2015). Corrosion is estimated to be responsible for approximately 65% of the failure of underground storage tank (UST) systems, 35% is due to other causes such as third party damage. It has been reported that vast majority of UST and piping failure are associated with external corrosion, primarily due to their exposure to corrosive soil, while only a small percentage can be attributed to internal corrosion (Guan, 2003). The average corrosion cost has been estimated to be about 3.5-4.5 % of the Gross National Product of most industrialized nations (Corrosion Costs and Preventive Strategies in the United States, 2013). Aside the high cost of maintaining USTs, the impact of the failure can cause wastage, fires or explosions that threaten human and environmental safety from spill, over fill or leaking of tanks and piping. However, the major drawback to this application is it is prone to corrosion attack due to its interaction with its service enviroments, which can lead to structure degradation, system failure, loss of quilateral and subsequently lead to injury and loss of life (Ajayi *et al.*, 2014).

Fortunately, the USTs can be replaced, upgrade or remove the tanks and the long-term protection prognosis for safe economical and good option of corrosion protection. However, corrosion such as protective coatings has been developed to address the challenges of external corrosion protection systems of USTs for flammable and combustible liquids using underground steel storage tanks. Various corrosion protective coatings have been used including bitumen, plastic baggie, tape coatings, coal tar epoxy, FRP, and 100% solids rigid polyurethane coating to accompany the development

of various steel technology institute (STI) specifications (Guan, 2003). These coating were fine in preventing atmospheric corrosion but useless for protection against corrosion in many underground environments. Most of the coatings are also easy to apply and relatively inexpensive, but it is environmentally unfriendly and can be removed and damaged by casual contact (Guan, 2003).

2.11 Application of Tin Metal as a Coating Material

The application of tin as a coating material dated back to man's metal-working history when, it was used as a decorative finish to bronze. The most likely reason for this initial application was due to low melting point of tin coupled with its ability to wet and adhere to other metal surfaces. It was not until the industrial era that engineering uses of tin and tin-alloy coatings were arrived upon. While industry widely acknowledges the existence and application of tin coatings, not as many were aware of the field's scope (Han *et al.*, 2013). These encompass the complex technology of tinplate manufacture/use as well as an extraordinary variety of coatings that contain metals (apart from tin) and tin compounds (Hu & Jie, 2015). Tin is used extensively owing to its high resistance to corrosion in a large number of environments. The greatest use is for the production of tinplate, used in the packaging industry. Low-carbon steel in the form of strip or sheet is given a thin coating of tin on both sides and the two methods that are used commercially for producing tinplate are hot dipping and electrolytic plating (Wansah *et al*., 2014).

Tin plate made via hot-dipped tin plating is made by cold rolling steel or iron, pickling to remove any scale, annealing to remove any strain hardening, and then coating it with a thin layer of tin. Originally, this was done by producing individual or small packs of plates, which became known as the pack mill process. In the late 1920s strip mills began to replace pack mills, because they could produce the raw plates

in larger quantities and more economically.

Recently, batch hot-dip galvanizing, also known as general galvanizing, produces a tin coating by completely immersing the steel product in a bath (kettle) of molten zinc represented in Figure 2.10. Prior to immersion in the tin bath, the steel is chemically cleaned to remove all oils, greases, soil, mill scale, and oxides. The surface preparation consists of three steps: degreasing to remove organic contaminants, acid pickling to remove scale and rust, and fluxing, which inhibits oxidation of the steel before dipping in the molten zinc. Surface preparation is critical, as the zinc will not react with unclean steel.

After surface preparation, the steel is immersed in the molten (443.3^{o}C) tin bath. The bath consists of more than 98% pure Tin and less than 2% additives, most commonly aluminum, nickel, and bismuth, which help with tin fluidity and consumption, coating appearance, etc. While in the galvanizing kettle, the molten tin metallurgically reacts with the iron in the steel to form the coating. After removal from the zinc bath, the coating is inspected for conformance to ASTM, CSA, or ISO specifications.

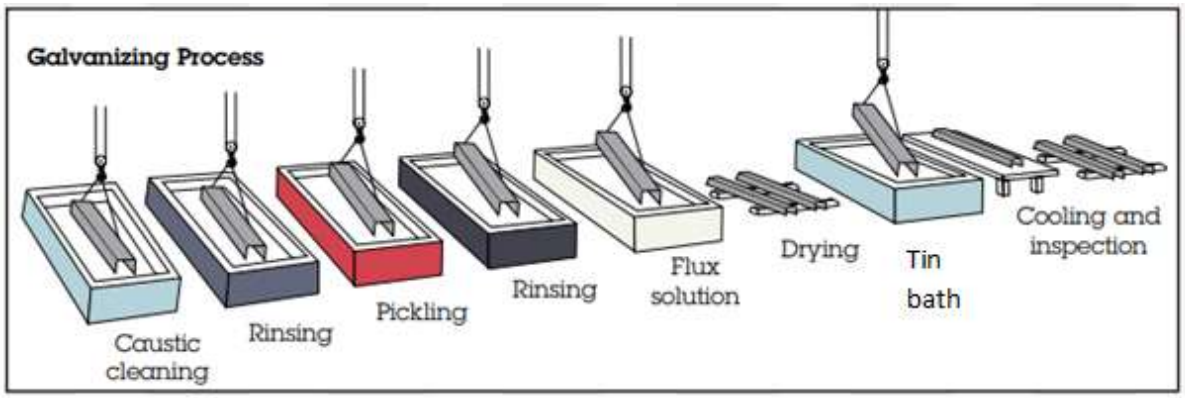

Figure 2.10: Batch Tin Plating Process (American Galvanizers Association, 2019)

In electroplating, the item to be coated is placed into a container containing a solution of one or more tin salts. The item is connected to an electrical circuit, forming

the cathode (negative) of the circuit while an electrode typically of the same metal to be plated forms the anode (positive). When an electric current is passed through the circuit, metal ions in the solution are attracted to the item. To produce a smooth, shiny surface, the electroplated sheet is then briefly heated above the melting point of tin. Most of the tin-plated steel made today is then further electroplated with a very thin layer of chromium to prevent dulling of the surface from oxidation of the tin. Similar to sheet galvanizing, the operation is continuous and coating thickness is minimal. Applied in a steel mill, sheet or strip is fed through entry equipment into a series of washes and rinses then into the tin plating bath.

2.12 Application of Nickel for Corrosion Prevention

Nickel (Ni) is a metallic element used as a component in hundreds of alloys; as a catalyst and also corrosion-resistant plating product. Rebak (2013) reported that 61% of the Ni produced worldwide is used in the fabrication of stainless steels. Over 90% of Ni-containing products are recycled at the end of their useful life, and can continue to be recycled without limit. Large number of alloying elements can be added to Ni to produce different type of alloys which are tailored for specific applications (Rebak, 2013). Commercial Ni alloys is being revised continuously every year since a new alloy seems to appear in the market.

A comprehensive review on the historical development of Ni alloys was reported in the past by Agarwal and Kloewer (2001). The commercially available Ni alloys are categorized into two large groups: corrosion-resistant alloys (CRA) targeted for wet or condensed aqueous systems applications and super alloys or high-temperature alloys (HTA) targeted for applications in dry or gaseous corrosion systems.

A CRA is an alloy that is resistant to general and localized corrosion in a variety of corrosive environments to carbon and stainless steels. In contrast, the corrosion resistance intrinsically included in the term CRA should not be understood as immunity against any type of corrosion. The temperature boundary condition between the CRA and the HTA is approximately 538^{o}C. This CRA/HTA classification does not exclude that CRA may be used at temperatures higher than 538^{o}C and vice versa. Specifically, the CRA are often selected for their ability to resist corrosion in a given environment and less importance may be given to their mechanical strength (Sarmiento *et al*., 2017). However, most HTA require playing a dual role, that is, besides their capacity to withstand the aggressiveness of the high-temperature corrosive environment, HTA also need tokeep significant strength at high temperatures (Rebak, 2013).

2.13 Nanotechnology in Corrosion Prevention

Recently, significant advancements have been made to improve the management of steel corrosion through research, development and implementation; and nanotechnology has been playing an increasing important role in supporting innovative technological advances. Nanotechnology is generally understood to involve the manipulation of matter on a near-atomic scale to produce new structures, materials, systems, catalysts and devices that exhibit novel phenomena and properties (Bose *et al*., 2010). These materials exhibit unique physical, chemical and biological properties at the nanoscale. Nanotechnology offers the possibility of introducing technologies that are more efficient and environmentally sound than those used today (Wansah *et al.,* 2014).

2.14 Nanoformulation Coatings as Alternative to Corrosion Prevention

Nanocomposites coating is a phenomenon in which two or more metals/non-metals nanoparticles are added to metal plating in order to modify and improve both mechanical and physical properties (Lee, 2012). In the last two decades, many

researchers have used nanocomposite coating because it delivers many on-demand properties such as corrosion resistance, mechanical and functional properties to a treated surface (Jiang *et al*., 2017). The cost effective and simple techniques used for coating metal surface on substrate include; electrodeposition (Kammona *et al*., 2009), electroless plating (Novakovic and Vassiliou, 2009), plasma thermal spraying (Zhao *et al*., 2014), chemical conversion coatings (Zeng *et al.,* 2014), gas phase deposition (physical vapour-deposition and chemical vapour deposition), ion implantation, laser surface alloying, and organic coating (Tudela *et al.,* 2014). Several authors have studied the effects of nanocomposite on the microstructural, mechanical, thermal, and electrical properties. Recently carbon nanotubes (CNTs) was utilized as reinforcement or nanocomposite (Dong *et al.,* 2009). It was observed that, adding CNTs into conventional solder alloy, convincingly increases the overall activities. This implies that interaction on bond between the metal matrix and the CNTs plays a significant role in improving the properties of the substrate.

Furthermore, the exceptional properties of carbon nanotubes (CNTs) such as high electron mobility, high thermal conductivity, high tensile strength and high surface area, make it a better candidate for composite on metal /metal alloy over corrosion inhibitors. Besides, CNTs has high tensile strength greater than that of steel even though with only one-sixth the weight of steel (Laoui, 2010).

Xu *et al.* (2017) reported that CNTs can be useful in the deposition of composites coating due to its nanometersize and excellent properties. In addition, Hu and Jie (2015) reported that when CNTs were used as nano-composite to Pb-Sn anti-friction alloy, the friction coefficient of the material decreased self-lubricating and wear properties of the composite materials improved. In addition, Laoui (2010) also produced CNTs-copper nanocomposites via the electrochemical co-deposition method resulting to a mechanical

strength three times than the pure metal. The improved in mechanical strength was as result of even distribution of CNTs and enhanced CNTs/copper interfacial bonding. Particle reinforced composite coatings can also be formed by incorporating inorganic non-metal nanoparticles such as TiO_2 (Novakovic & Vassilliou, 2009), Ni-P and SiC (Lee, 2012).

However, researchers have observed a weak interaction between Sn and CNTs and in order to improve and strengthen the interfacial interaction, appropriate surface coatings were utilized on the nanotubes and the choice of Ni-Sn alloy was due to formation of stable binary phases between Ni and Sn. In addition, Ni has good wettability, which can form a continuous coating on the CNTs and a corresponding in binding energy (Han *et al*., 2013).

2.15 Review of the Mechanisms of Coating

The mechanism of the formation of nanocomposite electrochemical coatings (including electroplating and electroless plating) has been investigated since the 1960s. The three main steps which includes: (i) electrophoretic movement of positively charged particles to the cathode, (ii) adsorption of particles at the electrode surface by van der Waals forces, and (iii) mechanical inclusion of particles into the coating layer define the whole reaction (Ger & Hwang, 2002; Chen & Gao, 2011).

In fact, nanoparticles are inert and cannot participate in chemical reactions during the coating formation, whereas they can affect the formation process. Generally, nanoparticles with high surface activity and high surface energy can be easily absorbed by some other objects and thus affect the reaction process. This effect on the formation of different coatings has different reaction mechanisms. For this, a schematic for the formation processes of nanocomposite coatings prepared in the treatment baths with

controlled addition of nanoparticles is preliminary presented, as seen in Figure 2.11. Some of the possible reaction processes of the nanocomposite coatings are depicted as follows.

2.15.1 Suspension in the treatment bath

With the immersion of nanoparticles into the treatment bath, they are dispersed in the bath through some effective dispersion methods to form a suspension system. Generally, the nanoparticles in the chemical conversion bath are relatively stable before the anions and cations in the bath reach saturation at the initial stage (Narayanan, 2005).

However, the nanoparticles-adsorbed metal ionic cloud (referred to as the particle-metal ionic cloud) is formed as soon as the particles are introduced into the plating bath containing an abundance of metal ions (Chen & Gao, 2011) as shown in Figure 2.11 (a).

2.15.2 Adsorption on the substrate surface

In Figure 2.11 (b), the nanoparticles themselves with both high surface activity and large specific area are subsequently, physically adsorbed on the freshly deposited surface in the chemical conversion treatment bath due to the dynamic field by the dispersion methods and Brownian motion of the nanoparticles in the bath (Dastjerdi and Montazer, 2010; Tudela *et al*., 2014). These can provide more nucleation sites for the primary deposition of insoluble salts and effectively reduce the activation energy during the formation of a new phase. On the other hand, the particle–metal ionic clouds in the plating bath are easily adsorbed on the underlying substrate during electrochemical treatments. According to reports by Ger and Hwang, 2002 and Chen and Gao, 2011, who were working independently, these particle–metal ionic clouds are transported to the hydrodynamic boundary layer under the action of forced convection, migrated across the layer, and then conveyed by diffusion to the cathode.

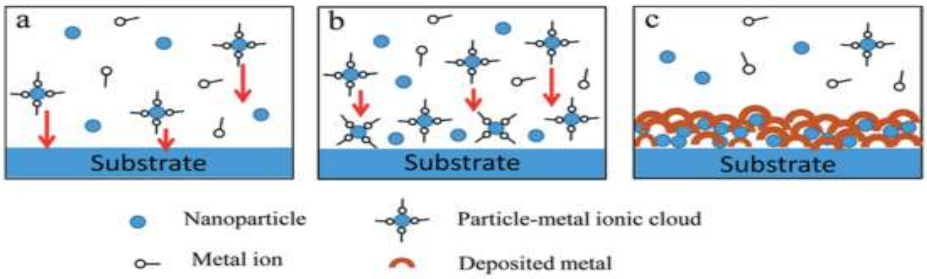

Figure 2.11: Schematic Formation Process of Nanocomposite Coatings on a Substrate and the Formation of Nanocomposite Coatings (Chen and Gao, 2011)

Regarding chemical conversion coatings, when anions and metal cations in the bath reach saturation, deposition or crystallization of insoluble salts with nanoparticles as core is achieved, and then the grains quickly grow to form bigger crystals. Finally, many crystals increasingly pack, and finally, a complete and dense coating on the surface is formed (Sheng *et al*., 2011).

As for electrochemical coatings, after the clouds are entirely or partly reduced, the particles are irreversibly deposited and incorporated into the metal matrix as the metal ions are discharged with reduction reactions as shown in Figure 2.11 (c) (Chen *et al*., 2010). However, the excess number of nanoparticles in the treatment bath will have an adverse effect on the formation of the nanocomposite coating because excessive nanoparticles may seal the substrate surface by agglomeration, thus restraining the initial reactions in the formation of the coating.

2.16 Soil Environment

Soil is a complex system of solid, liquid and gaseous phases, physically and chemically associated with each other. The solid phase is by far the most heterogeneous component, even in small volumes of soil, being composed of different sized organic particles of silica, silicate, clay, metal oxides, and other minor components all

associated, to some extent, with organic material. The organic matter consists of a number of materials ranging from un-decomposed plant or animal tissue through various intermediate levels of decomposition to a comparatively stable amorphous brown and or black material. Compositional variables of a soil include moisture, oxygen, salt content, acidity, as well as the presence of various forms of bacteria. Climatic factors such as; temperature, rainfall, air movement, sunlight, amongst others, can cause marked alterations in properties of soil. Steel, particularly plain carbon ones are found most economical for underground structures.

2.16.1 Underground corrosion in metal structures

Steel structures buried underground such as, utility piping, pipeline, tanks and pilings placed in direct contact with soil environment are prone to corrosion attack. The method often used in the previous practice of corrosion protection for underground pipelines was to increase the wall thickness of the pipeline (Lim *et al*., 2013). The main reason of increasing wall thickness is to prolong the life span of the pipeline when subjected to corrosion in soil. The factors that influence corrosion in soil including oxidation-reduction (redox) potential, electrical resistance (resistivity), soluble ion content, pH, moisture content, rates of microbes in soil and many more. Most of these factors can be empirically measured to determine soil corrosivity (Sosa and Alvarez-Ramirez, 2009). The complexity of electrochemical process in soil may influence the steel pipe to corrode due to the presence of different soil electrolytes (Escalante, 1995). Li *et al*. (2003) added that the relationship among physicochemical parameters and soil corrosiveness is very intricate; therefore, the soil corrosiveness evaluated by these parameters is often undependable (Sosa & Alvarez-Ramirez, 2009). Comprehensive field research on corrosion of buried pipes revealed that soil's corrosive environment is the root cause of failures of buried pipes (Kleiner and Rajani 2001; Alamilla *et al*.,

2009; Cole and Marney 2012; Asadi & Melchers 2018; Qin *et al*. 2018). For example, according to comprehensive surveys undertaken by the American Water Works Association (USA), almost 70% of buried ferrous metal pipes fail due to the corrosive soil, as shown in Figure 2.12 (Romer & Bell, 2001).

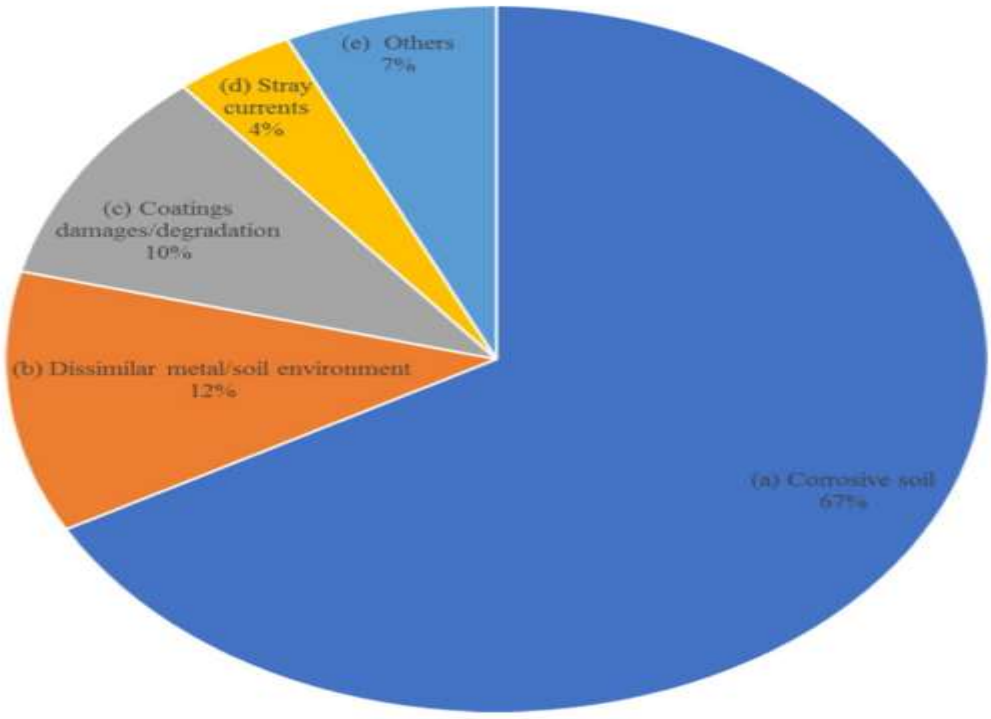

Figure 2.12: Reported Causes of Corrosion of Buried Pipes. Redrawn, originally, by Romer and Bell (2001)

The degradation that occurs due to corrosion is the general cause of the alteration and destruction of a large part of natural and man-made materials. It is estimated that approximately 25% of annual steel production is destroyed by corrosion (Arriba-Rodriguez *et al*., 2018). The corrosion of buried steel structures occurs when concentration cells are generated.

This process takes place when a metal is in contact with soils of different characteristics or due to differences in the material. The current flows through the earth from the anodic area to the cathodic area and through the steel tube of the cathode area, until it

again moves to the anodic area to complete the circuit (Roberge, 2008). In most cases, the portion of the structure that is in the most conductive soil acts as an anode and the part located in the ground with low conductivity acts as a cathode. The same soil acts as an electrolyte and the structure is the metallic contact that is necessary for a corrosion cell to be generated (Payne, 1999). Corrosion occurs at the place where the current is discharged from the metal to the ground in the anodic areas. In the cathodic zones, the flow of current goes from the ground to the metallic structure, keeping the construction protected (Pritchard *et al*., 2013). In the anodic area of the structure, the anodic reaction occurs and produces the loss of metal ions, that is, the corrosion of the metal. In the cathode, the cathodic reaction or reduction reaction occurs (Stansbury & Buchanan, 2000). Depending on the soil, different cathodic reactions may occur. For instance, the electrochemical reactions that govern the anodic and cathodic reactions are influenced by the presence of bicarbonate (Eliyan and Alfantazi, 2014). In particular, the mechanism of corrosion reactions on the exterior surface of buried structures when exposed to hydrated conditions containing carbon transporting agents is in given Equation 2.13 as follows (Eliyan and Alfantazi, 2013).

$$Fe(OH_2) + HCO_3^- \rightarrow FeCO_3 + H_2O + OH^- \quad (2.13)$$

2.17 Corrosion in Soils

Soil is a very complex corrosive environment and, therefore, the corrosion of metals in this situation is extreme (Arriba-Rodriguez *et al*., 2018). The cause of this instability derives from the constantly changing underground environment. The degradation of a buried material is strongly dependent on the characteristics of the soil in which it is buried (Arriba-Rodriguez *et al*., 2018). Most of the destructive processes that affect buried metals are of an electrochemical nature, mainly associated with the

characteristics of the soils in which they are located (Yan *et al*., 2008a). The main factors that influence the corrosion of these infrastructures are discussed as follows.

2.17.1 Soil texture

The soil texture is an indication to the size of mineral spread present in a soil sample; these include the sand, silt and clay found in the soil. Soil texture therefore, consists of the size distribution of the mineral particles that form the soil. The terrain is made up of clays (with diameters of less than 0.002 mm), silts (with diameters between 0.002 and 0.5 mm), and finally sands, exhibiting the largest particles (with diameters greater than 0.05). These particles are in turn are subdivided into thick, medium, and thin. Depending on the values taken by the percentages of sand, clay, and silt, the classification of the soil in different families is defined according to the ternary diagram shown in Figure 2.13.

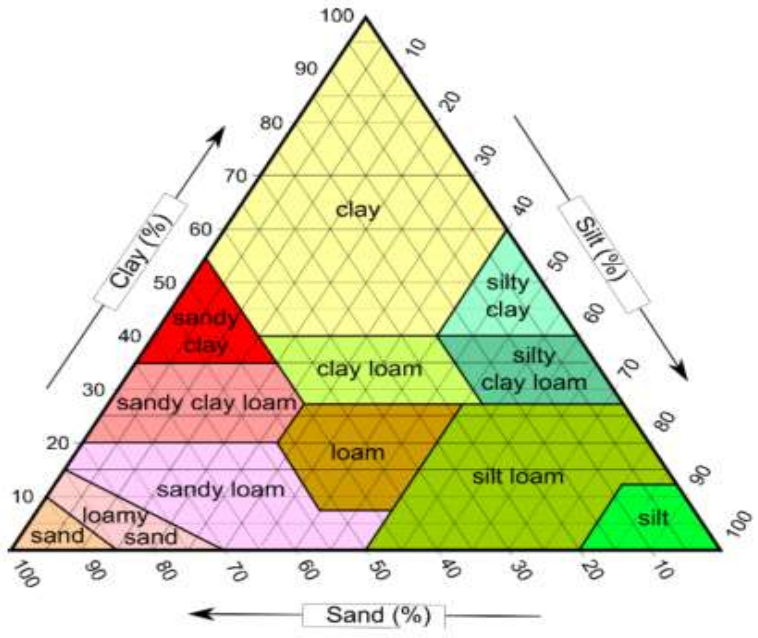

Figure 2.13: Ternary Diagram of the Soil Composition (Arriba-Rodriguez *et al*., 2018)

2.17.2 Redox potential

Redox potential is essentially a measure of the degree of aeration of the soil: a high redox potential indicates a high level of oxygen. The value of soil redox potential depends on the dissolved potential indicates a high level of oxygen. The value of soil redox potential depends on the dissolved oxygen content in the pore water and provides some information about the conditions in which the oxygen content in the pore water and provides some information about the conditions in which the reducing bacteria of the soil could grow sulfate (Veleva, 2005). Low values of redox potential may suggest reducing bacteria of the soil could grow sulfate (Fiedler *et al*, 2007). Low values of redox potential may suggest that conditions are favorable for anaerobic microbiological activity (Yahaya *et al*., 2011).

2.17.3 Conductivity/Resistivity

Due to the relationship between corrosion and conductivity, resistivity has been considered the main variable to study in the field of soil corrosivity (Bradford *et al*., 2000). As the flow of ionic currents is associated with corrosion reactions, highly resistive soils tend to retard their effects (Bayliss & Deacon 2002; Zhu *et al*., 2011). The soil resistivity generally decreases with the increase in water content and the concentration of ionic species. It is important to note that resistivity alone is not enough to evaluate the risk of corrosion, so its usefulness as the only absolute indicator is very limited (Busby *et al*., 2012). Soil resistivity may be measured by a few traditional techniques such as the Wenner four-pin method or, more recently, by electromagnetic measurements. Measurements of resistivity can be made both in situ and at the laboratory. However, the laboratory resistivity measurements sometimes do not correlate well with field results (Ferreira *et al*., 2007).

Due to the historical importance of resistivity in terms of its performance in the corrosion of metals, there are several tables that relate the resistivity of the soil to the degree of corrosion (Hernandez, 2007). The most widely used methods to assess aggressiveness were put forth by NACE and American Society for Testing and Materials (ASTM), which are summarized in Table 2.2 (ASTM G187, 2012; Bhattarai 2013). These types of tables are easy and fast to use but their main problem is that they only consider one parameter, the resistivity of the soil. Therefore, its applicability is very limited in the design phase of buried metallic structures.

Table 2.2: Corrosivity Ratings based on Soil Resistivity according to American Society for Testing and Materials (ASTM G187-12: Standard Test Method for Measurement of Soil Resistivity Using the Two-Electrode Soil Box Method) and National Association of Corrosion Engineers (NACE) (Berke *et al*., 2016)

Soil Resistivity (Ω.cm)	**NACE**	**ASTM**
>10000	Negligible	Very mildly corrosive
5001-10000	Mildly corrosive	Mildly corrosive
2001-5000	Mildly corrosive	Moderately corrosive
1001-2000	Moderately corrosive	Severely corrosive
501-1000	Corrosive	Extremely corrosive
0-500	Very corrosive	Extremely corrosive

In 1946, Starkey and Wight developed a model relating the corrosion in soil to the redox potential (Arriba-Rodriguez *et al*., 2018), as shown in Figure 2.14.

Figure 2.14: The Relationship between Soil Corrosivity and the Redox Potential (Arriba-Rodriguez *et al*., 2018)

2.17.4 The pH

pH is the measure of the acidity or basicity of a solution. The pH of a material plays a significant role in how aggressive corrosion can be. The acidity of soil comes from mineral leaching, decay of acidic plants like (coniferous tree needles), industrial wastes, acid rain, and certain forms of microbiological activity. Alkaline soils tend to have high sodium, potassium, magnesium, and calcium contents; these elements produce calcareous deposits on buried structures that have protective behavior against corrosion. The pH level has an influence on the solubility of corrosion products and also the nature of microbiological activity (Arriba-Rodriguez *et al*., 2018).

Several studies on corrosion has suggested that buried metallic are susceptible to corrosion at any pH value. However, a project carried out by Tibu and Oliveira considered that pH is not a dominant factor in the corrosion mechanism when the soils have a pH in the range between 4 and 8.5 (a common range in soil) (Tiba & Oliveira, 2012). Despite these contradictions, research on this field of corrosion coincides with the fact that more acid soils have a much higher risk of corrosion in structural materials

such as steel. On the other hand, alkaline soils tend to have high concentrations of magnesium and calcium, which often form deposits on buried surfaces with protective properties against corrosion. The most widespread method for measuring pH is through pH papers based on color changes.

In the same univariate approach, other researchers considered pH to be the key factor in the corrosion process (Arriba-Rodriguez *et al.*, 2018). Some models provide an approximate relationship between the pH of the water extract of the soil and its corrosivity, for instance that shown in Figure 2.15.

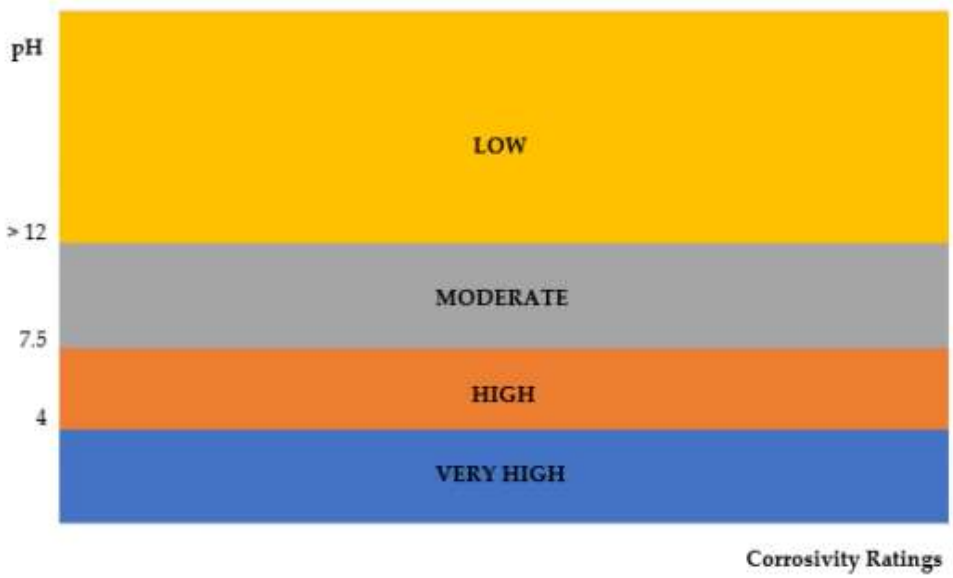

Figure 2.15: The Relationship between Soil Corrosivity and the pH (Arriba-Rodriguez *et al.*, 2018)

Soon, scientists realized that the mechanism of corrosion in buried structures is the result of the iteration of many factors, and it was dangerous to consider only one. As a result, researchers began to create qualitative models that relate the corrosivity ratio to more than one variable. In 1963, Pourbaix represented corrosion in diagrams depending on the potential and the pH (Figure 2.16) (Arriba-Rodriguez *et al.*, 2018). These diagrams were called Potential-pH diagrams or Pourbaix diagrams, after their creator.

This approach offers a great amount of thermodynamic information in an agile and efficient format. However, although it incorporates two variables in the study of corrosion, it still does not consider the numerous factors that intervene in the corrosion phenomenon (Ahmad, 2006).

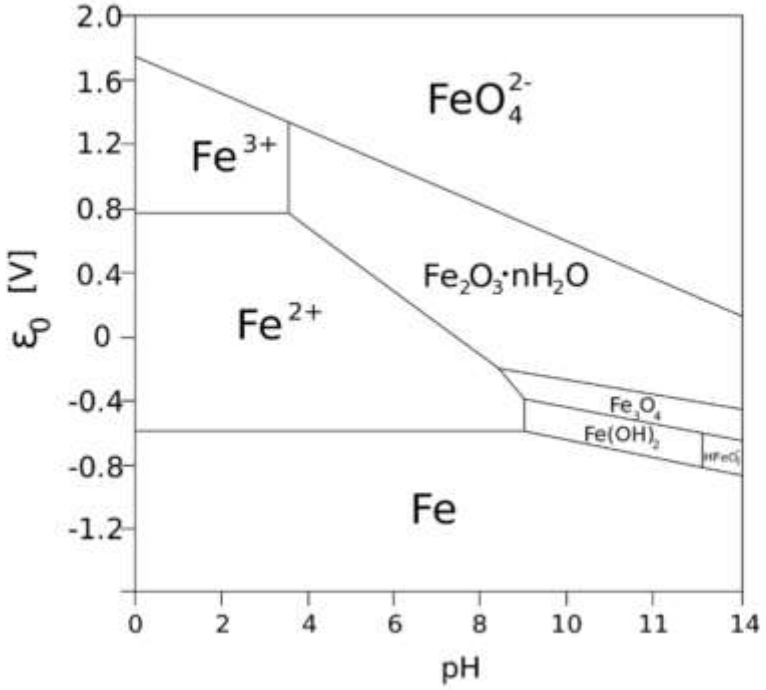

Figure 2.16: Porbaix Diagram for Iron (Arriba-Rodriguez *et al*., 2018)

A relevant and extended model to estimate corrosion was developed in the European standard EN 12501-2 on the protection of metallic materials against corrosion (EN12501-2, 2003). The standard provides a qualitative estimation of corrosive soil taking into account two variables: pH and resistivity. This method suggests some guidelines for determining the corrosion load on soils. Its limitation is due to the fact that it only establishes three different levels of corrosion: high, medium, or low, as shown in Table 2.3.

Table 2.3: Corrosive Soil Load Function of pH and Resistivity According to (EN 12501-2, 2003)

pH	Resistivity (Ω.cm)	Corrosion
<3.5	Any	High
3.5-4.5	<4500	High
	>4500	Medium-High
4.5-5-5	<4500	High
	4500-5000	Medium-High
	>5000	Medium
5.5-6.0	<1000	High
	1000-5000	Medium-High
	5000-10000	Medium
	>10000	Medium-Low
6.0-9.5	<1000	High
	1000-3000	Medium-High
	3000-10000	Medium
	10000-20000	Medium-Low
	>20000	Low

2.17.5 Presence of moisture

The water plays a critical role as fundamental electrolyte in the electrochemical corrosion action (Roberge, 2008). Shreir *et al*. (2010) identified three types of soil moisture:

i. Free ground water: Basically, this represent to the water table of the substrate, beneath which water is constantly present. The profundity to free

ground water can fluctuate, subordinate upon topographical and climatic elements.

ii. Gravitational water: Whereby water, ordinarily as an after effect of precipitation, enters the soil surface and permeates downwards. In the long run this water achieves the free ground water table, regularly quickly, particularly in coarser grained soils (sand and gravel as an example).

iii. Capillary water: Water that is held inside of the "capillary" spaces between clay and silt particles, this asset is the thing that plants and creatures living inside of the soil mass depend on for their water utilization. The large sandy soils have a little measure of fine water accessible. Water substance and water movement in soils can be seen as a variable of water flow patterns, ground topography, soil profiles and the position of the water table, oil type and water saturation limits (Cole and Marney, 2012).

In 2015, the results of a study to evaluate the effect of soil moisture on corrosion confirmed its influence on corrosion rates. The reason for this is that liquid water represents the essential important influence on corrosion rates (Pereira *et al*., 2015). The reason for this is that liquid water represents the electrolyte for electrochemical corrosion reactions. Therefore, factors such as soil moisture, water essential electrolyte for electrochemical corrosion reactions. Therefore, factors such as soil moisture, retention capacity, groundwater level, and water mobility in the soil must be taken into account.

2.17.6 Ions content

The chemical components most related to corrosion are chlorides and sulfates. Chloride ions are generally harmful because they participate directly in the reactions of anodic

dissolution of metals (Li *et al*., 2007). In addition, its presence tends to decrease soil resistivity. Chlorides may be present in soils naturally or come from external sources, such as the spillage of salt on roads in winter. The concentration of chloride ions is prone to significant variations depending on the degree of soil moisture (Ismail & El-Shamy, 2009). As for the corrosive effect produced by sulfate ions on metals, it is lower than chlorides. However, its risk increases with the possibility that the sulfates become highly corrosive sulfides due to the activity of bacteria that can lead to the reduction of anaerobic sulfate (Lee & Characklis, 1993).

2.18 Corrosion Measurement

Corrosion measurements are used for determining corrosion properties of metal specimens. The corrosion properties include the corrosion rate, electrochemical potential, electrochemical current density, capacitance behaviors, charge resistance, and so on.

2.18.1 Weight loss

This is the one of the simplest non-electrochemical and most convenient methods that use change of weight of a coupon after exposing the metal specimen of known area to a particular environment for a specified period. In this method, the initial dimensions such as length, diameter and weight of the specimen are measured accurately and then they are embedded in concrete. After that, the reinforced concrete is exposed to an artificially created or natural available environment for the course of time known as exposure duration. After the exposure duration, the concrete blocks are taken out, broken and then specimens are removed from concrete, and then they are again cleaned and weighed (Rathi *et al*., 2017).

Thus, the loss in this obtained and corrosion rate is found from the formula given in

Eqution 2.14.

$$\text{Corrosion rate mm/year} = \frac{87.6 \times W}{D \times A \times T} \quad (2.14)$$

where W= weight loss in milligrams D= Density of steel in gm/cm^3 A= Surface area of steel in cm^2 T= Time of exposure in hr (Umoren *et al*., 2008).

Weight-loss corrosion measurements are simple, because they require no specialized equipment other than an accurate balance. Although, weight-loss methods are slower than other techniques (usually >1 week), but multiple samples can be run simultaneously. This method gives the average corrosion rate over an extended period of time. The results from laboratory weight-loss studies have been used to determine the relative corrosiveness of different operating parameters such as, amine type or concentration, steel type, vapor versus liquid phase to mention a few (Pearson & Cousins, 2016).

2.18.2 Electrochemical corrosion measurements

Electrochemical corrosion techniques are essential in predicting the service life of metallic components used in chemical and construction industries. They measure the corrosion rates, the oxidizing power of the environment, and evaluate the effectiveness of corrosion protection strategies. The following direct current “dc” electrochemical methods are discussed in this chapter: linear polarization technique, Tafel extrapolation, and open circuit potential (OCP) vs. time measurements. Electrochemical impedance spectroscopy (EIS) is introduced as an alternating current technique “ac.” This technique uses alternating current to measure frequency-dependent processes in corrosion and estimates the change of polarization resistance (Popov, 2015).

2.18.2.1 Potentiodynamic polarization measurements

Since the corrosion reaction is mostly electrochemical, corrosion behaviour of metals can be evaluated with electrochemical techniques. A polarization test is one of the common techniques (ASTM F1089, 2002; ASTM F746, 2014). The potentiodynamic polarization technique is used to determine the potential region at which a metal or alloy is passive when exposed to a particular environment. It is able to estimate both the ability of the material to spontaneously passivate as well as the critical current density required for the passivation. Potentiodynamic polarization measurements therefore, predicts the way a material will behave when exposed to a corrosive environment. This method identifies the corrosion active region, the onset of the passivation, the critical current density, the primary passive potential, the current passive region, and the voltage span of the passive region (Berradja, 2019).

In anodic polarization tests, the anodic reaction of the specimen is accelerated by applying anodic overpotential and the current response is measured. According to the various parameters obtained, such as the magnitude of current density and pitting potential, the corrosion behaviour of the metals can be evaluated. In practice the anodic reaction is accelerated by applying anodic current using a potentiostat. A potentiodynamic polarization test (linear sweep voltammetry), in which the potential of the specimen is swept at a constant speed, is generally carried out. To obtain the response near the steady state, the sweep rate of potential should be as slow as possible. On the other hand, a potentiostatic polarization test is recommended to obtain the response at a steady state because the response can reach the steady state during the period when the potential is kept for several minutes (Hiromoto, 2010).

The potential of the working electrode is measured against the referen’[ce electrode and the current flowing between the working electrodes (WE) and counter electrode (CE) is

measured using a potentiostat. A saturated calomel electrode (SCE) or standard silver–silver chloride electrode (SSE) is used for a reference electrode (RE) and platinum or carbon is used for a CE. The tip of the reference electrode is set close to the surface of the working electrode to minimize the IR drop due to solution resistance (Hiromoto and Mischler, 2006).

2.18.2.2 Tafel extrapolation method

The Tafel extrapolation methods provides a direct measurement of the corrosion rate and of the corrosion potential, and it is very useful in predicting the corrosion properties of various corrosion systems. This technique monitors the corrosion rate with an efficiency that is equal or greater than the convectional weight loss method (Berradja, 2019).

Corrosion current density, which corresponds to the corrosion rate at the corrosion potential, can be obtained by the Tafel extrapolation method.Sufficiently apart from the corrosion potential by ±50 mV, the current density (i_c) increases with the increase in overpotential (η), which is described by the Tafel equation (Equation 2.14) derived from the Butlar–Volmer Equation.

$$\eta = a_c + b_c \log i_c \tag{2.14}$$

where b_c is the Tafel slope (Hiromoto, 2010).

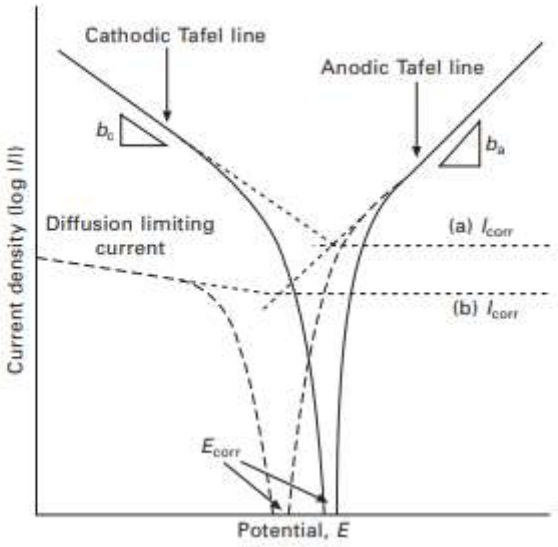

Figure 2.17: Schematic Illustration of the Tafel Extrapolation Method (Ecorr = Corrosion potential, Icorr = Corrosion current density, bc = Cathodic Tafel slope, ba = Anodic Tafel slope, Solid line = Both cathodic and anodic Tafel line appear on the polarization curve, Dashed line = Only anodic Tafel line appears on the polarization curve) (Hiromoto, 2010)

As shown in Figure 2.17, the intersection of the straight lines on anodic and cathodic polarization curves corresponds to the corrosion current density. Typical values of Tafel slope are 0.05~0.23 (Sugimoto, 2009). When the cathodic current is limited by diffusion of the cathodic reactant, as shown by the dashed line in Figure 2.17, the intersection of the anodic Tafel line and the limiting current line corresponds to the corrosion current density. It should be noted that the typical anodic Tafel line does not often appear on alloys in physiological solutions because several redox reactions take place in parallel.

2.18.2.3 Electrochemical impedance spectroscopy (EIS) theory

A technique of applying a sinusoidal perturbation to a system is a frequency domain measurement called Electrochemical Impedance Spectroscopy (EIS). Electrochemical impedance spectroscopy is mainly the proficiency of a circuit element to resist the flow of electrical current as stated below the Ohm's Law. The evaluation of coating

performance by extracting the characteristic parameters from Bode plots of the EIS has a useful theoretical and practical value (Zhang *et al*., 2019).

Electrical impedance spectroscopy (EIS) is a powerful technique that can be used in a broad range of applications, such as microbiological analysis (Ramirez *et al*., 2008), food products screening (Grossi *et al*., 2014), corrosion monitoring (Zhu *et al*., 2016), quality control of coatings (Amirudin and Thieny, 1995), characterisation of solid electrolytes (Rafiuddin, 2016) and human body analysis (Clemente *et al*., 2013). EIS dates back to 1894 when W. Nerst measured the dielectric constant of aqueous electrolytes and other organic fluids (Nernst, 1894). However, it was only in the mid-1980s that the interest in EIS really grew substantially, due to computer-controlled digital instruments allowing quick and easy measurements as well as complex data processing and analysis.

In an electrochemical cell, (EIS) employs a small AC signal to perturb a specimen over a wide frequency range and monitors the response of the cell to it.

The advantages of EIS over linear polarization (LPR) are:

i. It allows separation and evaluation of different components of the system, for example, separation of solution resistance from polarization resistance.
ii. EIS can be used to study coated surfaces more effectively.
iii. It can be used to determine the properties of surface layers. The analysis of EIS data is rather complex and may not provide a clear picture for many applications.

A flow diagram of the EIS steps is shown in Figure 2.18. Experimentally obtained EIS data for a given electrode system may be analyzed by using an exact mathematical

model based on plausible physical theory. This gives the theoretical impedance Ztheo(ω). The experimentally obtained impedance could also be analyzed with an empirical equivalent circuit denoted by Zec(ω). In either case, the experimental impedance data Ze(ω) can be compared to the predicted impedance data Ztheo(ω) or Zec(ω) by fitting the data using reduction of errors between experimental and fitted data (Lowe, 2002).

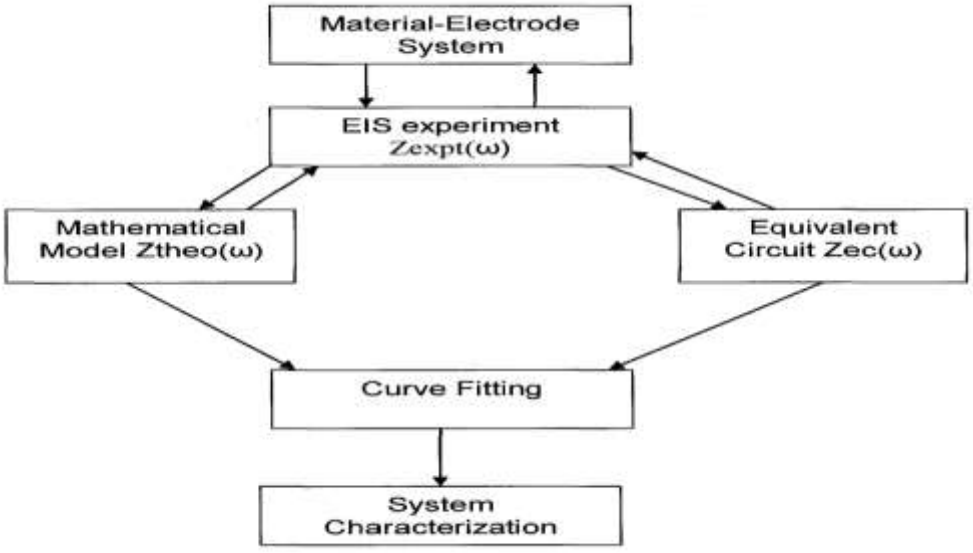

Figure 2.18: Flow Diagram for Measurement and Characterisation of a Material-Electrode System (Orazem and Tribollet, 2008)

When a specimen is placed in an electrolyte and under steady state conditions, the surface potential of the specimen approaches the corrosion potential. If an external perturbation voltage is applied to the system, a net current can be observed. If the perturbation signal is small, then the observed response is approximately proportional to the applied potential. There are three types of perturbation signals that may be applied: A step voltage, white noise and sinusoidal bias. The most common approach is to apply a single frequency bias and measure the real and imaginary parts of the resulting current by using either an analog circuit, or, a fast Fourier transform analysis of the response (Orazem and Tribollet, 2008).

Commercial equipment are available, which automatically assess the impedance of a system as a function of frequency in the frequency range of 1 mHz to 1 MHz. Therefore, if the voltage perturbation signal is Equation 2.15;

$$v_{(t)} = V_0 Cos(w_t) \tag{2.15}$$

The corresponding current response is presented in Equation 2.16.

$$i_{(t)} = I_0 Cos(w_t - \varphi) \tag{2.16}$$

With $v_{(t)}$, the impressed potential with respect to Ecorr; V_0, the magnitude of impressed potential in V; ω, the frequency of the sinusoid in radian per second; t is the time; i(t), the current response; I_0, the magnitude of the current response; φ, the phase difference between the current and the voltage, then the equivalent impedance Z is defined in Equation 2.17 as:

$$Z = \frac{v_{(t)}}{i_{(t)}} = \frac{v_0}{i_0}.\exp(j\emptyset) \tag{2.17}$$

In general, the impedance is denoted in Equation 2.18 as

$$Z(w) = z_0(w)\exp[j\emptyset(w)] \tag{2.18}$$

There are two methods for graphical representation of the related impedance: Nyquist plots and Bode plots. Nyquist plot is a plot of the real part versus the imaginary parts of the effective impedance. Bode plot is the plot of the magnitude versus the frequency and separately, the phase versus the frequency of the related impedance components. For example, let us consider a Randle's cell whose impedance is given by Equation 2.19.

$$Z(w) = R_s + \frac{R_p}{1+j\omega C\, R_p} \tag{2.19}$$

The Nyquist diagram is shown in Figure 2.19 (a) and the Bode plots are shown in Figure 2.19 (b). The topology of the impedance and the value of resistors may be obtained by either of the graphs. However, only the Bode plot can obtain the value of the capacitor since the Nyquist plot has lost all frequency information (Orazem &

Tribollet, 2008).

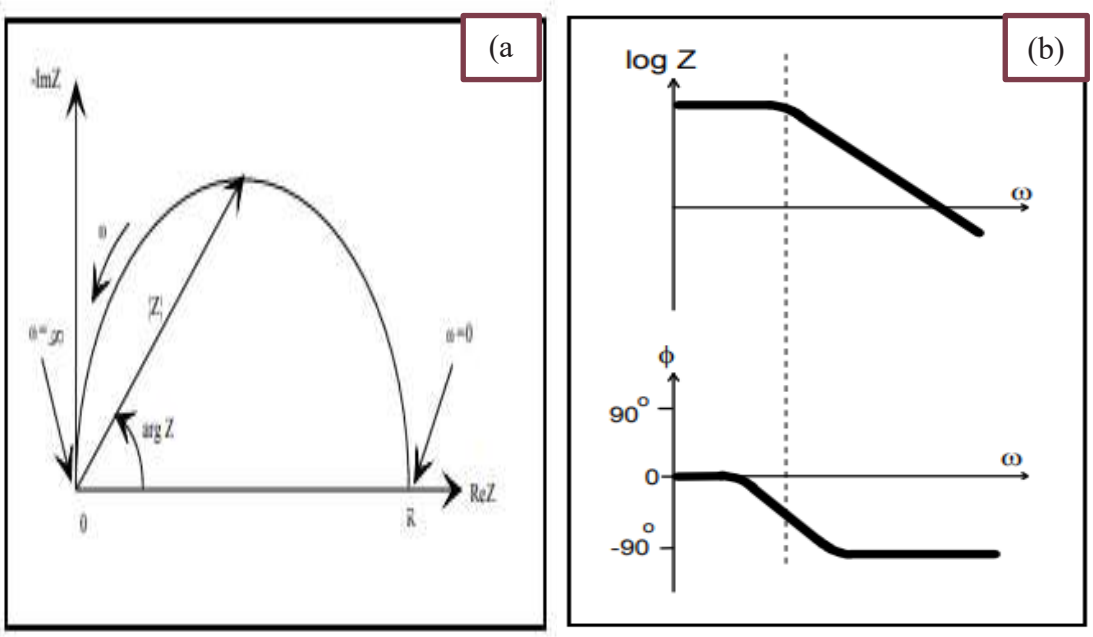

Figure 2.19: (a) Nyquist Plot with Impedance Vector and (b) Bode Plot with One Time Constant (Lowe, 2002)

The elements of the EIS measurements are related to physical properties of the cell. Some of the common components are:

i. Solution resistance (SR)- The resistance of an ionic electrolyte depends on the ion concentration, type of ions and temperature. It also depends on the geometry of the electrochemical cell and the path of the current flow.

ii. Double layer capacitance (C_{DL})- This capacitance is formed at the interface of the test specimen and the surrounding electrolyte. It forms when the ions in the electrolyte attaches to the surface resulting in a separation of charges between electrolytic ions adsorbed to the electrode surface and electrons in

the electrode. The separation between these charges is in the order of Angstroms. The value of double layer capacitance depends on electrode potential, temperature, concentration of ions, types of ions, oxide layer, and roughness of the surface.

iii. Polarization resistance (P_R)- An electrode becomes polarized whenever its potential is changed from its open circuit potential value. Polarization results in current due to electrochemical reactions at the electrode surface. The rate of current flow is controlled by kinetics of the reactions and diffusion of reactants.

iv. Charge transfer resistance (R_{ct})- When there is a single kinetically controlled electrochemical reaction present, it gives rise to a charge transfer resistance.

v. Diffusion Impedance - Diffusion of ions between metal and bulk solution results in an apparent impedance called the Warburg impedance. At high frequencies, Warburg impedance is small since the diffusing reactants do not need to move very far. At lower frequencies the Warburg impedance is high as the reactants have to diffuse farther into the electrolyte.

vi. Coating capacitance- The capacitance of the capacitor separated by a dielectric material is given by Equation 2.20.

$$C = \varepsilon_0 \varepsilon_r \frac{A}{d} \tag{2.20}$$

where $\varepsilon_0$the permittivity of is free space; ε_r is the dielectric constant; A is the area of the parallel plates and d is the separation between plates (Barsoukov and Macdonald, 2005). Table 2.4a-2.4d gives a summary of previous corrosion assessment carried out by various author using either weight loss, PDP or EIS.

Table 2.4a: Summary of Corrosion Test Techniques Success Rate(s) on Metallic Nanocomposites

Nanocomposite	carbon steel	Technique	Electrolyte	Corrosion resistance	Reference
Zn-Ni doped SnO_2	Mild steel	EIS and Pd-P	3.65% NaCl	The Tafel and electrochemical impedance studies proved that the presence of the Ni doped SnO_2 in Zn-coating increased the corrosion resistance property of Zn-deposit as compared to pure Zn-deposit. Increasing corrosion resistance from 364.2-Ωcm^2 to 2151 Ωcm^2 and decreasing corrosion rate from 3.55 $\times 10^5$ g/h to 1.0 $\times 10^5$ g/h.	Deepa and Venkatesha 2018

Al_2O_3-Ni	Steel plates	EIS and Pd-P	0.5 M NaCl and 0.5 M K_2SO_4	The corrosion rate calculated by polarization potentiodynamic curves was smaller in 0.5 M K_2SO_4 (4.74 m/year) than in 0.5 M NaCl (5.03 m/year). While from EIS data, polarization resistance (Rp) for NaCl was smaller 12.44 kΩ cm^2 compared to 29.88 12.44 kΩ cm^2 for K_2SO_4. Al_2O_3-Ni was a better coating feedstock in K_2SO_4 compared to NaCl.	Ciubotariu *et al*. 2008
Al-epoxy	Steel	EIS	0.1 MNaCl	From EIS analysis, it was observed that the charge transfers resistance (Rct) of steel coated by epoxy with 40% nanoparticle was higher (5.5 kΩ cm^2) than epoxy-coated steel (20 kΩ cm^2) in the wet/dry corrosion test. This behavior showed that the addition of Al nanoparticle resulted in high corrosion resistance in wet/dry test.	Madhankumar *et al*. 2012

Table 2.5b: Summary of Corrosion Test Techniques Success Rate(s) on Metallic Nanocomposites

Nanocomposite	carbon steel	Technique	Electrolyte	Corrosion resistance	Reference
Zn- α-Fe_2O_3-silicate resin	Steel	EIS	Sea water	Coating Resistance (Rc) evaluate the protective performance of the coatings. (ZS5+M16) with higher micaceous iron oxide content had the largest (Rc) 22.6 kΩ cm^2 in comparism to ZS5+M8 which had the lowest concentration of micaceous iron with (Rc) value of 16.02 kΩ cm^2	Zhao *et al*. 2019

Zn and Cu	carbon steel	EIS and Pd-P	Soil with 5% wt NaCl	Corrosion rates of zinc and copper electroplated samples were 58% and 94% lower than carbon steel, respectively, tested in the same condition	Shoaib *et al*., 2018
Ni-P/TiO_2 and Ni-P/CNT	Aluminum alloy	Pd-P and Immersion tests	3.5 wt% NaCl	The corrosion resistance of the nano-composite coatings was substantially increased to a maximum at 10 g/L TiO_2 and CNT. However, the CNT coating exhibited superior corrosion resistance (7.39 k$\Omega \cdot cm^2$) compared to the TiO_2 co-deposited coating with value (4.46 k$\Omega \cdot cm^2$). Furthermore, the weight loss of the Ni-P/TiO_2 and Ni-P/CNT decreased as the concentration of TiO_2 and CNT nanoparticles increases. 10 g/L CNT/Ni-P had the lowest value of 14.001 g/m^2 after 720 h immersion. The general sequence was 5083 substrate > Ni-P> Ni-P/TiO_2 > Ni-P/CNT.	Lee, 2012

Table 2.6c: Summary of Corrosion Test Techniques Success Rate(s) on Metallic Nanocomposites

Nanocomposite	carbon steel	Technique	Electrolyte	Corrosion resistance	Reference
HNT-epoxy	Caron Steel	EIS	3.5% NaCl	Best corrosion resistance of 1.16×10^6 Ω cm^2 was obtained at 10-wt% of HNT-epoxy as against a resistance of 12839-Ω cm^2 provided by 0-wt% HNT-epoxy.	Zhang *et al*. 2019

SnS/PVB, MoS_2/PVB, SnS-Zn/PVB, and MoS2-Zn/PVB Polyvinylbutyral	Copper Sheet	EIS, PDP and Immersion tests	3% NaCl	MoS_2-Zn/PVB had the best protection efficiency for all three corrosion protection-testing methods; 76 % from weight loss results, 99.75% from EIS data and 72.9% for potentiodynamic polarization measurement.	Qu *et al*., 2019
Cu-TiO_2	Mild steel	EIS, PDP and Immersion tests	5% NaCl	Cu-25TiO_2 had the best corrosion resistance of 475 Ωcm^2. While the weight loss method showed that, the Cu25TiO_2 also provided better corrosion resistance than the Cu-20TiO_2 coating. The potentiometric polarization test revealed that the Cu-25TiO_2 had the highest corrosion resistance, with increasing of TiO_2 nano particle content in the composite coatings, the corrosion current (I corr) decreased from 7.731 (A) to the much lesser values 7.359 (A) and the corrosion potential (Ecorr) shifted from -0.377V to more positive value 0.413V to for the uncoated steel.	Raghav *et al*., 2014

Table 2.7d: Summary of Corrosion Test Techniques Success Rate(s) on Metallic Nanocomposites

Nanocomposite	carbon steel	Technique	Electrolyte	Corrosion resistance	Reference

Al-TiB_2/TiC	Aluminum Matrixl	EIS, PDP and Immersion tests	3.5% NaCl	According to the weight loss rate, polarization curves and EIS results, Al-5 wt.% TiB_2/TiC composite with 20% rolling reduction had the best corrosion resistance in from weight loss results. This was also with the PDP result were it had the highest E_{corr} value of -0.724 4.6V and I_{corr} value of 4.6×10^{-6} A·cm^{-2} EIS data showed that the corrosion resistance of the composites decreases gradually with the rolling reduction increased from 20% to 90%, which is consistent with the weight loss and PDP results.	Nie *et al*., 2019
ZnO/CuO	Mild Steel	EIS, PDP and Immersion tests	1 M HCl	The protective performance and corrosion inhibition efficiency of sample ZnO/CuO 150ppm was the best approximately at 92.31% for both from EIS data and PDP results.	Sadek *et al*., 2019

2.19 Review of Existing Methods of Corrosion Prevention

Effective mitigation of corrosion damage of metals has been established with the development of suitable approaches to retard the corrosion. A successful corrosion mitigation strategy needs effective approaches with the selection and development of corrosion protection/prevention techniques (Khadija *et al.,* 2018). Corrosion prevention and control entails the characteristics of a system design to reduce corrosion, materials selection, non-destructive inspections for corrosion detection, coatings, cleaning materials, and washings, finishes, repairs, and other maintenance activities. One of the established techniques against corrosion damage is the use of corrosion inhibitors (Kolawole *et al*., 2018). A corrosion inhibitor is a liquid or solid substance when added in a suitable concentration to an environment reduces the corrosion rate by reducing the corrosivity of the environment (Malik *et al*., 2011).

However, the use of corrosion inhibitors has proven to be the easiest and cheapest method for corrosion protection and prevention in acidic media. These inhibitors slow down the corrosion rate and thus prevent monetary losses due to metallic corrosion on industrial vessels, equipment, or surfaces. Inorganic and organic inhibitors are toxic and costly and thus recent focus has been turned to develop environmentally benign methods for corrosion retardation. Many researchers have recently focused on corrosion prevention methods using green inhibitors for mild steel in acidic solutions to mimic industrial processes. Chigondo and Chigondo (2016) provided an overview of types of corrosion, corrosion process, and mainly recent work done on the application of natural plant extracts as corrosion inhibitors for mild steel.

In acidic media, nitrogen-base materials and their derivatives (sulfur-containing compounds, aldehydes, thioaldehydes, acetylene-like compounds, and various alkaloids: papaverine, strychnine, quinine, and nicotine) have been used as inhibitors. In neutral

media, benzoate, nitrite, chromate, and phosphate have been found to act as good corrosion inhibitors.

Meanwhile, use of some inhibitors, such as chromate, has been banned because of toxicity and the environmental hazards they create. Several factors including the cost and the amount, easy availability, and (most importantly) safety to the ambient environment must be considered when choosing an inhibitor.

Hence, there is a need to make use of environmentally friendly, non-toxic, extracts of naturally occurring plant materials as corrosion inhibitors also known as green corrosion inhibitors. Extracts of plant materials contain a wide variety of organic compounds. Some of the green corrosion inhibitors that have been used in the past are extracts from aloe vera, banana plant juice, mango, orange, passion fruit, cashew peels and tobacco leaves. (Kolawole *et al*., 2018).

Rani and Basu (2012) discussed green inhibitors for corrosion protection of metals and alloys. According to them corrosion control is important from technical, economical, environmental, and aesthetical point of view. Oladele and Okoro (2011) investigated corrosion effect of mild steel on orange juice. It was observed that the corrosiveness of sweet orange juice on mild steel was mainly a function of its acidity. According to this research packed orange juice with preservative was most corrosive followed by natural juice. Iyasara and Ovri (2013) carried out an investigation on corrosion inhibition of stainless steel (314l) using molasses. It was observed that the solution of the molasses inhibited the corrosion of the stainless-steel samples to an extent depending on the concentration of the molasses and the type of medium. According to them, the physical adsorption of the inhibitor (molasses) on the surface of the stainless steel was a reason for corrosion inhibition.

Inhibiting effect of *Prosopis africana* (Iron Tree) seed extracts were assessed on a sample of low carbon steel in 1M HCl with varying proportion of the seed extract using gravimetric, Tafel polarization and gasometrical measurement techniques. The results show that weight loss/corrosion rate decreases with increase in the extracts' concentrations. Good inhibiting efficiency of Prosopis Africana extracts with optimum inhibiting efficiency of 97.7% at 1.0 g/l after 120 h' exposure in gravimetric measurement was attained. TAFEL polarization results revealed that the Prosopis Africana extract shows that the corrosion current density decreases with the increase in the concentration of the extract. The extract is found suitable as green inhibitor for corrosion of low carbon steel in the studied medium (Shuaib-Babata *et al*., 2019).

Aduagba *et al*. (2016) tested Akee apple leaves extract (AALE) for inhibition of corrosion of mild steel in sulphuric acid solution using gravimetric and gasometric measurement. The corrosion of mild steel was investigated at 40-60^{0}C in 2M H_2SO_4 solution. The result of the inhibition revealed AALE efficiently delayed the dissolution of mild steel with inhibition efficiency obtained from gravimetric and gasometric at 60^{0}C are 72.19 % and 74.32 % at addition of 0.5 g/l concentration of AALE respectively. The increase in inhibitor (AALE) concentrations results in decrease in corrosion rate and increase in inhibition efficiency. The inhibitive adsorption parameters show the corrosion process followed the Langmuir adsorption isotherm with physical adsorption mechanism.

The inhibitive ability of Bitter leaf (*Vernonia amygdalina*) root extract was investigated on corrosion of mild steel in 1.5 M sulphuric acid solution using weight loss, hydrogen evolution and thermometric measurements at temperature ranges of 30-60°C. The results showed corrosion rate of mild steel in the presence of inhibitors decreases and increase as the temperature increases. The inhibitor exhibits excellent inhibition

efficiency on mild steel corrosion in H_2SO_4 solution as 90 %, 84.82 %, 79.65 % and 76.90 % of inhibition efficiency achieved with addition of 0.5 g/l concentration of bitter leaf root extract (BLRE) at 30°C, 40°C, 50°C and 60°C temperature respectively. The inhibition efficiency increases with in concentration of inhibitor and decreases with rise in temperature (Awe *et al.*, 2015).

The inhibition of mild steel corrosion in sulphuric acid solution was studied with application of Africa parquetina leaves extract (APLE) using Gravimetric, Gasometric and Thermometric measurements. The showed that the inhibition efficiency at optimum concentration 0.5 g/l was 87.78 % and it was increased with the increase in concentration of (APLE) but decreased with increase in temperature. The adsorption of inhibitor obeyed Langmuir adsorption isotherm and the free energy of adsorption suggested that it was physisorption. Finally, the Dubinnin-Radushkevich isotherm model also suggested the techniques adopted in the corrosion measurement were in good agreement (Abdulrahman *et al*., 2015). Other plants extract as green corrosion inhibitors have been reviewed by Rathi *et al*. (2017). However, Isolation of element (surface) from the corrodent has been considered to be the cheapest and efficient means to control corrosion. Isolation process is the regime of paints (coatings) and liners using isolators on surface to protect metals from rust (Nagham *et al*., 2019).

Inorganic isolators or coatings involve both sacrificial coatings, which protects the metal surface from rust. There are two types of chemical coating: organic coating and inorganic coating, like some polymers, dyes, and plastic, nickel and non-metallic coatings like ceramics (Nawfel, 2015).

Sol-gel-coated layers has been reported as one of the isolator that exhibit good adhesion to the metal substrate due to the formation of chemically adsorbed M─O─Si bonds,

resulting in a good anticorrosion performance (Khadija *et al*., 2018).

Ali and Allehaibi (2017) reported the protection abilities of unmodified and modified GPTMS-VTMS sol-gel films with different Ti- and Al-alkoxides concentrations against zinc corrosion in 0.5 M HCl solution. It was shown that the presence of the modifiers, either Ti or Al, facilitates the formation of the network structure and increases slightly the thermal stability of sol-gel materials. Weight-loss and electrochemical measurements proved that the highest protection ability of sol-gel coatings is assigned with low modifiers concentrations. The protection efficiency is increased from 69.2 to 96.2% and 95.8% upon modification with 0.005 M of Ti and Al modifiers, respectively. On the other hand, higher modifier concentrations may cause a galvanic corrosion which results in lower protection efficiency values. Corrosion inhibitors and nanoparticles can be added in the silane sol-gel network to improve corrosion resistance.

Balan *et al*. (2014) examined the effect of adding activated cerium nitrate nanoparticles into a coated sol-gel matrix on low-carbon steel substrates. Hybrid sol-gel films have been prepared from mixture of TEOS and GPTMS. Silica, alumina and their equimolar mixtures are used as nanoparticles with a concentration of 250 ppm. The SEM confirmed crack-free surface for prepared substrates with different pretreatments.

Inorganic corrosion inhibitor was introduced into the coating via encapsulation in the nanoparticles reported by Tavandashti and Sanjabi (2010). Organosiloxane sol was prepared by mixing GPTMS, TEOS and isopropanol to obtain a sol with 75 mol% organic content. The high corrosion-resistance performance of such coatings is due to the presence of encapsulated cerium nitrate corrosion inhibitor that can be released at the defects within the coating, hindering the corrosion reactions at defective sites.

Asadi *et al*. (2014) investigated the cloisite concentration effect on the protective performance of sol-gel coating, prepared from GPTMS, TEOS and methyltriethoxysilane on mild steel substrate. The optimum concentration of nanoparticles was determined. The data indicated superiority of the hybrid film embedded with 1000 ppm of cloisite nanoparticles. Confirming the electrochemical data, FTIR spectra and water contact angles showed that the nanoparticles well dispersed in the silane film might improve barrier properties moreover, a good trend correlation was observed between the noise resistance and low-frequency |Z| data.

Naderi *et al*. (2013) studied the synergistic effect of incorporation of nanoclay along with cerium nitrate as a corrosion inhibitor into an eco-friendly silane layer consisting of GPTMS, TEOS and methyltriethoxysilane applied on pure Al. EIS and polarization results showed that the high protective nature of film containing cerium is due to film deposition on cathodic regions, thus preventing entrance of aggressive species to the surface. FTIR spectra proved the presence of the inhibitor in the film structure. N-nanoparticles silane coating in the presence of cerium salt provided higher corrosion protection compared to the film with only incorporated nanoclay.

The anti-rust coatings concede a barrier between the metal surface and atmospheric corrosive materials like polymers or azo dyes. Halo-polymer is basically a resinbased chemical material that supplies very good protection against rust, contain chemical materials which resists high temperatures and also made up of epoxy materials thatresist abrasion as well as rust (Ali *et al*., 2016; Anbarasi & Vasudha 2014; Slepski *et al*., 2014) as resistant metals or azo compounds.

Polyester coating had been used to mitigate steel pipeline in both oil and gas industries. However, this polymer coating allowed the penetration of solutions, which are corrosive

to the systems. These resulted to malfunctions in the system and allowing penetration of corrosion environments thereby making corrosion resistance of the coating weak. Previous researchers had shown that polyester reinforced with other materials such as Al_2O_3, SiO_2 and TiC also determines the coating behaviours of the system. This reinforcement improves the microhardness, wear and corrosion accordingly (Dumain *et al*., 1999).

The corrosion resistance of composites' coatings may be ascribed to the fact that there is always barrier between the substrate and the adsorbate. Particle size reinforcement with polymer reduces the space within thereby making the coating better. Findings had also shown that he absorption of water in this polymer coating is far higher than if the polymer is being reinforced with particle sizes of Al_2O_3, and SiO_2 (Hedayati *et al*., 2012; Obasi *et al*., 2012; Kenneth *et al*., 2014; Liu *et al*., 2015; Suleiman *et al*., 2016). The results shown from the previous studies confirmed that agricultural waste powders are rich in some of the refractory materials. These refractory materials are calcium oxide (CaO), silica (SiO_2), alumina or bauxite (Al_2O_3). Works had shown that some of the agricultural wastes can be used as fillers, which mitigate corrosion had been carried out (Suleiman *et al*., 2018).

Katariya *et al*. (2013) assessed the effect of coating mild steel with Zeolite ZSM-5 on the corrosion resistance against varying concentrations of different organic acids (acetic acid, formic acid and citric acid) at temperatures up to 60°C under stagnant and stirred conditions. The results showed that for 6 h duration of contact between zeolite coating and acid solutions, corrosion inhibition efficiency up to 98% is achieved. The extent of mild steel corrosion decreased in the order of formic acid > citric acid > acetic acid, and corrosion resistance though only slightly, decreased with solution temperature and concentration.

Al-Sarraf and Yaseen (2018) studied the protection method with composite coating of unsaturated polyester and reinforced by Caolin at weight percentage (20%). The results showed an improvement in the corrosion resistance of protected steel by coatings compare with uncoated steel, as well as improvement in mechanical properties and adhesion strength of composite coatings.

The pure polyester reinforced with snail shell powder (SSp) applications as coating to steel pipeline was carried out. The steel pipelines coated with polyester/SSp being heat-treated at 150 °C were investigated for corrosion resistance by Tafel test in seawater. The corrosion resistance properties of polyester/snail shell powder coatings were significantly improved. This was attributed to the hard coatings after heat treated. Current density (icorr) of the steel pipeline, steel pipeline/polyester, steel pipeline/ polyester reinforced with 10 wt.% and 15 wt.% SSp in seawater was 36.61, 10.47, 9.05 and 0.81 $\mu A/cm^2$ respectively. The test showed that addition of snail shell powder increases wear resistance of the coating reinforced with snail shell powder than polyester alone. From the above findings, the steel pipeline coated with polyester/snail shell powder in the range of 10–15 wt.% can be used conveniently in seawater environment (Suleiman *et al*., 2018).

Allahyarzadeh *et al*. (2016) developed nickel–tungsten functionally graded (FG) coatings using pulse electrode position. Electrochemical and pin-on-disk wear tests were performed to investigate corrosion resistance and wear behaviour of the coating, respectively. Results showed that with reduction of duty cycle or increasing of frequency along this eight-layer structure, the tungsten content increased upward the surface. Results showed the superior wear resistance of the coating as compared to that

of pure nickel. Moreover, the coefficient of friction decreased from 0.74 to 0.49 by an increase in the sliding distance.

Composite materials of PMMA and hBN were developed and deposited on steel by dip-coating. The produced coatings were submersed in NaCl and HCl solutions to analyze corrosion resistance. The results showed that the PMMA/hBN composite coatings improved the corrosion resistance in comparison with pure PMMA. Additionally, the coatings are crack free and well bonded to the metallic substrate (Coana *et al*., 2013).

Rezaeiolum *et al*. (2017) fabricated multilayer Ni–Mo–Al_2O_3 and Ni–Mo coatings on the low carbon steel using pulse electrodeposition technique from a citrate-ammonia bath. The coatings with different number of layers (32, 128 and 512) were electrodeposited by the periodic alteration of duty cycle (between 20 and 90%) at a constant frequency of 400 Hz and an average current density of 6 A dm^{-2}. The corrosion resistance of the coatings was estimated using potentiodynamic polarisation and electrochemical impedance techniques and wear properties was also evaluated using pin-on-disk wear test. Potentiodynamic polarisation and electrochemical impedance in 3.5 wt-% NaCl solution showed that 128-layer nanocomposite coatings had the highest corrosion resistance. By increasing the number of the layers in Ni–Mo coatings, their hardness was improved from 563±20 Hv0.1 to 714±42 Hv0.1, while the wear rate was decreased from 9.87 to 5.16 $\mu g N^{-1}$ m^{-1}. The addition of nanoparticles showed favourable impacts on the coating's hardness and wear properties.

Functionally graded Zn–Ni–Al_2O_3 coatings were electroplated by continuously changing the duty cycle/frequency. Two types of graded coatings were deposited; the first type was synthesised through gradual reduction in the duty cycle from 88 to 11% at a certain frequency and the second type was plated by increasing the frequency

gradually from 100 to 1500 Hz at a constant duty cycle. Microstructure and composition of coatings were determined by scanning electron microscope equipped with energy-dispersive spectroscopy. Corrosion behaviour was studied by potentiodynamic polarisation and electrochemical impedance spectroscopy (EIS); and tribological properties were evaluated using the pin-ondisc test. The results showed in the first type, Ni and alumina contents, and microhardness were increased towards the surface. However, in the second type, composition was less affected through frequency alterations. Increasing the frequency raised the corrosion rate in the range of 2.9–8.7 μA cm^{-2} and improved the wear resistance (Shrgeshty *et al*., 2018).

Khodair *et al*. (2018) studied corrosion rate of mild steel in different aqueous solutions at different operating conditions using weight loss technique in the absence and presence of epoxy coating. It was found that corrosion rates increased with temperature and sailt concentration and decreased with pH values. Presence of coating reduces the corrosion rates to significant values in acidic solutions. Maximum coating efficiency was 97% in acidic solution, while the lower one was 29.8 % in solutions in absence of nanoparticles. Nano scale MgO was used effectively with epoxy coating in saline solutions and improve the coating performance with maximum value of 97.3%.

Potentiodynamic polarization and EIS spectroscopy have been used to study the corrosion behavior of composite coating in 3.5% NaCl solution. Results showed that ceria doping presented higher corrosion resistance than undoped silica-titanium composite layer and also the passive region of the doped films in potentiodynamic tests expanded with respect to undoped silica-titanium composite layer. The film corrosion resistance is noticed due to the inhibition action of cerium. There is a critical cerium concentration, above it cracking occurs, this can be related to the high expansion coefficient of cerium oxide (Shi *et al*., 2010).

Traditionally, corrosion control has been maintained using various methods including process control, cathodic protection, reduction of the metal impurity, and incorporation of suitable alloys, as well as application of surface treatment techniques. Cathodic Protection is used to mitigate or prevent the corroding interface of the steel pipeline by altering the electrochemical condition. Altering the electrical potential field around the pipe causes an alteration in the electrochemical nature of the corroding surface, the rate of oxidation is reduced and the reduction process is accelerated by applying a negative potential and making the pipe a cathode. Corrosion control is enhanced by cathodic protection, which also alters the environment at the pipe surface. The pH of any electrolyte at the pipe surface is increased, the oxygen concentration is reduced and deleterious anions, such as chloride, migrate away from the pipe surface (Kolawole *et al*., 2018).

Yaro *et al*. (2013) controlled corrosion of steel tube in sea water by cathodic protection using Sacrificial anode technique. Weight loss method was used to determine the rate of zinc consumption as a function of pH, temperature, time, and solution velocity. The sacrificial anode cathodic protection of short steel tube using zinc strip extended axially in the pipe revealed that under the present range of conditions, the rate of zinc consumption increases with increasing temperature, flow rate and time and with decreasing pH. The zinc consumption with very low pH is very high and the cathodic protection becomes unreliable.

2.20 Research Gap

Different nano-coating formulations and materials have been carefully reviewed as employed by various researchers to protect steel against corrosion, these nano-coating have also been tested against corrosion using various methods which have been enumerated in the the review of related literature. However, the research gaps that have

been filled by this research include;

Formulation of unique nano-coatings such as, NiO-SnO_2, NiO-CNTs, SnO_2-CNTs, and particularly a novel NiO-CNTs-SnO_2 nanocomposite, which was been fabricated and employed in anti-corrosion studies for the first time. Based on reviewed literature, it can be noticed that most of the corrosion studies carried out make use of simulated environmental conditions, but this research brought to lime light the effect of real environmental impact on the nano-coated steel by burying them in soil for twelve months. Finally, this research reported the effect of process parameters such as pH on the micro-structure, morphology, and dispersion of NiO and SnO_2 in CNTs which is paramount in designing a nano-composite for anti-corrosion studies.

CHAPTER THREE

3.0 MATERIALS AND METHODS

3.1 Materials

The major materials and equipment used for this research work are presented in Tables 3.1 and 3.2. All the chemical/reagents and gases used in this study shown in Table 3.1 are of analytical grades with percentage purities in the range of 98.0 - 99.5%. The supplied chemicals/reagents were used without further purification while the list of eqiupment used for the characterisation of the nanocomposites and carbon steel is presented in Table 3. 2.

Table 3.1: List of Reagents

S/N	Chemical reagent	Availability	% Purity
1	Tin (II) chloride dehydrate ($SnCl_2.2H_2O$)	Sigma Aldrich	98
2	Nickel (II) chloride hexahydrate ($NiCl_2.6H_2O$)	Sigma Aldrich	99
3	Concentrated Hydrochloric acid (HCl)	Chemical Engineering FUT, Minna	99
4	Sodium Hydroxide (NaOH)	Chemical Engineering FUT, Minna	99
5	Ethanol (99% w/w)	Chemical Engineering FUT, Minna	99

Table 3.2: List of Equipment

S/N	Equipment/Model number	Uses	Location
1.	Scanning Electron Microscope (HRSEM) + EDX FD 1250	For surface morphology and microstructure of materials.	Department of Physics, University of the Western Cape, South Africa
2.	Transmission Electron Microscope TECNAI G2 F20.Twin.	For microstructure and particle size of the material.	Department of Physics, University of the Western Cape, South Africa
3.	XRD	XRD-6000	Shimadzu Scientific Instruments, University of the
4.	Potentiometer/Galv-anosta Auto Lab PGSTAT	For corrosion measurement	Western Cape, South Africa African University of Science and Technology, Abuja Nigeria

3.2 Methods

The methods used in the synthesis of the nanoparticles and nanocomposites are discussed from Section 3.2.1.

3.2.1 Samples collection and pre-treatment

Three different plants namely *African cactus, Ackee apple* and *African parquetina* were collected from the different locations within Minna metropolis. These plant parts were washed properly to remove dust particles and other contaminants which might be present. This was then followed by drying the leaves under room temperature for a period of four weeks. The dried leaves were ground to powder for further use. Presented in Plate I are images of plant leaves used in this study.

Plate I: Plants selected for Phytochemical Screening: (a) *AfricanCautus (b) Ackee Apple* (c) *African Parquetina*

3.2.2 Phytochemical screening of plant samples

The phytochemical screening was conducted on the three selected plant leaves to determine the concentrations of total phenols, tannins and flavonoids, which are the active bio-chemicals responsible for the reduction of metal precursors to zero valence state.

3.2.2.1 Determination of total phenolic content

The concentration of phenolics in plant extracts was determined using spectrophotometric method. Folin-Ciocalteu assay method used for the determination of the total phenols content is described as follow: 1 cm^3 of extract and 9 cm^3 of distilled water was taken in a volumetric flask (25 cm^3) and mixed together. 1 cm^3 of Folin-Ciocalteu phenol reagent was added to the mixture and shaken well followed by the addition of 10 cm^3 of 7 % Sodium carbonate (Na_2CO_3) solution to the mixture after 5 minutes. The volume was made up to 25 cm^3. A set of standard solutions of gallic acid (20, 40, 40, 60, 80 and 100 µg/cm^3) were prepared. The mixture was incubated for 90 min at room temperature and the absorbance for test and standard solutions were determined against the reagent blank at 550 nm with an Ultraviolet (UV) /Visible spectrophotometer. Total phenols content was expressed as mg of GAE/gm of extract and calculated from Equation 3.1 (Ghasemzadeh *et al*., 2010).

$$TTPC = G\frac{V}{N} \quad 3.1$$

where TPC is the Total phenolic content in mg/g, G is the concentration of gallic acid established from the calibration curve in mg/cm^3, V is the volume of the extract in ml, N is the wt of the plant extract in mg.

3.2.2.2 Determination of tannin content

The level of tannins in the selected plants were determined using Folin - Ciocalteu method described as follows: About 0.1 cm^3 of the sample extract was added to a volumetric flask (10 cm^3) containing 7.5 cm^3 of distilled water and 0.5 cm^3 of Folin-Ciocalteu phenol reagent. Subsequently, 1 cm^3 of 35 % Na_2CO_3 solution was added and further diluted with distilled water. The mixture was shaken well and kept at room temperature for 30 min. A set of reference standard solutions of tannic acid (20, 40, 60, 80 and 100 μg/cm^3) were prepared. Absorbance for test and standard solutions were measured against the blank at 725 nm with an UV/Visible spectrophotometer. The tannin content was expressed in terms of mg of GAE /g of extract and calculated from Equation 3.2 (Rajeev *et al*., 2012).

$$TC = T\frac{V}{N} \quad (3.2)$$

where TC is the Tannins content in mg/g, T is the concentration of tannic acid established from the calibration curve in mg/ml, V is the volume of the extract in cm^3, N is the wt of the plant extract in mg.

3.2.2.3 Determination of total flavonoid content

Total flavonoid content was measured by the aluminum chloride colorimetric assay. The reaction mixture consists of 1 cm^{3}of extract and 4 ml of distilled water was taken in a 10 ml volumetric flask. To the flask, 0.30 ml of 5 % sodium nitrite was treated and after 5

minutes, 0.3 cm^3 of 10 % aluminum chloride was mixed. After 5 min, 2 cm^3 of 1M Sodium hydroxide was treated and diluted to 10 ml with distilled water. A set of reference standard solutions of quercetin (20, 40, 60, 80 and 100 μg/cm^3) were prepared in the same manner as described earlier. The absorbance for test and standard solutions were determined against the reagent blank at 510 nm with an UV/Visible spectrophotometer. The total flavonoid content was expressed as mg of QE/g of extract and calculated from Equation 3.3 (Har and Ismail, 2012).

$$TFC = Q\frac{V}{N} \tag{3.3}$$

where TFC is the Total flavonoid content in mg/g, Q is the concentration of quercetin standard established from the calibration curve in mg/ml, V is the volume of the extract in ml, N is the wt of the plant extract in mg.

3.2.3 Preparation of the aqueous extract of *African cactus*

A known weighed (5 g) of the leaves was added to 100 cm^3 of distilled water in a 250 cm^3 conical flask. The resulting mixture was stirred and heated at 80°C for 90 min and then filtered. The filtered extract was stored in a refrigerator until further use. The extract is shown in Plate II.

Plate II: *African cactus* Plant Extract

3.3 Synthesis of Nanoparticles (NPs)

The synthesis of tin and nickel nanoparticles was carred out via the procedure in Sections 3.3.1 and 3.3.2

3.3.1 Synthesis of Tin (IV) oxide nanoparticles (SnO_2 NPs)

Green synthesis of SnO_2 was adopted from the method used by Senthilkumar and Rajendran (2017), with slight modifications. A known volume (20 cm^3) of 0.40 M $SnCl_2.2H_2O$ solution was added to 50 cm^3 of the aqueous extract of African cactus and the resulting mixture was heated at 58°C for 2 h. Thereafter, the pH of the solution was adjusted to 10 using 1 M NaOH. The mixture was then stirred on a magnetic stirrer at 150 rpm for 3 h. The stirring was accompanied with the transformation of greenish yellow coloured solution into pale yellow, an indication of tin (IV) oxide formation of nanoparticles. The pale-yellow residue formed were centrifuged to remove the residual particles and then dried in an oven at 80°C for 6 h. These as-prepared samples were coded accordingly. The residue was then calcined at 500°C for 3 h and the obtained samples were pulverized with an agate mortar and stored in sterile sample bottle for further use. This procedure was repeated for other pH values (8 and 12). The synthesised SnO_2 and the dried products are shown in Plate III. The parameters varied for the synthesis of SnO_2 nanoparticles were optimized as shown in Tables 3.3 and 3.4.

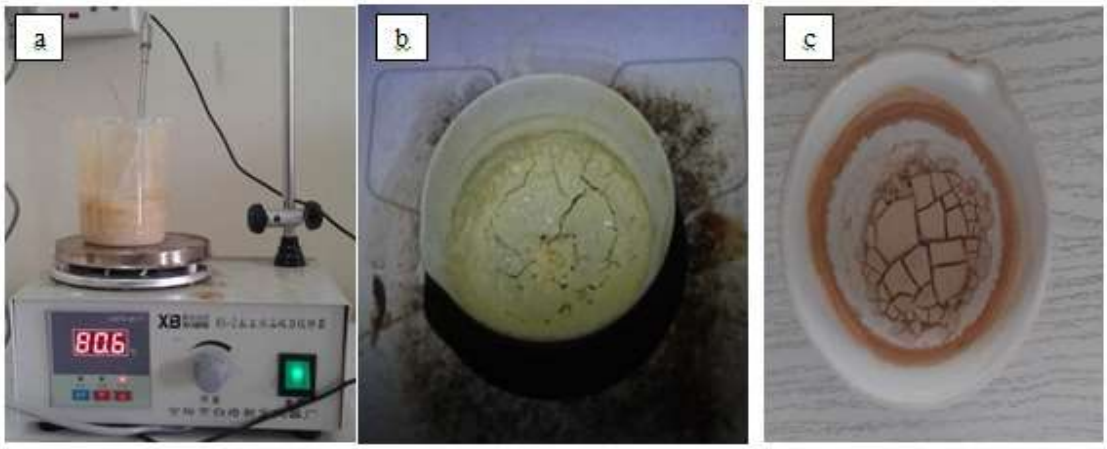

Plate III: (a) Synthesised SnO_2 NPs after 2 h (b) Purified Dried SnO_2 NPs (c) Calcined SnO_2 NPs

Table 3.3: Variation of Parameters for the Response Surface Methodology Based on Box-Behnken Design for the Preparation of SnO_2 Nanoparticles

Factors	Levels		
	-1	0	1
Solution pH (X_1)	10	11	12
Precursor concentration (X_2)	0.350	0.375	0.400
Synthesis temperature (X_3)	25.0	57.5	90.0

Table 3.4: Box–Behnken Experimental Design for SnO_2 NPs

Std Order	Run Order	X_1	X_2 (moldm^{-3})	X_3 ($^{\circ}$C)	Y_0 (nm)	Y_1 (nm)
13	1	11	0.3750	57.50		
6	2	12	0.3500	57.50		
7	3	10	0.4000	57.50		
11	4	11	0.4000	25.00		
1	5	10	0.3750	25.00		
4	6	12	0.3750	90.00		
3	7	10	0.3750	90.00		
12	8	11	0.4000	90.00		
8	9	12	0.4000	57.50		
14	10	11	0.3750	57.50		
15	11	11	0.3750	57.50		
2	12	12	0.3750	25.00		
10	13	11	0.3500	90.00		
9	14	11	0.3500	25.00		
5	15	10	0.3500	57.50		

where Y_0 is the experimental response (crystallite size), and Y_1 is the predicted responses (crystallite size)

3.3.2 Synthesis of nickel oxide nanoparticles (NiO NPs)

The procedure for this synthesis was developed by Mariam *et al*. (2014) with slight variations. Nickel (II) chloride hexahydrate ($NiCl_2.6H_2O$) (99.99 % purity) was used as the precursor (Merck chemicals, India). 50 ml of the plant extract was mixed with 20 ml of 0.37 M of aqueous ($NiCl_2.6H_2O$) solution drop wisely with constant stirring at 53 ºC for 2 h, the pH was adjusted to 8 by using 1 M NaOH, and the colour of the product was blackish green after the reduction reaction. The precipitate was collected washed with distilled water to remove any residue and unreacted plant extracts and subsequently dried in an oven at 80ºC for 6 h. The resultant product was finally transferred into a ceramic crucible and heated in a furnace at 500 °C for 3 h as shown in Plate IV. Clear black NiO NPs in powder form obtained were stored for further analysis. The parameters varied for the synthesis of NiO nanoparticles were optimized as shown in Tables 3.5 and 3.6.

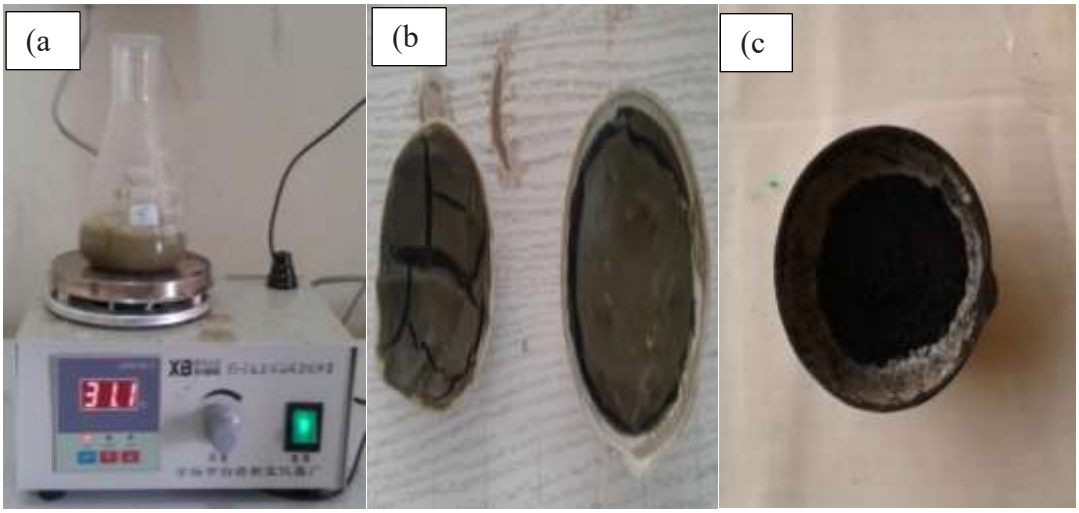

Plate IV: (a) Synthesised NiO NPs after 2 h (b) Purified Dried NiO NPs (c) Calcined NiO NPs

Table 3.5: Variation of Parameters for the Response Surface Methodology based on Box-Behnken Design for the Preparation of NiO Nanoparticles

Factors	Levels		
	-1	0	1
Solution pH (X_1)	8	10	12
Precursor concentration (X_2)	0.25	0.31	0.37
Synthesis temperature (X_3)	25.0	52.5	80.0

Table 3.6: Box–Behnken Experimental Design for NiO NPs

Std Order	Run Order	X_1	X_2 (moldm^{-3})	X_3 ($^{\circ}$C)	Y_0 (nm)	Y_1 (nm)
1	1	8	0.25	52.50		
11	2	10	0.25	80.00		
8	3	12	0.31	80.00		
5	4	8	0.31	25.00		
3	5	8	0.37	52.50		
6	6	12	0.31	25.00		
2	7	12	0.25	52.50		
13	8	10	0.31	52.50		
4	9	12	0.37	52.50		
7	10	8	0.31	80.00		
12	11	10	0.37	80.00		
9	12	10	0.25	25.00		
10	13	10	0.37	25.00		
15	14	10	0.31	52.50		
14	15	10	0.31	52.50		

Y_0 = Experimental response (crystallite size), Y_1= Predicted responses (crystallite size)

3.4 Production of Carbon Nanotubes

Carbon nanotubes (CNTs) were produced by a catalytic chemical vapour deposition method (CCVD) which involves the decomposition of carbon source (acetylene gas) in a tubular quartz reactor onto the Fe-Ni/kaolin catalyst. A known weight (1.0 g) of Fe-Ni/kaolin catalyst support in a crucible was heated at 10^{o}C/min in a CVD, while argon gas was flown over the Fe-Ni/kaolin catalyst at 15 mL/min. As the CVD reached the reaction temperature (750^{o}C), the argon flow rate was adjusted to 100 mL/min and

acetylene gas flow rate was equally adjusted to 200 mL/min. The reaction continued until the deposition time of 45 min was attained and the CNTs was produced. The percentage yield of CNTs produced was determined using Equation 3.4.

$$CNTs\ Yield\ (\%) = \frac{W_{Product} - W_{catalyst}}{W_{catalyst}} \times 100\ \% \quad (3.4)$$

where $W_{Product}$ is the total mass of the catalyst and final carbon products after CVD reaction process and $W_{catalyst}$ is the initial mass of Fe-Ni/kaolin catalyst.

3.4.1 Surface purification of multi walled carbon nanotubes (CNTs)

Prior to refluxing, 10 g of CNTs was sonicated for 1.5 h in a mixture of 1000 $cm^3$of 68% HNO_3 and 97% H_2SO_4 in the ratio of 3:1 to reduce the particle agglomeration and remove residual impurities that may exist. Subsequently, the mixture was refluxed under stirring speed at 100 °C for 3 h and purified CNTs was produced and washed severally with distilled water until pH 7 was reached. Finally, the purified CNTs were dried at 120°C for 6 h.

3.5 Preparation Nanocomposites

The synthesis of each nanocomposite was carried out via the procedure as follows.

3.5.1 Preparation of NiO-SnO_2 nanocomposites

The synthesis of NiO-SnO_2 nanocomposites in the ratio of 1:1 for Ni and Sn respectively was carried out as follow: Ten (10 cm^3) of 0.5 M aqueous solution of $SnCl_2.2H_2O$ was added to an equal volume of 0.5 M aqueous solution of $NiCl_2.6H_2O$ initially and the solution obtained was stirred for 30 min. Afterwards, 50 cm^3 of the plant extract was added drop by drop under constant stirring at 80^oC for 2 h. The pH was adjusted to 10 using 1 M NaOH and to complete the reaction, the mixture was further stirred for 2 h. The precipitate formed was decanted, washed with ethanol and

distilled water several times followed by drying in oven at 80^{o} C for 6 h. The oven dried sample was then calcined at 500^{o} C for 3 h in the furnace. This procedure was repeated using Ni:Sn ratio of 1:2 and 2:1 respectively. All the samples were then pulverized and stored in sterile containers.

3.5.2 Preparation of NiO-CNTs nanocomposites

Firstly, 0.45 g of the purified CNTs was first dispersed in 60 cm^3 of ethanol and water (1:4) in the 250 cm^3 conical flask placed on the ultrasonic water bath and sonicated for 1 h. Afterwards, 40 cm^3 of the NiO suspension (ethanol and water (1:4)) containing 0.45 g of NiO was added, and the mixture comprising (CNTs/NiO) in the ratio of 1:1 was continuously sonicated for another 4 h. The resultant NiO-CNTs product was washed thoroughly with ethanol and water and dried in an electric oven at 80°C for 6 h to obtain NiO/CNTs nanopowder. The procedure was repeated using different ratio of NiO/CNTs such as 1:2 and 2:1 respectively.

3.5.3 Preparation of SnO_2-CNTs nanocomposites

SnO_2/CNTs nanocomposite was prepared by the dispersion of 0.5 g of purified CNTs in 100 cm^3 mixture of ethanol and water (1:4) and sonicated for 30 min. Subsequently, 0.5 g of SnO_2 powder was added to the mixture to obtain SnO_2-CNTs in the ratio of 1:1. The mixture was continuously sonicated for an additional 4 h. Afterwards, the mixture was centrifuged and the SnO_2-CNTs particles was recovered and washed severally with ethanol and distilled water. The resultant product was dried in an electric oven at 80 °C for 6 h to obtain SnO_2-CNTs nanocomposites. This procedure was repeated using different blending ratio, SnO_2-CNTs of 1:2 and 2:1.

3.5.4 Preparation of NiO-CNTs-SnO_2 nanocomposites

In this case, 0.5 g of the purified CNTs dried powder was dispersed in 60 cm^3 of ethanol

and the mixture was sonicated for 30 min. Thereafter, 20 cm^3 of 0.5 g containing NiO suspension (in ethanol and water in the ratio of 1:4) was added to the dispersed CNTs in ethanol. Then, 0.5 g of the SnO_2 nanoparticles in 20 cm^3 of ethanol and water (in the ratio of 1:4) was also added. Afterwards, the three different suspensions of NiO, $SnO_2$and CNTs-ethanol mixture were further ultra-sonicated for 4 h. The resultant mixture produced a NiO-CNTs-SnO_2 nanocomposite in the ratio (1:1:1) and was centrifuged at 4000 rpm for 30 min. Finally, the nanocomposite was washed with ethanol and water respectively, severally and dried in an electric oven at 80°C for 6 h and put in the appropriate container. This procedure was repeated for NiO-CNTs-SnO_2 nanocomposites in the ratios of (1:2:1), (1:1:2) and (2:1:1) respectively.

3.6 Characterisation of Nanoparticles and Nanocomposites

The as-synthesised nanoparticle and nanocomposites were characterised with a number of techniques. The characterization includes the determination of crystallinity by XRD, morphology by HRSEM, microstructure by HRTEM, chemical composition by EDS, and surface oxidation state of elements by XPS.

3.6.1 X-ray diffraction (XRD)

X-ray diffraction analysis were carried out using Emma 0141 X-Ray machine by GCB Scientific Equipment Pty Ltd. About 0.2 g of the sample was ground and the powder was placed in a sample holder. The voltage and current of the X-ray machine were set for the source and the computer software was activated for Cu Kα wavelength of 0.15406 nm. The machine was calibrated using pure silicon standard sample. After calibration, the sample was loaded into the machine for scanning. The X-Ray diffraction patterns were recorded on the machine at room temperature within the range of 5 to 90° on the 2θ scale with a scanning speed of 0.05 °/s. towards the end of the scan, the d-

spacing for each peak was calculated from the 2θ values. This procedure was repeated for all samples. the interplanar spacing for each diffraction angle (d-spacing) was calculated using Braggs law (Equation 3.5), and was compared with the search and match routine of known materials.

$$n\lambda = 2d\ sin\theta \tag{3.5}$$

where $\lambda =$ wavelength of X-Ray = 0.15406 nm, $d =$d-spacing in nm, $\theta =$ Diffraction angle in radians.

The unit cell parameters were calculated and indexed $(h\ k\ l)$.The average crystallite size of the nanomaterials was calculated from the analysis of the peaks in the X-Ray diffraction patterns using the Scherrer's equation as presented in Equation 3.6 (Monshi *et al*., 2012).

$$D = \frac{k\lambda}{\beta cos\theta} \tag{3.6}$$

where $k =$ Scherrer's constant = 0.94, $\lambda =$wavelength of X-Ray, $\beta =$ Full Width at Half Maximum and $\theta =$ diffraction angle.

3.6.2 High resolution scanning electron microscopy

High Resolution Scanning Electron Microscope (HRSEM) Zeiss Auriga was employed in this study. Prior to the analysis, 0.05 g of each sample was sprinkled on a sample holder with a carbon adhesive tape on it. This was sputter-coated with Au-Pd Quorum T15OT for 5 min and the samples were subsequently, characterised at different magnifications. The microscope was operated at Electron High Tension (EHT) of 5 kV for imaging. Other operating parameters are presented in Table 3.7.

Table 3.7: HRSEM Operating Settings

Operating Parameters	Conditions
Current	10 Ma
Magnification	Varies
Aperture	0.4 mm
Resolution	1 nm, but sometimes varies
Emitter	Thermal field emission type
Working distance	4-10.4 mm
Voltage	5 Kv
Signal A	In-lens

For the determination of the elemental composition of the samples using Energy Dispersive Spectroscopy (EDS) measurements, the secondary electron mode was activated for the imaging. A homogenous region of the sample was identified and the microscope operated using electron high tension (EHT), of 20 kV for about 30 min at 150^{o}.

3.7 Soil Analysis

In order to find the relationship between the soil's physicochemical properties and the corrosion of as-received and coated AISI 1020 mild steel coupons buried in the soil for 12 months, an analysis through moisture content, pH, conductivity, conductivity, redox potential, sulphate and chloride ion concentration were determined by standard analytical techniques and reported as follows;

3.7.1 Determination of moisture content

A known weight (10 g) of well homogenized freshly collected soil sample was weighed into a crucible labelled M_1. The homogenized samples were then decanted to remove the large stones, twigs and roots. After which the sample was dried in air oven at $105^{o}C$ for a period of 4 h. The dried sample was then cooled in a desiccator. Thereafter, the weight of the sample was taken and recorded as M_2. The moisture content was

calculated using the relationship presented in Equation 3.7.

$$(\%)\ \text{Moisture content} = \frac{(M_1 - M_2)}{M_1} \times 100 \quad (3.7)$$

where:

M_1: is the initial weight in (g)

M_2: is the final weight in (g)

3.7.2 Determination of pH of soil samples

The soil samples collected at different depth of 0.5 m, 1 m and 2 m were sieved with a 6.3 mm sieve. Then, calibration of the pH metre was done using buffer solution of pH 7, followed by adjusting the pH metre with buffer solution of an unknown pH. Then, 20 ml of distilled water was added to 20 g of air-dried soil in a 50 cm^3 beaker. This mixture was allowed to stand for 30 min with intermittent stirring using a glass rod. The electrode was then immersed into the soil water suspension in the beaker, and the pH value was determined from the automatic display of the pH metre.

3.7.3 Determination conductivity

A known weight (20 g) of fresh soil sample was weighed into a 100 cm^3 beaker followed by the addition of 40 cm^3 of distilled water. The mixture was stirred vigorously on a magnetic stirrer. The mixture was allowed to stand for 30 min. Conductivity was then measured by immersing the cell into the solution, holding approximately 1.5 cm above the bottom of the beaker and making sure that it is not in contact with the bottom of the beaker or the walls of the glass. Readings were displayed on the screen in µS/cm.

3.7.4 Oxidation reduction potential (ORP)

A known weight (20 g) of fresh soil sample from which stones, twigs and larger materials was placed in a beaker. 40 cm^3 of distilled water was added and stirred

vigorously on a mechanical shaker. Soil sample was allowed to stand for 30 min. The redox, potential was then determined by measuring the potential difference between platinum electrodes. The platinum electrode was immersed in the sample held inside a beaker; the ORP was then recorded in millivolt (mV) after the reading has stabilized.

3.7.5 Determination of sulphate

A known volume (100 cm^3) of extracted sample was measured into a 250 cm^3 conical flask. Then, 20 cm^3 of NaCl-HCl solution and glycerol-alcohol solution were added. Sample was then agitated for 10 min. Thereafter, 0.3 g of Barium chloride sample was added and agitated for 2 min. The mixture obtained was then poured into an absorption cell and absorbance was measured at 420 nm after 3 min. The sulphate ion was calculated with Equation 3.8:

$$\mathrm{Mgso_4^{2-}L^{-1}} = \frac{1000 \times \mathrm{MgSO_4^{2-}}}{\mathrm{V}} \quad (3.8)$$

where V is the volume of the sample (cm^3)

3.7.6 Determination of chloride

Hundred (100) cm^3 of extract was measured into a 250-cm^3 conical flask and 1 cm^3 of potassium chromate (K_2CrO_4) was added into the solution and titrated with 0.014 M, $AgNO_3$ standard solution to the first appearance of a red silver chromate end point. A blank was also carried out using same treatment. The level of chloride in the collected soil sample was calculated using Equation 3.9.

Therefore:

$$Cl^-(mg/L^{-1}) = \frac{35.453 \times 1000 \times 0.014\ (V_1 - V_2)}{V_S} \quad (3.9)$$

where

V_1= the Volume of titrant for the sample (cm^3)

V_2=the Volume of titrant for the blank (cm^3)

V_S= the volume of the sample

3.7.7 Determination of pore space

Soil sample was transferred into graduated beakers to measure their volume. This volume was correctly recorded as Vs and a known quantity of water was measured into a graduated cylinder and correspondingly recorded. The soil samples were saturated with water getting as close to the exact top of the soil in the beaker, but not over the top. The volume of the water used up were then subtracted from the starting volume in the graduated cylinder. This shows how much water it took to saturate the soil. The volume of the water used is equal to the pore volume, Vp which was calculated using Equations 3.10, 3.11 and 3.12.

$$\text{Porosity} = \frac{Pore\ volume}{Total\ Volume} \times 100\% \quad (3.10)$$

$$\text{where Total Volume} = V_s + V_p \quad (3.11)$$

$$P_t = \frac{V_P}{V_S + V_P} \times 100\% \quad (3.12)$$

where P_t = porosity

3.8 Preparation of Steel Coupons

Steel coupons with respective exposed surfaces of (0.5 cm^2) were prepared by mechanical grinding with up to 600-grit water-cooled SiC papers in order to obtain a flat and reproducible surface, and subsequently cleaned in an ultrasonic bath for 1 minute in acetone.

3.9 Dip Coating

Dip-coating is a facile and economical technique widely used in many industrial fields to deposit onto any substrate, including metallic, ceramic, polymer films, and fibrous materials (Tang and Yan, 2016). In the dip-coating process the uncoated sample is immersed in a liquid and then withdrawn with a well-defined withdrawal speed at controlled temperature and atmospheric conditions. During the process, the environmental conditions (atmosphere and temperature) control the solvent evaporation from the diluted sol. During this stage, a densification of the solution occurs, leading eventually to a gelation phenomenon, favored by the presence of solid filler, with the formation of a compact and homogeneous film well adherent to the substrate. The thickness of the coating is mainly defined by the picking speed, the filler content, and the viscosity of the liquid (Calabrese & Proverbio, 2019).

3.9.1 Preparation of dispersions for dip coating

To begin with, a stock slurry mixture was prepared by pre-dispersing 20 g of colloidal NiO-SiO_2 (1:2) suspension, in a 250 cm^3 beaker containing 100 cm^3 of distilled water in an ultrasonicator for 30 min. Subsequently, 5 g of epoxy resin was blend with 0.5 g of a hardener and stirred at 500 rpm for 5 min, using the overhead stirrer. The dispersed NiO-SiO_2 (1:2) suspension was poured right afterwards and stirred for additional 5 min to obtain a homogenous mixture of modified epoxy/nanocomposite coating in form of a slurry. The above procedure was repeated using equal weight of NiO-CNTs (1:1), SnO_2-CNTs (1:2), NiO-CNTs-SnO_2 (1:2:1) and NiO-CNTs-SnO_2 (1:1:2) blend with epoxy resin and hardner respectively.

3.9.2 Coating of the steel coupons by dip coating

The coating was in accordance with the procedure reported by Hasnidawani *et al*. (2017) with some modifications. Before the deposition procedure, the as-received

carbon steel panels were sand blasted by quartz sands (0.5 mm particle size), washed and rinsed using acetone with ultrasonication. The metal coupons were coated by dipping the corresponding specimen in a beaker containing each sample of epoxy-nanocomposite gel films as prepared in Section 3.9.1, and withdrawing at a constant rate manually. After the dip coating process, the specimen was first dried at 80°C for 15 min in a dryer box to remove the water in the coating. They were then cured at 300°C for 30 min at 5 °C·min^{-1} ramping temperature, and allowed to cool down to the room temperature (27°C) in an ambient environment to obtain NiO-CNTs (1:1), SnO_2-CNTs (1:2), NiO-CNTs-SnO_2 (1:2:1) and NiO-CNTs-SnO_2 (1:1:2) coated steel coupons respectively.

3.10 Determination of the Coating Hardness Value

The hardness value of the as received, annealed and coated samples were determined using MV1-PC Vickers microhardness tester displayed in Plate V. The tester is equipped with monitor that is use to display the microscopic view of the sample surface to enable accurate determination of the indentation surface area that is impressed on the sample. The illumination system and the power for the tester were turned on. The sample was mounted on the stage clamp such that the indenter is perpendicular to the sample surface. The measuring microscopic was focus with low objective on the surface of the sample, the intensity of the light and the aperture were adjusted for optimum resolution and contrast. The area on the sample to be tested was selected and the stage clamp was moved so that the selected area was below the pyramidal diamond indenter with 130^{o} angle between its faces.

Plate V: Microhardness Tester for Analyzing Specimens

The load of 0.3 kg was gradually and applied and sustained for 15 s after which the load is automatically removed and the stage clamp holding the sample is returned to the microscope measuring objective. The impression was displayed on the monitor, while the micro hardness and hardness improvement values were calculated using the relationship presented in Equations 3.13 and 3.14 as developed by Oliver (2004).

$$H = \frac{P_{max}}{A_c} = \frac{(\alpha P_{max})}{h_c^2} \tag{3.13}$$

$$HI = A_s - A_i \times 100 \tag{3.14}$$

The procedure was repeated such that five different value were measured from each sample and the average values were recorded. H, $P_{max,}$ h_c and A_c are defined as the dynamic micro-hardness (Gpa), the peak load (kg), the contact depth (m), and contact area (m^2), respectively, α was a constant that depends on the indenter shape. In this study, α was kept at 15.08, which corresponded to the indenter with a tip angle of 130°. For Equation (3.14), HI is the hardness improvement, A_S is the micro hardness of the as

received metal coupon (Gpa) and A_i is the micro hardness of the coated metal coupon of interest.

3.11 Corrosion Measurement

Integrity tests for the as-received and coated AISI 1020 mild steel were successfully carried out in a real soil medium. These were conducted by gravimetric method such as weight loss measurement, and electrochemical methods like; Potentiodynamic polarization (PDP) and Electrochemical Impedance Spectroscopy as described in the following Sections.

3.11.1 Weight loss measurement

The uncoated and coated samples were buried in the ground, 2 m below the sea level for a period of 12 months. The weight loss method of corrosion measurement was employed to examine the influence of soil parameters on the corrosion rate of the as-received and coated specimen. Soil was considered as corrosive medium and the experimental samples were buried in the soil according to ASTM 162-99 (2004) standard for the installation process, and soil medium preparation for some period of time. In this work, 5 different control samples and the samples coated with NiO- SnO_2 (1:2), NiO-CNTs (1:1), SnO_2-CNTs (1:2), NiO-CNTs-SnO_2 (1:2:1), and NiO-CNTs-SnO_2 (1:1:2) composite coating formulations were weighed and buried underground for the period of 3-12 months; at 3 months (2160 h) interval then the coupons were retrieved to measure the weight the loss in accordance to the coupon cleaning procedure of ASTM G01-03 (1999). The other samples left in the ground were subsequently withdrawn after 6, 9, and 12 months. At each withdrawal the samples were cleaned and reweighed. The weight loss results were recorded. The area of the specimen was calculated with Equation 3.15.

$$\text{Specimen Area} = 2\,(\text{LB} + \text{BW} + \text{LW}) \tag{3.15}$$

where L is the length of the specimen, B is the breadth and W is the width of the specimen.

Weight loss was calculated by finding the difference between weight of each sample before and after buried, using the Equation 3.16 (Aduagba *et al*., 2016);

$$W = W_b - W_a \tag{3.16}$$

W_b is the weight before buried, W_a is the weight after buried. The average values of sample weight loss were tabulated to obtain corrosion penetration rate.

The corrosion penetration rate (CPR) of control and different composite coated samples was determined in mils per year (MPY), using Equation 3.17 (Amadi and Ukpaka, 2016).

$$CPR = \frac{534W}{DAT} \tag{3.17}$$

W is the weight Loss of the specimen g(cm^3), D is the constant density of the specimen (7.85 g/cm^3), A is the Area of the specimen (cm^2) and T is the Exposure period (hr). The protection efficiency of the coating was then calculated using the expression in Equation 3.18.

$$I(\%) = \left(\frac{CPR_1 - CPR_2}{CPR_1}\right) \times 100 \tag{3.18}$$

where $I(\%)$ is coating efficiency, CPR_1 is the corrosion penetration rate of mild steel before buried, CPR_2 is the corrosion penetration rate of mild steel specimen after buried in soil.

3.11.2 Electrochemical measurements

The corrosion resistance property of the as-received and coated coupons were examined on an Auto Lab PGSTA electrochemical workstation at room temperature in a soil medium by using the Eletrochemical measurements such as Potentiodynamic

Polarization Technique (PDP) and Eletrochemical Polarization Spectroscopy (EIS) as described in the next Sections.

3.11.2.1 Soils preparation for electrochemical measurements

The soil sample was extracted from Lau, Ilorin, Kwara State, Nigeria at (6°44' N, 5°51' E). After measurements of the physicochemical parameters, the sample was dried in an oven at 40°C for two days after they were triturated and passed through a sieve in order to homogenize the particle size to 5 microns approximately. After sieving, a constant mass of 3 kg of the dried and sieved soil was collected. Then, 2 L of deionized water was added to saturate the mass of the collected soil in a 100 cm^3 beaker. The deionized water was used to homogenize and dissolve the soluble species present in the soil. After which, AISI 1020 steel was immersed in the soil; and natural evaporation at room temperature was allowed for a period of 12 h, simulating the raining and drying conditions on the soil and working electrode. In this manner, the impedance and polarization tests in the immersion time and moisture content were recorded.

3.11.2.2 Preparation of the working electrode (WE)

The working electrode (WE) was embedded into Teflon and the exposed surfaces (0.5 cm^2) were prepared by mechanical grinding with up to 600-grit water-cooled SiC papers in order to obtain a flat and reproducible surface, and subsequently cleaned in an ultrasonic bath for 1 minute in acetone. In order to reduce the iR-drop all electrodes were placed at a distance of 3 mm from the WE.

3.11.2.3 Potentiodynamic polarization (PDP) and electrochemical impedance spectroscopic (EIS) measurements

The electrochemical measurements were performed using 3-electrode system as shown in Figure 3.1, at room temperature according to the procedure reported Shoaib *et al*. (2018).

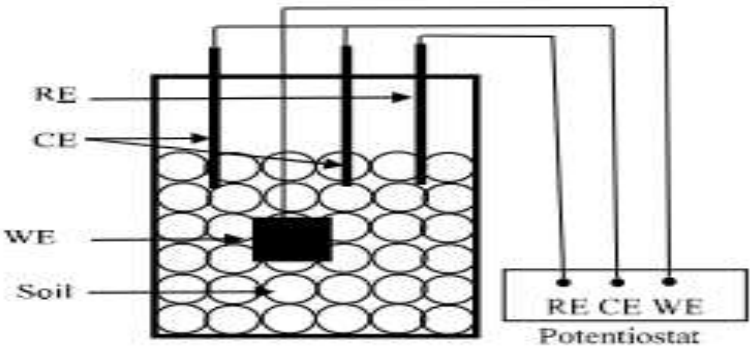

`

Figure 3.1: Schematic Diagram of Experimental Setup (Shoaib *et al*., 2018)

Experimental setup using potentiostat is presented in Plate VI. Rectangular shaped AISI 1020 steel, and samples coated with NiO- SnO_2 (1:2), NiO-CNTs (1:1), SnO_2-CNTs (1:2), NiO-CNTs-SnO_2 (1:2:1), and NiO-CNTs-SnO_2 (1:1:2) were used as working electrodes (WE). Two graphite electrodes joined through electrical connector were used as counter electrode (CE), and silver/silver chloride (Ag/AgCl) was used as reference electrode (RE). Surface area ratio between WE/CE was 0.909. Electrochemical measurements were performed using Gamry 600 potentiostat-galvanostat electrochemical system. Prior to each electrochemical measurement, metallic samples were cleaned as per ASTM G01 (1999). Then the samples were buried into 3000 g of soil containing predetermined, pH, moisture contents, chloride contents, and resistivity value. Open circuit potential of working electrode was monitored for 3600 sec. After reaching steady-state potential, electrical impedance of working electrode was recorded with frequency range from 0.01 to 100000 Hz and amplitude of 10 mV, because there was no evidence of electrical properties of the bulk soil at frequencies lower than 103 Hz which is attributed to dispersed or colloid particles soil with low moisture content according to Quej-Ake *et al*., 2015). Potentiodynamic Polarization analysis was carried out with starting and ending potential of -1300 and 300 mV, respectively, and scan rate of 1 mV/s. Electrochemical Impedance Spectroscopic data was fitted using program Z-

simp win 3.21 software.

Plate VI: Gmary 600 Potientiostat for Electrochemical Measurements

The experimental data was fit to plots in Microsoft® Excel. The Excel model were obtained for the two electrochemical methods that relied upon the Tafel diagram and Nyquist plot.

The Tafel polarization curve exhibited linear behaviour in the E against log (i) plots called Tafel behaviour. The E_{corr} and i_{corr} were determined by extrapolation of the slope of the polarization curves back to the corrosion potential. The intersection point represented the corrosion current density i_{corr} or corrosion rate and the corresponding potential at that point was the E_{corr}.

Corrosion penetration rate (MPY) for Potentiodynamic Polarization was obtained from Equation 3.19 as reported by Popov (2015).

$$\text{CPR (MPY)} = \frac{0.131\ X\ I_{corr}\ X\ EW}{d} \quad (3.19)$$

where d is the density of iron metal (7.874 kg/m^3), and EW is the equivalent weight per valence state of iron metal in oxidized form of 2.

The corrosion protection efficiency (% CPE.) of coated mild steel samples was determined from the measured corrosion current density of nanocomposite formulated coated mild steel electrode (icorr) using Equation 3.20.

$$\text{CPE (\%)} = \frac{i_0 - i_a}{i_a}\ X\ 100 \quad (3.20)$$

where i_a is corrosion current for the as-received (uncoated) sample, i_0 is the corrosion current for the coated samples at different coating conditions (Abdulrahaman *et al*., 2017).

CHAPTER FOUR

4.0 RESULTS AND DISCUSSION

4.1 Synthesis of NiO and SnO_2 nanoparticles

In this study, green synthetic route was employed to produce NiO and SnO_2 nanoparticles from nickel (II) chloride hexahydrate ($NiCl_2.6H_2O$) and tin (II) chloride dehydrate ($SnCl_2.2H_2O$) precursors and *African cactus* plant extract. Three parameters that affect the synthesis of the mentioned nanoparticles via green synthetic route namely: (i) the pH of the solution, (ii) precursor concentration and (iii) the synthesis temperatures, were selected for the study and optimized with response surface methodology (RSM) using the Box-Behnken design. These gave rise to the development of models as discussed below.

4.1.1 Development of models

Statistical Model for the prediction of the particle sizes during the green synthesis of NiO and SnO_2 were developed as follows:

4.1.1.1 Model for the synthesis of NiO nanoparticles

The statistical Minitab 19 software has been used to study the regression analysis of experimental data and to draw the response surface plot. The statistical parameters were estimated using ANOVA. For the synthesis of NiO, the required experimental range and coded level of variables are given in Table 4.1, which shows the design of experiments together with the experimental results. As the output proposed by the named software with the linear model.

Table 4.1: Experimental Runs of Box–Behnken Design with Comparison between Predicted and Experimental Size of NiO Nanoparticles

Std Order	Run Order	X_1	X_2 (moldm^{-3})	X_3 ($^{\circ}$C)	Y_0 (nm)	Y_1 (nm)
1	1	8	0.25	52.50	8.87	8.87
11	2	10	0.25	80.00	9.44	9.46
8	3	12	0.31	80.00	9.15	9.21
5	4	8	0.31	25.00	6.82	6.73
3	5	8	0.37	52.50	6.15	6.11
6	6	12	0.31	25.00	9.13	9.16
2	7	12	0.25	52.50	11.91	11.78
13	8	10	0.31	52.50	9.12	9.10
4	9	12	0.37	52.50	8.92	8.88
7	10	8	0.31	80.00	6.18	6.16
12	11	10	0.37	80.00	6.94	6.86
9	12	10	0.25	25.00	9.85	9.90
10	13	10	0.37	25.00	7.04	6.99
15	14	10	0.31	52.50	9.12	9.10
14	15	10	0.31	52.50	9.12	9.10

Y_0 = Experimental response (crystallite size), Y_1= Predicted responses (crystallite size)

The final empirical model in terms of a coded factor for the crystallite size, which is the responses (Y, nm), is given in Equation 4.1:

$$Y_1 = 2.98 + 2.347X_1 - 49.1X_2 + 0.0853\,X_3 - 0.0819X_1^2 + 47.2X_2^2 - 0.001286X_3^2 - 0.563X_1X_2 + 0.0030X_1X_3 + 0.0470X_2X_3 \quad (4.1)$$

where, Y_1 is the response (crystallite size in nm) for NiO. X_1, X_2, and X_3 are the process factors representing solution pH, precursor concentrations (mol/dm^3) and synthesis temperature ($^{\circ}$C) respectively. The output by the named software for the analysis of variance (ANOVA) and summary of the model for the synthesis of NiO are presented in Table 4.2 and 4.3.

Table 4.2: ANOVA Results for Quadratic Model of NiO NPs Using Box Behnken Design

Source	DF	Adj SS	Adj MS	F-Value	P-Value
Model	9	34.8515	3.8724	341.93	0.000*
X_1	1	15.3735	15.3735	1357.48	0.000*
X_2	1	15.18	15.18	1340.4	0.000*
X_3	1	0.1596	0.1596	14.09	0.013*
Square	3	3.9871	1.329	117.36	0.000
$\boldsymbol{X_1^2}$	1	0.396	0.396	34.97	0.002
$\boldsymbol{X_2^2}$	1	0.1067	0.1067	9.42	0.028
$\boldsymbol{X_3^2}$	1	3.492	3.492	308.35	0.000
2-Way Interaction	3	0.1512	0.0504	4.45	0.071
X_1X_2	1	0.0182	0.0182	1.61	0.260**
X_1X_3	1	0.1089	0.1089	9.62	0.027*
$X_2 X_3$	1	0.024	0.024	2.12	0.205**
Error	5	0.0566	0.0113	--------	--------
Lack-of-Fit	3	0.0566	0.0189	--------	--------
Pure Error	2	0	0	--------	--------
Total	14	34.9081	--------	--------	--------

*Significant at < 0.05% level; ** Not significant, R^2 = 0.9984, R^2(adj) =0.9955, R^2(pred) = 0.9740, S=0.106419.

Table 4.3: Model Summary for NiO

S	R-sq (%)	R-sq(adj)(%)	R-sq(pred)(%)
0.106419	99.84	99.55	97.40

As shown in Tables 4.2 and 4.3, a good agreement exists between the predicted results and those obtained from experiments for NiO nanoparticles. The ANOVA results of NiO nanoparticles as presented in Tables 4.2 revealed that the second order regression model was found significant with a high confidence level (95%). All predicted coefficients were estimated by ANOVA analysis with a highly significant p value ($p < 0.05$) and an R-squared value of 0.9984, which indicates the higher validity to the predicted nanoparticle sizes, while the F-value of the synthesis process was found to be 341.93,

which indicates the significant nature of the model. From Table 4.3, a relatively high value of adjusted and predicted R-squared coefficients (R^2 adj = 0.9955 and R^2(pred) = 0.9740) were obtained which indicates that the final prediction is in good agreement with the experimental results. Similar results were obtained by Ba-Abbad *et al*. (2015), while working on the synthesis of NiO using the same design via sol gel method. They obtained comparatively high correlation coefficients (R^2 adj=0.9677 and R^2(pred) = 0.9859) which were close to values gotten during the course of this study.

4.1.1.2 Model for the synthesis of SnO_2 nanoparticles

For the synthesis study of SnO_2 nanoparticles, the required experimental range and coded level of variables are given in Table 4.4. As the output proposed by the named software, the linear model was not aliased.

Table 4.4: Experimental Runs of Box–Behnken Design with Comparison between Predicted and Experimental Size of SnO_2 Nanoparticles

Std Order	Run Order	X_1	X_2 (moldm^{-3})	X_3 ($^{\circ}$C)	Y_0 (nm)	Y_1 (nm)
13	1	11	0.3750	57.50	9.85	9.86
6	2	12	0.3500	57.50	14.14	14.14
7	3	10	0.4000	57.50	6.71	6.73
11	4	11	0.4000	25.00	9.16	9.24
1	5	10	0.3750	25.00	7.35	7.28
4	6	12	0.3750	90.00	11.51	11.60
3	7	10	0.3750	90.00	6.81	6.80
12	8	11	0.4000	90.00	7.89	7.90
8	9	12	0.4000	57.50	13.56	13.49
14	10	11	0.3750	57.50	9.85	9.86
15	11	11	0.3750	57.50	9.85	9.86
2	12	12	0.3750	25.00	13.42	13.45
10	13	11	0.3500	90.00	10.05	10.00
9	14	11	0.3500	25.00	10.98	10.99
5	15	10	0.3500	57.50	9.84	9.93

Y_0 = Experimental response (crystallite size), Y_1= Predicted responses (crystallite size)

The final empirical model in terms of a coded factor for the crystallite size, which is the response (Y, nm) and is given in Equation 4.2:

$$Y_2 = 285.5 - 22.33X_1 + 0.2255X_3 - 888.9X_2 + 0.7325X_1^2 - 0.000767X_3^2 + 768.0X_2^2 - 0.01054X_1X_3 + 25.50X_1X_2 - 0.1046X_2X_3 \quad (4.2)$$

where, Y_2 is the response (crystallite size in nm) for SnO_2 nanoparticles. X_1, X_2, and X_3 are the process factors such as, solution pH, precursor concentrations (mol/dm^3) and synthesis temperature ($^\circ$C) respectively. The output by the named software for the analysis of variance (ANOVA) and summary of the model for the synthesis of SnO_2 are presented in Table 4.5 and 4.6

Table 4.5: ANOVA Results for Quadratic Model of SnO_2 NPs Using Box Behnken Design

Source	DF	Adj SS	Adj MS	F-Value	P-Value
Model	9	77.9284	8.6587	1237.84	0.0000*
X_1	1	60.0608	60.0608	8586.25	0.0001*
X_2	1	7.392	7.392	1056.76	0.0004*
X_3	1	2.7028	2.7028	386.39	0.0002*
Square	3	5.649	1.883	269.19	0.0008
$\boldsymbol{X_1^2}$	1	1.9811	1.9811	283.22	0.0043
$\boldsymbol{X_2^2}$	1	0.8507	0.8507	121.62	0.0001
$\boldsymbol{X_3^2}$	1	2.4225	2.4225	346.32	0.0006
2-Way Interaction	3	2.1238	0.7079	101.2	0.0001*
X_1X_2	1	1.6256	1.6256	232.4	0.0001*
X_1X_3	1	0.4692	0.4692	67.08	0.0001*
X_2X_3	1	0.0289	0.0289	4.13	0.098**
Error	5	0.035	0.007	---	---
Lack-of-Fit	3	0.035	0.0117	---	---
Pure Error	2	0	0	---	---
Total	14	77.9634	---	---	---

*Significant at < 0.05% level; ** Not significant, R^2 = 0.9996, R^2(adj) =0.9987, R^2(pred) = 0.9928, S=0.0836361.

Table 4.6: Model Summary for SnO_2

S	R-sq (%)	R-sq (adj) (%)	R-sq (pred) (%)
0.0836361	99.96	99.87	99.28

From the Table 4.5, the regression model *F*-value of 1237.84 is relatively high and indicates the significant nature of the model. The Prob>F was 0.000 which means that there is 0.000 % chance that a "regression model *F*-Value" could occur due to noise. The P values for pH, tin precursor concentration, and synthesis temperature were all less

than 0.05; which signify rejection of the null hypothesis and therefore, considering these factors major as determinants in the synthesis of SnO_2 nanoparticles. Table 4.6 revealed that a correlation value (R^2) of 0.9996 for the quadratic model which indicated that the model can explain 99.96% of the variability in the synthesis of SnO_2 nanoparticles. While a relatively high correlation values for adjusted and predicted coefficients (R^2 adj = 0.9987 and R^2(pred) = 0.9928) were obtained which indicates that the final prediction is in good agreement with the experimental results.

4.1.1.3 Adequacy of the regression models

In order to optimize relatively smaller size nanoparticles by avoiding poor and undesired results, a fit of the (synthesis) experimental data was performed and the results are presented in Figures 4.1(a-d) and 4.2 (a-d) for NiO and SnO_2 nanoparticles respectively. The Figures shows all the diagnostic plots of NiO and SnO_2 nanoparticles used in the optimization process to evaluate the adequacy of the regression model. In both cases for NiO and SnO_2 nanoparticles, the normality of results was checked by plotting the normal probability versus standardized residuals (estimated from standard deviation) as shown in Figures 4.1 (a) and 4.2 (a). The results showed that all experiments were near the continuous line and was attributed to the fact that no obvious problems with the normality of the design were observed. The effect of standardized residuals and the predicted crystallite size was a random scattering of all points rather than a funnel-shaped pattern. This indicated that the response had an original observation of variance and that there was no problem with the predicted crystallite size. Generally, from Figures 4.1 (b) and 4.2 (b) the values of the standardized residuals have to be always within the interval of -3.5 to +3.5, therefore, values for the observed crystallite size should not be considered valid for any value beyond these values according to Rauf *et al*. (2008).

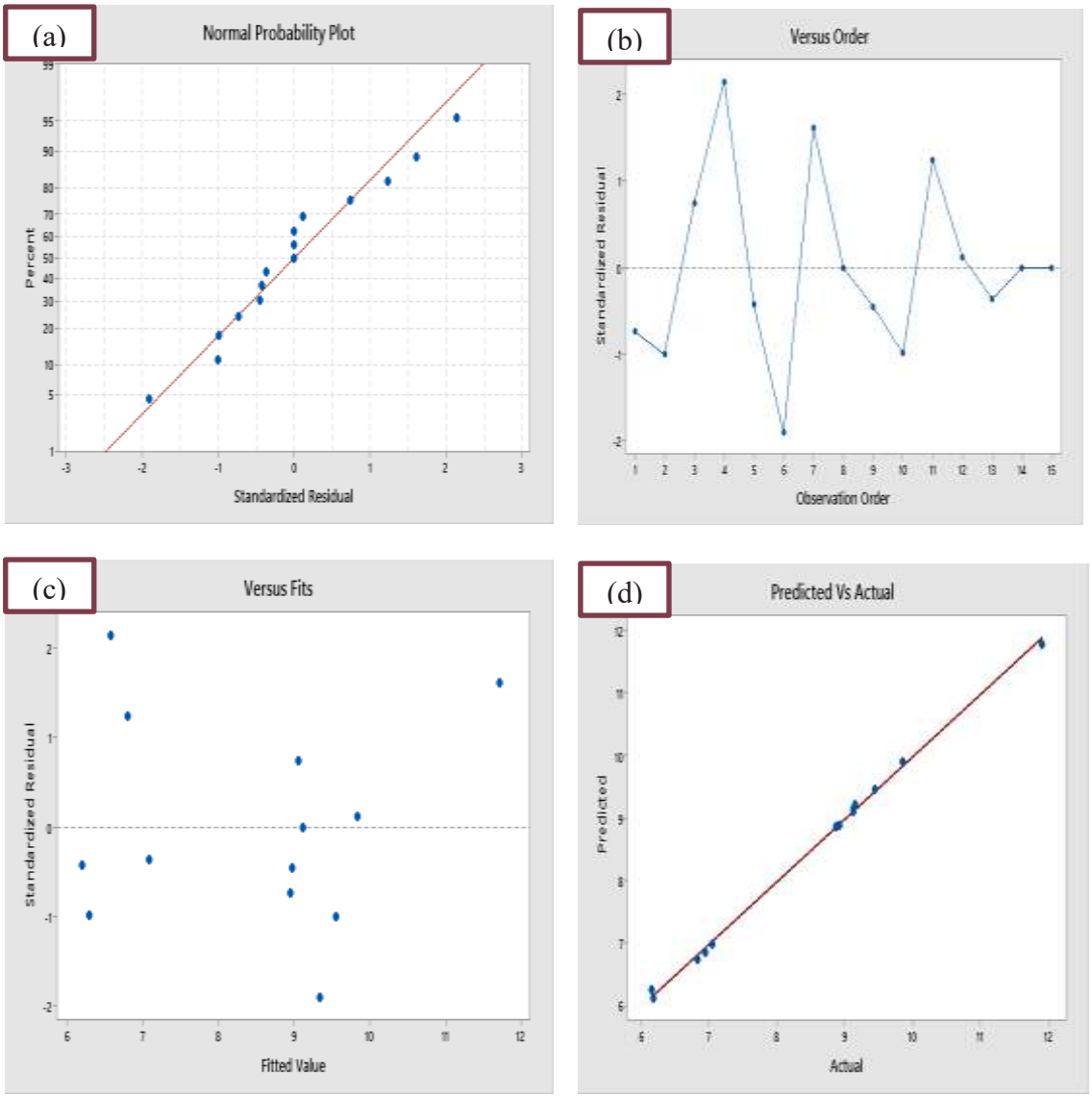

Figure 4.1: All Diagnostic Plots of Optimization NiO NPs Process using Box Behnken Design, (a) Normality, (b) Standardized residuals, (c) Outlier T, (d) Actual and Predicted Size of NiO NPs

(a)

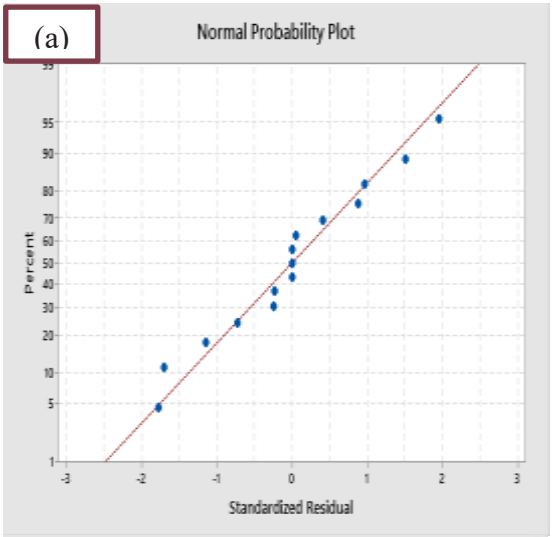
Normal Probability Plot
Percent
Standardized Residual

(b)

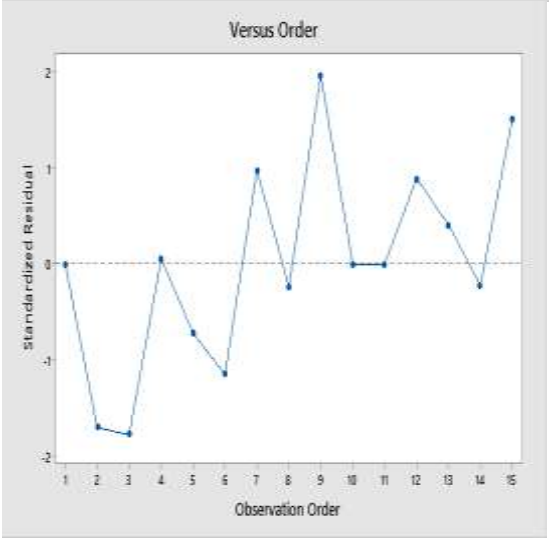
Versus Order
Standardized Residual
Observation Order

(c)

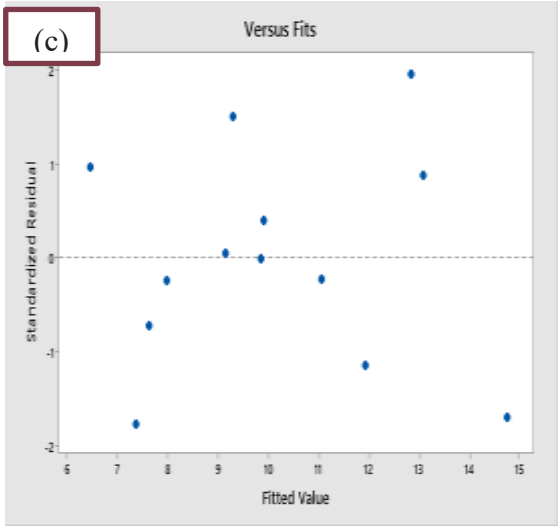
Versus Fits
Standardized Residual
Fitted Value

(d)

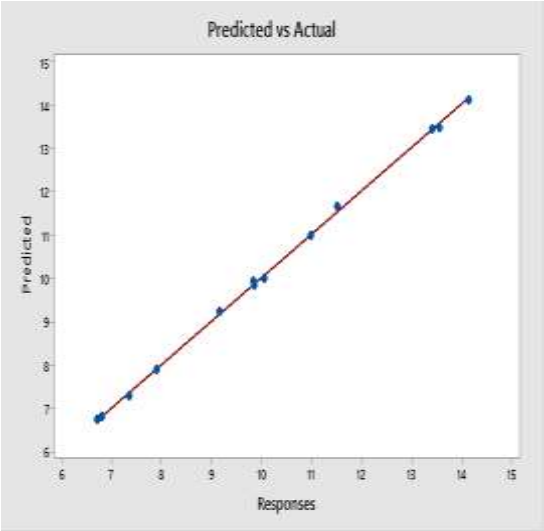

Figure 4.2: All Diagnostic Plots of Optimization SnO_2 NPs Process using Box Behnken Design, (a) Normality, (b) Standardized residuals, (c) Outlier T, (d) Actual and Predicted Size of SnO_2 NPs

In this study, both NiO and SnO_2 nanoparticles optimization had a standardized residual value between the range of ±2.0 as presented in Figures 4.1 (b) and 4.2 (b) respectively, which gives a good fitting of the prediction. Furthermore, the outlier of the observation runs shows a good distribution as presented in Figure 4.1 (c) and 4.2 (c) for NiO and SnO_2 nanoparticles respectively, with no run out of the considered range.

To assess the validity of the prediction, the predicted values of NiO and SnO_2 NPs sizes were compared to experimental ones and are given in Figures 4.1 (d) and 4.2 (d). These results show that the predicted and experimental points are in a good agreement as illustrated by all points arranged very closely to the diagonal line.

4.1.1.4 Effect of synthesis factors as surface and contour plots

The effect of each factor on the synthesis of NiO nanoparticle was investigated in a 3-D response surfaces and contour (2-D) graphs created using the second order polynomial model. Figures 4.3 and 4.4 show the effect of the different interaction between the most

significant factors by varying two factors within the experimental ranges. These effects were explained individually using statistical values with more evidence to how the effects occurred within the varying of the factors range.

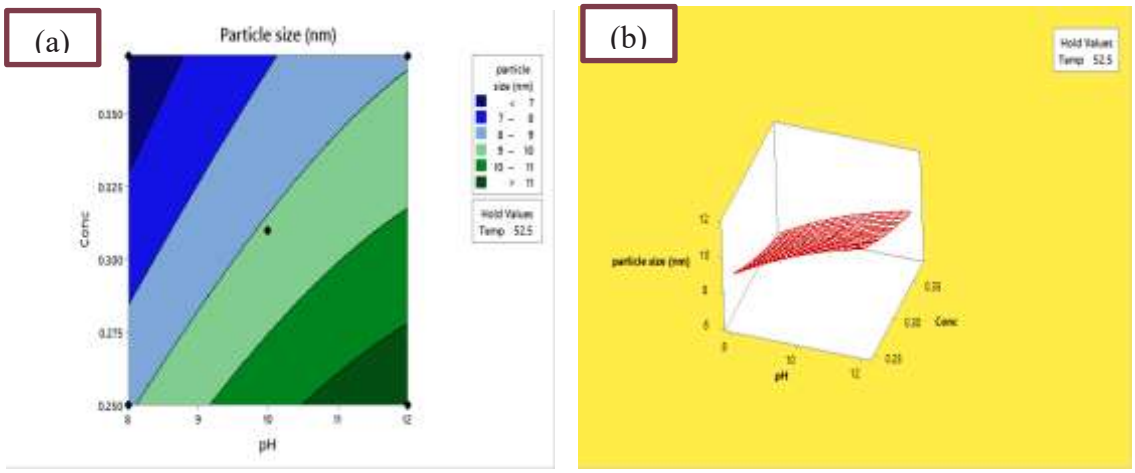

Figure 4.3: (a) Effect of Interaction between the Precursor Concentration and pH on the NiO Nanoparticle Size as 3D Response Surface and (b) 2D Contour Plot

Figure 4.3 (a) and (b) shows the interaction between two process parameters (pH and precursor concentration, while the temperature was held at 52.5^{o}C. The graphs clearly suggest that the smallest crystallite size (< 6 nm) was obtained when the pH value was between 8-8.5 and concentration in the range of 0.330-0.375 mol/dm^3. The highest crystallite size of (12 nm) was at a higher pH of 12 and precursor concentration of 0.25 ml/dm^3, while the temperature was at 52.5^{o}C for both cases. This emphasized the significance as this two main effect or interacting factors when running the experiment for a particular crystallite size.

On further investigations the main compound after the reaction between the nickel chloride precursor and hydroxide ion (OH^-) from NH_4OH and phenolic acid in the plant extract was nickel hydroxide ($Ni(OH)_2XH_2O$ green precipitate). Effects of precursor concentration was estimated from 0.25 to 0.37 (mol/dm^3). It was observed that the size decreases with increased in the precursor concentration from 0.25 to 0.37 (mol/dm^3).

The smaller size of NiO nanoparticle was found at concentration of 0.37(mol/dm^3), which was attributed to the complete reaction of the phenolic and tannic compounds from the plant extract and (OH^-) from the NH_4OH in the reaction mixture with nickel chloride (adequate amount to complete the reaction). The benefit of appropriate amount of the nickel chloride precursor in the mixture was that it could prevent the particles from forming aggregates. During the formation of nickel hydroxide, ($Ni(OH)_2.X\ H_2O$) at the optimum nickel precursor concentration of 0.37 (mol/dm^3), each Ni^{2+} ion would undergo reaction with an OH^- to form a more stable compound, thus decreasing the aggregation of particles under faster nucleation rate (Ba-Abbad *et al.*, 2013). Equations 4.3 to 4.7 illustrates the reactions in a stepwise direction.

$$NH_4OH_{(s)} \rightarrow NH^+_{4(aq)} + OH^-_{(aq)} \quad (4.3)$$

$$NiCl_{2.}6H_2O \rightarrow Ni^{2+}_{(aq)} + 2Cl^-_{(aq)} + 6H_2O_{(l)} \quad (4.4)$$

$$Ni^{2+}_{(aq)} + 2OH^-_{(aq)} + XH_2O_{(aq)} \rightarrow Ni(OH)_{2.}XH_2O_{(s)} \quad (4.5)$$

$$Ni(OH)_{2.}XH_2O_{(s)} \rightarrow Ni(OH)_{2(s)} + XH_2O_{(g)} \quad (4.6)$$

$$Ni(OH)_{2(s)} \rightarrow NiO + XH_2O_{(g)} \quad (4.7)$$

The precursor concentrations of 0.25 and 0.31 (mol/dm^3) caused more agglomeration that resulted in bigger size. These results could be due to extra amount of tannic and phenolic acid influencing the nucleation and growth of NiO nanoparticles by inhibition of hydrolysis and condensation reactions as reported earlier by (Ba-Abbad *et al.*, 2015). Additionally, excess of tannic and phenolic acid could induce a rapid nucleation with slower growth rates that may result in production of bigger particle size of NiO nanoparticles as observed by Gang *et al*. (2013).

On the other hand, the size of the NiO nanoparticle increased with increase in pH value of the reaction media from 8 to 10, with the smallest size was obtained at a pH of 8.0. The main reason for the increase in size after pH adjustment with ammonium hydroxide

could be due to incomplete ionization of the tannin and phenolic constituents at pH of 10.0 resulting to the formation of $NiO(NH_3)_6$ according to the Equation 4.8.

$$Ni(OH)_2 + 6NH_4OH_{(aq)} \rightarrow [NiO(NH_3)_6]_{(aq)} + 7H_2O_{(l)} \quad (4.8)$$

The cross-links or bridges between the two Ni^{2+} ions in the presence of the ammonium ions led to the inhibition of NiO particle growth after addition of tannic and phenolic acid during the last the step (Gang *et al*., 2013). However, when the pH was adjusted to 8.0, the particle size decreased because higher saturation of solution $NiO(NH_4)_6$ led to the increase of the particle growth rate compared to pH at 10.0 (Zhang *et al*., 2009). The effects of nickel precursor concentration and pH are clearly demonstrated by the 3-D graphs, and 2-D contour plots see (Figure 4.3 (a) and (b)), which indicated that greater effects are expected when the pH and the precursor concentration are both optimized.

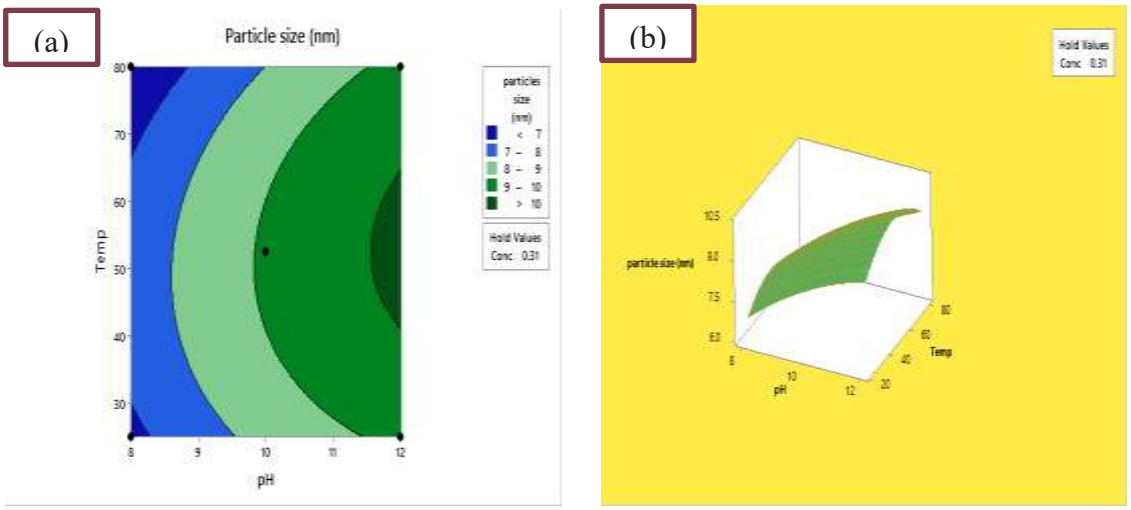

Figure 4.4: (a) Effect of Interaction between the Temperature and pH on the NiO Nanoparticle Size as 3D Response Surface and (b) 2D Contour Plot

For Figure 4.4 (a) and (b), the interaction between pH and temperature are illustrated graphically using the contour (2D) and surface plots (3D) respectively. While the concentration was held at 0.31 mol/dm^3 both graphs revealed that the minimum crystallite size of (< 6 nm) was obtained experimentally at a pH in the range of 8-8.5

and temperature of 67-80^{o}C. While the largest particle occurred mainly at a pH of 12 and temperature of 50^{o}C clearly depicted the two main effects were significant in the determination of the crystallite size of the synthesised NiO Nps, and a careful combination could give rise to desired crystallite size when the concentration was held constant at 0.31 mol/dm^{3}.

The pHs of the reactant mixture and the synthesis temperature were considered to be most significant factors that affected the size of the NiO nanoparticles. Figure 4.4 (a-b) shows that a significant influence on particle sizes was observed when both factors were considered together. This was confirmed by ANOVA analysis ($p < 0.05$) as given in Table 4.5. However, the size of the NiO nanoparticle was more vulnerable to the solution pH compared to the synthesis temperature whereby the sizes varied markedly with an increase in the pH from 8 to 10 as well as temperature from 25 to 80°C. Accordingly, the results showed that physical effect of synthesis temperature was less dominant than the chemical effect by pH on the size of nanoparticles. These phenomena indicated the occurrence of the chemical effect by pH on the reaction rate of hydrolysis and condensation with control of pH (adding ammonium hydroxide). The effect of pH exhibited during this synthesis was similar to that described earlier for precursor concentration, which resulted in the increase, or decrease of particle size as also reported by Chen *et al*. (2009). As shown in the 3-D and 2-D contour plots of pH values, no more significant increase of particle size was observed by varying pH value from 8.0 to 9.0 while keeping the synthesis temperature at lower value of 25°C. By increasing the temperature from 25 to 80°C, sizes of particles were increased at pH values ranging from 8.0 to 10.0. The slightly decreasing particle size at pH of 9.0 was observed due to the faster particle growth in the presence of more ammonium hydroxide amount compared to pH at 8.5. However, the largest effect was observed at pH of 8.0

and temperature of 52.5 °C. Under this condition, the particle size of 6.17 nm was observed compared to 9.10 nm at pH of 10.00 at the same temperature. This was attributed to the fact that the smaller particles sizes at pH of 8.0 easily aggregated to become bigger at higher temperature of 52.5°C.

Generally, the NiO nanoparticles sizes exhibited sharp increase with increase in the synthesis temperature from 25 to 52.5 °C under varying pH values from 8.0 to 10.0 as reported in previous synthesis of NiO NP using the sol gel method by Ba-Abbad *et al*. (2015). In conclusion, the effects of the nickel precursor concentration, solution pH, and synthesis temperature were clearly demonstrated by the Box Behnken results, which showed that a good interaction between these factors resulted in highly accurate predictions to produce relatively smaller particle size of NiO. However, an alkaline media of reactants with moderate synthesis temperature as well as enough concentrations of of nickel chloride and aqueous plant extract were found to be favourable conditions to produce significantly smaller particle size of NiO.

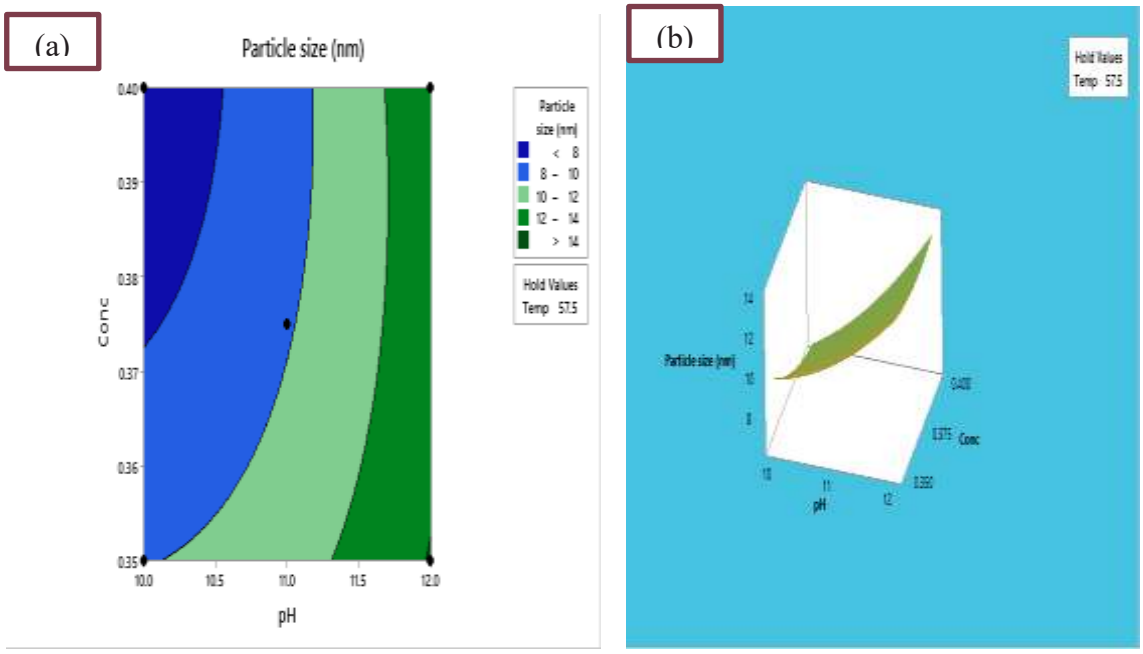

Figure 4.5: (a) Effect of Interaction between the Precursor Concentration and pH on the SnO_2 NPs Size as 3D Response Surface and (b) 2D Contour Plot

The effect of the interaction between pH and precursor concentration is illustrated on the (2D) contour and (3D) response plots in Figure 4.5 (a) and (b). For the pH range (10-12), after the addition of ammonium hydroxide (NH_4OH), the pH of the solution increases, however, the smallest crystallite sizes were obtained when the pH value was lowest (10). In solution, the ratio of OH^- ions and Sn^{+2} ions are stoichiometric, therefore, as the pH begins to increase from 10 to 12, the size of the nanoparticles also increase rapidly. Plausibly, the elevated pH value created a high super saturation level due to the large concentration of hydroxyl ions in solution, resulting in an extremely fast nucleation process generating tiny nuclei (Yan *et al*., 2008b). The tiny nuclei that form will dissolve and reprecipitate on the growing secondary particles through Ostwald ripening as shown in the Equations 4.9-4.13

$$SnCl_2 + H_2O \rightarrow Sn^{+2} + 2Cl^- \quad (4.9)$$

$$NH_4OH_{(s)} \rightarrow NH^+_{4(aq)} + OH^-_{(aq)} \quad (4.10)$$

$$Sn^{+2} + 2OH^- \rightarrow Sn(OH)_2 \quad (4.11)$$

$$Sn(OH)_2 \rightarrow SnO + H_2O \uparrow \quad (4.12)$$

$$SnO + H_2O \rightarrow SnO_2 + H_2 \quad (4.13)$$

Farrukh *et al*. (2010) had earlier noted that a slow addition of ammonium hydroxide through decomposition of urea improves the condensation of free Sn-OH and Sn-Cl species during the synthesis of SnO_2 nanoparticles, leading to a more fully condensed tin oxide framework and larger particle size. In the case of precursor concentration, low concentration of tin precursor reactants caused the reaction rate and the nucleation process to become slow which resulted in a broad size distribution of the SnO_2 nanocrystallites (Farrukh *et al*. (2010). In addition, the probability that growth units combined into crystal plane was also significant (Liu *et al.,* 2014). Whereas high concentration of the tin precursor (0.40 mol/dm^3) at a low pH (10) when the synthesis

temperature was held at (57.50°C), resulted in an increase in the reaction rate and nucleation process giving rise to tiny particles.

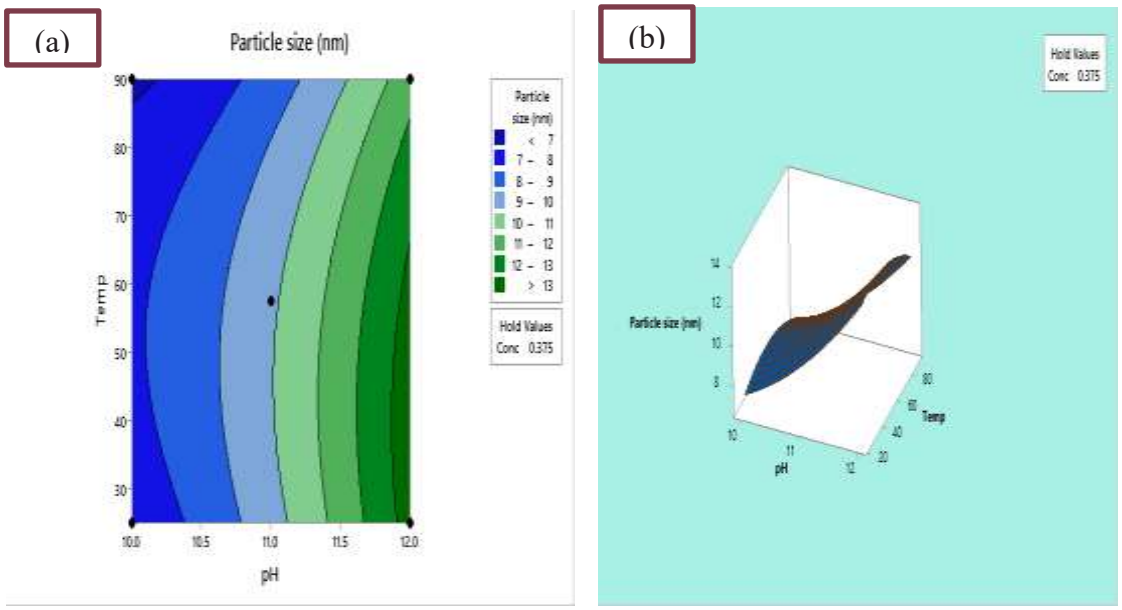

Figure 4.6: (a) Effect of Interaction between the Temperature and pH on the SnO_2 NPs Size as 3D Response Surface and (b) 2D Contour Plot

The overall effect between this interaction is a decrease in the crystallite sizes of the SnO_2 nanoparticles formed. For Figure 4.6 (a) and (b), the effect of interaction between the temperature and pH on the SnO_2 NPs size as (3D) Response Surface and (2D) Contour Plot were evaluated. From both graphs, it was revealed that the minimum crystallite size of (< 7 nm) was obtainable from the experiment when the precursor concentration is held at 0.375 mol/dm^3 and pH is at 10.0, while the reaction temperature is at 90°C. Whereas, for the largest crystallite size obtainable from the experimental runs, the pH was at 12 and the temperature about 43°C, occurring at a fixed concentration of 0.375 mol/dm^3. Therefore, alkaline at solution pH, the crystal size decreased with decreased temperature. Sui *et al*. (2010) reported that a well crystallized SnO_2 occurred at relatively high temperatures due to higher surface energy. Thus, the crystallinity of SnO_2 is a function of temperature. The reaction temperature affects not

only the reaction rate, but also the nucleation and growth rates of particles. Increasing the reaction temperature within a specific range enhances the diffusion, nucleation and growth rates.

In conclusion, at a constant temperature of 57.5^{o}C, increasing the precursor concentration of SnO_2 from 0.350 to 0.40 mol/dm^3 over a pH of 10.2 results to a minimum crystallite size of (< 7 nm). On the other hand, the maximum crystallite size of (14 nm) was obtained when the precursor concentration was varied between 0.350 to 0.40 mol/dm^3 at a pH of up to 11.8.

4.1.1.5 Optimization and model validation

Form Figures 4.1 to 4.6, the optimum conditions to produce smaller size of SnO_2 and NiO NPs was predicted based on the Box-Behnken design. The smaller crystallite size was estimated at a particular level for the three significant factors of pH, precursor concentration and synthesis temperature. According to the experimental results, any increase in the factors more or less than the optimal value leads to the increase in the crystallite size which is undesirable. The validation step is very important to check the prediction stability for the selected factors in producing smaller crystallite size of SnO_2 and NiO nanoparticles. Generally, the one very important term to investigate the validity of the prediction is the desirability function. A numerical optimization of the Design of Experiments (DOE) software was selected to obtain the maximum value of the desirability function (D = 1.000) according to the location of the specific points of the controlling factor. The optimization criteria have five options namely, none, maximum, minimum, target and within range which were applied to determine the optimum conditions for the crystallite size. In this study, all criteria were selected at the range option for all factors and the minimum option for the crystallite size (as target of this study).

To validate the prediction, experiments were carried out at the predicted optimal conditions which were, pH (8), precursor concentration (0.370 mol/dm^3) and synthesis temperature (52.50°C) for NiO, while for SnO_2 nanoparticle the synthesis optimum conditions were, pH (10), precursor concentration (0.400 mol/dm^3) and synthesis temperature (57.50°C). All experiments were replicated three times. The experimental crystallite sizes for NiO (6.15 nm) and SnO_2 (6.71 nm) were obtained by XRD and found to be very close to the predicted value of 6.11 and 6.73 nm respectively. This result can be considered as a good evidence for the selecting Box Behnken design to synthesise NiO and SnO_2 nanoparticles via the green synthetic route. Additionally, the appropriate choice of factor levels played an important role in the optimization of the synthesis and crystallite size prediction (Salimon *et al*., 2012).

In tandem to this study on optimization, Ba-Abbad *et al*. (2015) reported on the synthesis of nickel oxide nanoparticles through the sol gel method using Box–Behnken design. The optimum predicted conditions were obtained at molar ratio of 1:1.74, solution pH of 1.02 and calcination temperature of 400.08°C. The crystallite size from the optimized experimental conditions was found to be 14.31 nm, which was in good agreement with the predicted value of 13.74 nm. These results were consistent with the crystallite size from experimental conditions as well as the predicted values, which were obtained as (6.15 and 6.11 nm) respectively in the case of this study. This was because the predicted values in both studies were found to be less than the actual experimental values, but the difference between them was less than 1.

Furthermore, Akhir *et al*. (2016) described the synthesis of tin oxide nanostructures using hydrothermal method and optimization of its crystal size by using statistical design of experiment. In their report, nanostructures with smallest crystal size (7.88 nm) was obtained when precursor concentration was 0.16 M, at a treatment temperature of

120 °C and 12 h reaction time. On the other hand, the biggest crystal size (18.41 nm) was obtained at temperature of 180 °C, precursor concentration of 0.12 M and 12 h reaction time. The variation in the crystallite size obtained could be attributed to be difference in SnO_2 precursor, the variation in optimized synthesis parameters as well as the synthetic route adopted for the synthesis.

4.1.2 Synthesis of carbon nanotubes (CNTs)

The production of CNTs in this research was carried out by the catalytic vapor deposition method. Although, none of the synthesis parameters was varied or optimized. The synthesis was carried out in tubular quartz reactor placed horizontally in a furnace where the decomposition of acetylene (C_2H_2) gas was initiated. The catalyst (1 g) of (Fe-Ni/kaolin) was loaded at room temperature into a quartz boat (120 x 15mm^2) while the furnace was heated at 10^oC/min with a reaction temperature of 750^oC and argon flow rate adjusted between 100 cm^3 to 200 cm^3. The catalyst exhibited high metal-support interactions between Fe-Ni and the kaolin support, which promoted the catalytic properties for the subsequent growth of the CNTs resulting to a relatively high yield which was calculated to be (300.72%) using Equation 3.4 in Section 3.4. Aliyu *et al*. (2017) who synthesised multi-walled carbon nanotubes via catalytic chemical vapour deposition method on Fe-Ni bimetallic catalyst supported on kaolin reported that the optimum yield of 306% was obtained under the optimum conditions: 750°C reaction temperature, 60 min reaction time, 230 mL/min Ar flow rate, and 200 mL/min C_2H_2. Although the process parameters for the CNTs synthesis were not optimized in this study, a good yield was obtained with the interaction of temperature, time, argon flow rate, and acetylene as choosen for the study.

4.1.3 Synthesis of nanocomposites

The production of the various composites NiO-SnO_2, NiO-CNTs, SnO_2-CNTs, NiO-

CNTs-SnO_2 and in their various combing ratio as presented in Table 4.7.

Table 4.7: Combining Ratios for the Synthesis of the Nanocomposites

Nanocomposites	Combining Ratio			
NiO-SnO_2	1:1	1:2	2:1	_____
NiO-CNTs	1:1	1:2	2:1	_____
SnO_2-CNTs	1:1	1:2	2:1	_____
NiO-CNTs-SnO_2	1:1:1	1:2:1	2:1:1	1:2:1

The as-synthesised nanoparticles (NiO, SnO_2 and CNTs) were combined to synthesise the resulting composites with the corresponding ratio using the formula $3n + 1 = p$ for three different nanoparticles; NiO, SnO_2 and CNTs. Where n represents the number of composites per unit and p is the total numbers of possible outcomes, which is 13 since n = 4 for this study. Consequently, the binary composites NiO-SnO_2, NiO-CNTs and SnO_2-CNTs, gave a total of 9 outcomes NiO-SnO_2 (1:1, 1:2, 2:1), NiO-CNTs (1:1, 1:2, 2:1), and SnO_2-CNTs (1:1, 1:2, 2:1), whereas the single ternary unit gave rise to four possible combinations as follows; NiO-CNTs-SnO_2 in the ratios (1:1:1, 1:2:1, 2:1:1, and 1:2:1). Each of the synthesised nanocomposite in the Table 4.7 was further characterised in Section 4.2. To select the optimum nanocomposite with the best coating efficiency.

4.2 Characterisation of the Nanoparticles

Each as-synthesised nanomaterial was examined using analytical techniques as discussed as follows.

4.2.1 HRSEM analysis for CNTs samples

The HRSEM image of as-synthesised and purified CNTs are shown in Plate VII (a-b). It can be observed that the as-synthesised CNTs consisted of a coily and irregular diameter of CNTs with large amount of amorphous carbons and residual catalyst particles which might be due self-pyrolysis (Sonia & Nazmul, 2018). In fact, the amorphous carbon

covers the surface of catalyst particles and makes them passive, leading to less catalytic growth, and consequently, reduction of the CNTs arrays length as shown in Plate VII (a).

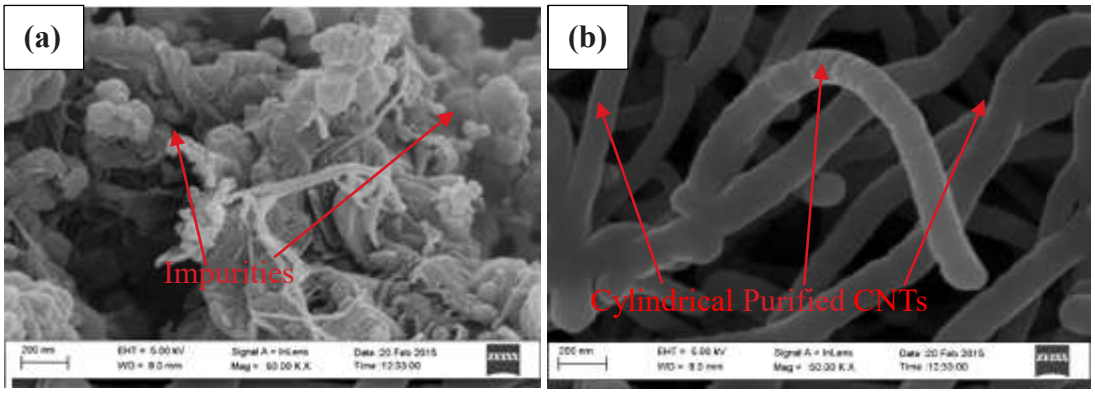

Plate VII: HRSEM Images of; (a) As-synthesised CNTs (b) Purified CNTs

On the other hand, acid treatment of the unpurified CNTs with a mixture of HNO_3 and HCl led to the oxidation of this amorphous carbon. Therefore, purified CNTs were free of amorphous carbon as shown in Plate VII (b). Additionally, it was also observed that purified CNTs arrays were longer and of uniform diameter than unpurified CNTs attributable to the reduction of amorphous carbon deposition which deactivates catalyst. Aliyu *et al.* (2017) pointed out that impurities such as catalyst metal particles, support materials, and amorphous carbon present in the matrix of unpurified CNTs affects its morphological arrangement for different applications; hence, the need to remove these impurities. From their results, as-synthesised unpurified CNTs exhibited a slight degree of agglomeration with some bright spots, which corresponded to the residual metal particles. However, after purification, the reformed CNTs exhibited better-defined tubular morphology.

4.2.2 HRTEM microstructure for CNTs samples

The microstructure of the synthesised CNTs were examined using High Resolution

Transmission Electron Microscopy (HRTEM) and the micrographs from low to high magnification as well as Selected Area Electron Diffraction (SAED) pattern are presented in Plate VIII (a-c). The HRTEM low magnification image in Plate VIII (a) revealed that the wall structure of the CNTs vary, with different diameter (15-23 nm). Also worthy of mentioning are the encapsulated metal nanoparticles within the narrow tubes. These were introduced during the growth of the CNTs and suggests that the size of the metal particles determines the diameter of the as-synthesised CNTs. The high magnification image in Plate VIII (b) suggests that the CNTs produced in this study were multi-walled in nature consisting of hexagonal concentric tubes of graphite arranged from the tip to bottom. Inter-planner distance or spacing (d) which is about 0.34 nm and 0.21 nm corresponds to graphite with crystal planes (003) and (110) that further corroborates the XRD results discussed in Section 4.2.7. Abdulrahaman *et al*. (2017) also reported micrographs of muti walled CNTs with residue of metallic catalyst encapsulated on the matrices of the tubes during growth with long parallel-graphitized sheets forming CNTs walls and tubes with several opening pores. Whereas, Aliyu *et al.* (2017), reported that the calculated interlayer spacing of approximately 0.33 nm was obtained for CNTs, which corresponded to the (002) distance of the graphite carbon. The variation in crystallographic plane and (d) spacing in this case could be due to the difference in synthesis parameters, catalyst type and support material.

Plate VIII (c) shows the corresponding Selected Area Electron Diffraction (SAED). The SAED pattern confirmed the graphitic nature of the CNTs with the innermost ring showing the strongest reflection plane of (003). The sharp rings obtained is an evidence that the prepared material is polycrystalline in nature, where each ring represent diffractions from crystals of similar size. The bright spots are also reflections from certain individual crystals.

The SAED patterns of all samples confirmed the graphitic nature of MWCNTs especially the innermost ring, which is due to the usual strongest reflection plane (003) of graphite. As illustrated in Plate VIII (c), the occurrence of the sharp rings at reciprocal lattice spacing (1/d) of 3.0, 4.7, 5.6 and 8.5 nm^{-1} are in good agreement with those reported for graphite. Mohammed *et al.* (2017) also reported SAED pattern of MWCNTs and observed sharp rings attributable to the MWCNT at reciprocal lattice spacing of 2.9, 4.8, 5.7 and 8.5 nm^{-1}.

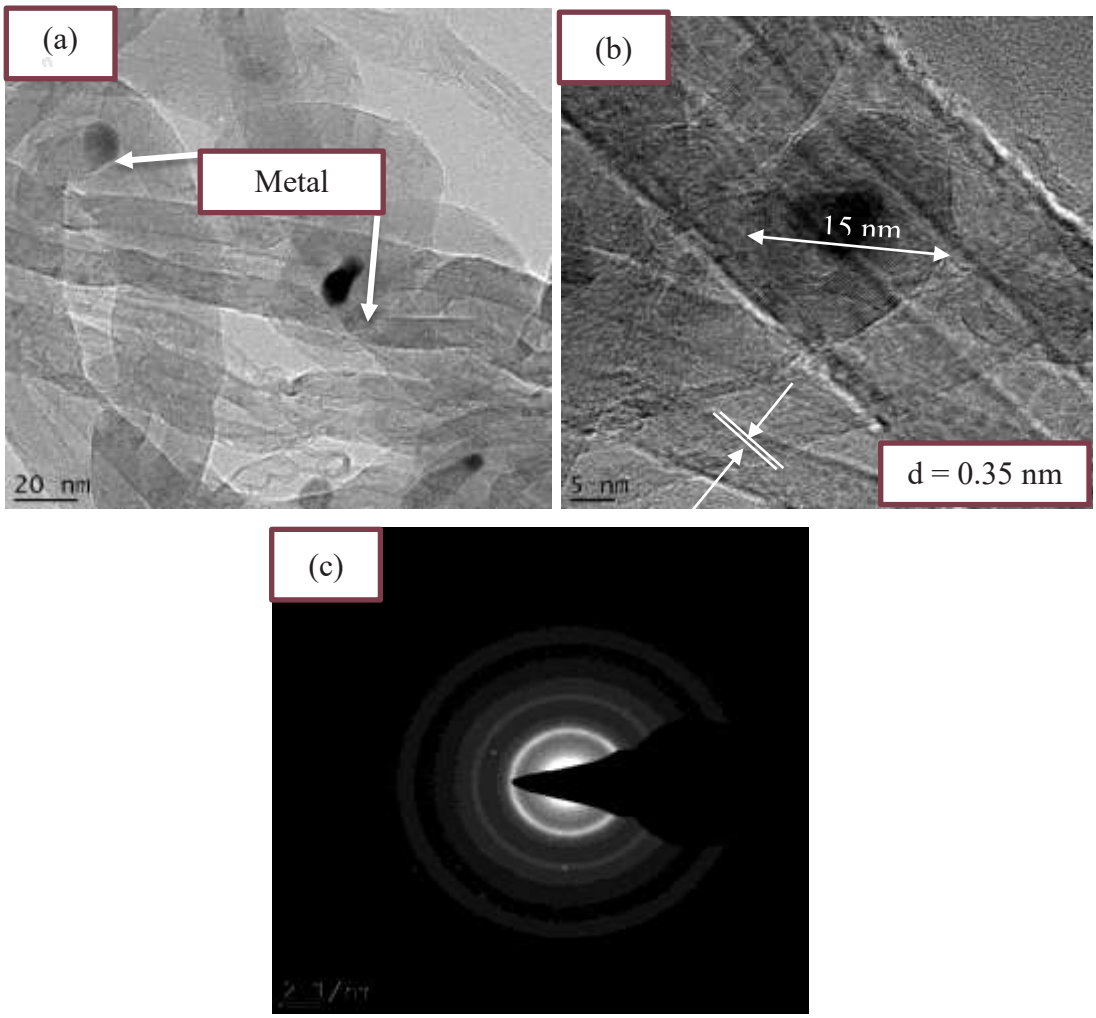

Plate VIII: HRTEM Results (a) Low, (b) High Magnification and (c) SAED images of CNTs

4.2.3 HRSEM/EDX analysis of NiO nanoparticles

Plate IX (a-c) represents HRSEM images of NiO nanoparticles. It was observed at pH 8, in Plate IX (a) that irregularly shaped nanoparticles of NiO were formed. Whereas Plate IX (b-c) showed an increase in agglomeration as the pH of the solution increased from 10 to 12. This could be linked to polymer adherence and magnetic interaction between the Ni precursor and plant extract (Wang *et al*., 2008). Reddy *et al*. (2014) established a similar trend of increased clustering during the synthesis of NiO, when the solution pH was increased from 8 to 11.

The grain sizes estimated by HRSEM were consistent with those obtained from XRD analysis for the nanoparticles at different pH of 8, 10 and 12.

The EDX results of the as-synthesised NiO nanoparticles is shown in Figure 4.7, and it can be seen that Ni and O were the dominate elements, while others such as, Ca, Cl and Si may be due to impurities associated to the nickel precursor and plant extract. Ezhilarasi *et al*. (2016) whom synthesised NiO nanoparticles using *Moringa Oleifera* extract via green synthesis also reported the formation of pure NiO nanoparticles, which was confirmed by energy dispersive X-ray analysis (EDX). The compositional analysis obtained revealed that Ni and O were major components of the nanoparticles, which was in good agreement with their XRD analysis.

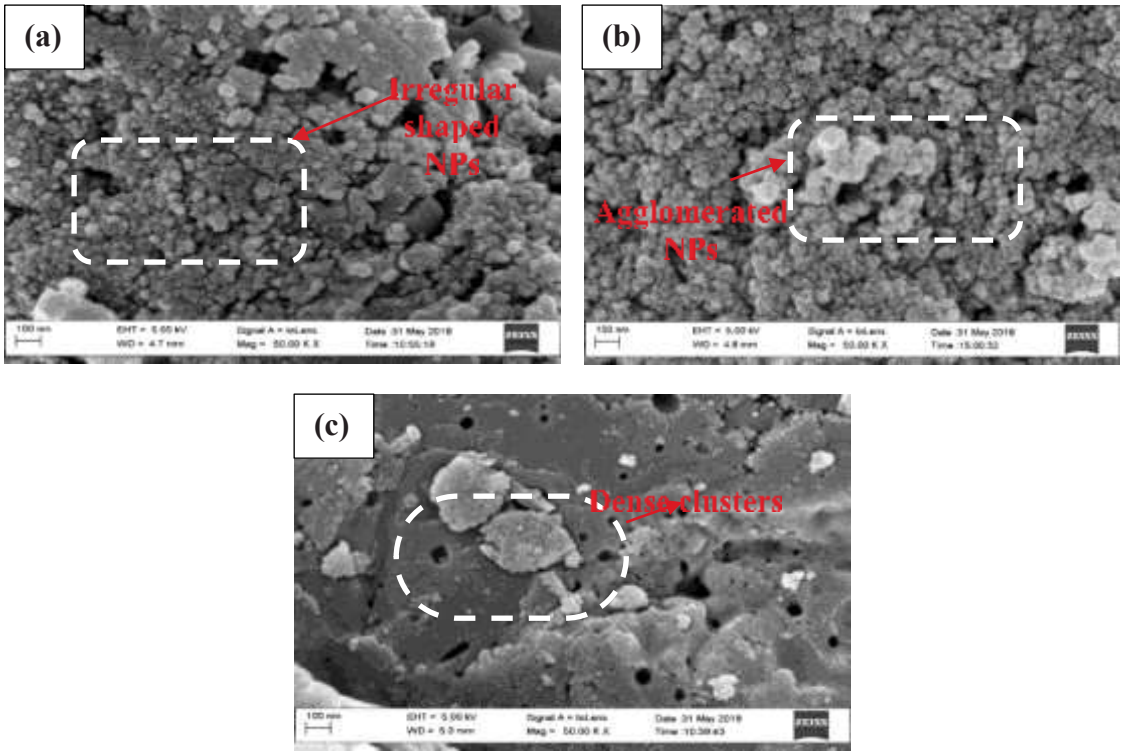

Plate IX: HRSEM Analysis of NiO Nanoparticles at Different pH (a) 8 (b) 10 and (c) 12 Calcined at 500°C

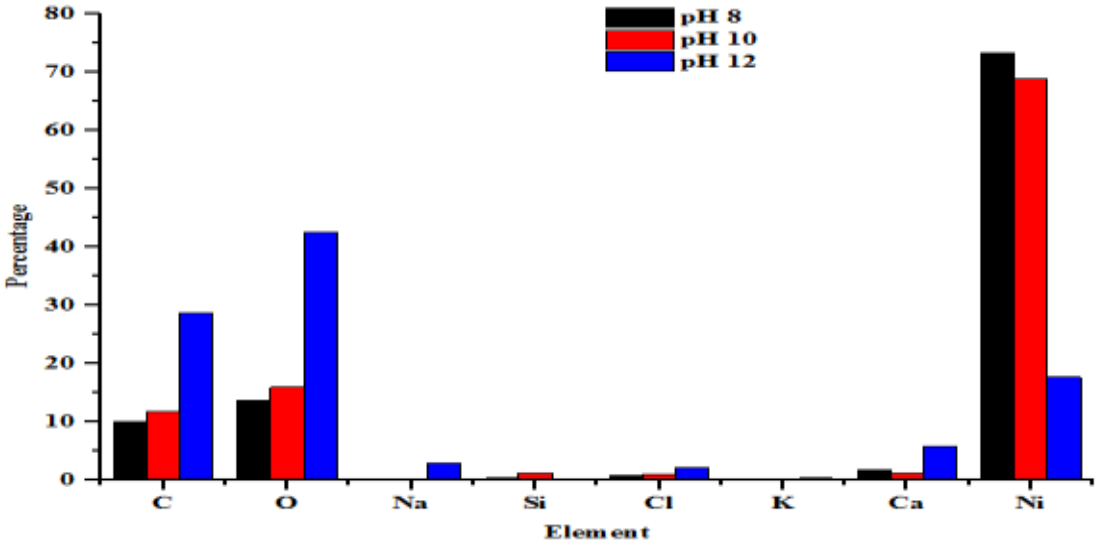

Figure 4.7: EDX Analysis of NiO Nanoparticles at pH 8, 10 and 12 Calcined at 500°C

4.2.4 HRTEM microstructure of NiO nanoparticles

HRTEM results at low, high magnification and SAED images of NiO nanoparticles are presented in Plate X (a-c). Plate X (a) shows the quasi-spherical and hexagonally shaped

microstructure of NiO nanoparticles. From the image, it was observed that a large number of NiO nanoparticles were slightly agglomerated with crystallite sizes as measured by the ImageJ software was between 10.45 to 4.03 nm, which is close to the values obtained from XRD analysis (6.12 nm) using Scherrer's formula. Variations in crystallite size could be attributed to the difference in average particle size distribution as employed by the different techniques.

Plate X (b) represents the HRTEM of the sample at low magnification and reveals directional lattice fringe patterns corresponding to the single crystalline nature of NiO nanoparticle. The interplaner spacing (d) (distance of two successive lines), measured from the fringe pattern is 0.21 nm, corresponding to the (200) crystal plane, which is also observed in XRD study, shown in section 4.2.8. Plate X (c) shows the (SAED) originated from the NiO nanoparticle and the planes calculated from the diffraction rings are same with the planes obtained from XRD study in Section 4.2.8.

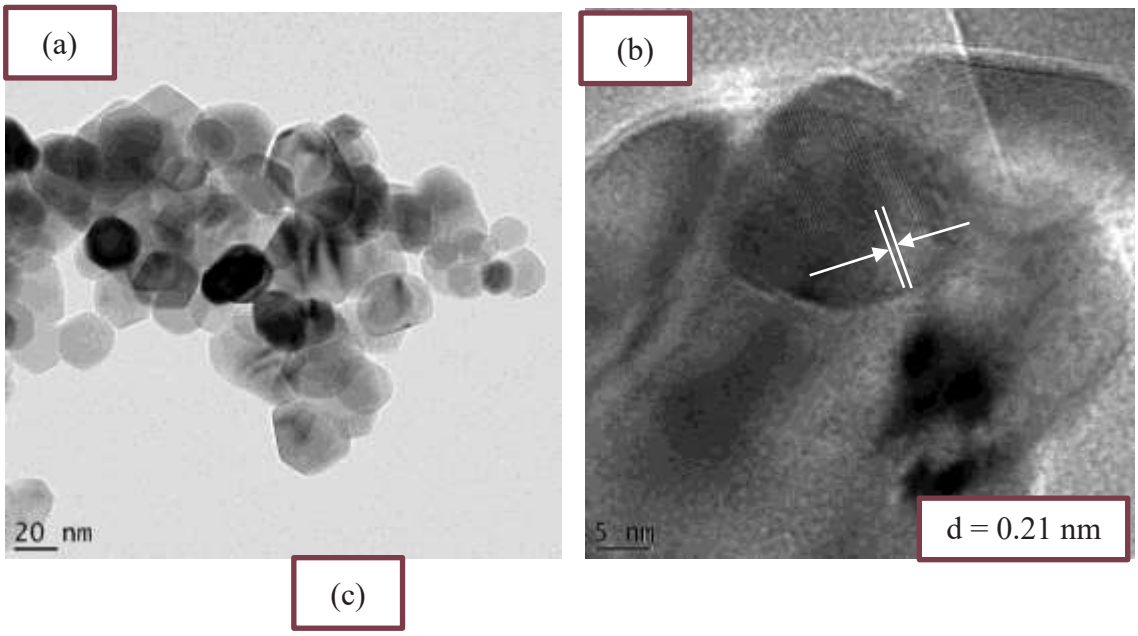

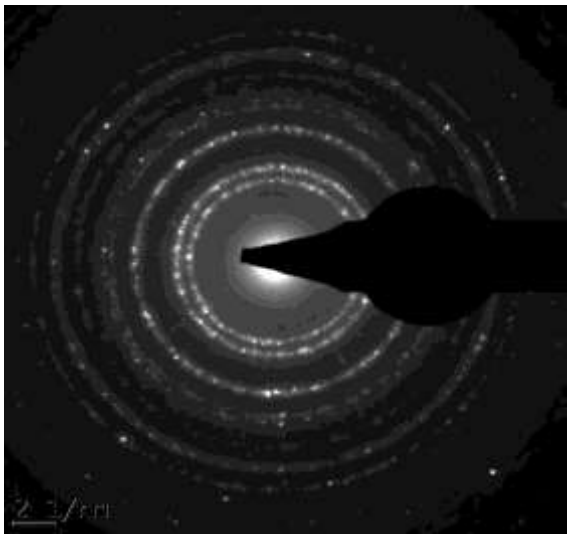

Plate X: HRTEM Results at (a) High, (b) Low Magnification and (c) SAED Images of NiO

The appearance of strong diffraction spots rather than diffraction rings confirmed the formation of single crystalline nickel oxide (Chakrabarty and Chatterjee, 2008). Teoh and Li (2012) reported similar results with the measured lattice distances in the HRTEM image, approximately 0.22 nm for the NiO nanoparticle corresponding to the (200) crystallographic plane.

However, Su *et al.* (2012), demonstrated that mesoporous NiO nanocrystals dominantly exposed {110} planes on hexagonal surfaces together with minor crystal planes such as {002} and {111} facet, forming a close-packed hexagonal nanoplatelet which occupied about 66% of the total surface area. The discrepancy in the dominant NiO planes could be attributed to the different method of synthesis adopted for the various studies.

4.2.5 HRSEM/EDX analysis of SnO_2 nanoparticles

Plate XI (a-c) shows the HRSEM micrograph of the as-synthesised SnO_2 nanoparticles. Nano clusters or aggregated particles and little impurities are present as revealed from the analysis of EDX presented in Figure 4.8.

Morphology of the SnO_2 nanoaprticles synthesised using green synthesis procedure

strongly depends on the amount of H^+ or OH^- ions in the solution. Plate XI (a) shows agglomerated spherical shaped structures at pH 10. On increasing the solution pH to 11 at the same calnination temperature, the size of the agglomerated structure slightly decreased and the particles were unevenly distributed (see Plate XI (b)). Similar trend was observed at pH 12 as shown in Plate XI (c). The reason for this modification of the surface morphology can be explained in terms of OH^- and H^+ ions concentration in the reacting mixture. NH_4OH (the base solution) reacts with the precursor solution containing tin chloride and the plant extract leading to the formation of $Sn(OH)_2$ compound during the reaction process and later dissociates into Sn^{2+} and OH^- ions.

When the concentration of Sn^{2+} and OH^- ions were more than the critical value, (Sn^{2+}) plays a major role in the formation of SnO_2 nuclei. However when pH was increased, changes in the OH^- ions concentration occur and decrease the density of H^+ ions than that at lower pH. Thus on further increase in the solution pH to basic region, the concentration of H^+ ions decreases while that of the OH^- ions increased to form the correponding structures (Wahab *et al*., 2009).

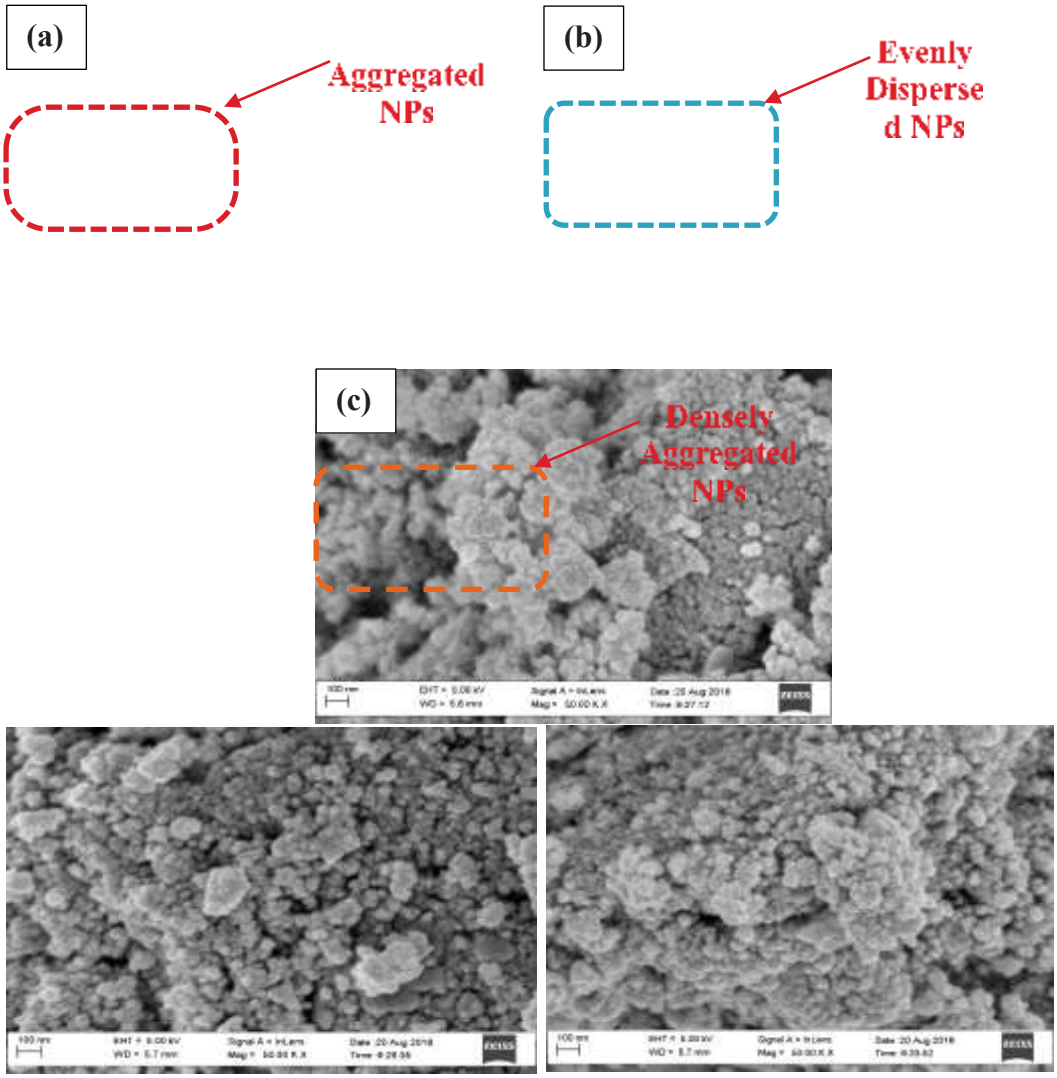

Plate XI: HRSEM Analysis of SnO_2 Nanoparticles at Different pH of (a) 10 (b) 11 and (c) 12

In basic medium (>pH 7), the OH^- ions interact with positively charged Sn^{2+} and form SnO_2. In this work at higher pH 8, that is (10, 12) hydrolysis and condensation took place and irregular shaped spheres were predominaently formed with more compact aglomeration.

Subramaniam *et al*. (2017), also reported morphological variation due to the influence of solution pH when tin oxide nanoparticles was synthesised via sol-gel method. The authors noted that tin oxide synthesised at solution pH 6 and calcination temperature of 400 °C, contained slurry like morphology with no definite shape. However, when the

solution pH was increased to 8, at the same calcination temperature, the nanoparticles showed spherical shaped structures, with better dispersed and less agglomerated shaped as the pH was raised to 10 and a highly porous and foam-like structure observed at pH 12 respectively.

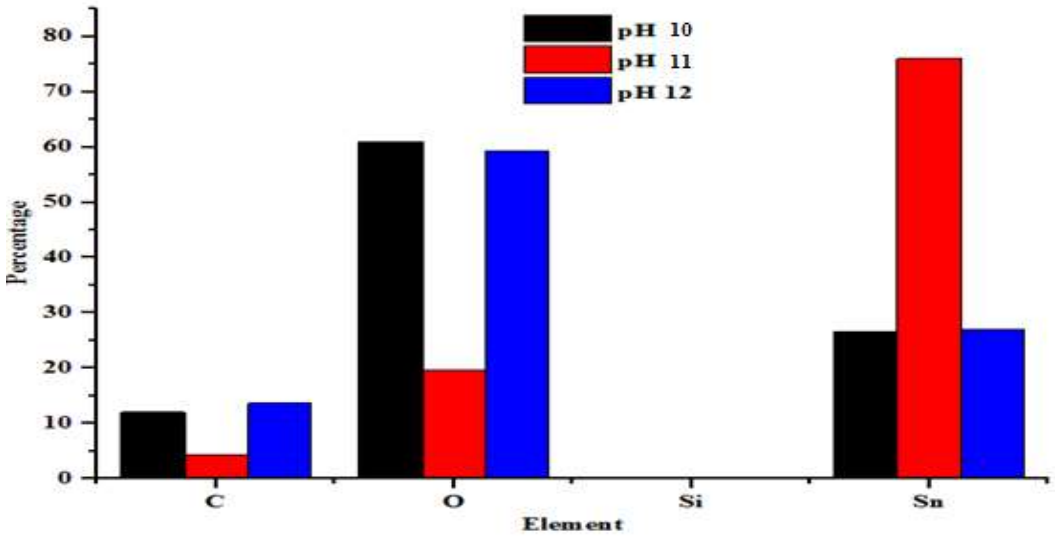

Figure 4.8: EDX Analysis of SnO_2 Nanoparticles at pH 10, 11 and 12 Calcined at 500^oC

Figure 4.8 represents the EDX spectrum of synthesised SnO_2 nanoparticles. The pattern depicts the presence of main constituents such as Sn and O. The existence of these atoms may confirm the formation of pure SnO_2 phase (Elango *et al*., 2015).

4.2.6 HRTEM microstructure of SnO_2

Plate XII (a-c) shows the low, high magnification and Selected Area Electron Diffraction patterns of SnO_2 nanoparticles. It is clear from the Plate XII (a) that the SnO_2 nanoparticles were distinct in nature with a spherical microstructure. HRTEM microstructure in Plate XII (b) revealed lattice fringes with a spacing of 0.33 nm, which corresponds to the interplanar distance of the (1 1 0) planes in tetragonal SnO_2.

Plate XII (c) which represents the SAED patterns revealed the presence of continuous ring patterns without any additional diffraction spots and rings of secondary phases. The

Four most intense fringe patterns corresponding to planes (110), (101), (211), and (301) and are consistent with the peaks observed in the XRD patterns in Section 4.2.9. XRD and HRTEM studies confirmed pure tetragonal structure of SnO_2 nanoparticles as evidenced from Plate XII (c). The ring to-the-center distance of each ring was measured as 3.01, 4.23, 4.41, 5.61, and 6.52 expressed in terms of nm^{-1} respectively. The reciprocal of these values gives the interplanar distance (d) (Patil *et al*., 2012). Similarly, Selvakumari *et al.* (2017) reported the lattice spacing of 0.3325 nm corresponding to the (110) crystal plane of SnO_2. While multiple rings observed in the (SAED) image with crystallographic planes {(110) (101) (211) and (202)} denoted the polycrystalline nature of SnO_2 nanoparticles, and the lattice plane (*hkl*) values of the rings confirmed the tetragonal crystal structure of SnO_2 nanoparticles.

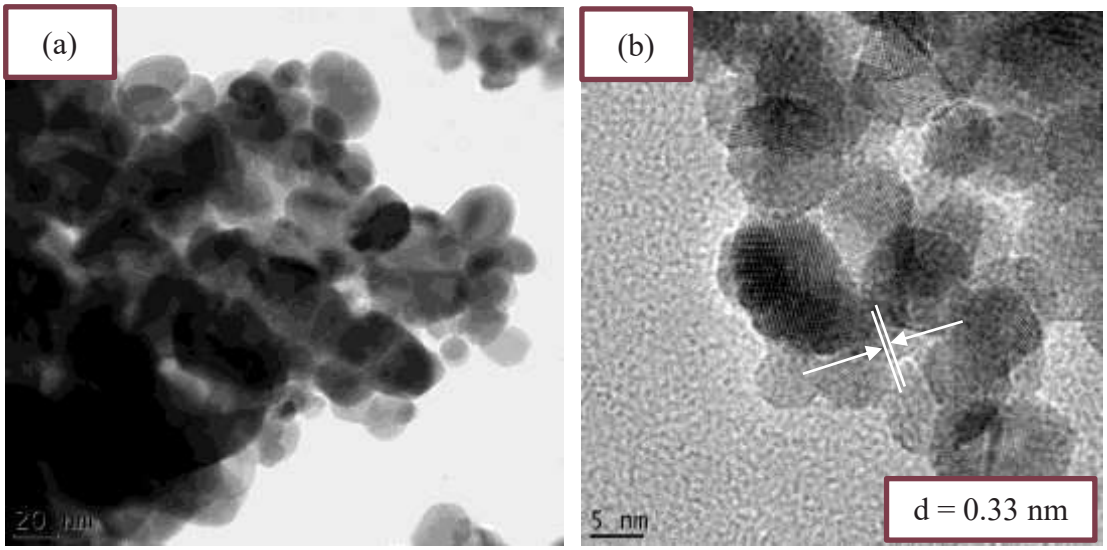

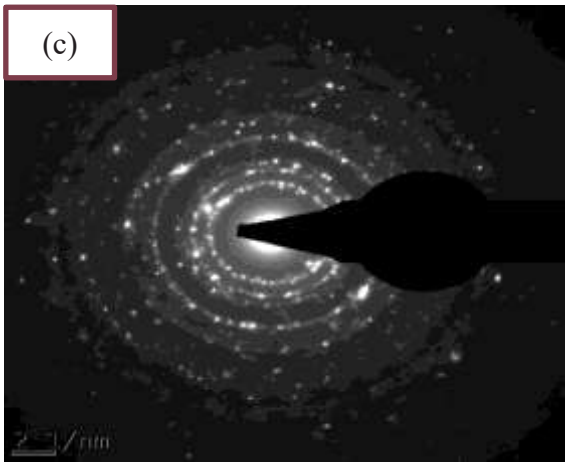

Plate XII: HRTEM Results at (a) High, (b) Low Magnification and (c) SAED Images of SnO_2

4.2.7 XRD analysis for synthesised CNTs samples

The mineralogical phase of the synthesised CNTs was examined using XRD and the XRD pattern of unpurified and purified CNTs is shown in Figure 4.9. As shown in Figure 4.9 (a) broad peaks were found at peaks at 2θ values at 26.32º and 43.35º with a miller indices of (003) and (110) for the two samples. The other crystal peaks such as (220) and (211) noticed were due to the presence of residual amorphous carbon and

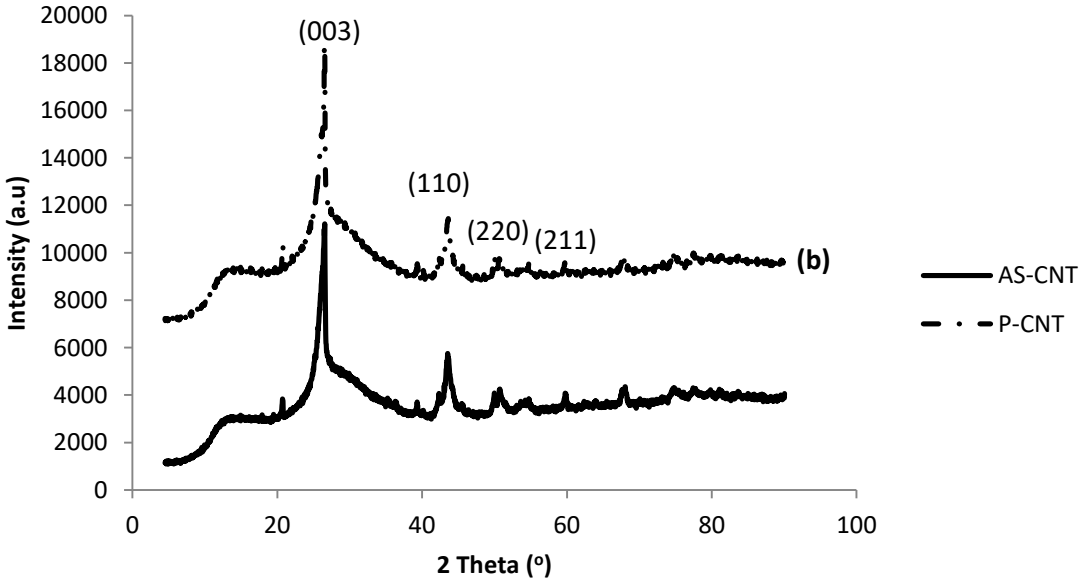

other elements such as Al, Si, Fe and Ni present in the CNTs.

Figure 4.9: XRD Patterns of (a) Unpurified (b) Purified Carbon Nanotubes (CNTs)

The Different XRD parameters used for the calculation of the lateral crystallite sizes of the CNTs are presented in Tables 4.8 and 4.9.

Table 4.8: XRD Parameters of Unpurified CNTs

Diffraction Angle, 2θ, (°)	**Peak Index (*h k l*)**	**Interplanar Spacing, d, (nm)**	**FWHM (radians) (nm)**	**Crystallite Size, D, (nm)**
26.48	003	0.3424	0.8568	9.95
43.29	110	0.2074	0.7224	12.36
51.34	220	0.1801	0.9229	9.98
59.94	211	0.1544	0.4079	23.48
	Average crystallite size			13.94

Table 4.9: XRD Parameters of Purified CNTs

Diffraction Angle, 2θ, (°)	**Peak Index (*h k l*)**	**Interplanar Spacing, d, (nm)**	**FWHM (radians) (nm)**	**Crystallite Size, D, (nm)**
26.01	003	0.3423	0.4268	19.95
43.89	110	0.2061	0.8124	11.01
51.24	220	0.1782	0.6329	14.54

59.92	211	0.1543	0.6179	15.50
	Average crystallite size			15.25

The Al and Si were also observed even after purification of CNTs and could be due to insolubility in the acid mixture (Dupuis, 2005; Kariim *et al.,* 2016). However, it was noticed that purified CNTs has fewer impurities compared to the as-synthesised CNTs. The miller indices of (003) and (110) of CNTs correspond to the spacing of 0.3424 nm and 0.2061 nm respectively. These values were closely related to that of graphite (0.335 nm). This further confirmed the graphitic nature of the CNTs peaks and the significant improvement in the order of crystallinity of the CNTs after the purification step. An increase in the internal diameter of the CNTs after purification from 13.94 nm to 15.25 nm also was noticed. This observable increase in the diameter resulted from the removal of residual metal particles from the pores of the as-prepared CNTs (Aliyu *et al.,* 2017).

4.2.8 XRD analysis for NiO nanoparticles

The NiO nanoparticles patterns were obtained by XRD and the result is shown in Figure 4.10. The XRD of as-synthesised NiO nanoparticles at different pH of 8, 10 and 12 revealed the existence of diffraction peaks at 2θ values of 37.25, 43.27, 62.88 and 75.42^{o} which corresponds to (110), (200), (220) and (311) planes. This depicts the formation of bunsenite, face cubic center phase nickel oxide at all the pHs (JCPDS card no. 47-1049).

The average crystalline size was obtained from peaks using the Scherrer Equation 4.14:

$$d = \frac{K}{\beta cos\theta} \quad (4.14)$$

where d is the crystallite size, K is Scherrer's constant which is 0.94 for spherical crystals with cubic symmetry, λ is X-ray wavelength at 0.15406 nm, β is the full width at half maximum (FWHM) and θ is the angle of reflection at full width.

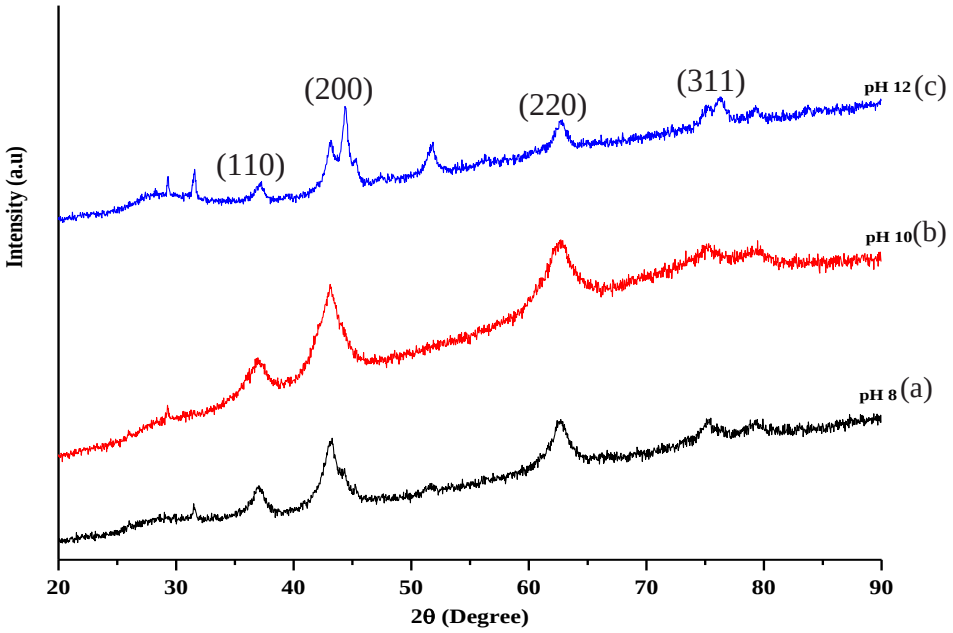

Figure 4.10: XRD Pattern for NiO Nanoparticles at (a) pH 8, (b) 10 and (c) 12

The Different XRD parameters used for the calculation of the crystallite sizes of the NiO at pH of 8, 10 and 12 are presented in Tables 4.10-4.12.

Table 4.10: XRD Parameters of NiO at pH 8

Diffraction Angle, 2θ, (°)	Peak Index (*h k l*)	Interplanar Spacing, d, (nm)	FWHM (radian) (nm)	Crystallite Size, D, (nm)
36.92	110	0.2433	1.3924	6.29
43.27	200	0.2089	1.8723	4.77
62.41	220	0.1487	1.0076	9.64
75.10	311	0.1264	1.4621	7.17
		Average crystallite size		6.97

Table 4.11: XRD Parameters of NiO at pH 10

Diffraction Angle, 2θ, (°)	Peak Index (*h k l*)	Interplanar Spacing, d, (nm)	FWHM (radian) (nm)	Crystallite Size, D, (nm)
37.18	110	0.2416	1.0503	8.33
44.53	200	0.2033	1.5523	5.78

62.93	220	0.1476	1.1106	8.76
76.27	311	0.1247	0.9021	11.69
	Average crystallite size			8.64

Table 4.12: XRD Parameters of NiO at pH 12

Diffraction Angle, 2θ, (°)	Peak Index (*h k l*)	Interplanar Spacing, d, (nm)	FWHM (radian) (nm)	Crystallite Size, D, (nm)
36.92	110	0.2433	0.8664	10.10
43.27	200	0.2089	1.1263	7.93
62.41	220	0.1487	0.9025	10.75
75.1	311	0.1264	1.0174	10.29
	Average crystallite size			9.76

Furthermore, the average crystallite sizes of NiO nanoparticles prepared at different pH values (8, 10 and 12) were of 8.12, 6.83, and 6.93 nm, respectively. The decrease in average crystallite size between pH 8 to 10 could be attributed to the increase in the nucleation rate with reaction mixture. While, the increase in particles size at pH 12 could be due to agglomeration of Ni-Ni atoms (Reddy *et al*., 2014).

Shahzad *et al*. (2015) reported a successful preparation of NiO nanoparticles with no significant change irrespective of the pH-value over a specified calcination or holding time. This however contradicts the findings in this study due to the difference in the method of synthesis. Nevertheless, similar trend was reported by Reddy *et al*. (2014), according to their work, different pH values of (8, 9, 10 and 11) had corresponding of crystallite sizes of 72, 66, 52 and 58 nm, respectively. Again, the crystallite size in this study are smaller to that reported by Reddy *et al*. (2014), due to different synthesis protocol, calcination temperature and concentration of the nickel salt precursor.

4.2.9 XRD analysis for SnO_2 nanoparticles

The XRD pattern of SnO_2 nanoparticles at pH (a) 8 (b) 10 and (c) 12 is shown in Figure 4.11. The diffraction peaks at 2θ values of 26.6°, 33.89°, 38.97°, 51.78°, 54.76°, 61.87, 64.72°, 65.90° and 78.71° are linked to the following crystal planes (110), (101), (111), (211), (220), (310), (112), (301) and (321), which correspond to a dominant cassiterite SnO_2 phase for all the studied pH according to JCPDS card no. 41-1445. The average crystallite sizes calculated using the Scherrer equation in Equation 4.14, were found to be 8.50, 7.43 and 9.83 nm at pH 8, 10 and 12 respectively.

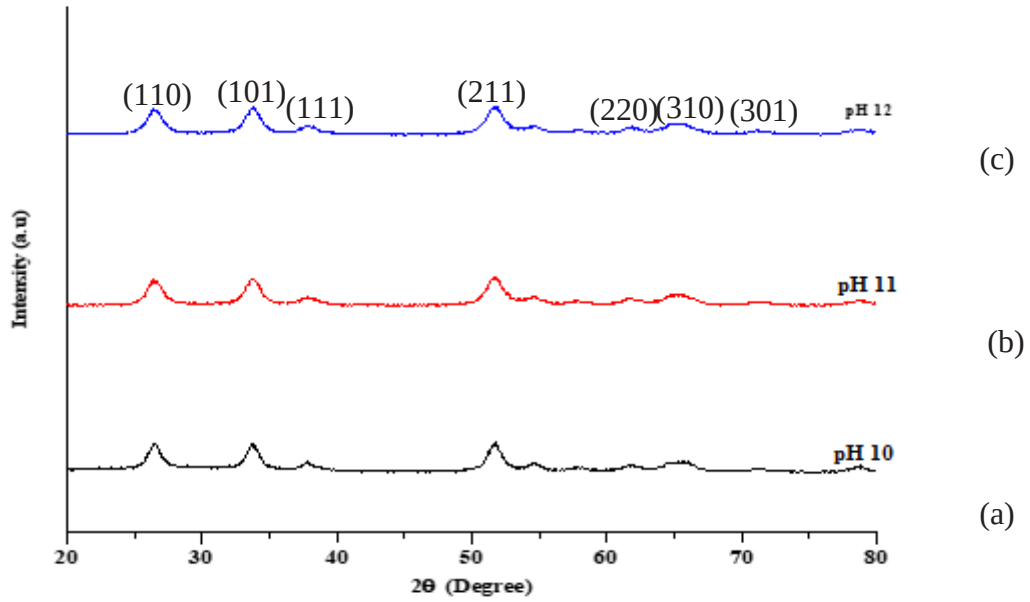

Figure 4.11: XRD Pattern for SnO_2 Nanoparticles at (a) pH 10, (b) 11 and (c) 12

The Different XRD parameters used for the calculation of the crystallite sizes of the SnO_2 at pH of 10, 11 and 12 are presented in Tables 4.13-4.15.

Table 4.13: XRD Parameters of SnO_2 at pH 10

Diffraction Angle, 2θ, (°)	Peak Index (*h k l*)	Interplanar Spacing, d, (nm)	FWHM (radians)	Crystallite Size, D, (nm)

			(nm)	
26.54	110	0.3356	1.6724	5.10
33.86	101	0.2645	0.9152	9.48
37.70	111	0.2384	1.2645	6.93
51.84	211	0.1762	1.4225	6.49
54.65	220	0.1678	1.0443	8.94
61.79	310	0.1500	1.1094	8.72
65.30	301	0.1428	1.2038	8.19
	Average crystallite size			7.69

Table 4.14: XRD Parameters of SnO_2 at pH 11

Diffraction Angle, 2θ, (°)	**Peak Index (*h k l*)**	**Interplanar Spacing, d, (nm)**	**FWHM (radians) (nm)**	**Crystallite Size, D, (nm)**
26.54	110	3.3558	1.4213	6.00
33.86	101	2.6452	0.6103	14.21
37.70	111	2.3842	0.7615	11.53
51.84	211	1.7622	0.8524	10.82
54.65	220	1.6781	1.0533	8.87
61.79	310	1.5002	1.2014	8.04
65.30	301	1.4278	1.2015	8.20
	Average crystallite size			9.67

Table 4.15: XRD Parameters of SnO_2 at pH 12

Diffraction Angle, 2θ, (°)	**Peak Index (*h k l*)**	**Interplanar Spacing, d, (nm)**	**FWHM (radians)**	**Crystallite Size, D, (nm)**

				(nm)
26.54	110	0.3355	0.9313	9.15
33.86	101	0.2645	0.6232	13.92
37.70	111	0.2352	0.5393	16.27
51.84	211	0.1762	0.5792	15.93
54.65	220	0.1678	0.7943	11.76
61.79	310	0.1504	0.8855	10.92
65.30	301	0.1428	0.6917	14.26
	Average crystallite size			13.17

This indicated that the smallest crystallite size was obtained at a pH of 10. Subramaniam *et al*. (2017) reported a similar research case, according to them, when the pH for the synthesis of SnO_2 was varied in the range of (6, 8, 10 and 11) the cyrstallite sizes were 11.9, 10.0 6.2 and 6.8 nm respectively. However, Merlin *et al*. (2018) while working on the influence of pH and temperature on the structure and size of tin oxide nanoparticles stated that the average size of SnO_2 nanoparticles increased from 28.77 to 30.82 nm when the pH was increased from 8 to 10 at 550°C then, decreased from 35.19 to 22.80 nm when the pH was also increased from 8 to 10 at 600°C. This suggested that calcination temperature along side pH influences the crystallite size more than pH alone. In this study, revealed that pH 10 was optimal for achieving small paticle size with a well defined peak, which could find application in corrosoin studies. This could be attributed to the fact that at pH 10, the OH^- concentration in the reaction mixture was sufficient to bring about the right anisotropic growth of crystals in the Sn^{+2} nuclueus

(Merlin *et al*., 2018). The crystallinity and compositional analysis indicated that the solution pH does not affect the quality of materials as observed from X-ray diffraction pattern and this established a key to control the structure of studied composite coating materials.

4.3 Results of Characterisation of the Synthesised Nanomaterials

Analytical techniques such as HRSEM-EDX, HRTEM-SAED, XRD, FTIR and XPS were used for the characterization of the as-prepared nanomaterials and the results discussed as follows.

4.3.1 HRSEM analysis of NiO, SnO_2 and NiO-SnO_2 nanocomposites

High Resolution Scanning Electron Microscope (HRSEM) analysis was employed to examine the morphology of the synthesised nanocomposites. The HRSEM micrographs of the synthesised nanoparticles; pristine NiO and SnO_2), as well as NiO-SnO_2 nanocomposites in the ratio of (1:1, 2:1 and 1:2, respectively) are illustrated in Plate XIII (a-e) respectively.

Plate XIII (a) revealed the formation of aggregated and homogenously distributed particles with no definite shape, while Plate XIII (b), demonstrated the presence of scattered tiny and big clusters of nanoparticles again with no precise shape. Upon the formation of nanocomposite between NiO and SnO_2 as shown in Plate XIII (c-e), there were visible changes in morphology of the nanomaterials. All the as-prepared NiO-SnO_2 nanocomposites with different molar ratios of NiO to SnO_2 formed spherical and hexagonal superstructures with sizes of between 6.25-32.5 nm.

A close inspection of Plate XIII (c) showed quasi-spherical aggregated nanocomposites, while Plate XIII (d) were of similar morphology with slightly less agglomeration and considered optimum due to more uniform dispersion of the particles over the whole

area. This gave rise to a better surface network for the protection of the coated steel surface over attacks from environmental conditions. However, for Plate XIII (e) the morphology was of a hierarchical microsphere that consisted of densely clustered hexagonal and spherical nanoplates of different sizes.

These noticeable agglomerations into clusters could be due to the attractive forces between SnO_2 and NiO particles held together into groups to form nanocomposites. Moghadam and Salavati-Niasari (2017), in a previous study described that each unit of the NiO-SnO_2 nanocomposites formed a flower like shapes with weak agglomeration.

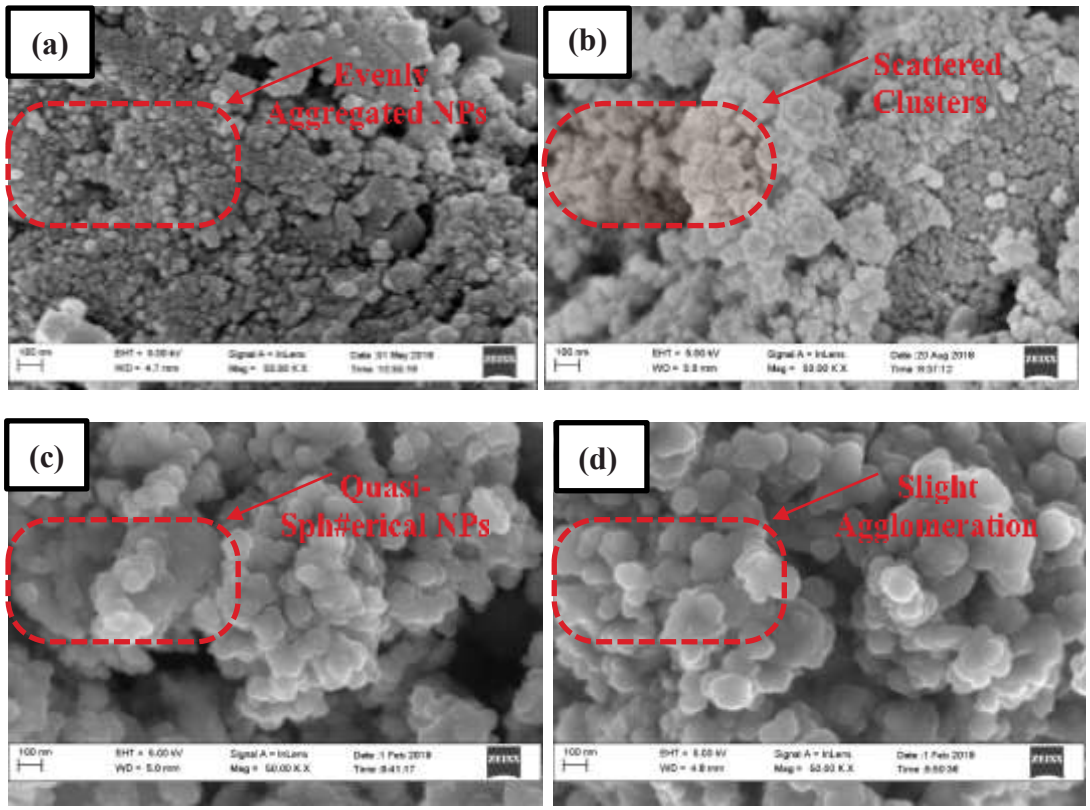

Densely Clustered Hexagonal and Spherical NPs

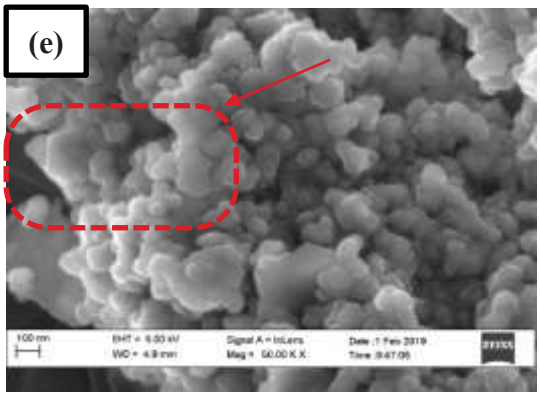

Plate XIII: HRSEM micrographs of (a) Pristine NiO, (b) Pristine SnO_2, (c) NiO-SnO_2 (1:1), (d) NiO-SnO_2 (1:2) and (e) NiO-SnO_2 (2:1)

While Zhang *et al*. (2016) pointed out that irregular shaped NiO and SnO_2 nanoparticles formed specific NiO-SnO_2 clusters irrespective of the mixing ratio between the NiO and SnO_2 precursors. These previous findings agree with the result of this research on the morphology of NiO-SnO_2 nanocomposites.

4.3.2 EDX analysis for NiO-SnO_2 nanocomposites

Energy Dispersive X-ray spectroscopy (EDX) analysis of the synthesised NiO-SnO_2 nanomaterials, shown in Figure 4.12, revealed the presence of (Ni), (Sn), (O) and (C) in different proportions.

From the insets in Figure 4.12, the atomic compositions of the identified elements (Ni:Sn:C:O) correspond to (21.04:20.76:41.58:16.62), (36.41:19.4: 37.32:6.87), (19.12:39.43: 31.26:10.19) for the sample NiO:SnO_2 (1:1) (A), NiO:SnO_2 (2:1) (B) and NiO:SnO_2 (1:1) (C) respectively.

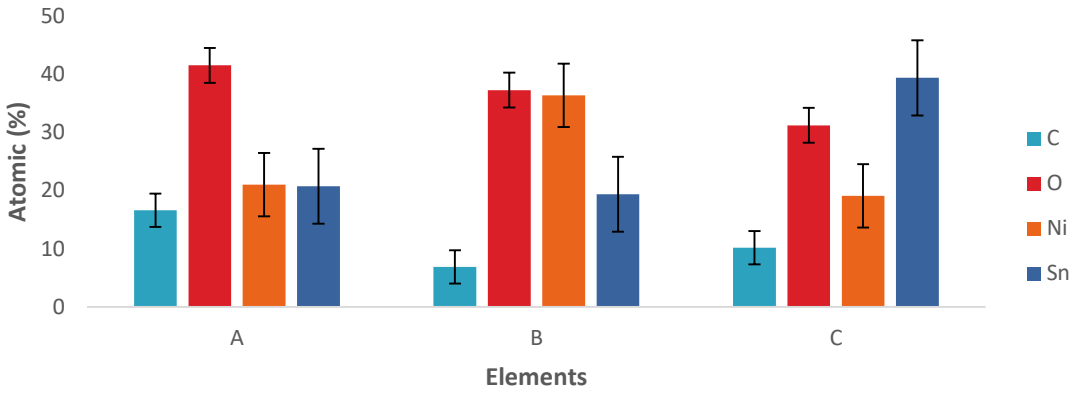

Figure 4.12: EDX Graph for NiO-SnO_2 Nanocomposites

where A is NiO-SnO_2 in the ratio (1:1), is NiO-SnO_2 in the ratio (2:1), and C is NiO-SnO_2 in the ratio (1:2)

The (EDX) results showed that there is only Ni, Sn, O and C elements in synthesised nanomaterials without any peaks of impurities. Additionally, the C may have originated from adhesive carbon tape used to hold the samples during the analysis.

4.3.3 HRSEM analysis of NiO, CNTs and NiO-CNTs nanocomposites

The prepared NiO, CNT, and NiO-CNTs nanocomposites, were analyzed using HRSEM to examine their morphologies and their corresponding HRSEM micrographs are displayed in Plate XIV (a-e).

As shown in Plate XIV (a), it can be noticed that Pure NiO nano-crystallites were aggregated, forming clusters with large grains. Whereas, purified CNT morphology showed the presence of less aggregated short and long tubular structures of different diameters shown in Plate XIV (b). It can be observed in Plate XIV (c-d) that the incorporation of CNTs as the support material onto the pure NiO nanoparticles resulted to morphological transformation from a cluster-like to a filamentous structure. This could be due to the fact that many defects and oxygen-containing functional groups

were formed on the surface of CNTs because of the purification process with the mineral acids. Subsequently, these defects and oxygen-containing functional groups can serve as active sites for the diffusion of the Ni precursor resulting to the formation of entangled tubular network across the whole surface (Yu *et al*., 2016). Therefore, this diffusion may be linked to the reaction of Ni^{+2} with π -conjugated skeleton of the CNTs, where the C atoms in the CNTs transformed from sp^2-hybridized to sp^3-hybridized C atom (Chen *et al*., 2014).

Plate XIV (c) comprises of CNTs-NiO (1:1) found to have homogenous distribution of the NiO particles over the area of the CNTs as a support material. However, in Plate XIV (d and e) as the ratio of CNTs-NiO is gradually increased from 1:1 to 2:1, it was observed that the NiO nanoparticles on the surface of CNTs started to agglomerate and the tubular network of CNTs became less visible. Nevertheless, the grain boundaries and shapes of the NiO nanoparticles deposited on the CNTs templates became more defined in comparison to NiO nanoparticles (Chen *et al*., 2014). This could be attributed to the fact that the density of Ni is 8.9 g/dm^3 while, that for CNTs is 1 g/dm^3so thus the mass per volume ratio occupied by CNTs is less than that occupied by NiO.

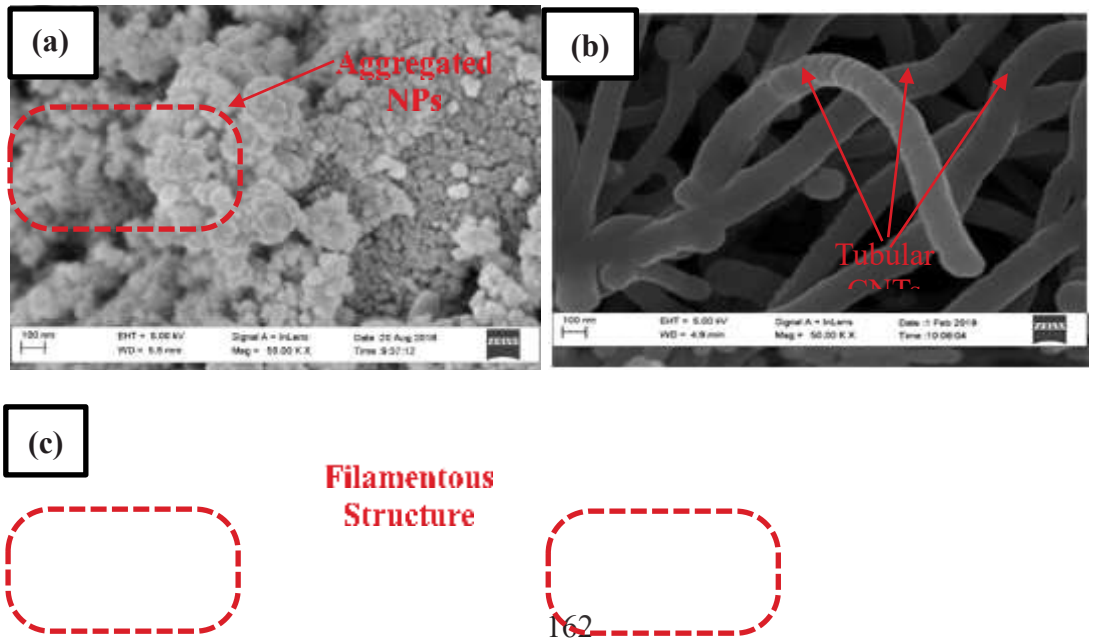

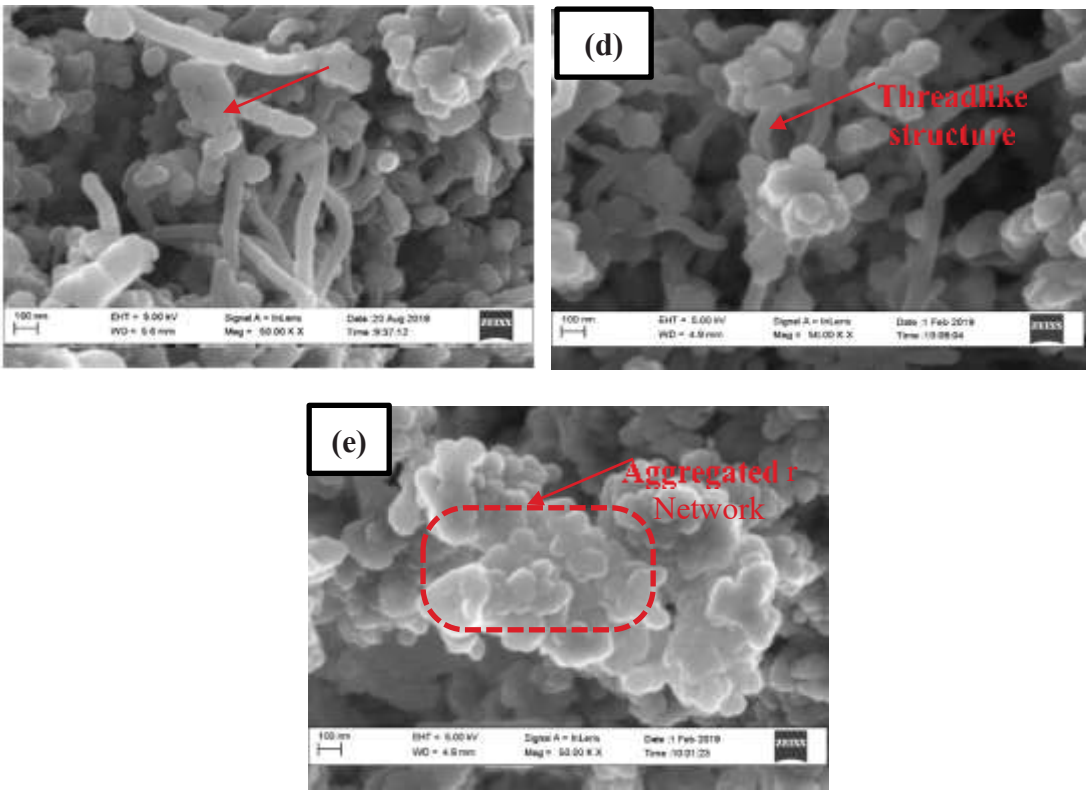

Plate XIV: HRSEM Micrograph of (a) Pristine NiO, (b) Purified CNTs, (c) NiO-CNTs (1:1), (d) NiO-CNTs (1:2), (e) NiO-CNTs (2:1)

This gave rise to a less aggregated and more uniformly dispersed units for the nanocomposite when the amount of CNTs in the composite was increased. Furthermore, the average outer diameter of individual CNTs was between the range of 20-35 nm but the average diameter of NiO-CNTs nanocomposites was >45 nm. This confirmed the formation of interlinked network or structure with thin but uniform wrapping of NiO on the surface of CNTs. This type of interlinked structure could improve the ability of NiO-CNTs nanocomposites to act as coating material to inhibit the corrosion of steel over bare NiO or pure CNTs individually (Abdeen *et al*., 2019). Similar deductions were made by, Gharegozloo *et al*. (2016), and Banerjee *et al*. (2018). Each researcher pointed out that addition of CNTs to a NiO-CNTs nanocomposite resulted in a better distribution of NiO nanoparticles, and also prevents agglomeration of NiO nanoparticles based on the diffusion theory mechanism. Therefore, NiO-CNTs composite exhibited a uniform morphology, with neither NiO aggregation nor the occurrence of two-phase (NiO and

CNTs) nanoparticles.

4.3.4 EDX analysis for NiO-CNTs nanocomposites

The EDX spectrum of synthesised NiO-CNTs nanocomposites is shown in Figure 4.13. The pattern in the chart clearly revealed the presence of main constituents such as, Ni and O from nickel salt precursor, as well as C from the purified CNTs. The existence of these atoms therefore, confirmed the formation of NiO-CNTs nanocomposites in the following atomic ratios (74.13:15.64:10.05), (62.66:15.27:22.07), and (71.83:15.47:12.69). The interaction of NiO with CNTs may have resulted to the formation of Ni-O-C bonds (Jafari and Jabbarzade (2016). However, while the amount of carbon in sample D and F was fairly constant (74.13% and 71.83%), the amount of carbon in sample E reduced to 62.66%, which could be ascribed to the fact that the ratio of CNTs in the sample E is less than those present in samples D and F from the compounding ratio.

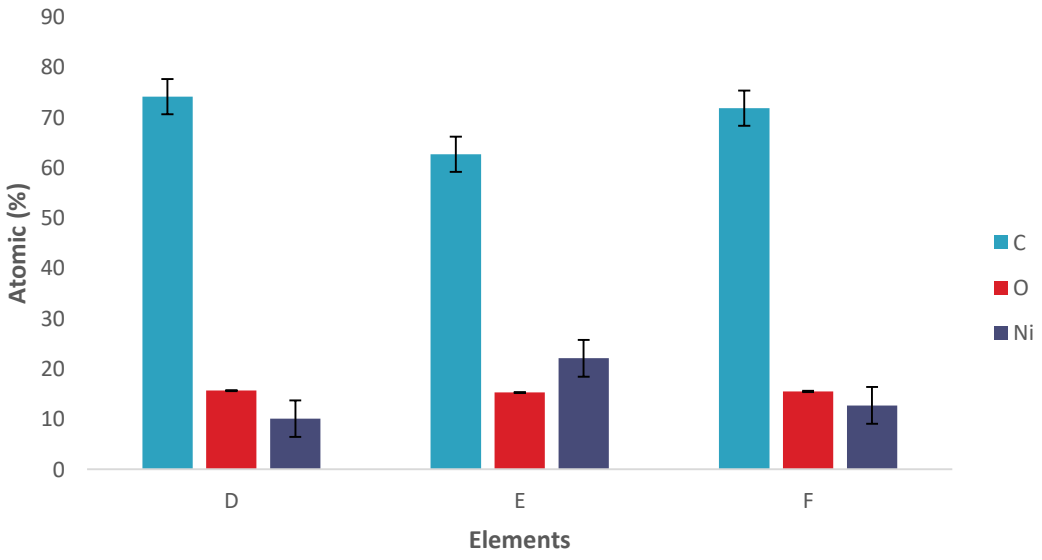

Figure 4.13: EDX Graph for NiO-CNTs Nanocomposites

where D is NiO-CNTs in the ratio (1:1), E is NiO-CNTs in the ratio (2:1), and F is NiO-

CNTs in the ratio (1:2)

4.3.5 HRSEM analysis of SnO_2, CNTs, and SnO_2-CNTs nanocomposites

The morphology of the prepared composites was determined using High Resolution Scanning Electron Microscope (HRSEM) and the corresponding images are shown in Plate XV (a-e). For the pristine SnO_2 nanoparticles in Plate XV (a), the particles were densely distributed showing quasi-spherical morphologies.

For Plate XV (b), purified CNTs with an outer diameter ranging between 30 - 35 nm were distributed randomly, and different filaments were loosely held in place by weak Van der Waal forces. CNTs-SnO_2 nanocomposites as presented in Plate XV (c-e), revealed the firmly attachement of SnO_2 particles onto the surface of the CNTs, during the formation of the nanocomposites. Overall, SnO_2 nanoparticles effectively decorated the CNTs wall, while some of the SnO_2 nanoparticles were also deposited within the inner ‘all of CNTs. The effect of the ratio of SnO_2-CNTs on the nanomaterial formed was also examined accordingly. It was observed that as the incorporated amount of SnO_2 to CNTs increased from 1:1 to 2:1, the CNT walls became less visible as displayed in Plate XV (e). This process may be described in the following way: the tubes of pristine CNTs were closed and the interior was in a state of vacuum. After they were treated with hydrochloric and nitric acid, some of them were chopped up or the tips were removed.

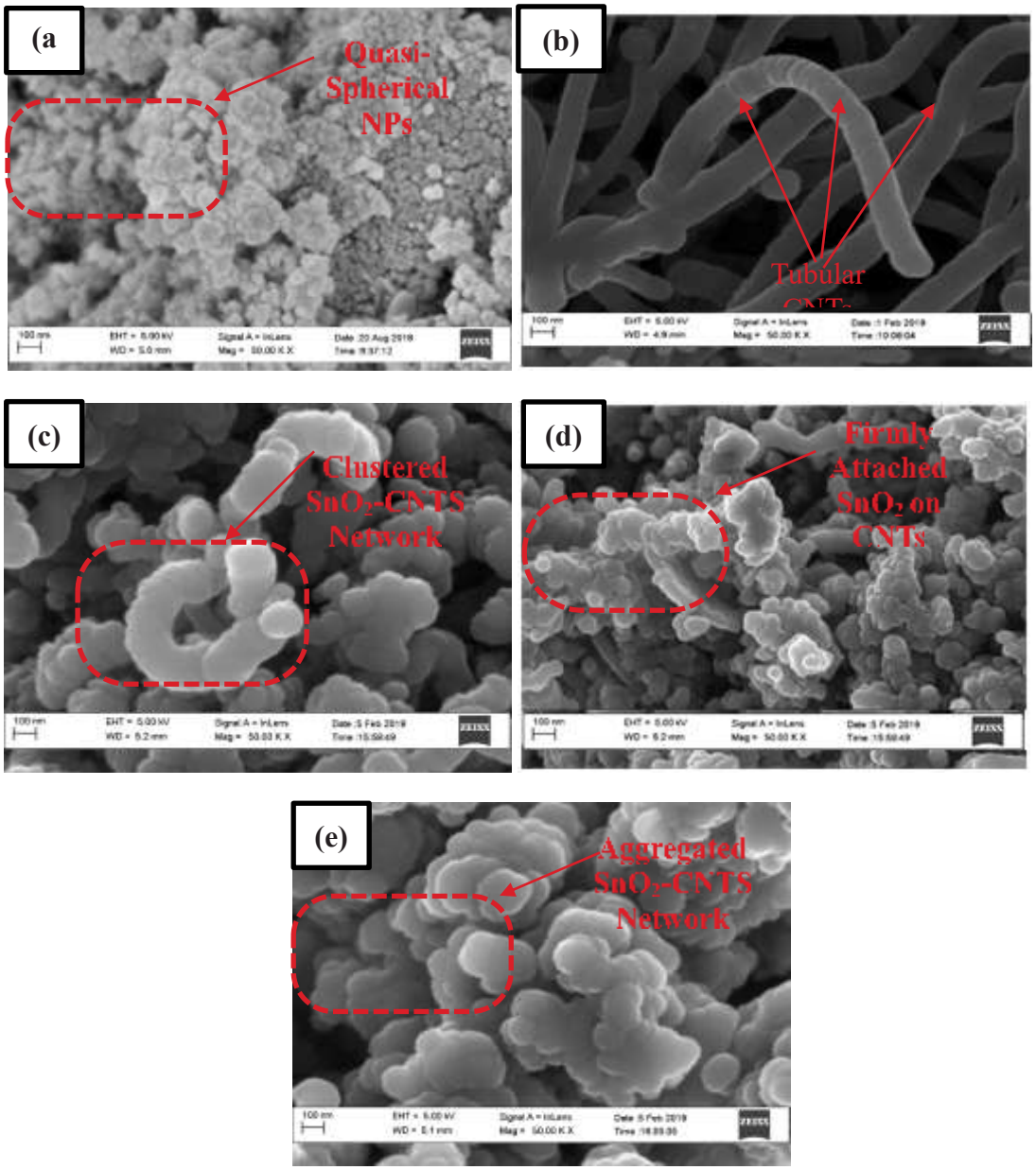

Plate XV: HRSEM Micrograph of (a) Pristine SnO_2, (b) purified CNTs, (c) SnO_2-CNTs (1:1), (d) SnO_2-CNTs (1:2) and SnO_2-CNTs (2:1)

Therefore, it was easy for Sn^{2+} ions to diffuse into the interior of the CNTs forming a Sn-C network bonded by Van Der Waal forces. In the post-treatment, Sn^{2+} converted into SnO_2 which was deposited on the surfaces of the CNTs (Fu *et al*., 2009). However, at a later stage, the deposition of the SnO_2 nanoparticles resulted in clusters obstructing the visibility of the CNTs. The optimum dispersion for this study was found at SnO_2 and CNTs (1:2) loading as presented in Plate XV (b).

The presence of CNTs therefore had a significant effect on the nanocomposition, acting as a frame for the efficient dispersion of SnO_2 nanoparticles. Not only that CNTs matrix prevented agglomeration of SnO_2 nanoparticles in the SnO_2-CNTs nanocomposite. This type of less agglomerated composites enhances the formation of better adhesive bonds between the surface of steel substrates and feedstock (Abdeen *et al*., 2019). After a successful incorporation of SnO_2 nanoparticles into the matrix of CNTs, it was noted that with increasing SnO_2 nanoparticles content beyond an optimum ratio, the SnO_2 nanoparticles on the surface of the CNTs showed a greater tendency towards aggregation (Xie and Varadan 2005; Fu *et al*., (2009); Feng *et al*., 2010; Phil *et al*., 2015; Yuliarto *et al.,* 2019). Therefore, careful examination of the HRSEM micrographs revealed the had the optimum amount of SnO_2 nanoparticles that should be incorporated in the CNTs matrix to provide uniform surface morphology or dispersion that would offer a good adhesive surface coating on a metallic substrate such as, steel to inhibit corrosion is (1:2).

4.3.6 EDX analysis for SnO_2-CNTs nanocomposites

The EDX spectrum of the as-synthesised SnO_2-CNTs composite is displayed in Figure 4.14, the elemental composition of samples, (SnO_2:CNTs (1:1)) (G), (SnO_2:CNTs (1:2)) (H), and (SnO_2:CNTs (2:1)) (I) consisted entirely of Carbon (C), Oxygen (O), and Tin (Sn) (Phil *et al*., 2015). The atomic ratio of these constituents elements in these samples were deduced to be (39.98:40:20.02), (30.01:33.3:36.69), (32.22:54.92:12.86) for (O:C:Sn) for samples G, H and I respectively. Which implied that the mass of Sn and C increased with a corresponding increase in combining ratio.

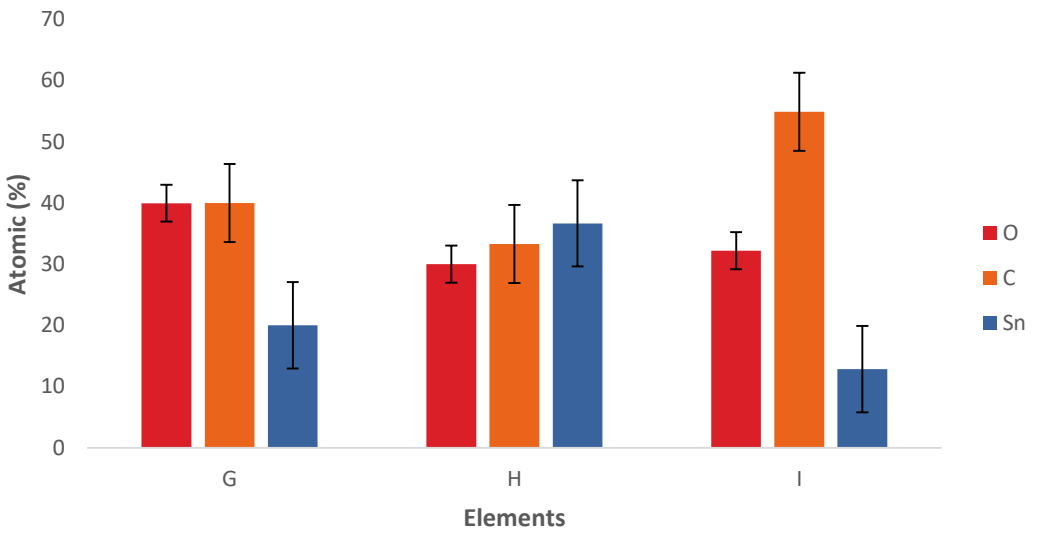

Figure 4.14: EDX Graph for NiO/CNTs Nanocomposites

where G is SnO_2-CNTs in the ratio (1:1), H is SnO_2-CNTs in the ratio (1:2), and I is SnO_2-CNTs in the ratio (2:1).

4.3.7 HRSEM analysis of NiO-CNTs-SnO_2 nanocomposites

High Resolution Scanning Electron Microscope analysis was conducted on the prepared NiO-CNT-SnO_2 nanocomposite and their corresponding micrographs are displayed in Plate XVI (a-g). Plate XVI (a and b) which displayed SnO_2 and NiO nanoparticles respectively consisted of aggregated and homogeneously distributed particles with no definite shapes. While, Plate XVI (c) showed the noodles, and reedy curved worms like morphology of typical CNTs. However, after the introduction of NiO and SnO_2 nanoparticles, there was a transformation in morphology (see Plate XVI (d-g)), from spheroid and hexagonal particles to quasi-spherical morphology of NiO-CNTs-SnO_2 nanocomposites.

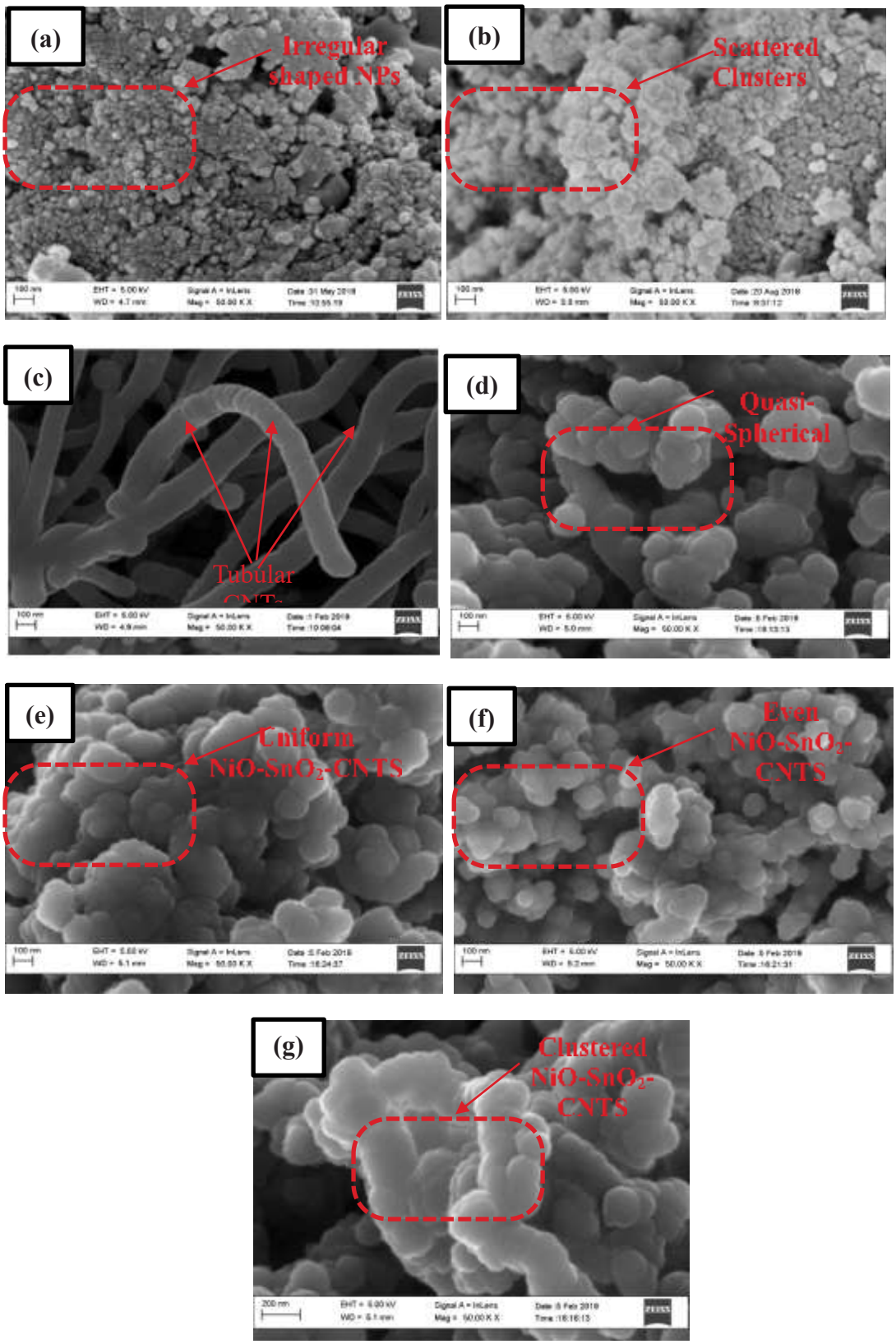

Plate XVI: HRSEM Micrograph of (a) Pristine NiO, (b) Pristine SnO_2, (c) Purified CNTs, (d) NiO-CNTs-SnO_2 (1:1:1), (e) NiO-CNTs-SnO_2 (1:1:2), (f) NiO-CNTs-SnO_2 (1:2:1) and (g) NiO-CNTs-SnO_2 (2:1:1)

These spheroids like particles were considered to be SnO_2 nanoparticles while, the hexagonal particles were considered to be NiO nanoparticles. Furthermore, Plate XVI (d-f) showed that alteration of the mixing ratio of CNTs in the mixture of SnO_2 and NiO, resulted in complete morphological transformation with better defined grain boundaries for the nanocomposites. It was also observed that the rate of CNTs surface coverage by SnO_2 and NiO nanoparticles differed due to different mixing ratios. Therefore, SnO_2 and NiO nanoparticles were non-uniformly dispersed within the CNTs surface, and in some regions bundles of CNT were found with irregular agglomeration. NiO and SnO_2 grain growth can be attributed to reduction of Ni^{+2} and Sn^{+2} ions onto defect zones created by functionalisation of CNTs under the influence of ultrasonic vibration in the mixture of ethanol and water as a solvent system. Morse so, during the purification of CNTs by acid reflux in concentrated HNO_3 and H_2SO_4, some functional groups, such as -COOH and -OH groups, and defects could be generated on the CNTs surfaces. These functional groups and defects provided locations for the deposition of Sn^{4+} and Ni^{2+} (Lin *et al*., 2015). Hence, the nucleation of previously mentioned spherical SnO_2 and hexagonally NiO shaped grains on the CNTs resulted in a smooth and compact microstructure with better defined boundary.

Therefore, increasing the dosage of these nanoparticles, resulted in increasing nucleation rate, which leads to the formation of finer and larger grains (Kartal *et al*., 2016).

However, Plate XVI (g) revealed that an increase in the amount of CNTs led to higher degree of clusters between NiO-SnO_2 nanoparticles and individual CNTs can be seen due to more rapid and uncontrolled nucleation of Ni^{+2}/Sn^{+4} in the composite and their defects structures as the dosage of CNTs is increased (Attarchi and Sadrnezhaad, 2009).

Normally, the introduction of CNTs therefore acted as support material for the uniform and effective dispersion of NiO and SnO_2 nanoparticles. Plate XVI (e) and (f) shows the optimum loading of NiO-CNTs-SnO_2 is in the ratio of (1:1:2) and (1:2:1) respectively. Above or below this optimum mixing ratio, the HRSEM micrographs showed a more aggregated and unevenly dispersed NiO-CNTs-SnO_2 composition, which may affect the bond strength of the coating-substrate interface thereby-making nanocomposite less effective as coating materials (Chen *et al*., 2014). In summary, NiO-CNTs-SnO_2 in the ratio of (1:1:2) is the better nanocomposite for the coating of mild steel due to its crack free granular morphology. Whereas NiO-CNTs-SnO_2 (1:2:1) nanocomposite coatings containing higher amounts of CNTs exhibits a relatively rougher morphology with micro-pores on the coating surface. This can be due to the non-uniform distribution of CNTs agglomeration in the coating matrix above NiO-CNTs-SnO_2 in the ratio of (1:1:2) concentration in the electrolyte. This result shows that, an optimum concentration of CNTs in the electrolyte is required to produce a coating with uniform morphology and high compactness without micro-pores, crevices and chemical heterogeneities which can act as active sites during the corrosion process (Aliyu & Srivastava, 2020).

4.3.8 EDX analysis for NiO-CNTs-SnO_2 nanocomposites

Energy dispersive X-ray spectroscopy (EDX) was used to further confirm the elemental composition of the synthesised NiO-CNTs-SnO_2 nanoparticles. The acquisition of EDX spectrum for quantitative elemental analysis of NiO-CNT-SnO_2 was performed in the specific zone and the result is shown in Figure 4.15. It revealed that the average composition of NiO-CNT-SnO_2 in terms of the atomic weight of constituent elements detected were in the following ratios (O:C:Ni:Sn): (41.68:30.71:36.13:9.82), (24.19:34.75:12.29:21.4), (16.63:17.9:39.71:22.76), (17.5:16.64:11.87:46.02) for

samples in the ratio (1:1:1, 2:1:1, 1:2:1 and 1:1:2) respectively. The elemental mapping also demonstrated that CNTs was compactly decorated with SnO_2 and NiO nanoparticles.

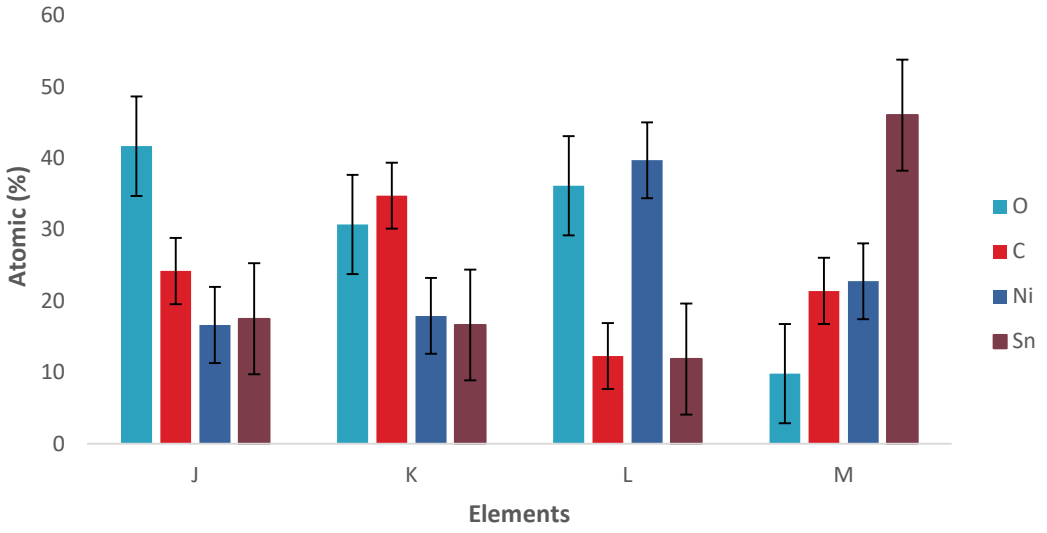

Figure 4.15: EDX Composition for NiO-CNT-SnO_2 Nanocomposites

where J is NiO-CNT-SnO_2 in the ratio (1:1:1), K is NiO-CNT-SnO_2 in the ratio (2:1:1), L is NiO-CNT-SnO_2 in the ratio (1:2:1), and M is NiO-CNT-SnO_2 in the ratio (1:1:2).

This experimental observation is very close to expected composition of NiO-CNTs-SnO_2 when the mixing ratio were varied between (1:1:1, 2:1:1, 1:2:1 and 1:1:2). Since no other element was detected, indicating the high purity of the as-synthesised composite.

Lin *et al*. (2015) also reported EDS similar elemental composition of Ni-doped SnO_2@MWCNTs composites, which consisted of clear peaks associated with C, Sn, Ni, O elements in their microwave assisted synthesis of multi-walled carbon nanotubes decorated with Ni-doped SnO_2 nanocrystal.

4.3.9 HRTEM microstructure of NiO-CNTs-SnO_2

Plate XVII (a) shows a typical HRTEM microstructure of NiO-CNTs-SnO_2

nanocomposite in which the nanoparticles were densely dispersed over the surface of the CNTs. The adherent metallic nanoparticles consisted of hexagonal and quasi-spherical morphologies for NiO and SnO_2 respectively, which were distributed across tubular CNTs surfaces. High-resolution TEM images of the attached nanoparticles in Plate XVII (b) revealed the interplanar spacing of individual particles in the SnO_2 (110) and the NiO (200) directions was approximately 0.3322 nm and 0.2092 nm respectively. These were intercalated between neighbouring planes of CNTs oriented in the (003) direction with a lattice spacing of 0.34 nm suggesting the formation of Van Der Waal and covalent bonds between surfaces of the NiO-CNTs-SnO_2 nanocomposite.

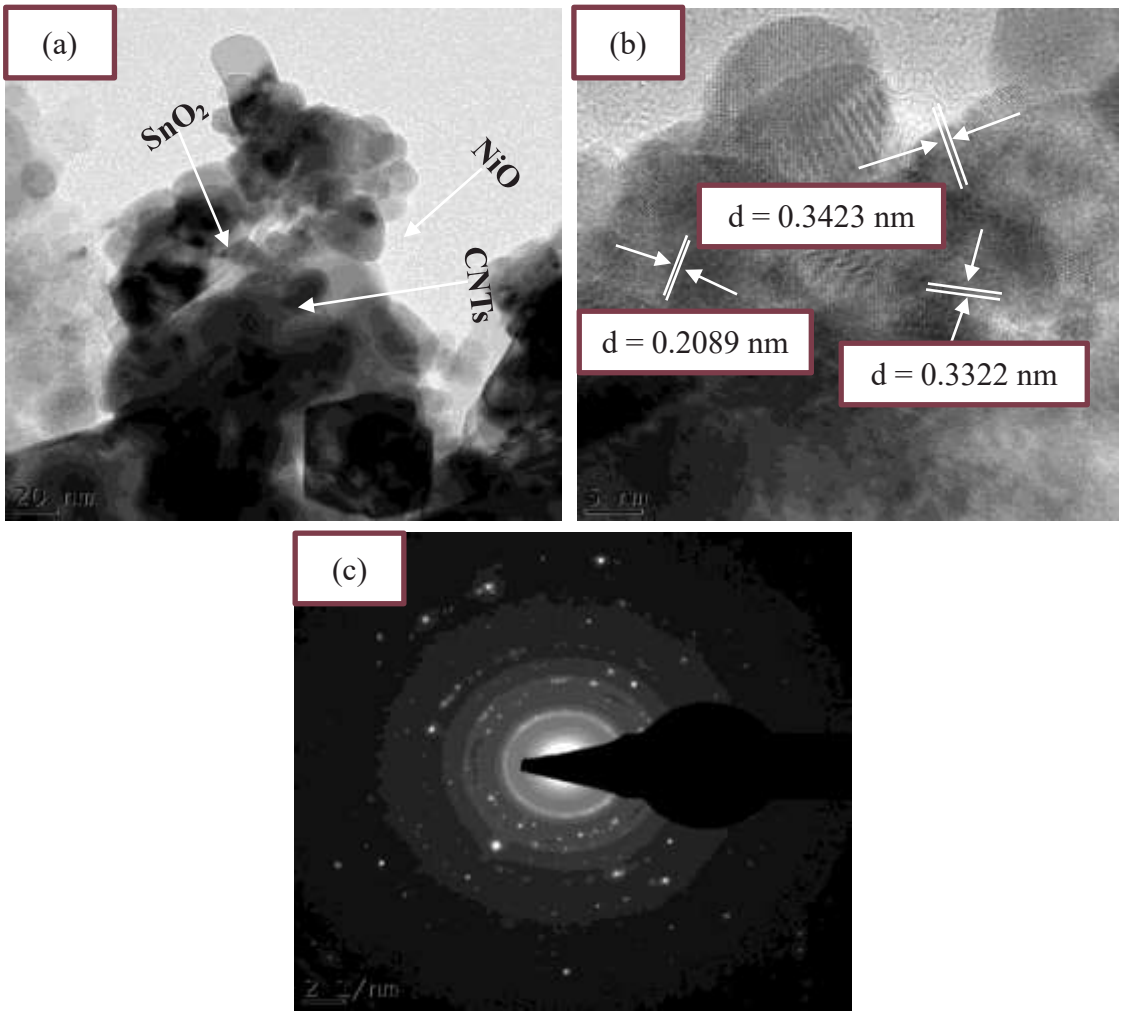

Plate XVII: HRTEM Results at (a) low, (b) high Magnification and (c) SAED Images of NiO-CNTs-SnO_2

The individual lattice spacing for each nanoparticle in the nanocomposite matched well with that of NiO, SnO_2 and CNTs nanoparticles, which were, synthesised separately. Meanwhile, the crystallite sizes of individual particles of NiO and SnO_2 were in the range of 6.8–22.3 nm and 7.4-30 nm, respectively, while the internal diameter of the CNTs ranged between 15-18 nm, this is in good agreement with the values from the Scherrer calculations from XRD analysis in Section 4.3.13.

Plate XVII (c) shows the corresponding (SAED) pattern of the NiO-CNTs-SnO_2 nanocomposite. The diffraction rings and discrete spots may be due to the very fine NiO and SnO_2 particles, and CNTs structures. Therefore, this diffraction pattern can be indexed as mixed NiO, CNTs and SnO_2 nanoparticles.

The result is not only consistent with the XRD results presented Section 4.3.13, but also with the HRTEM microstructures of the individual CNTs, NiO and SnO_2 as represented in Sections 4.2.2, 4.2.4 and 4.2.6 respectively which revealed that the nanocomposites consist of tubular CNTs, hexagonally dimensioned NiO, and irregularly or quasi-spherically shaped SnO_2 nanoparticles.

4.3.10 XRD analysis for NiO, SnO_2 and NiO-SnO_2 nanocomposites

Figure 4.16 displays the XRD patterns for NiO, SnO_2 and NiO-SnO_2 nanocomposites. From the XRD patterns, it was found that the NiO-SnO_2 nanocomposites had diffraction peaks with crystal planes, {(111), (200), (220)} which could be attributed to NiO at 2 theta values of (37.24^o, 43.28^o, 62.88^o) in the face centered cubic phase, which is in agreement with (JCPDS No 47-1049). The NiO/SnO_2 nanocomposites also had SnO_2 peaks such as, {(110), (101), (211)} at 2 theta values of (26.61^o, 33.89^o, 51.78^o), that was in agreement with (JCPDS No 41-1445), and was present in the tetragonal phase. This clearly indicates that the structure of NiO-SnO_2 nanocomposite was made of more

than one distinct phase.

Consequently, the diffraction peaks {(1110 and (200)} of NiO are strengthened gradually with increasing the element molar ratio of Ni to Sn in the sample NiO-SnO_2 (2:1), while crystallographic peaks such as {(110) and (101)} originating from SnO_2 are found to increase in the sample NiO-SnO_2 (1:2).

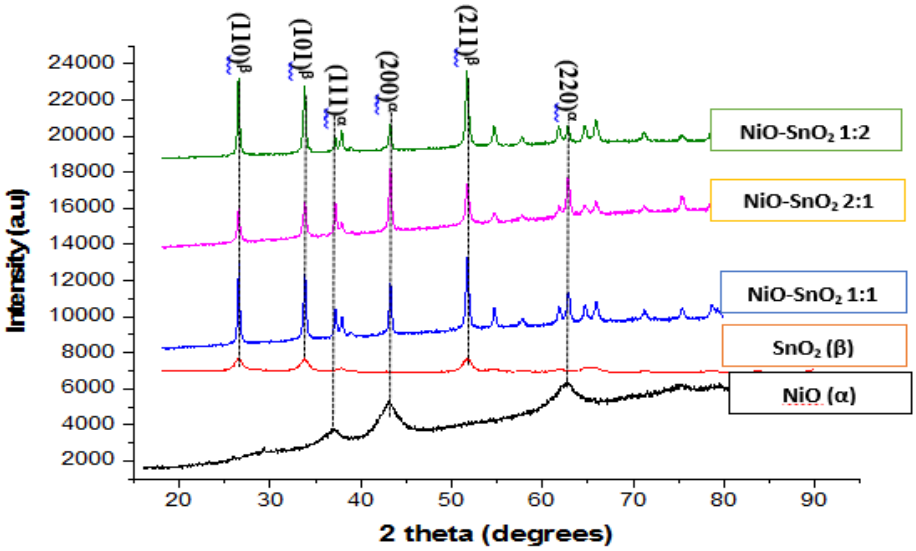

Figure 4.16: XRD Analysis of NiO, SnO_2 and NiO/SnO_2 Nanocomposites

This could be due to the increment in the concentration of nickel or tin salt respectively, as no characteristic peaks for impurity was observed, suggesting that the as-prepared samples are only composed of NiO and SnO_2. The crystallite size, interplanar distance and dislocation density NiO, SnO_2, and NiO-SnO_2 were calculated and presented in Table 4.16

Table 4.16: Calculated Values of FWHM, Crystallite Size, Interplanar Distance, and Dislocation Densities (δ) of NiO, SnO_2 and NiO/SnO_2 Nanocomposites

Samples	Average FWHM (radians)	Interplanar Distance, d, (nm)	Average Crystallite size (nm)	Average (δ) (Lines/nm^2)
Pristine NiO	1.4264	0.2089	6.1458	0.0264
Pristine SnO_2	1.4643	0.3356	6.6975	0.0223

NiO-SnO_2 1:1	0.7786	0.2089, 0.3356	23.1700	0.0019
NiO-SnO_2 2:1	0.3887	0.2089, 0.3356	15.9225	0.0039
NiO- SnO_2 1:2	1.0088	0.2089, 0.3356	26.7500	0.0014

According to Table 4.16, the crystallite size of the NiO-SnO_2 nanocomposite particles was calculated using Debye-Scherrer's formula in Equation 3.6 (Pusawale *et al*., 2011). The dislocation density, (δ), which represents the number of defects in the nanomaterial, was determined using the following Equation 4.15 by Williamson-Smallman (Mahalingm *et al*., 2015):

$$\text{Dislocation density; } \delta = \frac{1}{d^2} \qquad 4.15$$

where d is the crystallite size in (nm).

According to Table 4.16, it can be noticed that the average crystallite size increased from 23.17 nm for NiO-SnO_2 (1:1) to 26.75 nm for NiO-SnO_2 (1:2) as the ratio of SnO_2 nanoparticles in the composite increased. This can be explained based on the differences in ionic radius, for instance the ionic radius of Sn^{+4} (71 pm) is greater than that of Ni^{+2} (69 pm) giving rise to an expansion in the crystal lattice and creation of more oxygen vacancies (Mohamed and Aazam, 2012). Therefore, the attachment of Ni^{+2} into Sn^{+4}created a slight increase in crystallite size. Since, the XRD patterns in Figure 4.16 did not show any significant displacement of the peaks of NiO-SnO_2 nanocomposites as the ratio of NiO to SnO_2 in the nanocomposites was varied, the doping of Ni^{2+} ions into SnO_2 through the substitutional mode was excluded. Therefore, the formed NiO might be attached on the surface of SnO_2 nanoparticles. Furthermore, the crystallite size decreased from 23.17 nm to 15.92 nm as the ratio of NiO-SnO_2 was increased from (1:1 to 2:1) or 16.75 nm when the mixing ratio was of NiO-SnO_2 (1:2). This is attributable to the hindrance in further crystal growth when the concentration of Sn^{+4} or Ni^{+2} is

increased. Mohamed and Aazam (2012) reported a similar trend for NiO-SnO_2 nanocomposites prepared by a simple co-precipitation method, accordingly the crystallite size of the NiO-SnO_2 nanocomposites decreased with the addition of NiO nanoparticles.

In addition, Deepa and Venkatesha (2018), in their findings indicated that the presence of Ni doped SnO_2 nanoparticles synthesised via combustion method inhibited, the crystal growth. This therefore, lead to the reduction of the grain size of the NiO-SnO_2 composite and resulted to a compact structured surface and less number of surface pores.

On the other hand, the dislocation density was observed to decrease from (0.0019 Lines / nm^2 to 0.0014 Lines / nm^2) respectively, and this indicated the removal of defects with increasing addition of SnO_2 nanoparticles. Notably, Sakhare *et al*. (2013) explained that the increase in crystalline size and the reduction of amorphous phase are correlated with the quantum confinement when nanomaterials were built from the bottom up or top down approaches.

4.3.11 XRD analysis of NiO, CNTs and NiO-CNTs nanocomposites

As illustrated in Figure 4.17, the nanocomposites NiO-CNTs in the ratio of 1:1, 2:1 and 1:2 consisted of the diffraction peaks originally from NiO and CNTs nanomaterials.

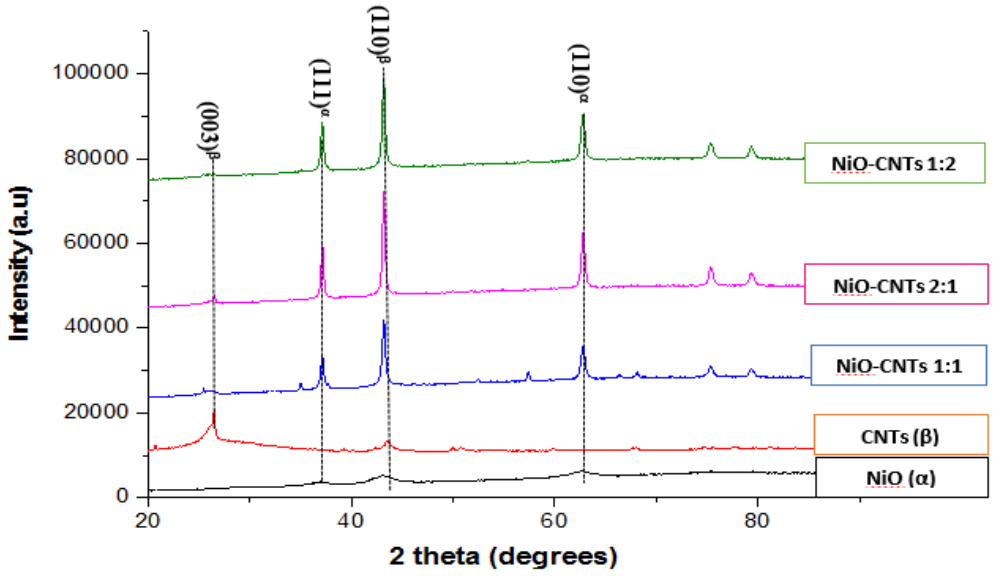

Figure 4.17: XRD Graph for NiO, CNTs and NiO-CNTs Nanocomposite

Diffraction Peaks with crystal planes, (003) and (101), at 2 theta angles (26.60^{o} and 43.45^{o}) originated from CNTs which was in agreement with the (JCPDS no 026-1049). While, distinct peaks from NiO crystallographic orientations with, (111) and (220) miller indices at 2 theta values of (37.25^{o} and 62.88^{o}), is also in agreement with (JCPDS no 047-1049). In terms of the intensity of the respective diffractive peaks, as the ratio of NiO:CNTs in the nanocomposite was varied from 1:1, to 1:2 and 2:1, the peaks belonging to NiO were more obvious than that of CNTs. While, the CNTs peak decreased in intensity. This could the due to the fact that the atomic radii of C^{+4} (0.16 Å) is smaller compared to that of Ni^{+2} (0.69 Å), therefore the C^{+4} ions could easily diffuse into Ni^{+2} ions resulting to NiO been coated on the CNT surface obstructed its diffraction, and responsible for the decreased in intensity of the CNTs diffraction peak. This was in accordance to previous studies carried out by Huang *et al*. (2015) who prepared NiO-CNTs nanocomposites by co-precipitation method. The crystallite size, interplanar spacing and dislocation density of NiO and NiO-CNTs are presented in

Table 4.17.

Table 4.17: Calculated Value of FWHM, Crystallite Size, Interplanar Distance and Dislocation Densities (δ) of NiO, CNTs and NiO-CNTs Nanocomposites

Samples	Average FWHM (radians)	Interplanar Distance, d, (nm)	Average Crystallite Size (nm)	Average (δ) (Lines/nm^2)
Pristine NiO	1.4264	0.2089	6.1458	0.0264
Purified CNTs	1.1063	0.3423	7.7143	0.0168
NiO-CNTs 1:1	0.7786	0.2089, 03423	14.9675	0.0046
NiO-CNTs 2:1	0.3887	0.2089, 0.3423	23.9275	0.0017
NiO-CNTs 1:2	1.0088	0.2089, 0.3423	15.9650	0.0039

According to crystallite size using the Dybe-Scherrer's equation, it can be noticed that as the ratio of NiO:CNTs was varied from 1:1 to 1:2 (increase in CNTs), the crystallite size was found to increase from 14.98 nm to 15.97 nm. This could be due to the growth of NiO nanoparticles on CNTs matrix as confirmed by HRSEM micrographs presented in Plate XV (c-e), which lead to an enlargement in particle size. Hence, an increase in the dosage of CNTs would give rise to a proportionate increase in the number of defects and functional groups, for interaction with Ni^{+2} ions. Consequently, upon diffusion this would result to expansion in the diameter of the whole NiO-CNTs composite. Thus, upon increasing the ratio of NiO in the NiO-CNTs, nanocomposite to 2:1, the crystal size increased to 23.9275 nm.

This is because of more NiO filling the defects within the CNTs framework. This may have also be responsible for the decrease in dislocation density to 0.0017 (lines/nm^2) compared to others. However, since theses defects were small and easily removed by post annealing after coating, this parameter cannot be independently used to consider the optimum nanomaterial from XRD data. Therefore, in tandem with the HRSEM micrographs in Plate XV (c), NiO-CNTs (1:1) with a crystallite size of 14.9675 nm and

dislocation density of 0.0046 Lines/nm^2 was considered the optimum-mixing ratio for the NiO-CNTs composite, which would offer suitable surface protection against corrosion in steel. Shi *et al.* (2006) had reported that Ni–Co matrix in the composite coating had an average grain size of 17 nm that was less than 42 nm, for Ni–Co-CNTs composite. The authors attributed this phenomenon to the competition between the nucleation and crystal growth. The carbon nanotubes provide more nucleation sites and hence retard the crystal growth. Subsequently, the corresponding Ni–Co matrix in the composite coating has a smaller crystal size. The discrepancy between their findings and results from this study may be due to the variation in synthesis method for preparing the composites as well as the heat treatment employed upon aging.

4.3.12 XRD analysis of SnO_2, CNTs and SnO_2-CNTs nanocomposites

Figure 4.18 shows the XRD patterns of pristine SnO_2 (α), purified CNTs (β), and SnO_2-CNTs in ratio (1:1, 2:1 and 1:2). The pristine CNTs showed two diffraction peaks at 2θ values of 26.60^o and 43.45^o with corresponding crystal planes of (003) and (101), typical of graphitic carbon and is in agreement with (JCPDS No 26-1049).

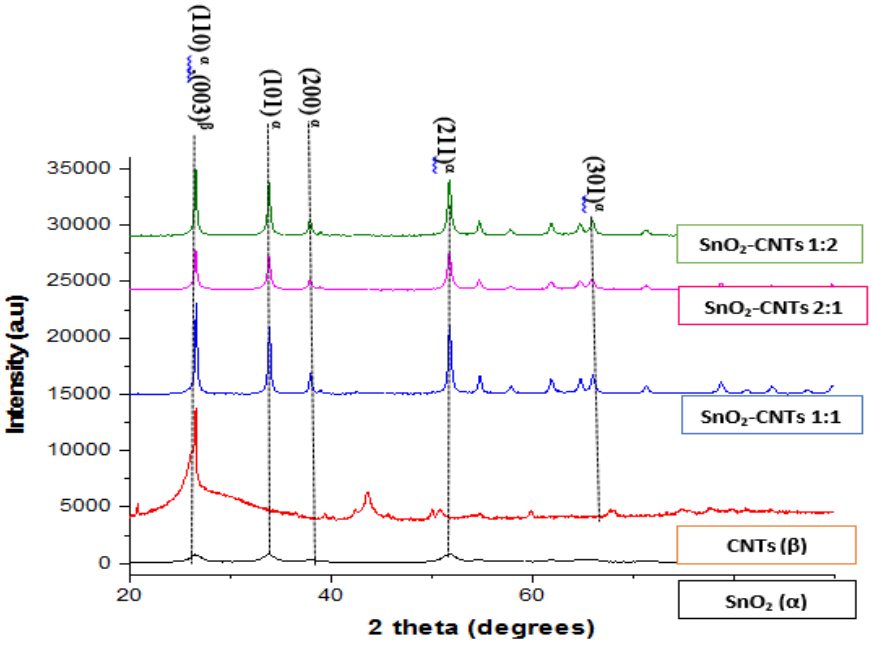

Figure 4.18: XRD Graph for SnO_2, CNTs and SnO_2-CNTs Nanocomposite

The diffraction peaks were observed for (SnO_2-CNTs) supported by HRSEM results displayed in Plate XVI (c-d) revealed growth of SnO_2 nanoparticles on CNTs thus, forming SnO_2-CNTs nanocomposites. The average crystallite sizes (d), interplanar distance, and dislocation densities of of SnO_2, CNTs and SnO_2-CNTs are presented in Table 4.18. The mean crystallite size of SnO_2-CNTs nanocomposite ranged from 20.30 nm - 26.95 nm as the ratio of SnO_2:CNTs was varied between 1:1, 2:1 and 1:2. The increment in crystallite size could be ascribed to the nucleation process that occurred within the CNTs network, as the amount of SnO_2 incorporated in the nanocomposite was increased (Yuliarto *et al*., 2019).

Table 4.18: Calculated Value of FWHM, Crystallite Size, Interplanar Distance and Dislocation Densities (δ) of SnO_2, CNTs and SnO_2-CNTs Nanocomposites

Samples	Average FWHM (radians)	Interplanar Distance, d, (nm)	Average Crystallite size (d) (nm)	Average Dislocation Density (δ) (Lines/nm^2)
Pristine SnO_2	1.4643	0.3356	6.6975	0.0223
Purified CNTs	1.1063	0.3423	7.7143	0.0168

SnO_2-CNTs 1:1	0.3499	0.3356, 0.3423	26.9533	0.0024
SnO_2-CNTs 2:1	0.4821	0.3356, 0.3423	20.3038	0.0024
SnO_2-CNTs 1:2	0.3754	0.3356, 0.3423	25.5666	0.0015

These agreed with the value estimated from the HRSEM micrographs. The average dislocation density as presented in Table 4.18 decreased from pristine SnO_2 (0.0223 Lines/nm^2) to SnO_2-CNTs 1:2 (0.0015 Lines/nm^2). The dislocation density was least for the optimally selected SnO_2-CNTs (1:2) was the least with a value of 0.0015 Lines/nm^2, which and indicate existence of least stress, cracks and defects in their crystal lattice as compared to the other SnO_2-CNTs nanocomposites. It is worth mentioning, that the dislocation density in this study was small and could be removed by heat treatment at a high temperature, where the thermal energy will allow the defects to mutually cancel each other or move out of the crystal through the surfaces (Rajput, 2015).

During the course of this study SnO_2-CNTs nanocomposite was heated to 900°C for 90 min after coating on the steel substrate, this was done to improve the adhesion and reduce the porosity of the coated surface (Härkönen *et al*., 2013). In summary, XRD data supports HRSEM analysis that SnO_2-CNTs in the mixing ratio of (1:2) had the potentials to provide superior mechanical and chemical properties that would offer better anti-wear, and adhesion strength between the interface of the coatings and metal substrate. This is expected to increase corrosion resistance as compared to pristine SnO_2. In tandem to this are reports by Feng *et al*. (2010); Phil *et al*. (2015) and Yuliarto *et al*. (2019) who independently synthesised SnO_2-CNTs via chemical synthesis and found that diffraction peaks such as (002) and (101) originated from the CNTs while (110), (101) and (211) were clearly observed from SnO_2 origin. The author attributed the increase in the grain size of the composite as the concentration of SnO_2 increased, to the

broadened widths of the SnO_2-CNTs diffraction peaks.

4.3.13 XRD analysis of NiO, SnO_2, CNTs and NiO- CNTs-SnO_2 nanocomposite

The mineralogical phases of the NiO-CNTs-SnO_2 nanocomposites was analysed using X-ray diffraction (XRD) spectra. Figure 4.19 shows the XRD patterns of NiO (α), SnO_2 (β), CNTs (γ), and NiO-CNTs-SnO_2 samples synthesised at different mixing ratio, namely; (1:1:1, 2:1:1, 1:2:1, 1:1:2) respectively.

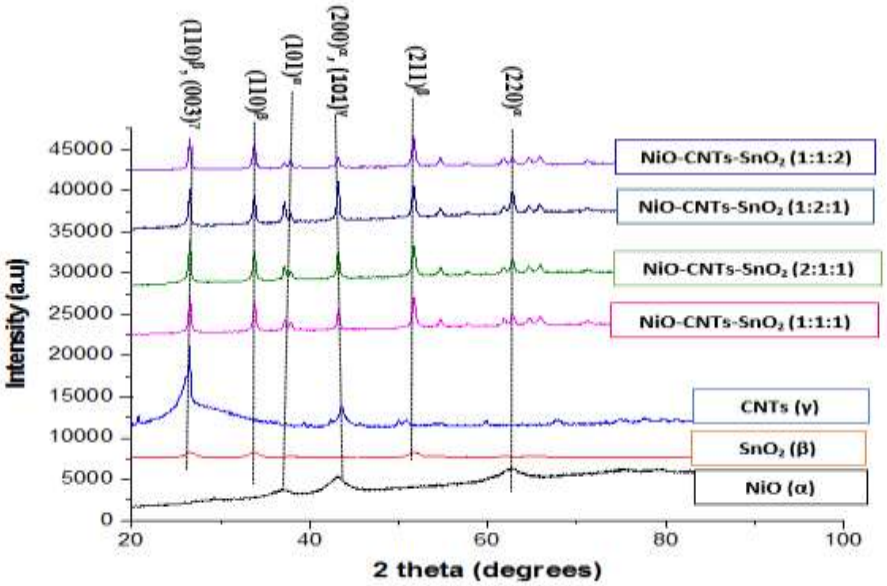

Figure 4.19: XRD Graph for NiO, SnO_2, CNTs and NiO-CNTs-SnO_2 Nanocomposite

Remarkably, all diffraction peaks that were close to the tetragonal structure of SnO_2 (JCPDS, No. 41-1445), were observed at (2θ) angles of 26.61°, 33.89° and 51.78° corresponding to (110), (101) and (211) planes, respectively. NiO crystallographic peaks corresponding to (111), (200) and (220) planes were detected at 37.23°, 43.28° and 62.88°, which is in agreement with (JCPDS, No. 47-1049). There was also the diffraction peak of carbon with miller indices (003) which was persistent from the original CNTs and reinforced with the plane (110) in the SnO_2 to give a remarkable peak in the composite after doping. Overall, the diffraction peaks for the NiO-CNTs-

SnO_2 composites were observed to decrease in their respective full width at half maximum (FWHM) broadness in the different nanocomposite ratios in the following order (1:1:1 < 2:1:1 < 1:2:1 < 1:1:2). The crystallite size of the NiO-CNTs-SnO_2 nanocomposite particles was calculated using Debye-Scherrer's formula, while the dislocation density, which represents the number of defects in the composite, was determined using Williamson-Smallman equation and interplanar distance (d) are presented in Table 4.19.

Accordingly, the average crystallite size was highest for NiO-CNTs-SnO_2 (1:1:1) (22.17 nm), and decreased to (20.58, nm) for NiO-CNTs-SnO_2 (2:1:1), however it increased to (21.22 nm) and (21.98 nm) for NiO-CNTs-SnO_2 (1:2:1) and NiO-CNTs-SnO_2 (1:1:2) respectively. This increase in crystallite size as the amount of the incorporated metallic particle was increased could be as a result of the atomic spaces occupied by these metallic particles in the CNTs matrix leading to a slight expansion in the interstitial envelopes.

This was highest for Sn^{+4} (71 pm) with an ionic radius greater than Ni^{+2} (69 pm). Although crystallite size was not the only prime parameter by which, the optimum nanocomposite for this study was selected, because particle dispersion and morphology superseded crystallite size. According to a study by Ghosh *et al*. (2006) nanocrystalline Ni–Cu alloy (35.8 wt.% Cu) coating with a 12.7-nm grain size had lower corrosion current density in 3 wt.% NaCl solution than the nanocrystalline Ni–Cu alloy (26.0 wt.% Cu) coating with a grain size of 6.6 nm.

Table 4.19: Calculated Value of FWHM, Crystallite Size and Dislocation Densities (δ) of NiO, SnO_2, CNTs and NiO-CNTs-SnO_2 Nanocomposites

Samples	Average FWHM (radians)	Interplanar Distance, d, (nm)	Average Crystallite size (d) (nm)	Average Dislocation density (δ) (Lines/nm^2)
Pristine NiO	1.4264	0.2089	6.1458	0.0264
Pristine SnO_2	1.4643	0.3356	6.6975	0.0223
Purified CNTs	1.1063	0.3423	7.7143	0.0168
NiO-CNTs-SnO_2 1:1:1	0.4169	0.2089, 0.3356, 0.3423	22.0160	0.0021
NiO-CNTs-SnO_2 2:1:1	0.4513	0.2089, 0.3356, 0.3423	20.5864	0.0024
NiO-CNTs-SnO_2 1:2:1	0.4413	0.2089, 0.3356, 0.3423	21.2221	0.0022
NiO-CNTs-SnO_2 1:1:2	0.4210	0.2089, 0.3356, 0.3423	21.9848	0.0021

This indicated that composition of the nanocoating can dominate the effect of lower grain size. For Ni–W alloy, the corrosion resistance of the nanocoating was affected by the acidity of the tested media more than the grain size of that nanocoating (Abdeen *et al*., 2019). Therefore, the NiO-CNTs-SnO_2 (1:2:1) and NiO-CNTs-SnO_2 (1:1:2) with crystallite sizes of (21.22 nm) and (21.98 nm) were considered optimum primarily because of their composition as revealed by HRSEM micrographs in Plate XVII (e) and (f). The exceptional morphology exhibited by the two composites have been associated with diffusion resistance, prevention of the transportation of charges and increased surface area which may passivate the surfaces of the coated steel (Patil and Radhakrishnan, 2006; Radhakrishnan *et al*., 2009).

Concurrently, the dislocation density was observed to decrease from (0.0264-0.0022

Lines/nm^2), with NiO-CNTs-SnO_2 of mixing ratio (1:1:2) which had the least value of 0.0021 Lines/nm^2, an evidence of the least defects in its crystal matrix (Zainudin *et al*., 2018). However, these range of values for dislocation density (δ) were all below 10^8 Lines/nm^2 and considered to cause negligible defects in the crystal lattice since heat treatment was capable of removing such kinds of small defects or cracks (Rajput, 2015).

4.3.14 X-ray photoelectron spectroscopy (XPS) analysis of the as-synthesised nanomaterials

XPS analysis of the as-synthesised nanomaterials were examined to provide detailed information about the composition and surface electronic structure of the as-synthesised nanomaterials. Briefly, the XPS survey spectrum of NiO-CNTs-SnO_2 and bare NiO, and SnO_2 were carried out. High Resolution XPS survey scans of C (1s) for NiO, SnO_2, CNTs and NiO-CNTS-SnO_2 are presented in Figure 4.20, this can be categorized into two sharp peaks located at 284.5 for CNTs assigned to C-C/C=C or (sp^2 C) bonds, 284.9 for NiO-CNTs-SnO_2 assigned to C-O (Jing *et al*., 2015). The presence of oxygenated carbon in the composite may indicate that carbon from the CNTs formed bonds with either NiO or SnO_2 after purification.

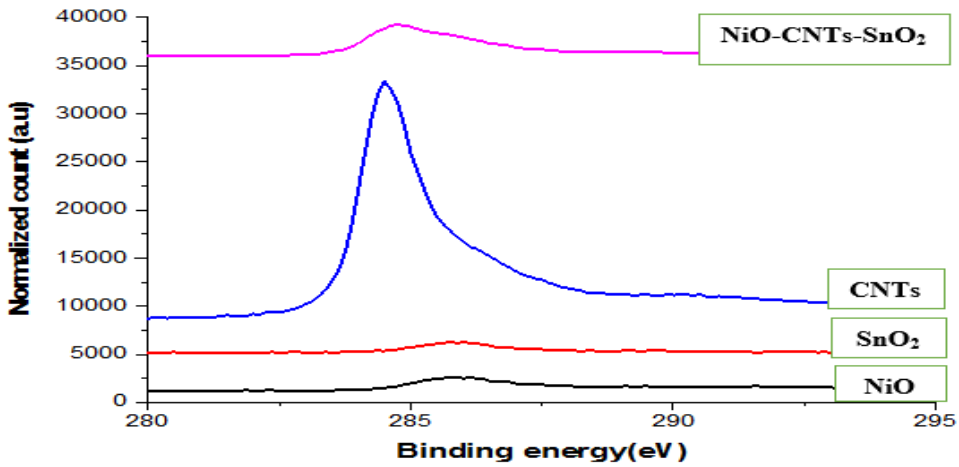

Figure 4.20: High Resolution Scan of C (1s) Envelopes in NiO, CNTs, SnO_2 and NiO-CNTs-SnO_2

While the low intensity peaks at 285.9 for NiO and 286.1 eV for SnO_2 could be

attributed to carbon from the plant extract and adventitious carbon based contaminant adsorbed on the surfaces of the samples (Zhang *et al*., 2003).

Figure 4.21 gives the XPS spectra of O 1s core level for the samples NiO, SnO_2 and NiO-CNTs-SnO_2. For O 1 s NiO spectrum, two peaks were obtained by deconvolution. The peak at 529.5 eV agrees well with the O^{2-} atoms in the Ni-O bonding structure (Huang *et al*., 2015; Elizabeth *et al*., 2017). The peaks of O 1s at 532.35 eV can be attributed to oxygen atoms chemically bonded in O-C=O (Chen *et al*., 2015). This also corresponds to the lattice oxygen and the deficient oxygen present in the NiO matrix (Xu *et al*., 2012).

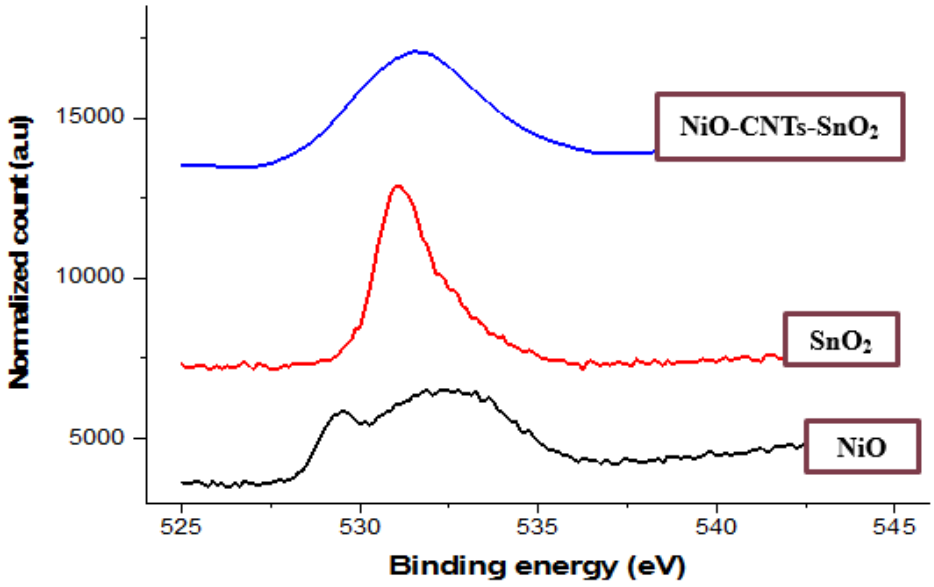

Figure 4.21: High Resolution Scan of O (1s) Envelopes in NiO, SnO_2 and NiO-CNTs-SnO_2

While the single peak in the O 1s spectrum of SnO_2 with binding energy of 530.9 eV is attributed to the lattice oxygen bonding to Sn^{4+}. This suggests that the oxidation number of tin in the composite is (+4). Accordingly, the O 1s spectrum of NiO-CNTs-SnO_2 showed an intense peak corresponding to Ni-O-Sn bond with binding energy 529.3 eV at the hetero-junction. However, the characteristic peaks of the nanocomposites exhibit

some shift compared to the bare NiO and the bare SnO_2. This could be because different chemical environments of O in the composite oxides can lead to the characteristic peak shift (Xu *et al*., 2012).

Figure 4.22 shows the Ni 2p High-Resolution XPS spectra of the bare NiO and the NiO-CNTs-SnO_2 nanocomposites.

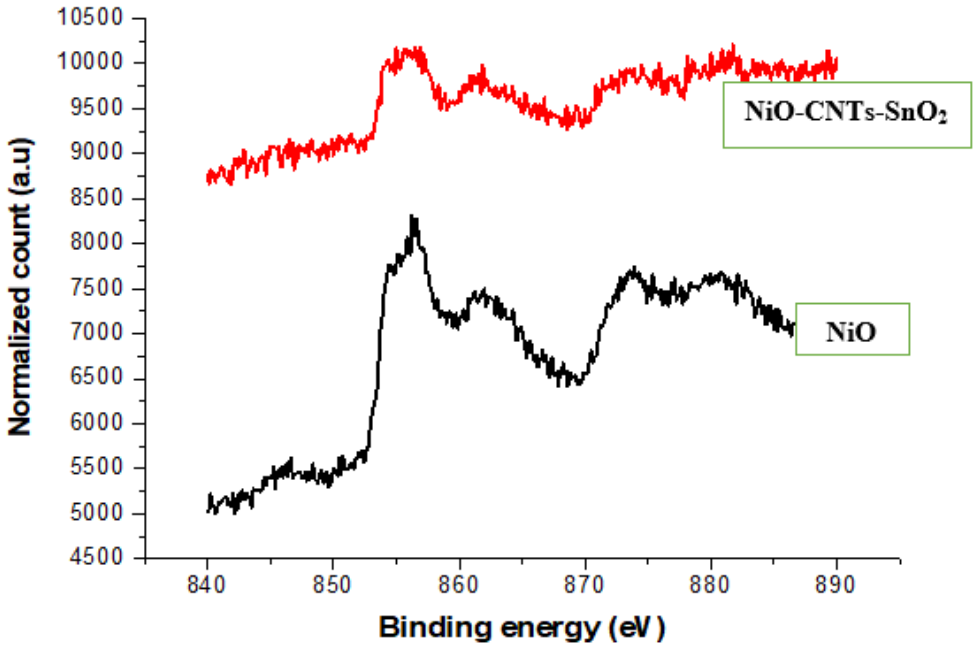

Figure 4.22: High Resolution Scan of Ni (2p) Envelopes in NiO and NiO-CNTs-SnO_2

As observed, the Ni (2p) spectrum of the bare NiO can be deconvoluted into four peaks. In the Ni (2p) XPS spectrum, two obvious peaks with binding energies at 855.8 and 873.7 eV are attributed to Ni (2p3/2) and Ni (2p1/2), respectively, with a spin-energy separation of 17.8 eV, which is characteristic of Ni^{2+} of NiO and in good agreement with the literature (Huang *et al*., 2015). In addition, the peaks at 861.9 and 879.8 eV represent the satellite peaks of Ni (2p3/2) and Ni (2p1/2), respectively (Yu *et al*., 2016). In a previous research by Soriano *et al*. (2007), the high peak at 855.8 eV was attributed

to NiO_5 or Ni^{2+} in pyramidal symmetry according to their experimental results and theoretical calculation. Accordingly, the Ni (2p) spectrum of the NiO-CNTs-SnO_2 nanocomposites can also be deconvoluted into four peaks with two obvious peaks at (855.1 and 873.70 eV) corresponding to the Ni (2p3/2) peaks and the Ni (2p1/2) peaks respectively. While the other two satellite diffractions at (860.98 and 878.91 eV) corresponds to Ni (2p3/2) peaks and the Ni (2p1/2) peaks separately. However, compared with the Ni (2p) peaks of the bare NiO, the Ni (2p) peaks of the nanocomposites shift slightly toward the lower binding energy. The binding energy shifts in the XPS spectra (Ni (2p) and Sn (3d)) of the NiO-CNTs-SnO_2 could be attributed to the different electronegativities of metal ions and the strong interaction (electron transfer) between the NiO and the SnO_2 (Zhang *et al*., 2016).

Subsequently, the Sn 3d high-resolution XPS spectra of the bare SnO_2 and the NiO-CNTs-SnO_2 nanocomposites are presented in Figure 4.23. For the bare SnO_2, spin-orbit components ((3d3/2) and (3d5/2)) of the Sn (3d) peak were both observed at approximately 495.2 and 486.7 eV, corresponding to Sn^{4+} in a tetragonal rutile structure (Wang *et al*., 2010). The peak centered at 486.2 eV corresponds to Sn (3d5/2), while the other located at 494.6 eV is assigned to Sn (3d3/2).

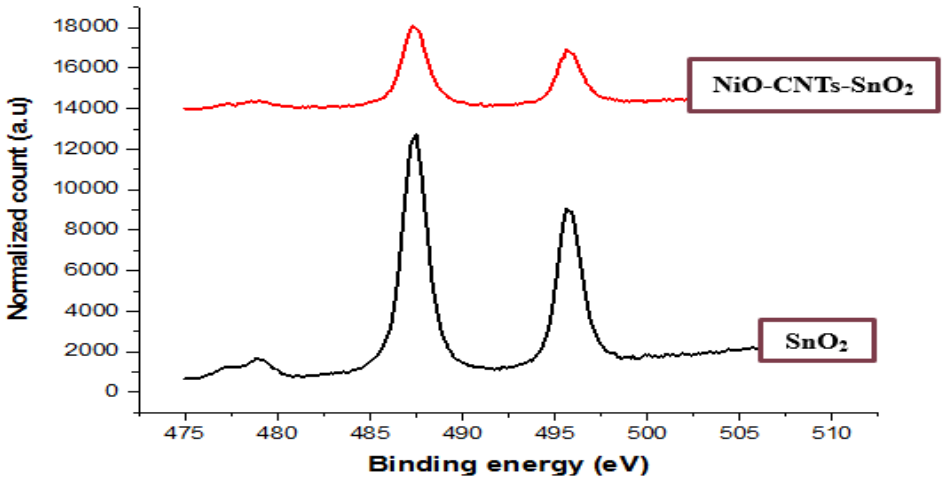

Figure 4.23: High Resolution Scan of Sn (3d) Envelopes in SnO_2 and NiO-CNTs-SnO_2

However, the binding energy of Sn (3d) for the nanocomposites NiO-CNTs-SnO_2 shifts slightly to the higher binding energy compared with the Sn (3d) peaks of the bare SnO_2. Generally, it is believed that the Ni-O-Sn bonds could be formed at the interface between the NiO and the SnO_2 (Zhang *et al*., 2016).

The formation of the Ni-O-Sn interface bonds in the NiO-SnO_2 nanocomposites has been confirmed by the O (1s) spectra as shown in Figure. 4.21. Herein, through combining with the hetero-interface observed in the HRTEM images in Plate XVII, the Ni-O-Sn interface bonds at the hetero-interface. This further suggests the significant chemical combination between the NiO and the SnO_2, in which the electron transfer is responsible for the binding energy shifts of Ni (2p) and Sn (3d), implying the formation of p-n heterojunction in the NiO-SnO_2 nanocomposites.

XPS survey scan were also analyzed to study the composition of each of the nanomaterial. Figure 4.24 presents the survey scan of purified CNTs.

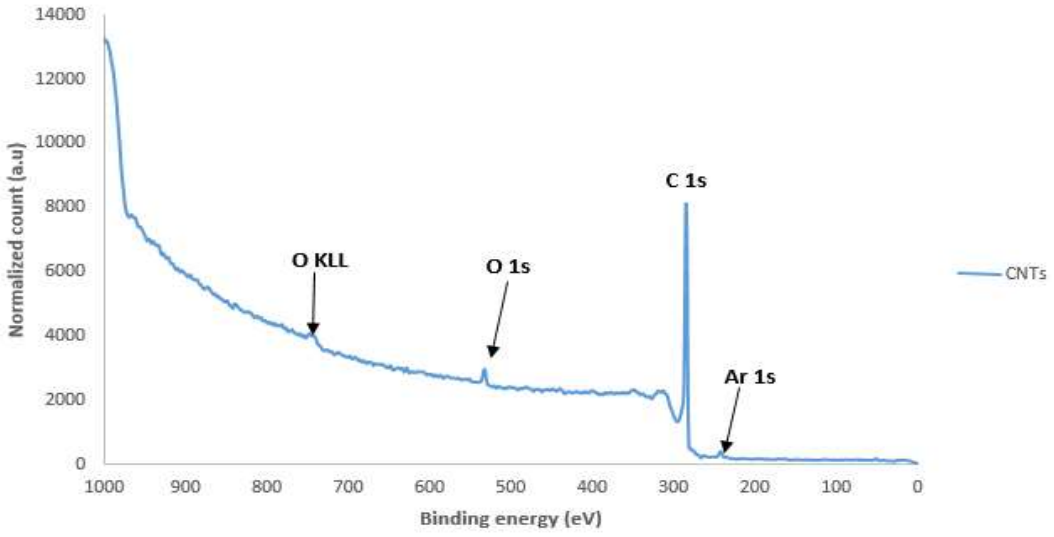

Figure 4.24: XPS Survey of Scan of CNTs

As expected, the sputtered sample had C, with small concentration of O, N, and Ar. The presence of C (1s) was identified at a binding energy of 284.5 eV, while O (1s), N (1s) and Ar (2 p) were identified at 535.5, 456.5 and 245.8 eV respectively. The presence of oxygen and nitrogen emanated from the acid used during the purification process, enhancing the formation of new functional groups such as O (1s) of oxidized oxygen. Furthermore, supplementary XPS survey spectra of NiO, SnO_2 and NiO-CNTs-SnO_2 Figures (4.25-4.27) have been included in this report, which clearly demonstrate that the samples mainly contain the elements species: carbon (C), oxygen (O) and Ni. For NiO, Sn C and O for SnO_2 and all of them combined for the composite NiO-CNTs-SnO_2 consistent with EDX results in Section 4.3.8.

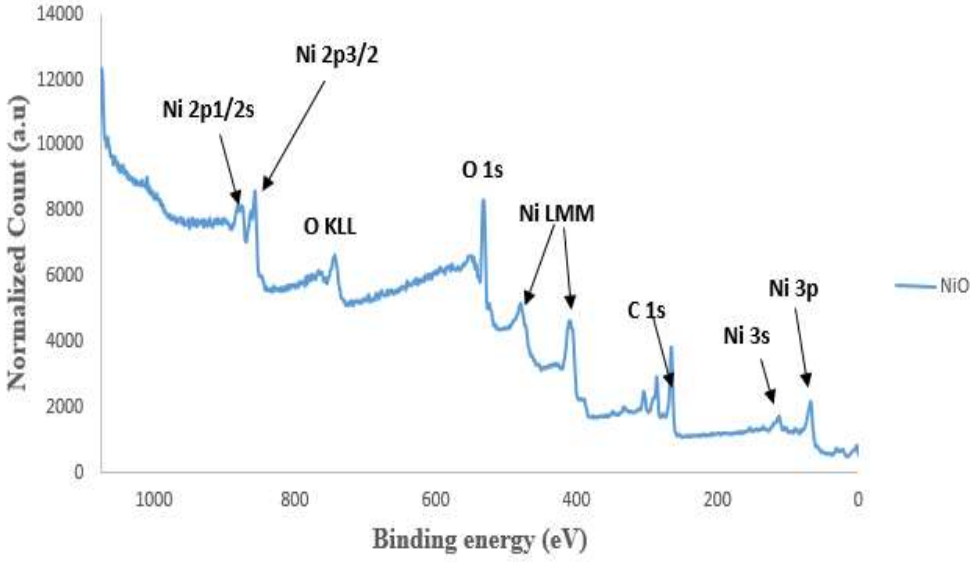

Figure 4.25: XPS Survey Scan of NiO

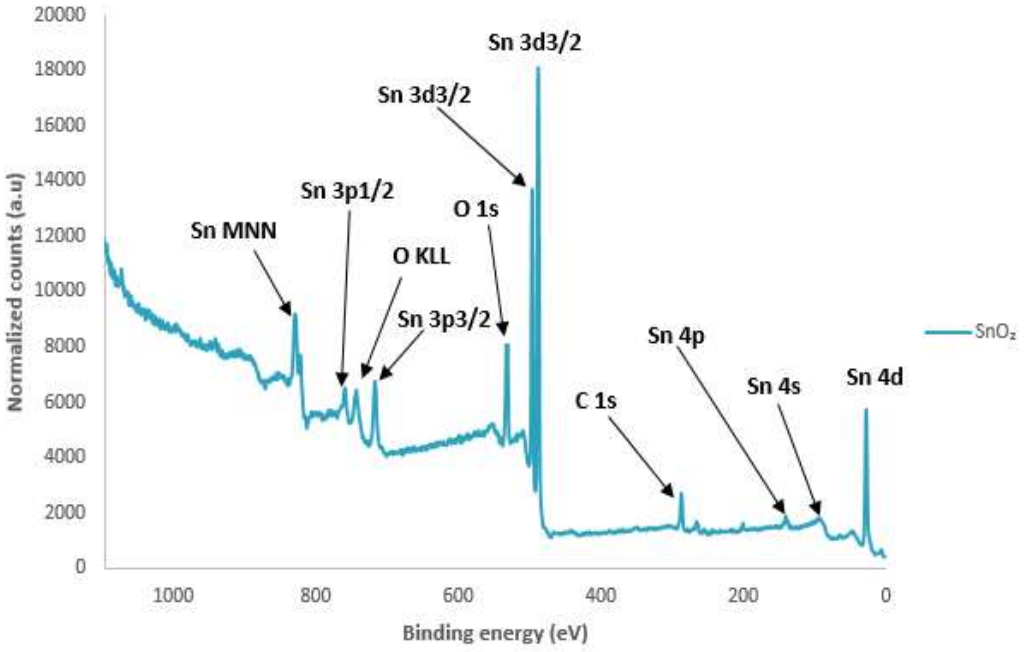

Figure 4.26: XPS Survey Scan of SnO_2

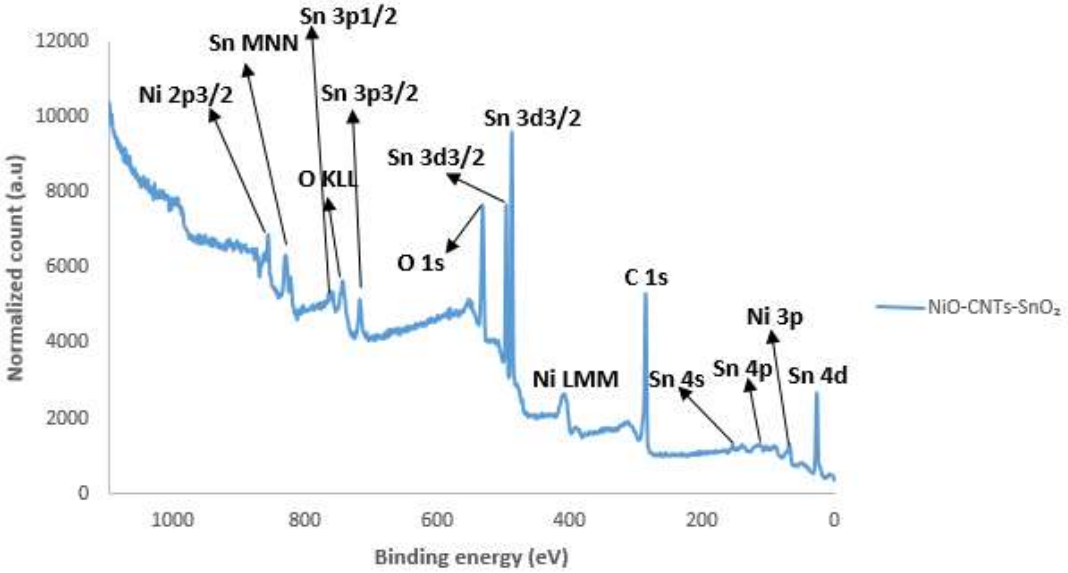

Figure 4.27: XPS Overview of NiO-CNT-SnO_2 Spectrum

4.4 Soil Analysis

The physiochemical properties of the soil environment were carried out in Section 3.7. Results from the analysis are presented in Table 4.20. The soil sample for all the corrosion assessment tests were carried out at a depth of 2 m. From Table 4.20, the textual class analysis reveals that the soil is evidently sandy loamy consisting of (87g/kg, 129 g/kg, and 784 g/kg), clay, silt and sand particles respectively.

Table 4.20: Physiochemical Parameters of the Soil Site Samples

Depth (m)	pH	R (Ωcm)	Cl^- (mg/kg)	SO_4^{2-} (mg/kg)	MC (%)	Clay (g/kg)	Silt (g/kg)	Sand (g/Kg)	Textural class
0.5	6.48	704	315.5	786	5.92	44	87	869	Loamy sand
1.0	6.72	468	441.5	629	13.39	67	115	819	Sandy loam
2.0	6.67	504	292.5	845	13.97	87	129	784	Sandy loam

The dissolved ions (chloride and sulphate) ranged between 292.5-441.5 mg/kg and 629-845 mg/kg respectively, chloride and sulphate ions are generally harmful because they participate directly in the reactions of anodic dissolution of metals (Li *et al*., 2007). While the moisture content varied from 5.92 to 13.79 % from depth 0.5 to 2.0 correspondingly this parameter can also influence corrosion in soils because liquid water represents the electrolyte for electrochemical corrosion reaction. The soil resistivity is a critical factor to determine its corrosivity.

Nevertheless, depending on moisture content, temperature and chemical content the soil resistivity value can vary within wide ranges with usual values, from 10 to 1000 (Ωcm), while exceptional values ranges from 1 to 10000 (Ωcm). The resistivity in this study was found to be between ranged between 468 to 704 Ωm, with values at 504 Ωcm indicating that the soil's resistivity at 2 m was in the usual range 10 to 1000 (Ωcm). In

addition, pH is also considered to be a key factor in corrosion process (Veleva, 2005). Some models provide an approximate relationship between the pH of the water extract of the soil and its corrosivity, showing that pH between 4.6-7.4 indicates highly corrosive soils as in the case of this study, the pH was in the range of 6.48 to 6.72. With the pH at depth 2 m given as 6.67, it could be concluded that the soil is highly corrosive to metals. However, both the resistivity and pH, have been combined to determine more appropriately the corrosivity of soils. According to the classification by EN 12501-2 (2003**)** when the pH is between 6.8-9.0 and the resistivity (< 1000 Ωcm) the soil is categorized s being highly corrosive. This therefore revealed that the soil samples for this study were highly corrosive considering these major physicochemical characteristics as presented in Table 4.20. Therefore, the classification of the soil in this study as highly corrosive would result to corrosion of the surfaces of bare steel when they were buried in the soil. However, the presence of the coatings is expected to provide a barrier between the soil environment and steel surface, which also passivates the metal surface and lessens the flow of water molecules, chloride and sulphate ions from the soil electrolyte. This would invariably result to the coatings protecting the steel surface from local corrosion, and providing a protection efficiency that is at least > 50% as compared to the bare metal.

4.5 Corrosion Test

The results of corrosion tests for weight loss measurement, Potentiodynamic polarization and electrochemical impedance spectroscopy were obtained and the results are presented in Tables 4.21 to 4.23 and Figures 4.28 to 4.32.

4.5.1 Weight loss

Corrosion of buried AISI 1020 steel involved chemical or electrochemical reactions, which formed corrosion products. The formation of this compound on the surface of

steel resulted in deterioration of its properties and consequently losing weight. In view of this, the Table 4.21 represent the different Corrosion Parameters (CP) obtained from Weight loss measurement; which include Weight Loss (WL) with Corrosion Penetration Rate (CPR) and Coating Efficiency (CE %) at different average temperatures within 3 to 12 months' interval.

Table 4.21: Weight Loss Corrosion Parameters

Experimental Samples	**Exposure Time (Month)**				**CPR (mpy)**	**CE (%)**
	3 (27.7 ^{o}C)	**6 (27.5 ^{o}C)**	**9 (26.6 ^{o}C)**	**12 (26.5 ^{o}C)**		
As-Received	2.57	2.96	3.12	3.65	0.0029	
NiO	0.59	0.78	1.01	1.32	0.0008	72.56
SnO_2	0.52	0.72	0.90	1.14	0.0007	75.59
CNTs	0.42	0.61	0.85	1.01	0.0006	79.01
NiO-SnO_2 (1:2)	0.38	0.51	0.71	1.01	0.0005	81.25
NiO-CNTs (1:1)	0.26	0.44	0.76	0.99	0.0005	83.62
SnO_2-CNTs (1:2)	0.18	0.34	0.62	0.97	0.0004	86.71
NiO-CNTs-SnO_2 (1:2:1)	0.10	0.24	0.46	0.73	0.0003	90.78
NiO-CNTs-SnO_2 (1:1:2)	0.15	0.18	0.22	0.31	0.0002	93.48

It could be observed from the Table 4.21 that, the values of weight loss decrease significantly for nanocomposite coated samples compared to as-received sample. The weight loss was also found moderate with the average temperatures of the soil in each period considered for the experiment. As the average temperature was found to be approximately constant.

The values of corrosion rate and coating efficiency listed in Table 4.21 at different period and average temperatures, showed the studied nanocomposite coated samples act as good protection for corrosion and the corrosion penetration rate result obtained decreased with applied hybrid nanocomposite coating such as NiO-CNTs-SnO_2 (1:2:1) and NiO-CNTs-SnO_2 (1:1:2) and significantly has little effect with average temperature.

The corrosion rate value obtained was used to determine the coating efficiency of the

studied nanocomposite coating in corrosion process. It is much cleared from the Table 4.21 that the coating efficiency increases with increase in nanocomposite coated samples and exhibit little effect with average temperatures. The decrease in coating efficiency was as a result of desolution of some weaken nanocomposite coating as lower value is obtained as 72.56% for NiO compared to the coating efficiency obtained for NiO-CNTs-SnO_2 (1:1:2) as 93.48 %. Solomon *et al* (2010) reported that changes in temperature of the soil led to slow desorption of the outer layer of coating samples and at the same time the underlying layer effectively protect the metal surface from corrosive element present in the soil.

This behavior of mild steel in soil in the absence and presences of nanocomposite coating were also clarified with plot of Weight loss versus exposure time with different average temperatures are presented in Figure 4.28. It was also observed from the plots that weight loss of mild steel decreases with hybrid nanocomposite coating such as NiO-CNTs-SnO_2 (1:2:1) and NiO-CNTs-SnO_2 (1:1:2) and average temperature has little or no effect in the weight loss.

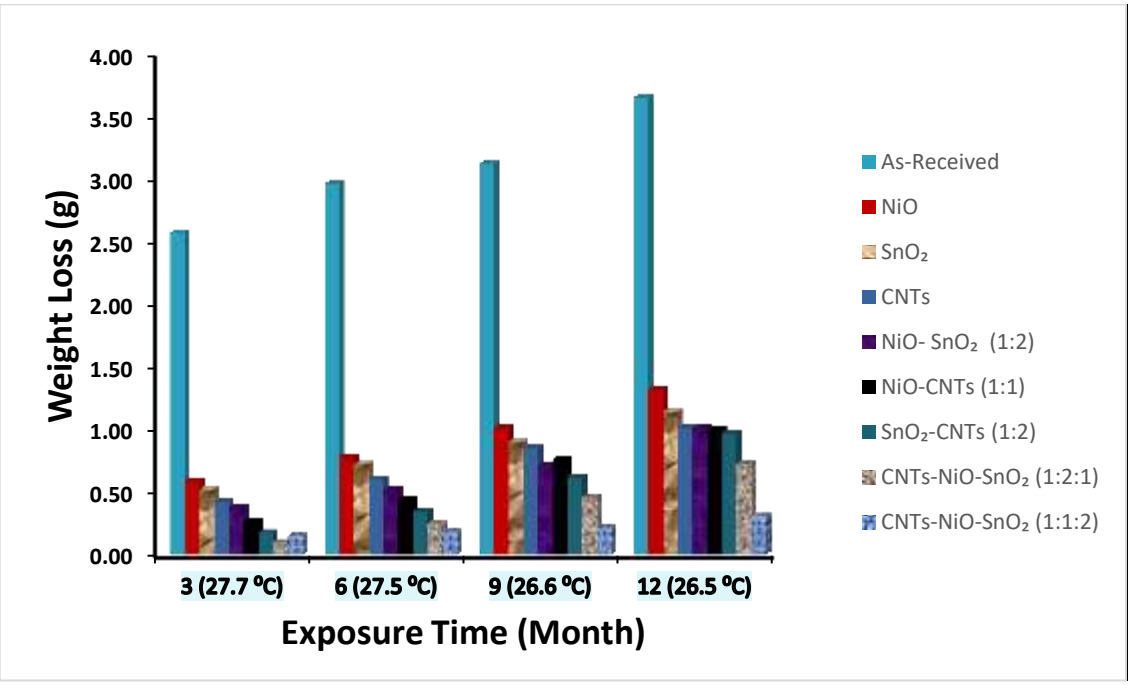

Figure 4.28: Plot of Weight Loss against Time of Different Nano Coating Materials

4.5.2 Potentiodynamic polarization (PDP) and Tafel plot

The electrochemical parameters related to Tafel plots like corrosion potential (Ecorr), corrosion current density (Icorr), protection efficiency and corrosion rate are shown in Table 4.21. Results show that the coated mild steel specimens exhibited significantly lower Icorr values and more positive corrosion potential (Ecorr) with respect to as received mild steel. This suggests that the coatings promote the generation of a more stable passive layer and protect the underlying metal against corrosion.

The corrosion density of 0.0955 A/cm^2 obtained for As-received sample significantly reduced to 0.0286, 0.02521 and 0.0221 A/cm^2 for NiO, SnO_2 and CNTs respectively. It can be observed that nano particle samples relatively mitigated the corrosion attack with the corresponding increasing corrosion potential (Ecorr). The icorr value of NiO-SnO_2 (1:2) coated sample was 0.0162 A/cm^2 at 6 h exposure time which was reduced to 0.0146 A/cm^2 in the case of NiO-CNTs (1:1), 0.0111 A/cm^2 in SnO_2-CNTs (1:2), 0.00973 A/cm^2 in NiO-CNTs-SnO_2 (1:2:1) and 0.0064 A/cm^2 in NiO-CNTs-SnO_2 (1:1:2) coated samples. The Icorr value was found to decrease on increasing the loading of carbon nanotube in composite coating. As a result, the corrosion protection efficiency (% P.E.) as calculated from Equation 3.20 was found to be highest at 89. 81% and 93.30% for specimens NiO-CNTs-SnO_2 (1:2:1) and NiO-CNTs-SnO_2 (1:1:2) respectively as shown in Table 4.22. Nano composite coating was found to be known for their brilliant barrier properties and good adhesion to their metal substrates under corrosive conditions.

Results also indicate that the addition of CNTs in composite coating improves the corrosion protection performance of metal. Moreover, lower Icorr values indicate the formation of protective strength on metal surface. It was observed that the Icorr values

of mild steel was found to decreased on increasing the loading level of hybrid nano composite coating.

Table 4.22: Potentiodynamic Polarization Parameters for Nano-coating of AISI 1020 Carbon Steel in Soil Electrolyte for 6 h

Experimental Sample	Ecorr (V)	Icorr(A/cm^2)	CPE. %	CR (mpy)
As-Received	-2.15	0.0955		0.0335
NiO	-1.73	0.0286	70.05	0.0100
SnO_2	-1.71	0.02521	73.60	0.0088
CNTs	-1.69	0.0221	76.86	0.0077
NiO- SnO_2 (1:2)	-1.67	0.0162	83.04	0.0057
NiO-CNTs (1:1)	-1.40	0.0146	84.71	0.0051
SnO_2-CNTs (1:2)	-1.15	0.0111	88.38	0.0039
NiO-CNTs-SnO_2 (1:2:1)	-1.10	0.00973	89.81	0.0034
NiO-CNTs-SnO_2 (1:1:2)	-1.05	0.0064	93.30	0.0022

Figure 4.29 shows various optimised nanocomposite polarisation curves. The nanocomposite coatings include NiO-SnO_2 (1:2), NiO-CNTs (1:1), SnO_2-CNTs (1:2), NiO-CNTs-SnO_2 (1:2:1) and NiO-CNTs-SnO_2 (1:1:2). The corrosion potential of -1.67 V was obtained for NiO-SnO_2 (1:2) shown in Table 4.2 and reduced to -1.05 V corrosion potential for NiO-CNTs-SnO_2 (1:1:2) coating. This indicates that barrier formation on the mild steel against corrosion is highly effective as high corrosion potential of -2.15 V was obtained for uncoated mild steel.

The corrosion protection efficiency (CPE %) of 83.04, 84.71, 88.34, 89.81 and 93.30 % NiO-SnO_2 (1:2), NiO-CNTs (1:1), SnO_2-CNTs (1:2), NiO-CNTs-SnO_2 (1:2:1) and NiO-CNTs-SnO_2 (1:1:2) respectively. This showed that the NiO-CNTs-SnO_2 (1:1:2) nanocomposite coating exhibit a very excellent corrosion resistant than other experimental samples and this correspond to the lowest corrosion rate of 0.0022 mpy as obtained in Table 4.22.

Figure 4.29 shows that the polarization potential of as received sample is −2.15 V, and the corrosion current density is 0.00955 A/cm^2. As the coating's corrosion potential (Ecorr) shown in Table 4.22 gradually increases from −1.73 to −1.69 V, the current density gradually decreases from 0.0286 to 0.0221 A/cm^2, and the corrosion rate can be gradually slowed down. By comparing the corrosion parameters of the control steel sample and the nano particles coating, it was found that the polarization potential of as-received was −2.15 V, much smaller than the corrosion potential of the nano composite coatings, so the coating has the function of protecting the base steel.

The electrochemical accelerated corrosion test measures the anti-corrosion behaviour of the coating in detail, the electrochemical parameters obtained by Tafel extrapolation of the curves as shown in Figure 4.29, polarization curves at 6 h. The corrosion potential (Ecorr) characterises the thermodynamic stability of the tested samples under the electrochemical corrosive condition as observed by Lu *et al.* (2019). The corrosion current density (Icorr) implies that the corrosion rate and breakdown potential are the lowest potential values at which pitting occurred according to Lu *et al.* (2019).

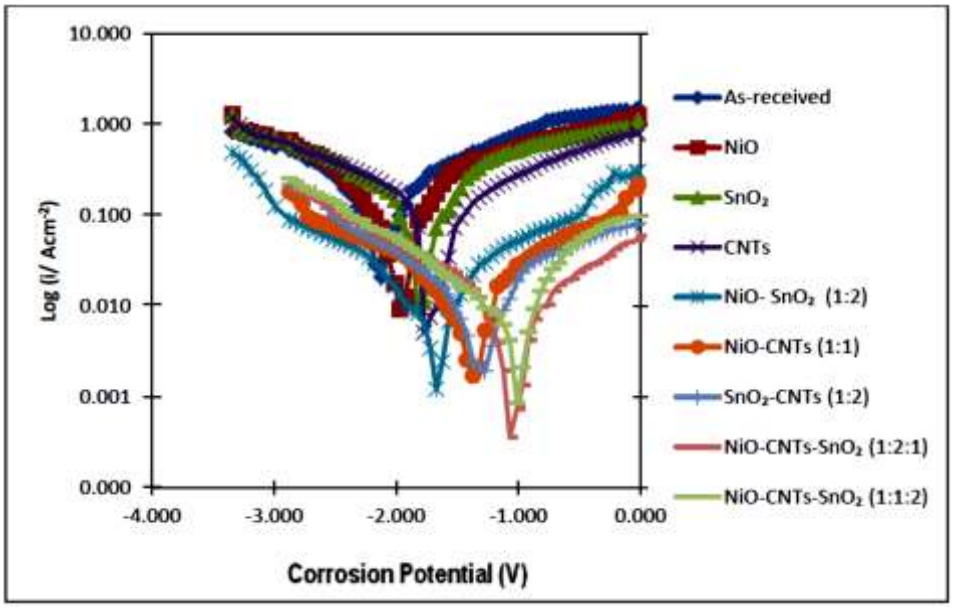

Figure 4.29: Tafel Graph of the Combined Samples

The corrosion current density of the base steel was also much higher than the corrosion current density of the nano particle coatings, so the control sample corrosion rate is higher than the corrosion rate of the nano particle coatings. Besides, the passivation films formed on the coating surface prevented the inner layer from being exposed to corrosive liquid, which could slow down the corrosion reaction. The reason might be that the coating began to experience a vigorous electrochemical reaction in the soil, which generated an oxidation product that hindered the rate of corrosion. The more positive Ecorr values and lower Icorr values of the base material indicate improved corrosion resistance properties of the coated specimens (Hao *et al.,* 2018).

From the polarization curve in Figure 4.29, a slight shift in polarisation potential value for the nano coated samples were compared to the uncoated sample. This shift in corrosion potential was observed without considering the order of the coating thickness and the value signifies barrier type of corrosion protection as it was in the positive direction of the potential. This is because the deviation in the shape of the curves indicates that both anodic and cathodic reactions were inhibited as reported by Abdulrahaman *et al.* (2017). The negative shifts of potential in some coatings are due to the occurrence of active corrosion process at the nano composite coating/metal interface. The more positive Ecorr values and lower Icorr values of the nano composite coating material indicate improved corrosion resistance properties of the coated specimens as the polarisation curves shifted right.

It can be observed from Figure 4.29 that the mild steel has lower potential and after coating the potential shifted towards the right. The result of 70.05, 73.30 and 76.86, % corrosion protection efficiency was achieved for NiO, SnO_2 and CNTs coating samples

respectively. This improvement in corrosion resistance after nano coating may be attributed to the hard and fine structure obtained after coating which helped in strengthening the coating of mild steel.

Bao *et al*., (2019) reported the CNT not only acts as a physical barrier to the corrosion process, but also improves the electrochemical properties to anti-oxidation. However, it has been reported that harsh acid treatment will introduce many defects on the surface of CNT which will decrease its conductivity significantly and it is attributed to carbon's high standard potential which will promote galvanic corrosion and to accelerate corrosion of surrounding metal (Daneshvar, 2016). As a result of this, soil contained different corrosive element at varying concentration and pH which can possibly penetrate the coated mild steel. These led to the failure of coatings and expose the surface of metal to the soil environment.

The observed results of nano coatings of steel coupon showed the weakening of the barrier property of the coating with the exposure time. In the presence of corrosive environment, the interfacial bonding between coating/metal is destroyed due to penetration of electrolyte into the interface. It breaks the chemical bonds and results in the failure of the coatings. The observed slightly high corrosion rates of nano particle coatings as shown in Table 4.22 were due to the presence of defects and pores that bring about the application of hybrid nanocomposite coating. This is because the defects and pores allowed the electrolyte diffusion, thus promoting the failure of the protective barrier (Abdulrahaman *et al.,* 2017). This occurs as a result of the degradation of the coating due to longer exposure to the corrosive soil. The corrosion current density of the base steel was also much higher than the corrosion current density of the nano composite coating. Besides, the passivation films formed on the coating surface prevented the inner layer from being exposed to corrosive liquid, which could slow

down the corrosion reaction. The reason might be that the coating began to experience a vigorous electrochemical reaction in the soil, which generated an oxidation product that hindered the rate of corrosion. According to Hao *et al.* (2018), the more positive Ecorr values and lower Icorr values of the base material indicate improved corrosion resistance properties of the coated specimens which is in agreement with this work. Besides, the passivation films formed on the coating surface prevented the inner layer from being exposed to corrosive liquid, which could slow down the corrosion reaction. The reason might be that the coating began to experience a vigorous electrochemical reaction in the soil, which generated an oxidation product that hindered the rate of corrosion (Hao *et al*., 2018).

On the one hand, the composite coating isolates the substrate from contact with the soil environment; therefore, corrosion of the substrate in direct contact with corrosive is avoided. On the other hand, even if the surface of the composite coating is scratched, the coating and the substrate are anodized in a closed loop, thereby protecting the substrate from corrosion (Daneshvar, 2016).

4.5.3 Electrochemical impedance spectroscopy (EIS)

The impedance spectra for as received AISI 1020 steel and as well as those coated with various concentration of NiO, SnO_2, CNTs, NiO-SnO_2, NiO-CNTs, SnO_2-CNTs, and NiO-CNTs-SnO_2 nanocomposites were discussed in this Section.

Electrochemical impedance spectroscopy technique was used to study the effects of moisture contents, chlorides and pH on electrochemical behavior of uncoated and coated carbon steel at a laboratory temperature 27^{o}C. A comparison of Nyquist plots of AISI 1020 carbon steel, NiO, SnO_2, CNTs, NiO-SnO_2, NiO-CNTs, SnO_2-CNTs, and NiO-CNTs-SnO_2 nanocomposites coated samples tested in a sandy loamy soil environment with 13.97 wt.% moisture, 292.5 mg/kg of chloride content and a pH of

6.67 at an OCP value of the respective coated and uncoated samples were carried out. In previous literatures, a well-shaped semi-circle was reported while in some cases, deviation from ideal semi-circle was observed (Xin & Li, 2014). The reason for deviation can be non-homogenous nature of soil (Wang *et al*., 2015).

The experimental impedance spectra were fit with two R-C electrical equivalent circuit (one time constants) for the bare steel and (two time constants) in the case of the coated metal then the program Z-simp win 3.21 software was used for fitting the experimental data as shown in Figures 4.30 and 4.31 respectively.

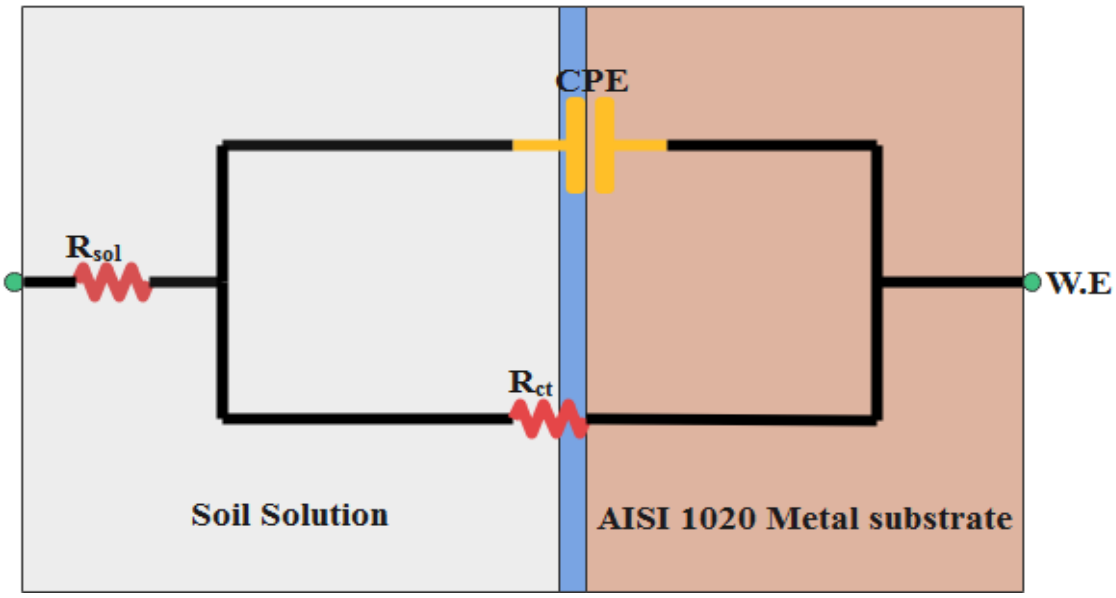

Figure 4.30: Equivalent Circuit for Bare AISI 1020 Metal

Figure 4.30 shows the electrochemical equivalent circuit which fits well with the bare AISI 1020 Metal in the soil solution showing one time constant. Whereas, the NiO, CNTs, NiO-CNTs (1:1) and NiO-CNTs (1:2) coated samples showed two protuberances and were modeled using a two-time constant circuit parameter as presented in Figure 4.31.

The first equivalent circuit (R_c-CPE_a) in series with soil solution resistance (Rsol) is related with the corrosion process occurring at the different interfaces involving a corrosion products resistance (R_c) and the capacitance contribution (CPE_a) of the

corrosion product grown on the steel surface. The second R-C in parallel is related to charge transfer resistance associated with steel deterioration (R_{ct}) and the capacitance contribution of the double layer constant phase capacitance (CPE_{dl}). The second R-C in parallel was used to describe the impedance diffusion response, where the R_{ct} element could be attributed to the diffusion of iron ions through the corrosion products (iron oxides mainly) to the solution (Quej-Ake *et al.*, 2014).

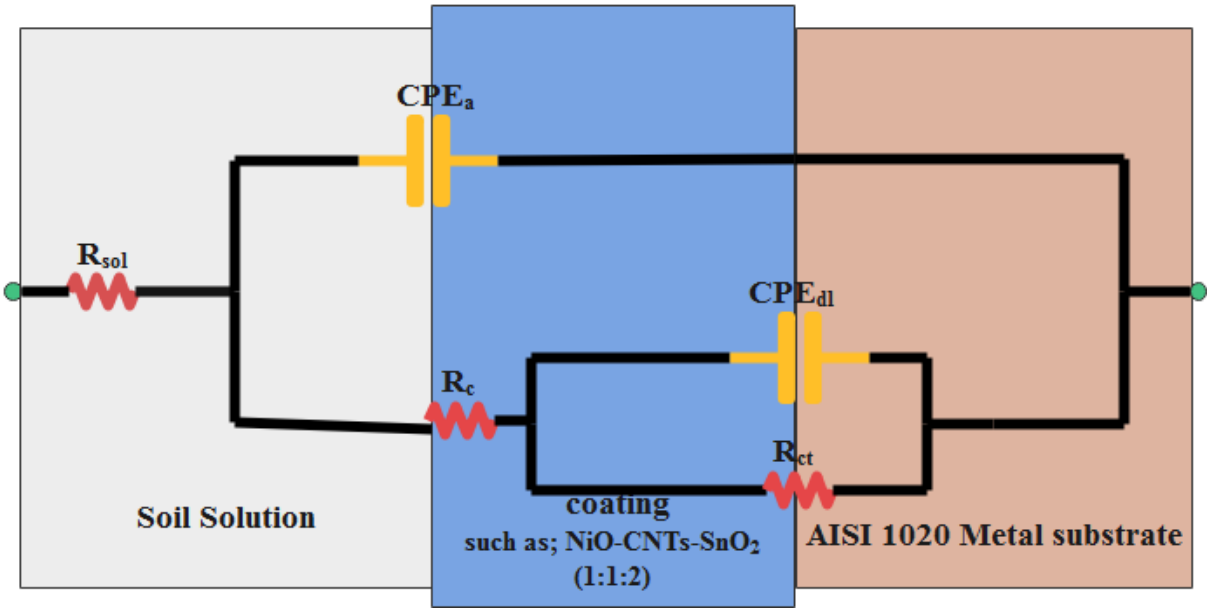

Figure 4.31: Equivalent Circuit Parameters of the Impedance that Best Fits the NiO, CNTs, NiO-CNTs (1:1), SnO_2-CNTs (1:2), NiO-CNTs-SnO_2 (1:2:1) and NiO-CNTs-SnO_2 (1:1:2) Coated Samples

Moreso, the fitted equivalent circuit in Figure 4.31 described the electrical parameters involved at characteristic frequencies in the soil solution. The equivalent circuit model was best fitted with a circuit of components such as, solution resistance (Rsol) which was due to resistance to flow of ions in the soil solution, charge transfer resistance Rct due to the charge transfer resulting from the metal surface and the solution interface and coating resistance (Rc) due to pores or defects in the coating. Other components that describe the system include the constant phase element (CPE) CPEa and CPEdl, which represents the constant phase element corresponding to coating and double layer

capacitance, respectively. CPE has become indispensable to electrochemical impedance spectra fitting measures and in corrosion study. CPE was employed to depict the frequency dependence of non-ideal capacitive behaviour and inhomogeneity of the coating surface (Chui *et al*., 2017). The dispersion coefficient (n) shows ideal capacitive behavior (n=1) which is difficult to achieve in coatings and n value below 1 shows the degree of roughness associated with the coating. The equivalent circuit model showed a good fit for all the impedance plots, with a two-time constant for the coated steel samples. The barrier coating showed high charge transfer resistance (Rct) due to the blocking of electrolyte penetration to the metal surface at the initial time of immersion. As time progressed, the weakening of the coatings was observed which lead to penetration of the water molecules leading to the formation of two capacitances due to coating electrolyte interface CPEa and electrolyte metal interface CPEdl. The presence of CPE in the two interfaces was due to water up-take that in turn was due to the micropores resulting from damage due to aggressive medium on the coating at a longer duration of immersion (Prasannakumar *et al*., 2020).

The obtained experimental data are tabulated in Table 4.23, with EIS parameters provided from the equivalent circuit consistsing of Rsol (resistance of soil medium), R_c (coating layer resistance), R_{ct} (charge transfer resistance), CPEa (capacitance of the coating layer constant phase element), and CPE_{dl} (double layer constant phase element's capacitance). Due to characteristic of soil environment, the surface of steels exposed to was not homogeneous, so this condition led to non-ideal frequency response.

Therefore, constant phase element was suggested instead of capacitor for modelling equivalent circuit (Ismail & El-Shamy, 2009). Hence, the capacitance was replaced by a constant phase element to achieve good results of the fitted circuit with experimental EIS plots. The constant phase element (CPE) implies the departure from the ideal

capacitance behavior of the working electrode due to the surface inhomogeneity and micro-roughness (Khalil *et al*., 2016; Das *et al*., 2018). The impedance obtained by CPE was given by Equation 4.16.

$$Z_{CPE} = Y_0^{-1}(i\omega)^{-n} \quad (4.16)$$

where Y_0 is CPE constant, i^2 = -1, an imaginary number, ω is the angular frequency ($\omega = 2\pi f$) and n represents the component of CPE which provides the details regarding the degree of the inhomogeneity of the metal surface, micro-roughness and porosity (Kumar and Gasem, 2015). Depending on the value of n, CPE can represent an inductance (Z_{CPE} =L, n=-1), a resistance (Z_{CPE} =R, n=0), and a Warburg impedance (Z_{CPE} =W, n=0.5). If n=1, the impedance of the CPE parameter is identical to that of a capacitor, and in the case of Y_0 gives a pure capacitance (C). The EIS parameters of the uncoated and coated AISI 2010 steel are presented in Table 4.3. The protection efficiency values (% P.E) were calculated using the Equation 4.17.

$$(\%P.E) = 1 - \frac{R_{ct(1)}}{R_{ct(2)}} \quad (4.17)$$

where $R_{ct(1)}$ and $R_{ct(2)}$ are the charge transfer resistances of the substrate in the absence and presence of the coating nanocomposites respectively (Atta *et al*., 2014).

Figure 4.32 presents the comparison of EIS plots acquired at OCP for the coated and uncoated AISI 1020 substrates. The Nyquist curve of all the samples consisted of a single capacitive loop and the capacitive radius of each arc increased with the sequence NiO<SnO_2<CNTs<NiO-SnO_2<NiO-CNTs<SnO_2-CNTs<NiO-CNTs-SnO_2(1:2:1)<NiO-CNTs<SnO_2 (1:1:2). This could be attributed to the fact that the size of the NiO and SnO_2 particles are large, therefore the amount of pores and microscopic voids formed in the coatings of NiO or SnO_2 nanocomposite are numerous.

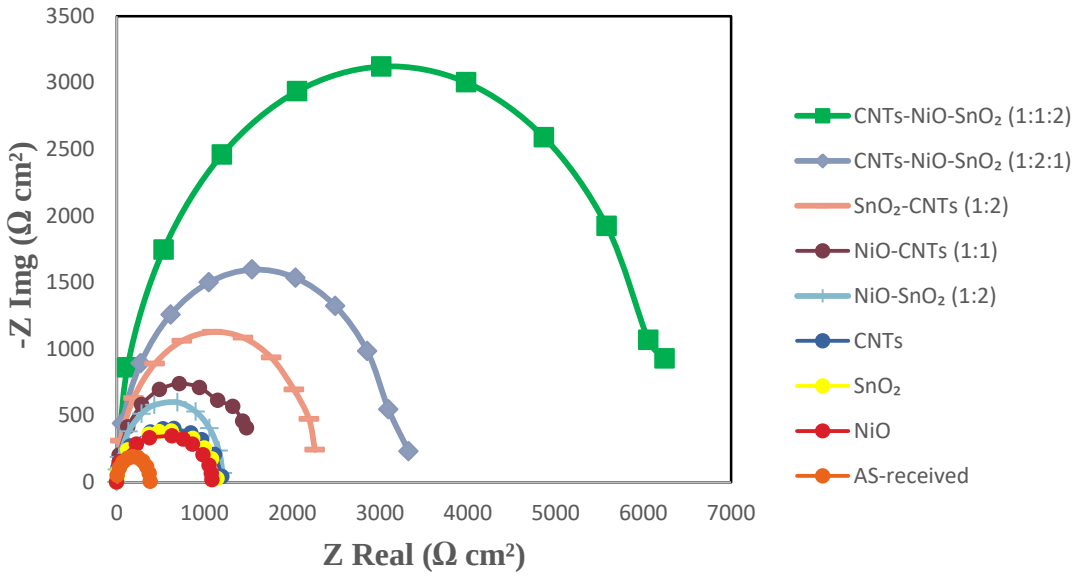

Figure 4.32: Nyquist plots of AISI 2010 Carbon Steel Coated with NiO-SnO_2, NiO-CNTs, SnO_2-CNTs and NiO-CNTs-SnO_2 Tested in Soil at Moisture Contents of 13.98 wt.%, pH of 6.67 and Chloride Content of 291 mg/Kg for 6h

Table 4.23: EIS Parameters

Coatings	R_{Sol} (Ωcm^2)	n_1	Rc ($K\Omega cm^2$)	CPE_a ($\mu F/cm^2$)	Rct ($K\Omega cm^2$)	CPE_{dl} ($\mu F/cm^2$)	n_2	P.E %
As Received	26.8	0.64	0.06	8.15	0.381	124.90	0.89	
NiO	29.06	0.65	0.07	5.76	1.087	90.37	0.89	64.95
SnO_2	30.13	0.65	0.07	5.12	1.144	88.43	0.89	66.70
CNTs	32.44	0.68	0.08	4.43	1.198	86.34	0.90	68.21
NiO-SnO_2 (1:2)	67.98	0.71	0.09	3.43	1.208	79.02	0.90	68.46
NiO-CNTs (1:1)	68.89	0.83	0.45	2.27	1.479	67.56	0.89	74.24
SnO_2-CNTs (1:2)	78.12	0.77	0.53	2.19	2.258	64.86	0.89	83.13
NiO-CNTs-SnO_2 (1:2:1)	85.87	0.88	0.86	1.26	3.327	48.90	0.91	88.55
NiO-CNTs-SnO_2	85.95	0.88	0.89	1.03	6.244	44.78	0.91	93.90

(1:1:2)

Thus, the surface of the coating is not dense enough to alleviate corrosion. Corrosion tends to occur in the area where the pores and microscopic voids exist. When CNTs are well co-deposited with the metal particles onto the surface of the coating, which form on the substrate because of the nanometer scale size of the carbon nanotubes. CNTs becomes widely distributed in the gaps of NiO and SnO_2 making the coatings to be very dense. Consequently, the presence of CNTs improved the anti-corrosion performances for the samples coated with NiO-CNTs-SnO_2 in the ratio (1:2:1 or 1:1:2), this can be deduced by their large capcacitive loop or arc in the Nyquist plot in Figure 4.32.

Furthermore, from the experimental data the synergistic effect of NiO and SnO_2 cannot be overemphasized since the charge transfer resistance ($Rct_)$ of NiO-CNTs-SnO_2 (1:2:1) (3.33 KΩ cm^2) and NiO-CNTs-SnO_2 (1:1:2) (6.24 KΩ cm^2) nanocomposite was found to be greater than those of NiO (1.87 KΩ cm^2), SnO_2 (1.144 KΩ cm^2), CNTs (1.20 KΩ cm^2) SnO_2-CNTs (1.50 KΩ cm^2) or NiO-CNTs (2.26 KΩ cm^2) individually. Meanwhile, with the increase of the CNTs concentration in NiO-CNTs-SnO_2, from ratio (1:1:2) to (1:2:1) the capacitive arc radius of the coating was observed to decrease slightly, indicating that the corrosion resistance of composite coatings gets worse with the increase of CNTs concentration above NiO-CNTs-SnO_2, from ratio (1:1:2). This result could be ascribed to the tubular structure of CNTs. CNTs are carbon-related materials with nanometer diameter and perfect hollow molecular structure. CNTs are inclined to agglomerate. Hence, too much CNTs deposited on the substrate would occupy the position of the NiO and SnO_2 matrices, leading to a large area of the carbon nanotubes wrapped together. This is very unfavorable to coating, resulting in the corrosion resistance of the coating reducing.

Hence, NiO-CNTs-SnO_2, (1:1:2) nanocomposite was considered as the optimum concentration for the best coating for AISI 1020 steel from EIS parameters in this study. It clearly had higher Rct value in view of more corrosion resistance property compared to other coating formulations.

In addition, from the Rct and CPE_{dl} presented in Table 4.23. The effect of values provided for Rct (coating layers' resistance) and CPE_{dl}, which represents the coating layers' constant phase element, were examined. Rct is usually empolyed to characterise the corrosion resistance of the coatings. The lower the value of Rct is, the poorer the corrosion resistance is. Figure 4.32 displays that with the increase of the CNTs the charge transfer resistance, R_{ct} of the (NiO-SnO_2) composite increases to the maximum and then decrease. The CPE_{dl} value of the as received (124.90 μF/cm^2), NiO (90.37 μF/cm^2), SnO_2 (88.43 μF/cm^2), CNTs (86.34 μF/cm^2) as well as NiO-SnO_2 (79.08 μF/cm^2) coating were found to be higher compared to that of the NiO-CNTs (67.86 μF/cm^2), SnO_2-CNTs (64.56), NiO-CNTs-SnO_2 (1:2:1) (48.90 μF/cm^2) and NiO-CNTs-SnO_2 (1:2:1) (44.78 μF/cm^2) composite coating. Plausibly, the presence of CNTs doped metallic SnO_2 and NiO hetero-juctions provided more stability for the coated surface and formed a strong corrosion barrier under the corrosive acidic soil environment with the presence of Cl^- and SO_4^{2-} ions at a pH <7. Therefore, NiO-CNTs-SnO_2 (1:1:2) had the minimum CPE_{dl} for the nanocomposite coatings due to the more homogeneous surface with good corrosion resistance property of the NiO-CNTs-SnO_2 (1:1:2) composite coating. Since CPE_{dl} displays the uniformity of the coating. The smaller CPE_{dl} is, the denser the coating is. These results may also be attributed to the role of the CNTs in modifying the structure. The nanoscale deposited CNTs reduce the surface and structural defects by filling the crevices, gaps and micron holes of the coating similarly observed by Yang *et al*. (2004); Alishahi *et al*. (2012). Considering Rct and CPEa, thus

it is concluded that the coating with a higher coating resistance and a better coating uniformity was NiO-CNTs-SnO_2 (1:1:2). The combination of the coating and the substrate was best at this concentration, which is further illustrated by the high protection efficiency of (93.90%) at this nanocomposition.

In summary Table 4.24, presents related work using EIS technique.

Table 4.24: Comparism of Corrosion Protection Efficiency of Some Related Literature and Present Research Work

S/n	Feedstock	substrate	P.E (%)	Reference
1	Ag-SnO_2	Mild steel	89.00	Raj *et al*. (2014)
2	Fe_3O_4	Mild steel	91.00	Atta *et al*. (2014)
3	Ni-P-CNTs	Carbon Steel	94.67	Gao *et al*. (2015)
4	CNTs	Steel	79.76	Abdulrahaman *et al*. (2017)
5	Zn-Ni doped SnO_2	Mild steel	83.07	Deepa and Venkatesha (2018)
6	Fe_2O_3-NRG/epoxy	Mild steel	83.85	Chhetri *et al*. (2019)
7	Kaolin-Zn/epoxy	Mild steel	97.74	Tabatabaei *et al*. (2020)
8	NiO	ASI 1020 steel	64.95	Present work
9	SnO_2	ASI 1020 steel	66.70	Present work
10	CNTs	ASI 1020 steel	68.21	Present work
11	NiO-SnO_2	ASI 1020 steel	68.46	Present work
12	NiO-CNTs	ASI 1020 steel	74.24	Present work
13	SnO_2-CNTs	ASI 1020 steel	83.13	Present work
14	NiO-CNTs-SnO_2 (1:2:1)	ASI 1020 steel	88.55	Present work
15	NiO-CNTs-SnO_2 (1:1:2)	ASI 1020 steel	93.90	Present work

Tabatabaei *et al*. (2020) reported an Rct value 52188 Ωcm^2 for kaolin-Zn/epoxy coated samples as against 1021 Ωcm^2 for bare steel after 6 h immersion in NaCl. While EIS study by Chhetri *et al*. 2019 revealed superior anti-corrosion performance of Fe_3O_4-NRG/epoxy coating in 3.5 wt% NaCl solution, the corrosion inhibition improved improved by ~ 83.5% with 0.5 wt% loading of Fe_3O_4-NRG. Futhermore, Deepa and Venkatesha (2018) worked on coated Mild steel with Zn-Ni doped SnO_2 in 3.5% NaCl

electrolyte. They concluded that presence of the Ni doped SnO_2 in Zn-coating increased the corrosion resistance property of Zn-deposit as compared to pure Zn-deposit. Increasing corrosion resistance from 364.2-Ωcm^2 to 2151 Ωcm^2 and decreasing corrosion rate from 3.55 $\times 10^5$ g/h to 1.0 $\times 10^5$ g/h with a protection efficiency of 83.07%. Concurrently, Gao *et al*. (2015) reported the corrosion behavior and wear resistance characteristics of electroless Ni-P-CNTs plating on carbon steel and pointed out that the addition of CNTs made the coating denser with an improved coating efficiency of 94.67%. Compared with Ni-P coating, the corrosion resistance of composite coating was better. However, too much CNTs deposited on the substrate occupy the position of the nickel and phosphorus, leading to a large area of the carbon nanotubes wrapped together which is very unfavorable to coating, resulting in the corrosion potential of the composite coating becoming negative gradually, indicating the corrosion resistance of the composite coating becomes worse. Furthermore, Raj *et al*., (2014) who coated mild steel with Ag-SnO_2 reported a P.E of 89.0%, Atta *et al*. (2014) reported a P.E of 91%, while Abdulrahaman *et al*. (2017), reported a P.E of 79.76%. Which were reasonably within the range reported for each of this type of coating materials in this study, but less than that of the NiO-CNTs-SnO2 (1:1:2) composite (93.9%) suggesting that this novel coating material has high and remarkable protection efficiency over AISI 1020 steel in a corrosive soil environment.

It is worthy of mentioning that Lee, (2012) who coated aluminum alloy with Ni-P/TiO_2 and Ni-P/CNT also pointed out that CNTs coatings exhibited superior corrosion resistance (7.39 $k\Omega \cdot cm^2$) compared to the TiO_2 co-deposited coating (4.46 $k\Omega \cdot cm^2$). These finding, corroborates with the findings in this study that the inclusion of CNTs in the right proportion within the NiO-SnO_2 nanocomposite intersperses in the gaps between the metal nanoparticles. Thereby tribologicaly acting as a kind of lard between

the coating and the other friction body and providing improved corrosion resistance as in the case of NiO-CNTs-SnO_2 (1:1:2) with 93.90% protection efficiency as compared to NiO-SnO_2 with 63.75%. From the EIS data the overall protection efficiency from the study is in the order, NiO< SnO_2< CNTs< NiO-SnO_2 (1:2) <NiO-CNTs (1:1) < SnO_2-CNTs (1:2) < NiO-CNTs-SnO_2 (1:2:1) < NiO-CNTs-SnO_2 (1:1:2).

4.6 Mechanical Test

The integrity of the AISI 1020 steel used in this study was investigated using X-ray Fluorescence (XRF), while micro-hardness test, an effective method to test the mechanical properties of the nanocoatings was used to investigate the indentation behavior of the nanocoating films as follows:

4.6.1 Steel used

AISI 1020 steel in form of coupons with 0.5 cm^2 (0.8 cm in diameter) of exposed area in this work was used. Table 4.25 shows the chemical composition of this steel.

Table 4.25: Chemical composition of AISI 1020 Steel (wt%)

Ba	**Al**	**C**	**Si**	**Ni**	**S**	**Cl**
0.032	0.084	0.17	0.955	0.04	0.108	0.174
K	**Ca**	**Ti**	**V**	**Cr**	**Mn**	**Fe**
0.13	0.109	0.031	0.026	0.074	0.277	91.997
Ag	**Ni**	**Bi**	**LOI**			
0.003	0.04	0.014	4.588			

LOI: Loss of ignition

The composition of the of AISI 1020 indicates that the steel coupons consisted of Fe (91.997) as major components signifying that the metal coupon is mild steel of other types of elements present were less than 1 % each.

4.6.2 Micro hardness test

The result of the hardness test conducted on the uncoated and coated samples is shown in the Figure 4.33. It can be observed that the sample coated with SnO_2 and CNTs gave

a hardness value of 116 and 124 respectively, which were lower than that of the as received sample.

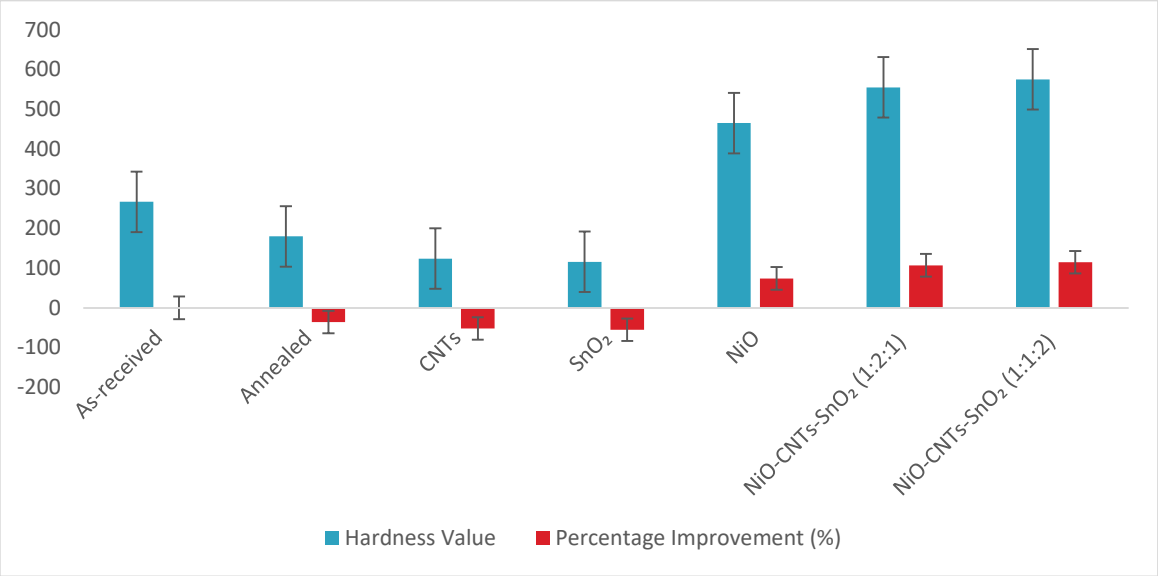

Figure 4.33: Micro-hardness Test Parameters

This is because Sn is a softer metal than steel and has lower melting point of 232°C. Based on this reason, surface alloying or solid solution strengthening did not occur on the steel surface or subsurface. Therefore, the micro hardness value obtained corresponds to tin which is a softer metal compared to steel (Xue *et al*., 2006). CNTs are porous materials that can collapse which could on the steel surface when subjected to lateral load and hardness as measured by indentation (Kim and Oh, 2011). Hence, the collapse behavior might be responsible for the low hardness value of the CNTs coated sample. On the other hand, nickel is a hard, strong and tough material and gave better hardness value as compared to the other nanocoatings. The composite coatings showed improved hardness due to the dispersion and strengthening effect of the SnO_2 and formation of NiO-SnO_2 intermetallic compound where nickel particles impeded the movement of dislocation in the matrix (Georgiou *et al*., 2017). The improvement of the composite coating with mixing ratio (1:1:2) could be attributed to reduced tendency of segregation caused by SnO_2 during solidification and possible grain refinement of the

resulting coating (Humberto *et al*., 2008).

4.7 Morphology of the As-received and Coated Coupons before and after Corrosion Test

The corrosion products formed at the surface of the uncoated and coated AISI 1020 steel was examined using HRSEM and XRD as follows:

4.7.1 HRSEM analysis of the As-received and coated coupons before and after weight loss measurements

Plate XVIII (a-l), presents the HRSEM surface morphologies of the bare AISI 1020 steel and coated samples after the electrochemical tests in the soil environment. Plate (a-b) reveals changes in the morphology for the uncoated steel surface before and after corrosion test respectively. While Plate XVIII (a) is free of major microscopic cracks or defects, it can be seen that circular deep micro-size metastable pits were formed on the surface of the exposed steel after the corrosion test see (Plate XVIII (b)). This is because the corrosion medium has penetrated into the surface of the unprotected steel and caused pitting and cervice corrosion. It is also plausible that defects such as circular pores and inclusions on the surface of the bare steel were formed as a result of degeneration between the metallic lattice and corrosion products initially deposited on the surface of the metal.

The sample in Plate XVIII (c) coated with NiO-SiO_2 before corrosion showed homogeneous, dense, rough, porous and crack free microstructure. The composite coating constituents were seen to be poorly distributed on the sample surface, which implies a weak surface adhesion (Luiz *et al*., 2016). As expected, pitting attack was noticed on the surface of sample see (Plate XVIII (d)) after subjecting it to corrosion in the soil. The level of corrosion on some spots were less as the coating on these spots are seen, this can be attributed to the uneven nature of the coated surface which gave rise to non-uniform deposition of the NiO-SnO_2 composite on the substrate. However, less

deterioration and circular cracks appeared on the surface of the coated sample as compared to the uncoated sample. Therefore, the presence of NiO doped SnO_2 nanocomposites provided a good corrosion barrier in the corrosion media (Deepa and Venkatesha, 2018).

The sample in Plate XVIII (e) was coated with NiO-CNTs, it can be seen that the CNTs appear well dispersed in the nickel matrix as the CNTs are relatively uniformly distributed within the matrix. This indicates that the above methods to disperse CNTs in NiO matrix was effective. The CNTs rooted in the nickel matrix covered the surface of the coating and, obviously, may protect it from wearing and corroding as the coating was free of crack and porosity. In Plate XVIII (f), images of the corrosion morphology of NiO-CNTs coatings were shown after weight loss test in soil environment for 9 months. The surface indicated a change in morphology. Nevertheless, lesser corrosion was observed on the surface of NiO–CNTs coating, which only contained very shallow and small pits see (Plate XVIII (f)) as compared to the NiO-SnO_2 composite coating. The results indicated that the NiO–CNTs coating had good resistance to corrosion, which was close to results obtained by weight loss method and electrochemical studies.

Chen *et al*. (2005) reported that integrating CNTs into Ni coating by electrodeposition improves the corrosion three times. They attributed this improvement to factors such as; CNTs fill the holes and gaps of the coating and act as a physical barrier. Moreover, the uniform dispersion of CNTs (which have higher standard potential) make many corrosion micro cells which will promote Ni (which has lower standard potential) polarization. Shi *et al*. (2004) also observed that CNTS have a major role on passivation of Ni-P-CNT coating. Another corrosion study carried out on electroless plated Ni-P-CNT composite by Alishahi *et al*. (2012) postulated that the presence of CNTs causes the preferential dissolution of Ni, which results to the formation of a phosphorous-rich

passivation layer that hinders corrosion.

The microstructure of the sample coated with SiO_2-CNTs in Plate XVIII (g) before corrosion, appeared dense with layers of rough coatings. This could be due to the depletion of the CNTs from the coating solution as a result of repeated coating which leads to the agglomeration of the SnO_2 that was observed on the smooth coating. The micrograph of the corroded sample Plate XVIII (h) revealed change in the microstructure of the SnO_2-CNTs coating due to attack by some corrosive constituents of the corrosive medium such as, Cl^- and SO_4^{-2} ions.

However, the CNTs were still preserved on the surface of the substrate. Some corrosion products were deposited on the surface of the coating, which signified galvanic corrosion, it can therefore be said the corrosive agents targeted and consumed or reacted with the SnO_2 in the coating thereby leaving behind the non-reactive CNTs constituent of the coating as evidenced in the EDX results in Section 4.7.2. Therefore, the presence of the CNTs in the composite improved the coating perform

of the composite, since the morphology of the corroded SnO_2-CNTs coatings revelaed fewer deterioration compared the NiO-SnO_2 coating. Hu and Jie (2015) had earlier reported that the SEM micrographs of Pb–Sn coated sample, showed large numbers of irregular crystal fractions that were uneven and present in stripe forms, indicating severe corrosion trends. Whereas Pb-Sn-CNTs coatings showed less evident surface inclusions after the corrosion test under the same conditions. It was revealed that the Pb–Sn alloy undergoes corrosion easily compared to that of the Pb-Sn-CNTs composite coating. This was atrrributed to the fact that CNTs reinforced the coating and made it more difficult for the composite coatings to dissolve in corrosion media as in the present study.Plate

XVIII (i) shows the HRSEM images of the sample coated with NiO-CNTs-SnO_2 composite at the ratio of 1:2:1. The morphology of this coated sample revealed random crystal-like flakes and grains distributed across the surface of the coating. These indicated that the CNTs were distributed uniformly through out coating and thereby provided more number of nucleation sites that controlled the crystal growth resulting in the formation of uniform grain size.

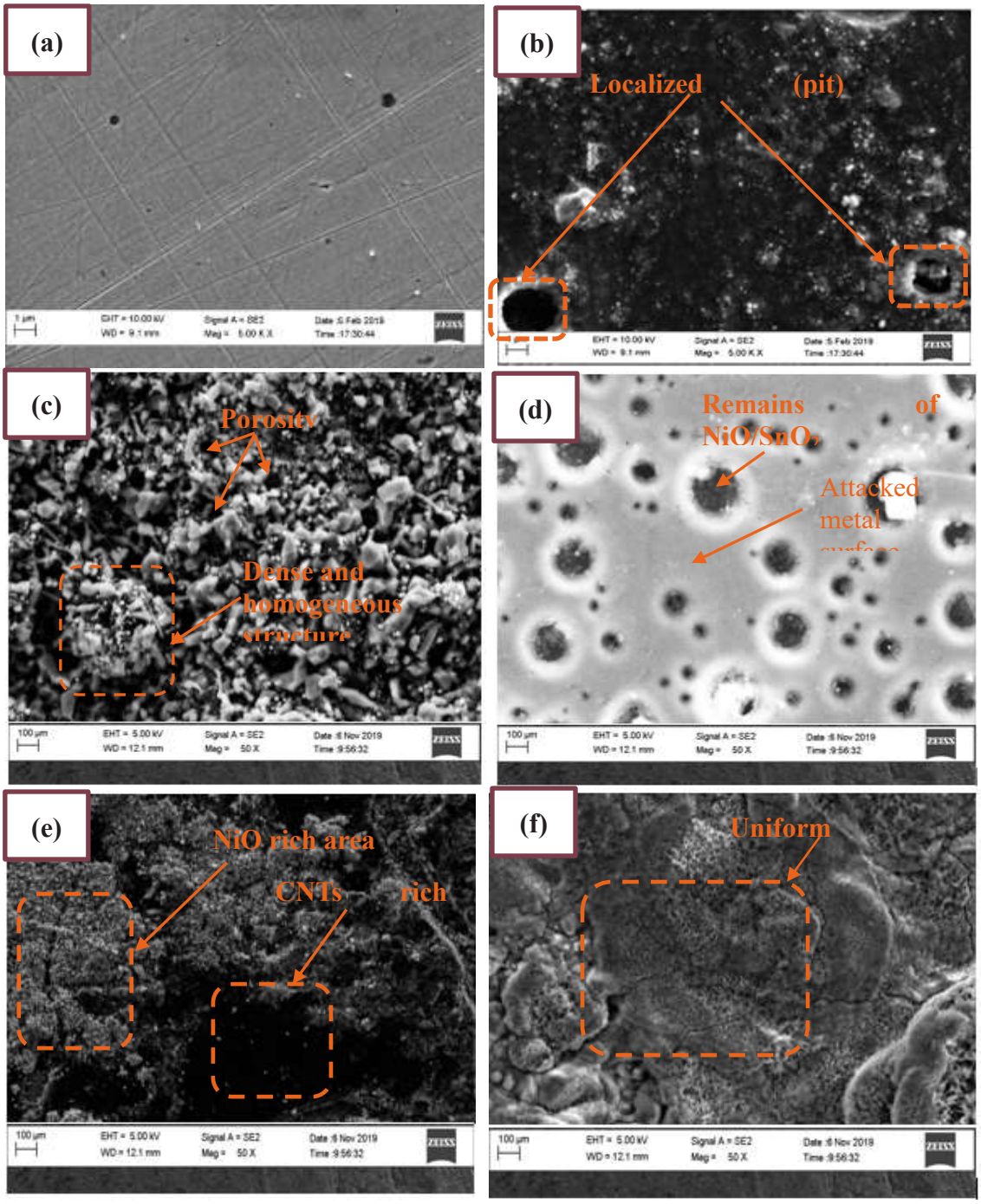

Plate XVIII: Micrograph of the As-received (a-b), Coated with; NiO-SnO_2(c-d),

NiO-CNTs (e-f), SnO_2-CNTs (g-h), NiO-CNTs-SnO_2 (1:2:1) (i-j), NiO-CNTs-SnO_2 (1:1:2) (k-l) before and after Weight Loss Experiment in the Soil Environment for 9 Months

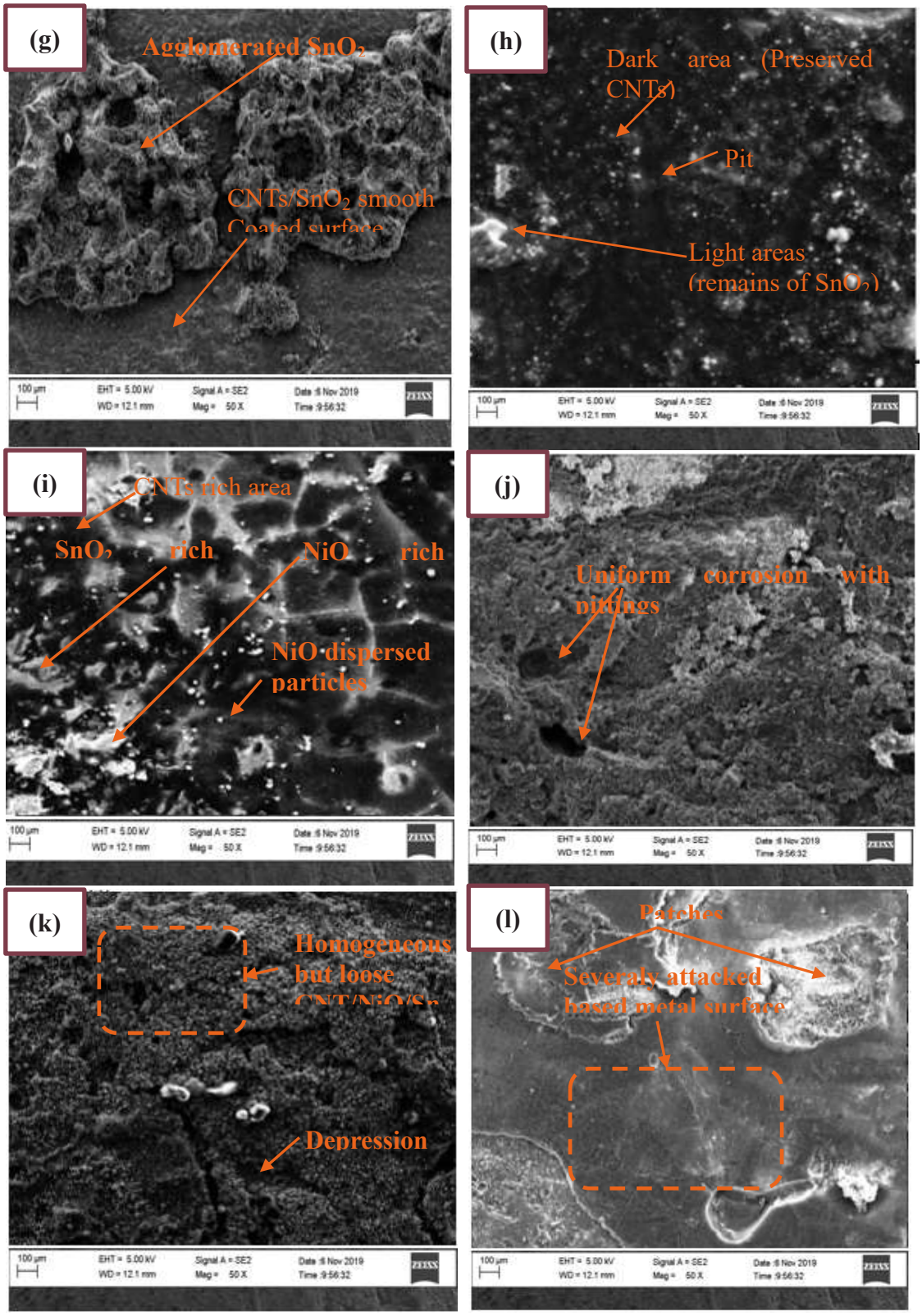

Plate XVIII: Continued

Plate XVIII (j) shows HRSEM images of composite coating after it was subjected to underground corrosion. The composite showed little appreciable change in the grain size and appearance. Furthermore, grains and flake-like crystals disappeared suggesting that during the superficial corrosion they behaved as anodic sites and got dissolved. Nevertheless, the level of corrosion in this case was less compared to the NiO-SnO_2, NiO-CNTs, and SnO_2-CNTs composites as these composites undergoes corrosion easily when compared to composite coating NiO-CNTs-SnO_2 composite at the ratio of 1:2:1. Which could be due to the fact that NiO-CNTs-SnO_2 composite acted as a good barrier, preventing the corrosive from attacking the base base metal (Møller *et al*., 2013).

The microstructure of the sample coated with NiO-CNTs-SnO_2 in the ratio of 1:1:2 was presented in Plate XVIII (k), the coating appeared homogeneous with superior fineness, uniformity and density compared to the NiO-CNTs-SnO_2 coating with the ratio (1:2:1), which confirms the uniform deposition of the codeposited CNT nanoparticles in the NiO-SnO_2 matrix of nanocomposite coating when the ratio is (1:1:2) see Plate XVIII (k).

The HRSEM images of surface corrosion of specimens after corrosion test Plate XVIII (l) shows that the electroless NiO-CNTs-SnO_2 nanocomposite coating in the ratio of 1:1:2 coating provides the best corrosion protection for the AISI 1020 substrate in this study, with uniform corrosion across the entire area. However, at a high CNTs concentration (1:2:1), the nanocomposite coating shows localized cracking phenomena. This is because CNTs has a higher standard potential compared with nickel and tin, therefore it could promote galvanic corrosion leading to acceleration in corrosion of surrounding metal. Also it will induce more boundaries which are more susceptible to corrosion. Especially in electrochemically deposited coatings, if the interfacial bonding

is not strong enough, they will increase the roughness and defects in the matrix and therefore reduce the corrosion resistance. Nevertheless when CNTs is present in the optimuim proportion, it fill the gaps and defects between NiO and SnO_2 nanoparticles and act as physical barrier since they are chemically inert. Moreover, due to high standard potential, CNTs could form networks with NiO and SnO_2 which possess passivation capability to form protective oxide/passive layer over the substrate. Conversely, by acting as proper nucleation sites, the network frame-work will be finer. It has been shown that in nanostructured coatings grain boundaries act as proper sites for nucleation and growth of passive layers. As a result grain refinement can result in uniform passivation and hence enhancement of corrosion resistance (Qin *et al*., 2010).

Praveen and Venkatesha (2009) had earlier established that Zn–Ni alloy undergoes corrosion easily when compared to a composite coating of Zn-Ni-CNTs and the improvement was atrributed was atrributed to the inclusion of the CNTs in the matrix. Whereas Lee (2012) obtanied a uniform and compact surface morphology in both Ni-P/nano-TiO_2 and Ni-P/nano- CNT composite coatings, and these composite coatings possessed better corrosion resistance than that in the 5083 aluminum alloy substrate and in the electroless Ni-P coating.

The coated samples, were annealed and sectioned, the cross sections were analyzed using HRSEM to evaluate the thickness, adherence, uniformity, homogeneity as well as the presence of a defined boundary between the nanocomposite feedstock on the steel substrate. Plate XIX (a-e) shows the micrograph of the cross sections of the samples. Micrograph Plate XIX (a) reveals a cross section of the sample coated with NiO-SnO_2, the coating thickness measured from the interface of the base metal and the coating surface was found to be 36.29 μm. Although the coating was devoid of cracks, the

surface boundary between the substrate and feedstock was found to be thin and therefore the adhesive forces between this interfaces was weak. The coat thickness for the sample coated with NiO-CNTs shown in Plate XIX (b) was 39.30 μm, there is a slight improvement in the surface boundary between the steel substrate and NiO-CNTs nanocoating, which translates into a better adhesion between the interfaces. Nevertheless, the surface of the coat was not homogenous or uniform which could present voids and cracks to set up concentration cells for pitting attacks in corrosive electrolytes. In Plate XIX (c) the thickness of SnO_2-CNTs increased to 63.08 μm, this is apparently accompanied by a corresponding improvement in a well-defined surface boundary between the substrate and feedstock interface. Again, the surface of the coating nanocomposite was not uniform, and therefore, roughness would mean more surface cracks and ridges that would limit the shelf life of the material in service. Not only that, this would also reduce the force of adherence binding the SnO_2-CNTs nanocomposite to the steel feedstock, hence this coating material would have a propensity to wear off easily.

For sample NiO-SnO_2-CNTs (1:2:1) as illustrated in Plate XIX (d), the coating thickness was found to be 64.20 μm, with remarkable improvement in the continuity and homogeneity of the nanocomposite over the surface of the feedstock. There is also a significant enhancement in the formation of a defined boundary between the surfaces of the feedstock and substrate as well, giving rise to a better adherence between the later and former. There is also an improved barrier and surface protection by the NiO-SnO_2-CNTs (1:2:1) nanocoating which is evident from the superior corrosion performance of the composite as compared to the previously described composites. For NiO-SnO_2-CNTs (1:2:1) as shown in Plate XIX (e), a coating thickness of 90.44 μm, was recorded which was the highest thickness observed for all the coatings.

Basically, the coat thickness of dip coating technique depends on varieties of factors such as, composition and viscosity of the solution, speed of withdrawal, immersion time, the rate of solvent evaporation and the angle at which the substrate is taken out (Neacşu, *et al*., 2016).

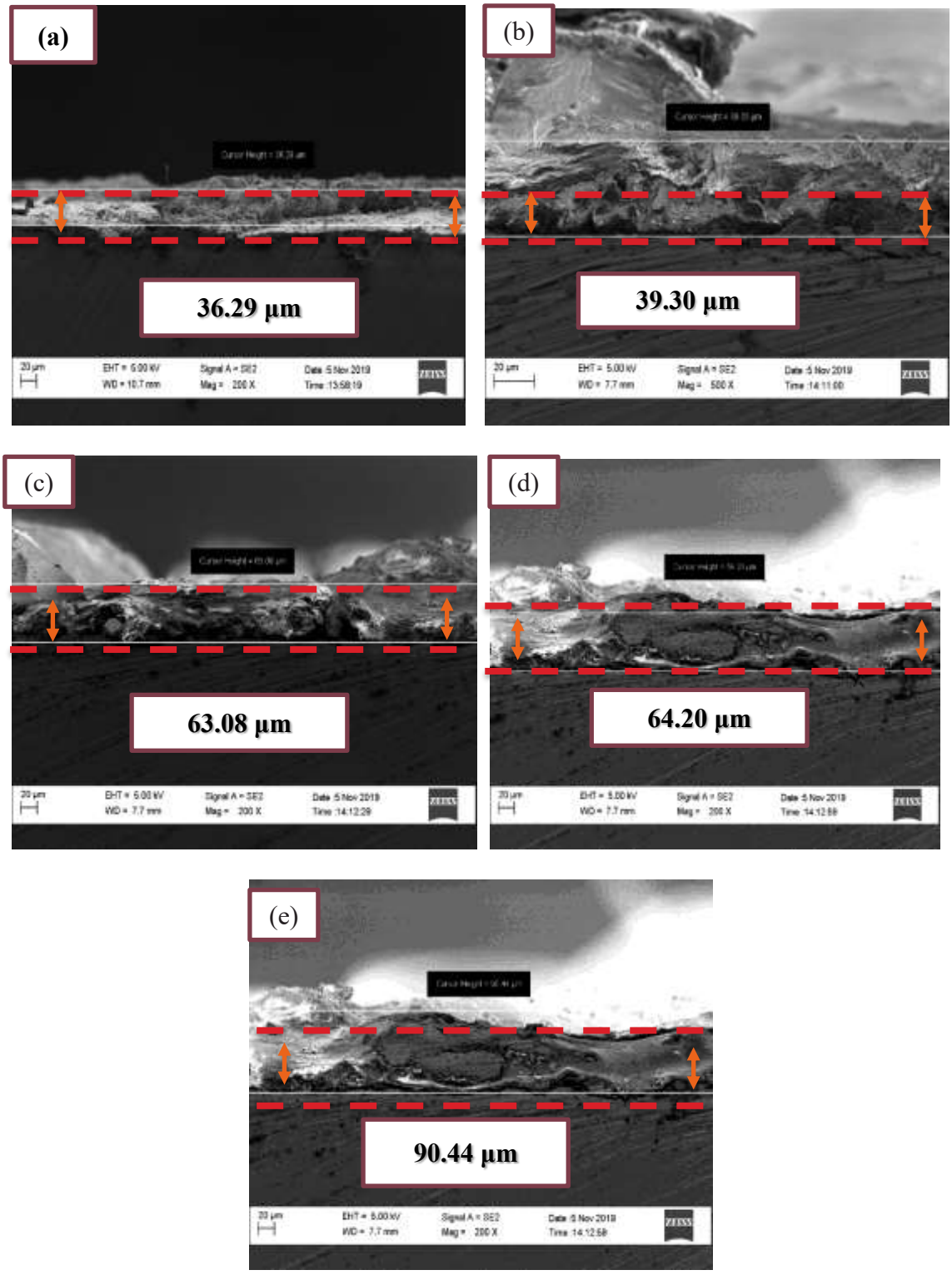

Plate XIX: HRSEM Image of Cross Sectional Micrograph of (a) NiO-SnO_2, (b) NiO-CNTs, (c) SnO_2-CNTs, (d) NiO-CNTs-SnO_2 (1:2:1) and (e) NiO-CNTs-SnO_2 (1:1:2) Nanocomposite Coatings

However, the addition of nanoparticles at optimum concentration enhanced the coat thickness of the nanocomposite therefore providing a better barrier protection (Lee, 2012).

Subsequently, the non-porous, smooth and homogenous morphology offered by the nanocomposition correlated with the incorporation of NiO, CNTs and SnO_2 in the ratio (1:1:2). The cross-section therefore showed no interfacial voids and defects between the substrate and feedstock, resulting to superior adherence between the later and former. Furthermore, this coating provided the best-defined boundary between the steel surface and the coating substrate according to this study, which is corroborated by the excellent corrosion performance of the coated samples in the soil environment. An earlier study by Lee, (2012) had revealed that the coating cross-sections of nanocomposites such as, Ni-P/10g/L TiO_2 (3.33 ± 0.05 μm) and Ni-P/10 g/L CNT (4.13 ± 0.05μm) are thicker than the Ni-P coating (2.35 ± 0.06 μm). Thus, the Ni-P/CNT nanocomposite coating at a high concentration of 10 g/L has the highest coating thickness of 4.13 ± 0.05μm accordingly; the CNT was superior to the TiO_2 because the Ni-P/CNT coatings were thicker than the Ni-P/TiO_2 coatings regardless of whether the nanocomposite coatings were compared at high or low concentrations of TiO_2 and CNTs.

4.7.2 EDX analysis of the Nanocomposite coatings before and after weight loss measurement

The EDX results in Table 4.26 showed the presence of Fe, Al and O in the AISI 1020 mild steel coupon. The presence of oxygen could be due to the presence of an oxide of

carbon and iron resulting from the annealing processes.

Whereas, the NiO-SnO_2, NiO-CNTs, SnO_2-CNTs and NiO-CNTs-SnO_2 composites were comprised of Ni, Sn, O and C in different proportions. With NiO-SnO_2 coating consisting of 44.13, 17.18 and 37.49 wt% of Ni, O and Sn respectively indicating that both NiO and SnO_2 have been co-deposited on the steel substrate.

For the NiO-CNTs coating the carbon content increased to 25.22 wt%, while Ni and O wt% were at 62.13 and 12.39 suggesting that the major components of the composite were successfully deposited on the metal substrate. Similarly, the EDX result in Table 4.26 for the SnO_2-CNTs coatings revealed Sn, O and C at 58.89, 14.54 and 26.29 by wt% indicative of the presence of these major elements on the coating deposited on the steel surface.

Table 4.26: The EDS Elemental Analysis Results for the As-received, NiO-SnO_2, NiO-CNTs, SnO_2-CNTs and NiO-CNTs-SnO_2 Nanocomposite Coatings before Weight Loss Measurement

Sample	As-received	NiO-SnO_2	NiO-CNTs	SnO_2 CNTs	NiO-CNTs-SnO_2 (1:2:1)	NiO-CNTs-SnO_2 (1:1:2)
Element	Wt%	Wt%	Wt%	Wt%	Wt%	Wt%
C	21.12	0.89	25.22	26.29	33.40	13.54
O	4.61	17.18	12.39	14.54	12.18	12.94
Al	0.67	-------	-------	------	------	------
Fe	83.6	0.31	0.26	0.28	0.22	0.23
Ni	------	44.13	62.13	------	28.86	26.75
Sn	------	37.49	----	58.89	25.34	46.54
Total	100	100	100	100	100	100

In the case of the NiO-CNTs-SnO2 composites, ((1:2:1) and (1:1:2)) the wt% of CNTs is observed to decrease from 33.40 to 13.54 wt% with a corresponding increase in the wt% of Sn from 25.34 to 46.54 wt% attributable to the variation in the mixing ratios individually. The presence of minute wt% of Fe in each coating could be due to the interaction between the iron substrate and the feedstock during heat treatment, which led to the formation of adhesive bonds as observed in the HRSEM micrographs in Plate

XIX (a-e). Table 4.27 shows the results of the AISI 1020 steel as well as the NiO-SnO_2, NiO-CNTs, SnO_2-CNTs and NiO-CNTs-SnO_2 composites coating after the weight loss experiment in the soil environment for 240 h.

Table 4.27: The EDS Elemental Analysis Results for the As-received, NiO-SnO_2, NiO-CNTs, SnO_2-CNTs and NiO-CNTs-SnO_2 Nanocomposite Coatings after Weight Loss Measurement

Sample	As-received	NiO-SnO_2	NiO-CNTs	SnO_2-CNTs	NiO-CNTs-SnO_2 (1:2:1)	NiO-CNTs-SnO_2 (1:1:2)
Element	Wt%	Wt%	Wt%	Wt%	Wt%	Wt%
C	8.68	2.06	24.57	26.08	32.18	12.70
O	24.53	20.30	20.68	22.65	16.80	15.87
Al	0.13	------	-------	------	-------	-------
Si	1.20	0.80	1.04	1.00	0.98	0.77
Cl	1.65	1.38	0.82	0.57	0.18	0.18
Fe	63.81	6.12	4.71	1.84	1.05	0.64
Ni	-------	34.22	49.26	------	24.00	25.35
Sn	-------	35.12	--------	47.86	24.81	44.49
Total	100	100	100	100	100	100

The results show that the wt% of iron decreased to 63.81, whereas C and O increased to 8.68 and 24.53 respectively. This could be due to the formation of corrosion products on surface of the unprotected steel coupons. Consequently, the presence of Si and Cl are observed, which is because of the presence of SiO_2 and Cl^- ions in the soil environment, the diffusion of the Cl^- ions onto the surface of the steel is evidenced as one of the key corrosion catalyst forming pits as shown in the Plate XVII (b). The data in Table 4.27 also confirm the presence Sn, Ni, O, Fe, C, Si and Cl in the NiO-SnO_2 nanocomposite coatings at 35.12, 34.22, 20.30, 6.12, 2.06, 1.38, 0.80 by wt% respectively. Notably the wt% of Fe (63.81) increased, while Sn (35.1) and Ni (34.22) were observed to decrease which could be attributed to the formation of corrosion products during the weight loss experiment. This also indicated that the NiO-SnO_2 coating had become damaged and

the substrate Fe had been exposed to the soil and acted as an anode. The presence of chloride (Cl^- ions) on a metallic surface indicated that anion in soil penetrated through corrosion product layer and reached the sample's surface. As a result of this penetration, the corrosion process was accelerated. However, it has been reported in literature the initial corrosion product formed on carbon steel is goethite (α-FeOOH) which provides a shield to the substrate metal against corrosion (Kwon *et al.,* 2007; Nie *et al.,* 2009). Similar trend was obtained for NiO-CNTs and SnO_2-CNTs the EDX analysis of corrosion products confirmed the presence of Sn, Ni, C, O, Si and Cl as the case may be. For both composites, the O content in the corrosion products was significant when compared with that of the coated sample. The O content was determined as 20.68 and 22.65 wt%, which was 1.7 and 1.5 times greater than that of the NiO-CNTs and SnO_2-CNTs coated samples respectively. This could be due to the formation of a few oxides/hydroxides during the corrosion process. Conversely, the amounts of Ni (49.26 wt %) and C (24.57 wt.%) for NiO-CNTs and Sn (47.86 wt%) and C (26.08 wt%) in the case of SnO_2 in corrosion products recorded a decrease when compared to the coated samples. The decreased amount of the aforementioned elements in corrosion products could be attributed due to either corrosion or extremely loosely bound oxides/hydroxides/chlorides of Ni, Sn and C. The soil (corrosive agents) reacts with the main components (Ni, Sn and C) of the coating and form a few corrosion products. Therefore, it is likely that the loosely bound oxides leach out in the solution or dissolve (resulting to a weight loss) while adherent oxides/hydroxides adhere to the coating surface to fill or block the coating pores (Lee *et al*., 2019).

The EDS data for NiO-CNTs-SnO_2 (1:2:1) presented in Table 4.27 revealed the presence of corrosion product. Elements obtained from the corroded layer of NiO-CNTs-SnO_2 (1:2:1) coated steel were determined as (Sn: 24.81, Ni: 24.00, C: 32.18, O:

16.80, Fe: 1.05, Si: 0.98, and Cl: 0.18). Furthermore, the decrease in the amount of Ni, Sn and C as well as the presence of Fe and Cl indicated the likelihood that corrosion products are formed. However, tin and nickel oxide provides a protective layer and protects the substrate metal from further corrosion. Nevertheless, the presence of Fe indicates that protective layer of Ni-CNTs-Sn was partially removed due to soil aggressiveness. In last case, the elements obtained from the corroded layer of NiO-CNTs-SnO_2 (1:1:2) coated steel were determined as (Sn: 44.49, Ni: 25.35, C: 12.70, O: 15.87, Fe: 0.64, Si: 0.77, and Cl: 0.18) also indicative of the formation of various corrosion products. On the other hand, it was observed that the decrease in the amount of the main elements (Sn, Ni and C) in the coating was less when compared to that of the same composite with the ratio (1:2:1). This could be attributed to fewer corrosion products formed, which also translates to a less significant weight loss as discussed earlier in Section 4.7.1. This is also evidenced by the minute amount of Fe (0.64 wt%) in the EDX data which connoted that Fe corrosion products formed in this case was almost negligible. Over all, it can be seen that Cl was present in trace amount in corrosion products too, it is evident that there is less quantity of Cl (0.18 wt%) when compared to the other coatings, which means reduced corrosion rate. Since the Cl anion is classified as aggressive because it directly contributes in electrochemical reaction causing corrosion.

The presence of Cl anion in corrosion product revealed that it had a strong tendency to promote corrosion rate even if the metallic surface is coated with NiO-CNTs-SnO_2. Therefore, there is a possibility of the formation of oxides/hydroxides/chloride of Sn, Ni and Fe, such as $Sn(OH)_4$/$SnCl_4$, $NiCl_2$/$Ni(OH)_2$ and the co-existence of O and Fe elements demonstrated that oxides of iron were present in corrosion products. Generally, (goethite) α-FeOOH and (lepidocrocite) γ-FeOOH are observed as corrosion

products of steel buried in the soil environment (Lee *et al*., 2019). In order to confrm these, characterization of the corrosion products via XRD was carried out and the details are explained in the subsequent section.

Wasim and Shoaib (2019) while working on the influence of chemical properties of soil on the corrosion morphology of copper and zinc coated carbon steel pipes had established that the elements present in the corrosion product (Zn, Cu, O, Cl) showed the possibility of the presence of copper/zinc chloride and copper/zinc oxide. The presence of Cl element in the corrosion layer of carbon, zinc-coated, and copper-coated steels was obviously due to the presence of Cl salts in the soil. Cl anion present in corrosion product in the EDX data evidenced the zinc or copper-coated carbon steel were penetrated or partially damaged during the corrosion process. However, the copper and zinc corrosion products formed, provided a protective layer, which protects the substrate metal from further corrosion.

4.8 XRD of the Uncoated and Coated Samples before and after the Weight Loss Test

XRD analysis was employed to examine both the coated and uncoated AISI 1020 steel before and after the corrosion test in the soil and reported in Sections 4.8.1- 4.8.6

4.8.1 XRD results of the AISI 10120 metal coupons before and after Weight Loss Measurement

Figure 4.34 shows the diffraction pattern of the As-received AISI 1020 steel coupon before AS (a) and after AS (b) corrosion test. The XRD results for both samples show the crystallographic peaks with corresponding crystal planes (110), (200), and (211) with diffraction angles at 2θ values of 44.67^{o}, 65.02^{o}, 82.34^{o} which matches to a ferrite crystal phase with a body-centered cubic structure (JCPDS No. 006-0696). Accordingly, a strongly broadened peak between 25.06^{o} and 35.12^{o} corresponds to the weakly

crystallized phase in the ferrite structure.

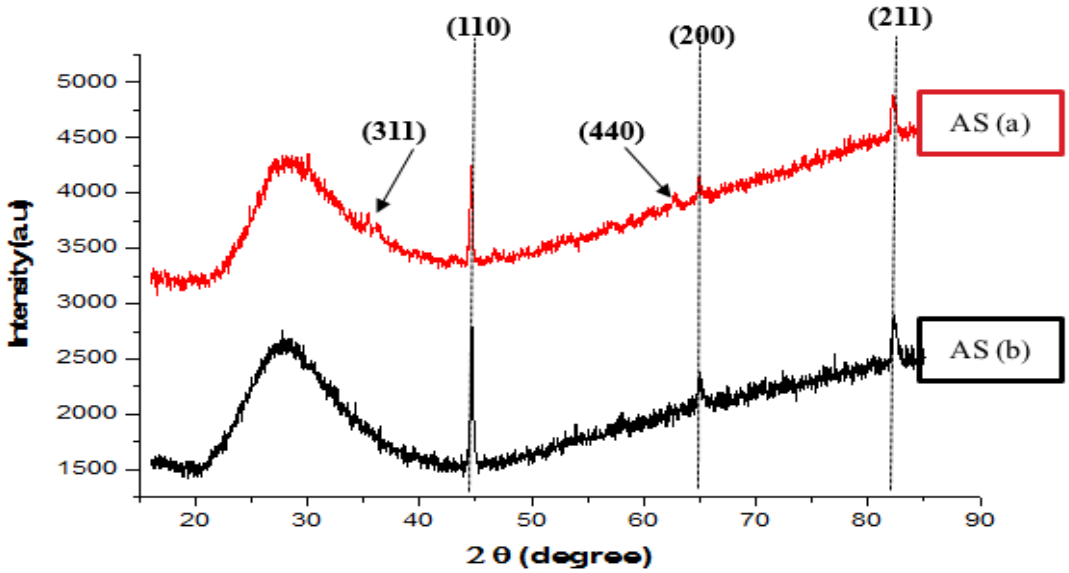

Figure 4.34: XRD Result for AISI 1020 before AS (a) and after Weight Loss Measurement

A close inspection of the crystallographic reflections of the corrosion product As (a) revealed the presence of two new diffraction peaks at (311) and (440), which corresponds crystal planes at 2θ values of 35.43° and 62.52° respectively. These peaks were plausibly formed after the steel coupons were subjected to the weight loss measurement, and denoted the presence of rust in the form of iron oxide (magnetite) $FeFe_2O_4$ in the face-central cubic phase (JCPDS No. 019-0629). However, the presence of impurities as a result of the rusting process could not be detected by XRD analysis.

4.8.2 XRD of the NiO-SnO_2 (1:1) coated samples before and after corrosion test

The X-ray diffraction (XRD) patterns of the NiO-SnO_2 (1:1) coated samples before and after the weight loss measurement are shown in Figure 4.35. All diffraction peaks in the sample before and after the corrosion test can be perfectly indexed as the cubic structure of NiO (JCPDS 047-1049), the tetragonal structure of SnO_2 (JCPDS 041-1445), body-centered cubic planes of Fe (JCPDS 006-0696) and rhombohedral structure of Fe_2O_3

(JCPDS 033-0664) respectively.

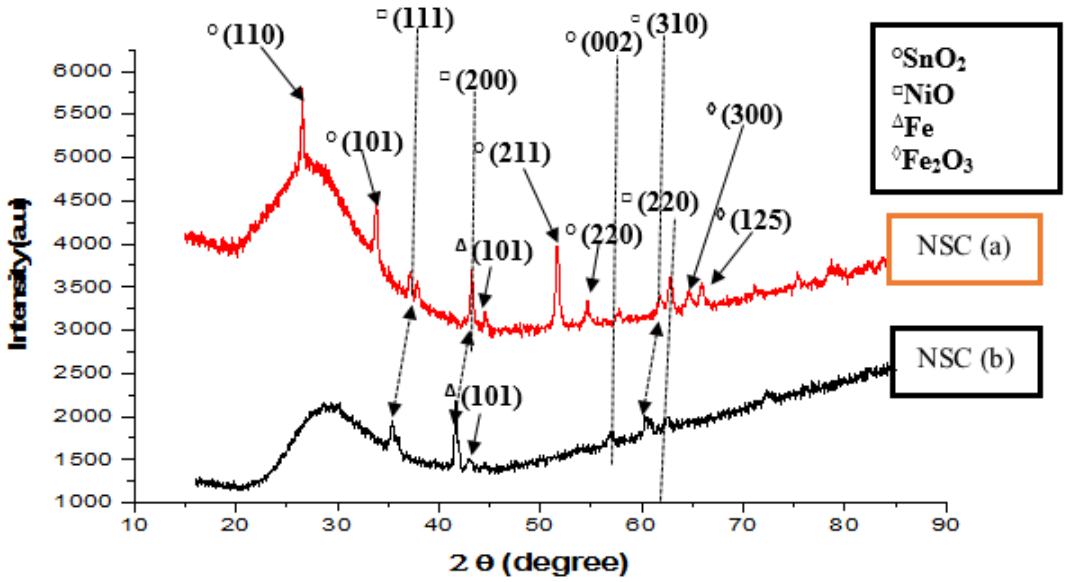

Figure 4.35: XRD Result for NiO-SnO_2 (1:1) Coated Samples before NSC (b) and after Corrosion Test NSC (a)

These consisted of crystallographic peaks with planes at (111), (200), and (220) at corresponding 2 theta values of 37.59°, 43.38°, 62.88° for NiO, and (110), (101), (211), (002), and (310) diffraction peaks with 2 theta values at 26.61°, 33.89°, 51.78°, 57.82° and 61.87° for SnO_2. While the crystal plane (101) at a 2θ value of 44.67 was attributed to Fe, and diffraction planes at (300) and (125) at 2θ values of 63.99° and 66.03° were ascribed to Fe_2O_3. In the case of the NiO-SnO_2 (1:1) coated coupon (NSC (b)) the indexed peaks for NiO at (110), (101), (211) and (002) showed the presence of face-centered cubic planes on the crystal lattice of the nanocomposite. However, for SnO_2, diffraction peaks at (110), (101) and (211) were of low intesities. After the corrosion test, XRD pattern of NiO-SnO_2 (1:1) corrosion product (NSC (a)) depicted a slight shift for all the crystallographic planes for NiO and prominent peaks appearing for SnO_2 at at peaks (110), (101) and (211) at 2θ values of 26.61°, 33.89° respectively. This may be attributed to the corrosion mechanistic reactions occurring the in the whole system as well as the formation of corrosion products. This was evidenced with planes new

diffraction planes (125) and (300) at 2θ values of 63.99° and 66.03° corresponding to Fe_2O_3 and indicated the formation of rust on the surface of the coat. Moreover, a close inspection of the photo-microstructure from HRSEM cross-sectional images in Plate XIX (a-e) showed the formation of Fe_2O_3 on the coat after the weight loss test.

4.8.3 XRD of the NiO-CNTs (1:2) coated samples before and after corrosion test

XRD pattern of steel coupon coated with NiO-CNTs (1:2) denoted as (NCC (b)) as well as the corrosion product after weight loss test (NCC (a)) are presented in Figure 4.36. The co-deposition of NiO-CNTs nanocomposites on the steel substrate are confirmed by the presence of (003) plane of CNTs at 2θ =26.60° and 2 planes of NiO that are (200), and (220) at corresponding 2 theta values of 43.38°, 62.88° (Figure 4.36). These results demonstrate that the NiO-CNTs nanocmposite is a mixture of two phases: face centered cubic NiO and hexagonal phase of CNTs deposited on a body-centered cubic phase of the steel substrate.

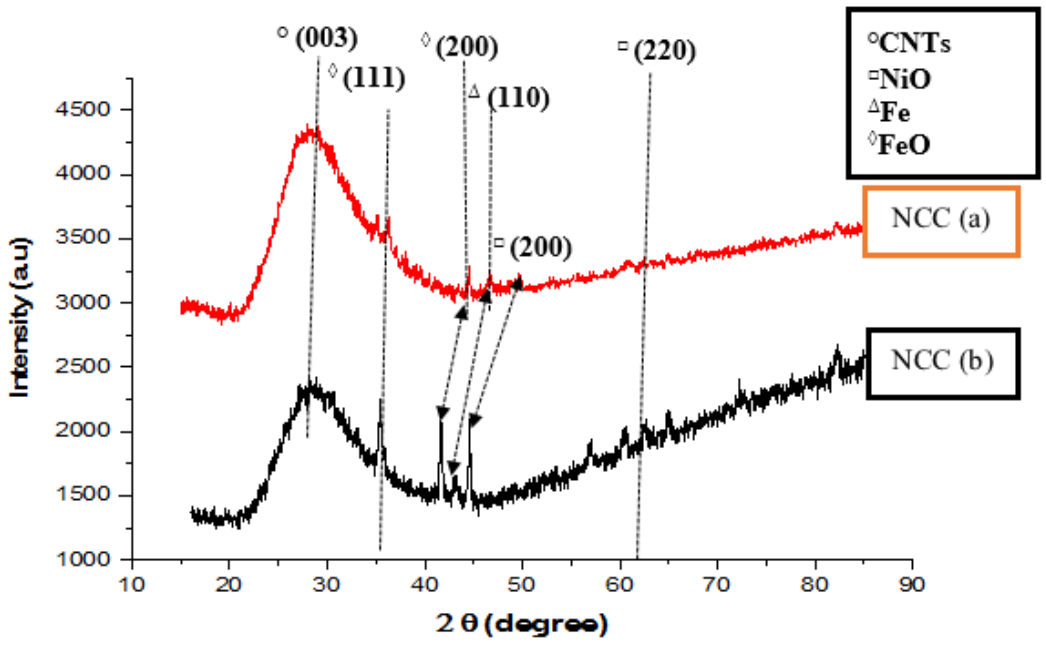

Figure 4.36: XRD Result for NiO-CNTs (1:2) Coated Samples before NCC (b) and after Corrosion Test NCC (a)

Conversely, crystallographic peaks at (111) and (200) at 2θ values appear to be present in both NCC (a) and NCC (b) pattern and could to the formation of an unstable iron oxide (FeO) on the surface of the substrate.

4.8.4 XRD of the SnO_2-CNTs (1:2) coated samples before and after corrosion test

Figure 4.37 shows the diffraction pattern on samples of SnO_2-CNTs before and after corrosion tests. The XRD results show the peaks with the following crytal planes (110), (101), (200), (211), and (221) with diffraction angles at 2θ = 26.55°, 33.86°, 37.12°, 51.87°, 62.95° which conforms to cassiterite crystal phase with a tetragonal rutile structure (JCPDS No. 41-1445). The diffraction peak at 2θ value of 26.60° was assigned to the (003) plane in graphite (JCPDS No. 26-1076). Whereas, orientation peaks at at a 2θ value of 44.49° (101), is typical of the body-centered cubic phase of Fe (JCPDS No. 06-0696).

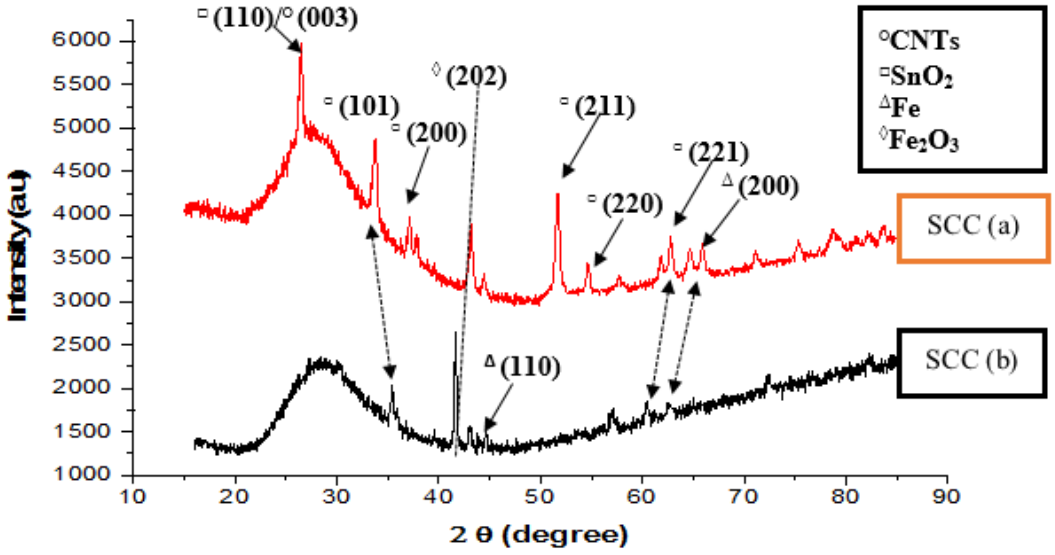

Figure 4.37: XRD Result for SnO_2-CNTs (1:2) Coated Samples before SCC (b) and after Corrosion Test SCC (a)

From Figure 4.37, the peaks appear to be less intense in the SSC (b) compared to the pattern in sample SCC (a), after the weight loss experiment for 9 months. This may be attributed to the fact that the corrosion test did not destroy the crystalline phases present initially, although some of the peaks with crystalline planes (101) and (221) appear to have shifted, they were never destroyed. In fact, diffraction peaks with crystalline planes (110) and (003) which did not appear at the SSC (b) pattern. Again, the presence of (202) which is indexed to Fe_2O_3 indicated the presence of corrosion product formed on the feedstock because of exposure time.

4.8.5 XRD of the NiO-CNTs-SnO_2 (1:2:1) coated samples before and after corrosion test

The XRD patterns of of NiO-CNTs-SnO_2 nanocomposite before and after the weight loss measurement in the soil is shown in Figure 4.38.

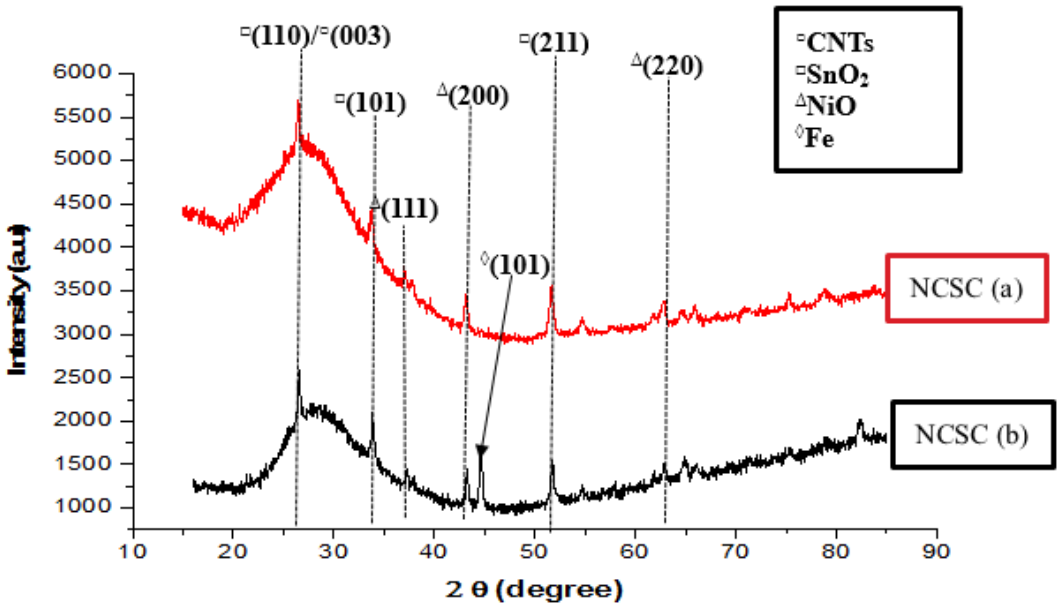

Figure 4.38: XRD Result for NiO-CNTs-SnO_2 (1:2:1) Coated Samples before NCSC (b) and after Weight Loss Test NCSC (a) for 9 Months

The deposited SnO_2 nanoparticles exhibits three broad diffraction peaks corresponding to (110), (101), and (211) reflections, which confirms the tetragonal structure of SnO_2

(JCPDS no. 41-1445). On the other hand, the NiO peaks have well appeared in addition to SnO_2 diffraction peaks. The observed diffraction peaks are related to (2 0 0) and (2 2 0), reflections, and indicates the co-deposition of cubic NiO in the nanocomposites (JCPDS no. 47-1049). While, diffraction peaks related to (101) and (003) are consistent with the body-centered cubic of Fe (JCPDS no.06-0696), and hexagonal structure of graphite (JCPDS no. 026-1076) respectively. From Figure 4.38 the XRD pattern for NiO-CNTs-SnO_2 (1:2:1) before NCSC (b) and after corrosion test NCSC (a) shows that apart from (101) which only appeared in the latter. All other diffraction peaks were replicated. It is observed the absence of any diffraction peak from the oxide of iron, this could be attributed to the fact that the NiO-CNTs-SnO_2 (1:2:1) was efficient in the provision of a coating barrier to prevent the formation of oxides of iron. Furthermore, the corrosion products formed by the NiO-CNTs-SnO_2 (1:2:1) formed a passivation layer blocking the pores against additional corrosion and preventing attack on the iron substrate.

4.8.6 XRD of the NiO-CNTs-SnO_2 (1:1:2) coated samples before and after corrosion test

In the case of Figure 4.39, diffraction peaks for NiO-CNTs-SnO_2 (1:1:2) coated samples before NCSC (b) after Corrosion Test NCSC (a) in the soil environment showed major a major difference in crystalline phases.

While the NCSC (b) had diffraction peaks (101), (200), (200), (101) and (221) originating from SnO_2, NiO and Fe respectively. NSSC (a) appeared to be amorphous and actually offered the the best corrosion resistance consistent from the study. This could be attributed to the fact that amorphous alloys offer better corrosion resistance compared to equivalent polycrystalline materials because the glassy film that passivates their surfaces prevents grain boundaries from forming (Hameed and Fekry, 2010).

However, the presence of possible corrosion products was not shown by the XRD analysis since most of this could have appeared as amorphous impurites.

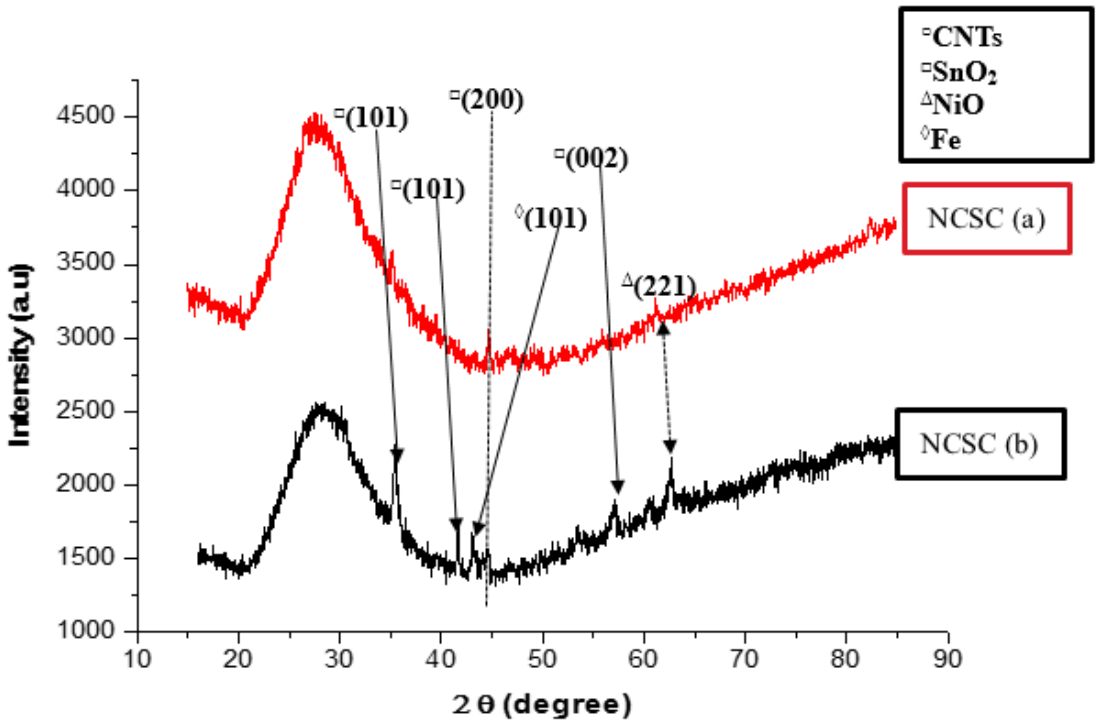

Figure 4.39: XRD Result for NiO-CNTs-SnO_2 (1:1:2) Coated Samples before NCSC (b) and after NCSC (a) Weight Loss Test in soil for 9 Months

Sadeghi *et al*., 2018 reported that the XRD patterns of the corrosion products formed on the NiCrMo coating after exposure at 600°C for 168 h was mainly composed of $NiCr_2O_4$ and MoO_3. Whereas the scale observed on NiCrMo-SiO_2 coating consisted of mainly Cr_2O_3 and SiO_2. When KCl was introduced, $NiCr_2O4$, MoO_3, and CrC_3 were formed on NiCrMo. However, no sign of CrC_3 was identified on NiCrMo-SiO_2. Lack of K_2CrO_4 in the XRD patterns of both coatings was was attributed to low penetration depth of x-ray.

4.9 Corrosion Mechanism for the Coating Process

The corrosion and rust formation on steel involve several steps of oxidation and reduction reaction in the anode or cathode as given in the Equations 4.18-4.26 below (Chang *et al.,* 2012).

At the cathode (surface of the composite)

$$O_{2(g)} + 2H_2O + 4e^- \rightarrow 4OH^- \quad (4.18)$$

At the anode (surface of the steel substrate)

$$Fe \rightarrow Fe^{2+} + 2e^- \quad (4.19)$$

$$Fe^{2+} \rightarrow Fe^{3+} + e^- \quad (4.20)$$

Further reactions

$$Fe^{2+} + 2OH^- \rightarrow Fe(OH)_2$$

(4.21)

(Magnetite is produced by incomplete oxidation)

$$3Fe(OH)_2 \rightarrow Fe_3O_4 + 2H_2O + H_2$$

(4.22)

Conversely,

$$Fe^{3+} + 3OH^- \rightarrow Fe(OH)_3 \quad (4.23)$$

In thr precence of chloride ion from the soil

$$Fe(OH)_3 + 6Cl^- \rightarrow 2FeCl_3^- + 2H_2O + H_2 + 4e^- \quad (4.24)$$

Since $(FeCl_3)$ is soluble in water; $FeO(OH)$ is precipitated

$$FeCl_3 + 2H_2O \rightarrow FeO(OH) + 3HCl \quad (4.25)$$

Which however, dehydrates and crystallizes to form hematite

$$2FeO(OH) \rightarrow Fe_2O_3 + H_2O \quad (4.26)$$

Or magnetite as the case maybe

$$12FeO(OH) \rightarrow 4Fe_2O_3 + 6H_2O + O_2 \quad (4.27)$$

Sufficient H_2O and O_2 and Cl^- ions are required for the formation of rust and dissolution of the steel for the corrosion to occur. The nanocomposite coatings play an important role for increasing the tortuosity of the diffusion pathways of water and oxygen

molecules to the substrate surface. This criterion was hence, observed because of the presence of properly dispersed NiO-CNTs-SnO_2 nanocoatings. Therefore, NiO-SnO_2 would hinder the formation of $FeO(OH)$ by the following mechanism. Plausibly, the NiO-SnO_2 coating protects the substrate by preferential dissolution of nickel occurring at open circuit potential, which causes tin enrichment in the coating surface layer. By reacting with water and scavenging chloride ions, the enriched tin surface could possibly form layers of adsorbed tin (IV) chloride anions that block the supply of water to the electrode, which is the first step in the formation of soluble Ni^{+2} species or a passive nickel film (Balaraju *et al.*, 2006; Lee, 2008). However, the improved corrosion protection in the presence of CNTs can be explained by two mechanisms of the nanocomposite coatings. Firstly, CNT nanoparticles act as inert physical barriers by occupying very small pores in the metal matrix, which modifies the NiO-SnO_2 hetero-junction in the microstructure and provides a superior corrosion resistance of the composite coating in comparison with the pure alloy coating. Via this mechanism, this is achieved by the incorporation of CNTs nanoparticles in the NiO-SnO_2 matrix (Lee, 2012).

In the second mechanism, incorporation of CNTs nanoparticles in the NiO-SnO_2 coating, forms corrosion microcells in which the CNTs nanoparticles act as a cathode and nickel acts as anode since the standard potential of CNTs (0.134 eV) is higher the standard potential of nickel (-0.236 eV). Such corrosion micro-cells facilitated anodic polarization. Therefore, in the presence of CNT nanoparticles, localized corrosion was inhibited, and was generally uniform (Chen *et al*., 2005; Aal, 2008). According to this mechanism, the resulting increase in SnO_2 content also gives the nanocomposite high chemical stability and high resistance to pitting attack from the mobile electrolytes such as Cl^- and SO_4^{2-} present in the soil solution. Overall, SnO_2 had an important effect on

the coating structure according to this study because the corrosion resistance of the composite NiO-CNTs-SnO_2 (1:2:1) had the best corrosion results from weight loss and electrochemical measurements. Consequently, the NiO-CNTs-SnO_2 (1:1:2) coating provided significantly better corrosion protection compared to the NiO-CNTs-SnO_2 (1:2:1) coating due to higher amount of SnO_2.

CHAPTER FIVE

5.0 CONCLUSION AND RECOMMENDATIONS

This chapter provides a summary of discussion, major findings and conclusion of the results in the previously discussed chapter. Recommendations for further study are also delineated.

5.1 Conclusion

In this work, to the best of our knowledge, NiO-CNTs-SnO_2 nanocomposite as a novel coating for corrosion protection of AISI 1020 steel was formulated for the first time. The following conclusions can be drawn from the studies;

Nickel (II) oxide, and tin (IV) oxide nanoparticles were synthesised using nickel (II) chloride hexahydrate ($NiCl_2.6H_2O$) and tin (II) chloride dihydrate ($SnCl_2.2H_2O$) precursors; with aqueous extract of *Africa cactus.*

While the production of multi-walled carbon nanotubes (CNTs) was carried out via catalytic chemical vapour deposition method on Fe-Ni/Kaolin catalyst. Optimization of process parameters such as, solution pH, precursor concentration and reaction temperature via surface response methodology (RSM) using the Box-Behnken method illustrated the effect of each parameter to the response factor (size of the nano-material, in nm). The optimum particle size of (6.15nm, 6.71 nm) was obtained at a solution pH of (8,10), precursor concentration of (0.37 mol/dm^3,0.40 mol/dm^3), and reaction temperature of (52.50°C, 57.50°C) for nickel and tin respectively.

NiO-CNTs, SnO_2-CNTs, NiO-SnO_2, and NiO-SnO_2-CNTs composites were prepared via wet impregnation/sonochemical methods involving variation of the amount of NiO, CNTs and SnO_2.

HRSEM-EDS analysis of the NiO-SnO_2(1:1) composite revealed a quasi-spherical morphology with slightly agglomeration and was considered optimum due to uniform dispersion of the particles over the whole area. NiO-CNTs-SnO_2 in the ratio of (1:1:2) and (1:2:1) were selected as optimum from this study because above or below this mixing ratio, the HRSEM micrographs showed a more aggregated and evenly dispersed NiO-CNTs-SnO_2 composition. EDS analysis of the as-synthesised nanomaterials showed the presence of major elemental components such as Sn, Ni, C, O in the corresponding composite. HRTEM of all sample containing CNTs revealed that the wall structure of the CNTs vary, with different diameter (15-23 nm) between neighbouring planes of CNTs oriented in the (003) direction with a lattice spacing of 0.34 nn. Whereas the directional fringe patterns of NiO samples corresponded to the interplaner spacing (d), of 0.21 nm, corresponding to the (200) crystal plane of NiO.

The interplanar spacing of individual particles contained SnO_2 corresponed to 0.33 nmin the direction of (110) plane. The SAED pattern confirmed the graphitic nature of the CNTs with the innermost ring showing the strongest reflection plane of (003). While the strongest reflection for NiO and SnO_2 were at (200) and (110) respectively. XRD results revealed the existence of diffraction peaks originating from bunsenite face cubic center NiO, graphitic carbon from CNTs and tetragonal casseterite phase of SnO_2 in the NiO-CNTs-SnO_2 nanocomposites. While XPS confirmed the presence of intermetallic bonding such as (Ni-Sn) in the NiO-SnO_2 composite as well as Nickel

oxycarbide-tin alloy which act as a protective layer against external corrosive agents in the soil.

The developed NiO, SnO_2, CNTs, NiO-CNTs, SnO_2-CNTs, NiO-SnO_2, and NiO-SnO_2-CNTs nanocomposites were applied on the surface of the AISI 1020 steel as nanocoatingsby a simple and facile deep coating process.

Physicochemical analysis revealed that the soil is highly corrosive with pH (6.48-6.7), resistivity (468-704 Ω.cm), moisture content (5.92-13.97%), chloride ion (292.0-441.5 mg/kg) and sulphate ion (629- 845 mg/kg) according to EN standard.

Futhermore, the corrosion behavior of the different NiO and SnO_2 based coatings (NiO-SnO_2, NiO-CNTs, SnO_2-CNTs, and NiO-CNTs-SnO_2, with ratio (1:1:2, and 1:2:1) were studied by weight loss measurements, potentiodynamic polarization curves and the modelling of EIS spectra in a real soil environment. The obtained parameters for circuit elements were interpreted. During the potentiodynamic polarization tests in soil electrolyte, the nanocomposite NiO-CNTs-SnO_2, (1:2:1), showed the exellent corrosoin resistance behavior with lowest corrosion current of 0.0064μA/cm^2 (descending 93% compared with AISI 10120 substrate). The corrosion rate was also decreased from 0.0335 mpy to 0.0022 mpy showing evidence of a slowed rate of uniform corrosion and the protection of the steel substrate.

EIS studies verified that charge transfer resistance Rct, was initially low and increased with the presence of the nanocoatings reaching the value of 6.244 KΩ·cm^2 for NiO-CNTs-SnO_2, (1:2:1) (raising about sixteen folds compared with AISI 10120 substrate), with a protection efficiency of 93.90%. Weight loss increased with the time the AISI 1020 steel coupons were buried in the soil electrolyte. The slowest corrosion rate was

recorded as 8.76E-08 mpy for NiO-CNTs-SnO_2 (1:1:2) after 12 months, which is the best nanocoating in the study. Lastly, a corrosion protection efficiency of 94% was established based on gravimetry, potentiodynamic polarization and electrochemical impedance measurements for ternary NiO-CNTs-SnO_2 (1:1:2) nanocomposite coating, suggesting that it could be a potential material for the protection of AISI 1020 steel coupons in soil environment.

5.2 Recommendations

Further studies are suggested as follows:

1. Research should be conducted in various soil test environments to establish the relationship between physicochemical properties in the soil such as, moisture content, resistivity and pH with corrosion rate in the same environment.
2. The thermal stability and flame retardancy performance should be carried out on the developed nanocomposites to access their effects or otherwise.

5.3 Contribution to Knowledge

1. The bio-reduction of nickel (II) chloride hexahydrate ($NiCl_2.6H_2O$) and tin (II) chloride dihydrate ($SnCl_2.2H_2O$) precursors; with aqueous extract of *Africa cactus to* Ni^0 and Sn^0 valent nanoparticles via green synthesis.
2. Box-Behnken Design was used to optimize process parameters such as, solution pH, precursor concentration and synthesis temperature in the synthesis of NiO and SnO_2 nanoparticles produced via green synthesis for the first time.
3. The development of Nickel oxycarbide tin nanocomposite ($Ni_{0.14}Sn_{0.16}OC_{2.59}$) as obtained from XPS analysis.
4. The application of the developed composite in the coating of AISI 1020 steel, with coating protection efficiency of up to 94%.

REFERENCES

Aal, A. A. (2008). Hard and corrosion resistant nanocomposite coating for Al alloy. *Material Science and Engineering: A*, 474(2), 181-187.

Abakay, E., Durmaz, M., Sen, S. & Sen, U. (2017). An electrochemical study of the corrosion resistance of niobium-aluminum carbonitride coating produced on steels by thermo-reactive diffusion technique. *Acta Physica Polonica A*, 132(3), 682–684.

Abdeen, D. H., Hachach, M., E. I. & Koc, M. (2019). A review on the corrosion behaviour of nanocoatings on metallic substrates. *Materials*, 12, 210.

Abdulrahaman, M. A., Abubakre, O. K., Abdulkareem, S. A., Tijani, J. O., Aliyu, A. & Afolabi, A. S. (2017). Effect of coating mild steel with CNTs on its mechanical properties and corrosion behaviour in acidic medium. *Advances in Natural Sciences: Nanoscience and Nanotechnology,* 8, 015016.

Abdulrahman, A. S., Kareem, A. G., Ibrahim, H. K. & Awe, I. C. (2015). The corrosion inhibition of mild steel in sulphuric acid solution by adsorption of African *Perquetina* leaves extract. *International Journal of Innovative Research in Science Engineering and Technology,* 4(4), 1809-1921.

Aduagba, K. G., Salawu, A. A., Ibrahim, H. K. & Aris, M. I. (2016). Treatment of corrosion of mild steel with Akee apple (*Blighia sapida*) leaves extract in sulphuric. *European Cooperation,* 11(18), 42–53.

Agarwal, D.C. & Kloewer, J. (2001). Nickel base alloys: Corrosion challenges in the new millennium, *Corrosion*, 01325, 1-5.

Agarwala, V., Agarwala, R. C. & Daniel, B. S. S. (2006). Development of nanograined metallic materials by bulk and coating techniques. S*ynthesis and Reactivity in Inorganic Metal-Organic and Nano-Metal Chemistry*, 36, 3–16.

Ahmad, Z. (2006). *Principles of Corrosion Engineering and Corrosion Control*; Elsevier: Oxford, UK. 243-234.

Ai, Y., Xia, L., Pang, F., Xu, Y., Zhao, H. & Jian, R. (2020). Mechanically strong and flame-retardant epoxy resins with anti-corrosion performance. *Composites Part*

B, 193(3), 108019.

Ajayan, P. M., Schadler, L. S., Giannaris, C. & Rubio, A. (2000). Single-walled carbon nanotube-polymer composites: Strength and weakness. *Advances in Materials*, 12, 750-753.

Ajayi, O. M., Odusote, J. K. & Yahya, R. A. (2014). Inhibition of mild steel corrosion using *Jatropha curcas* leaf extract. *Journal of Electrochemistry Science and Engineering,* 4 (2), 67-74.

Akhir, M. A. M., Mohamed, K., Lee, H. L. & Rezan, S. A. (2016). Synthesis of tin oxide nanostructures using hydrothermal method and optimization of its crystal size by using statistical design of experiment synthesis of tin oxide nanostructures using hydrothermal method and optimization of its crystal size by using statistical design of experiment. *Procedia Chemistry*, 19 (6), 993–998.

Akpoborie, J., Fayomi, O.S.I., Inegbenebor, A.O., Ayoola, A.A., Dunlami, O., Samuel, O.D. & Agboola, O. (2021). Electrochemical reaction of corrosion and its negative economic impact. *IOP Conference Series: Materials Science and Engineering.* 1107, 012071.

Alamilla, J. L., Espinosa-Medina, M. A. & Sosa, E. (2009). Modelling steel corrosion damage in soil environment. *Corrosion Science*, 1, 2628-2638.

Alaoui A, Kacemi, K. L, Ass, K. E. & Kitane, S. (2015). Application of Box-Behnken design to determine the optimal conditions of reductive leaching of MnO_2 from manganese mine tailings. *Russian Journal of Non-Ferrous Metals*, 56, 134-141.

Ali, S. M. & Allehaibi, H. (2017). Nano-structured sol–gel coatings as protective films against zinc corrosion in 0.5 M HCl solution. *Journal of Saudi Chemical Society*. 21(4), 473-480.

Ali, S., Ali, A. & Nawfel, M. B. (2016). Numerical investigation for enhancement of heat transfer in internally finned tubes using ANSYS CFX program, Basrah. *Journal of Engineering Science*. 16(2), 89–99.

Alishahi, M., Monirvaghefi, S. M., Saatchi, A. & Hosseini, S. M. (2012). The effect of carbon nanotubes on the corrosion and tribological behavior of electroless Ni–P–CNT composite coating. *Applied Surface Science*, 258 (7), 2439-2446.

Aliyu, A. & Srivastava, C. (2020). Morphology and corrosion properties of FeMn-Graphene oxide composite coatings. *Journal of Alloys and Compounds*, *821*, 153560.

Aliyu, A., Abdulkareem, A. S., Kovo, A. S., Abubakre, O. K., Tijani J. O. & Kariim, I. (2017). Synthesize multi-walled carbon nanotubes via catalytic chemical vapour deposition method on Fe-Ni bimetallic catalyst supported on kaolin, *Carbon*

Letters, 21, 33–50.

Allahyarzadeh, M. H., Aliofkhazraei, M., Sabour-Rouhaghdam, A. R. & Torabinejad, V. (2016). Functionally graded nickel–tungsten coating: electrodeposition, corrosion and wear behaviour, *Canadian Metallurgical Quarterly*, 55(30) 303-3011.

Al-Sarraf, A. R. & Yaseen, M. A. (2018). Preparing and Study the effects of Composite Coatings in Protection of Oil Pipes from the Risk of Corrosion that resulting from Associated water with Petroleum Products, IOP Conf. Series: *Journal of Physics: Conference Series,* 1003, 012103.

Amadi, S. A. & Ukpaka, C. P. (2016). Evaluation of the metals corrosion in soil environment of Niger Delta area of Nigeria. *Nigerian Journal of Oil and Gas Technology*, 104-117.

American Galvanizers Association, (AGA). (2019). Retrieved from https://www.galvanizeit.org/ 12-February 2019.

Amirudin, A. & Thieny, D. (1995). Application of electrochemical impedance spectroscopy to study the degradation of polymer- coated metals. *Progress in Organic Coatings*, 26, 1–28.

Ammar, A. U., Shahid, M., Ahmed, M. K., Khan, M., Khalid, A. & Khan, Z. A. (2018) Electrochemical study of polymer and ceramic-based nanocomposite coatings for corrosion protection of cast iron pipeline. *Materials*, 9, 332.

Anbarasi, K. & Vasudha, V. G. (2014). Corrosion inhibition potential of Cucurbita maxima plant extract on mild steel in acid media. *Chemical Science Review and Letters*, 3 (9), 45–51.

Andreatta, F., Aldighieri, P., Paussa, L., Di-Maggio, R., Rossi, S. & Fedrizzi, L. (2007). Electrochemical behaviour of ZrO_2 sol–gel pre-treatments on AA 6060 aluminium alloy. *Electrochimica. Acta,* 52, 7545–7555.

Angulakshmi, V. K. (2015). Effect of synthesis temperature on the growth of multiwalled carbon nanotubes from *Zea mays* Oil as evidenced by Structural, Raman and XRD Analyses, *Advances in Condensed Matter Physics*, Article ID 420619, 1-7.

Anthony, C. J. & Michael, L. H. (2009). Overview of chemical vapor deposition. In: Anthony C. J and Michael L. H. (Eds). *Precursors, processes and applications*. (pp 7477-7479). London, Published by the Royal Society of Chemistry.

Arriba-Rodriguez, L., Ortega-Fernandez, F., Villanueva-balsera, J. & Rodriguez-perez, F. (2018). Methods to evaluate corrosion in buried steel structures: A Review. *Metals*, 8, 334.

Asadi, N., Naderi, R. & Saremi, M. (2014). Determination of optimum concentration of cloisite in an eco-friendly silane sol-gel film to improve corrosion resistance of mild steel. *Applied Clay Science*, 95, 243-251.

Asadi, Z. S. & Melchers, R. E. (2018). Long-term external pitting and corrosion of buried cast iron water pipes. *Corrosion Engineering, Science and Technology*, 53(2), 93-101.

Ashik, U. P. M., Kudo, S. & Hayashi, J. (2018). An Overview of Metal Oxide Nanostructures. *Synthesis of Inorganic Nanomaterials,* 19–57.

ASM International. (2000). The Effects and Economic Impact of Corrosion. In Corrosion: Understanding the Basics; ASM International: Materials Park, OH, USA, 1-21.

ASTM Committee D162-99 on Standard Practice for Conducting and Evaluating Laboratory Corrosions Tests in Soils (2004). *ASTM standard and literature references for soil tests*. West Conshohocken, PA: ASTM.

ASTM Committee D4220-95 on Standard Practices for Preserving and Transporting Soil Samples (2000). *ASTM standard and literature references for soil tests*. West Conshohocken, PA: ASTM.

ASTM Committee F1089 on Standard Test Method for Corrosion of Surgical Instruments (2002). *ASTM standard and literature references for testing surgical instruments*. West Conshohocken, PA: ASTM.

ASTM Committee F746 on Standard Test Method for Pitting or Crevice Corrosion of Metallic Surgical Implant Materials. (2014). *ASTM standard and literature references for testing surgical instruments*. West Conshohocken, PA: ASTM.

ASTM Committee G01-03 on Standard Practice for Preparing, Cleaning and Evaluating Corrosion Test Specimen (1999). *ASTM standard and literature references for corrosion measurement*. West Conshohocken, PA: ASTM.

ASTM Committee G187-12 on Standard Test Method for Measurement of Soil Resistivity using the Two-electrode Soil Box Method (2012). *ASTM standard and literature references for soil tests*. West Conshohocken, PA: ASTM

Atta, A. M., El-mahdy, G. A., Al-lohedan, H. A. & Al-hussain, S. A. (2014). Corrosion inhibition of mild steel in acidic medium by magnetite myrrh nanocomposite. *International Journal of Electrochemical Science,* 9, 8446–8457.

Attarchi, M. & Sadrnezhaad, S. K (2009). Pulse reverse electrodeposition of spherical Ni-MWCNT composite skein. *International Journal of Engineering Transactions, B*, 22B, 161–168.

Awe I. C., Abdulraman, A. S., Ibrahim, H. K. & Kareem A. G. (2015). Inhibitive performance of bitter leaf root extract on mild steel corrosion in sulphuric acid solution, *American Journal of Material Engineering and Technology*, 3 (2), 35-45.

Ayuk, E. L., Ugwu, M. O. & Aronimo, S. B. (2017). A Review on synthetic methods of

nanostructured materials. *Chemical Research Journal*, 2(5), 97-123.

Ba-Abbad, M. M., Kadhum A. A, Mohamad A. B., Takriff, M. S. & Sopian, K. (2013). Optimization of process parameters using D-optimal design for synthesis of ZnO nanoparticles via sol–gel technique. *Journal of Industrial and Engineering Chemistry,* 19, 99-105.

Ba-Abbad, M. M., Chai, P. V., Takriff, M. S., Ben-, A. & Mohammad, A. W. (2015). Optimization of nickel oxide nanoparticles synthesis through the sol gel method using Box–Behnken design. *Materials and Design*, 86, 948-956.

Bahari, Y. M. M., Sadrnezhaad, S. K. & Hosseini, D. (2008). NiO nanoparticles synthesis by chemical precipitation and effect of applied surfactant on distribution of particle size. *Journal of Nanomaterials*.Article ID 470595, 1-4.

Baig, N., Kammakakam, I. & Falath, W. (2021). Nanomaterials: a review of synthesis methods, properties, recent progress, and challenges. *Material Advances*, 2, 1821.

Balan, P., Shelton, M. J., Ching, D. O. L., Han, G. C. & Palniandy L. K. (2014). Modified silane films for corrosion protection of mild steel. *Procedia Materials Science*, 6, 244-248.

Balaraju, J. N., Selvi, V. E., Grips, V. K.W. & Rajam, K. S. (2006). *Electrochimica Acta,* 52, 1064-1074.

Banerjee, D., Ghorai, U. K., Das, N. S., Das, B., Thakur, S. & Chattopadhyay, K. K. (2018). Amorphous carbon nanotubes − nickel oxide nano flower hybrids: a low cost energy storage material. *American Chemical Society Omega, 3,* 6311–6320.

Bao, W., Deng, Z., Zhang, S., Ji, Z. & Zhang, H. (2019). Next-generation composite coating system: Nanocoating. *Frontiers in Materials,* 6(4), 1-6.

Barsoukov, E. & Macdonald, J. R. (2005). *Impedance spectroscopy: Theory, experiment and applications*. Hoboken, New Jersey: Wiley-interscience Press.

Bayliss, D. A. & Deacon, D. H. (2002). *Steelwork corrosion control*. London, UK: CRC Press.

Beg, S. & Akhter S. (2021) Box–Behnken designs and their applications in pharmaceutical product development. In: Beg S. (eds) *Design of Experiments for Pharmaceutical Product Development* (pp. 91-124). Singapore: Springer Press.

Berke, N. S., Bucher, B. E., Little, D., & Von Fay, K. F. (2016). *Test Protocol to Evaluate the Effectiveness of Embedded Sacrificial Anodes in Reinforced Concrete*. Vancouver British Columbia Canada: National Association of Corrosion Engineers, 7524.

Berradja, A. (2019). Corrosion Inhibitors In: Ambrish Singh (Eds.), *Electrochemical techniques for corrosion and tribocorrosion monitoring: methods for the assessment of corrosion rates* (pp. 2-121). London, IntechOpen.

Bhattarai, J. (2013). Study on the corrosive nature of soil towards the buried-structures. *Scientific World Journals,* 11, 43–47.

Bose, S., Khare, R. A. & Moldenaers, P. (2010). Assessing the strengths and weaknesses of various types of pre-treatments of carbon nanotubes on the properties of polymer/carbon nanotubes composites: A critical review. *Polymer*, 51, 975 (2010).

Bradford, S. A (2000). *The Practical Handbook of Corrosion Control in Soils*. Edmonton, AB, Canada: CASTI Publishing Incoporation.

Brinker, C. J., Frye, G. C., Hurd, A. J. & Ashley, C.S. (1991). Fundamentals of sol-gel dip coating. *Thin Solid Films*, 201, 97–108.

Busby, J. P., Entwisle, D., Hobbs, P., Jackson, P., Johnson, N., Lawley, R., Linley, K., Mayr, T., Palmer, R. & Rines, M. (2012). A GIS for the planning of electrical earthing. *Quarterly Journal of Engineering Geology and Hydrogeology*, 45, 379–390.

Calabrese, L. & Proverbio, E. (2019). A brief overview on the anticorrosion performances of sol-gel zeolite coatings. *Coatings*, 9(409), 2-25.

Callister, W. D. & Rethwisch, D.G. (2012). Fundamentals of Materials Science and Engineering an Integerated Approach, (3rd ed.). Hoboken, NJ, USA: John Wiley & Sons Incoporation: 341-354.

Cao, W. (2016). Synthesis of Nanomaterials by Laser Ablation. *Skyspring Nanomaterials Incoporated*, 11-16.

Chakrabarty, S. & Chatterjee, K. (2008). Synthesis and characterization of nanodimensional NiO semiconductor. *Journal of Physical Sciences*, 13, 245-250.

Chang, C. H., Huang, T. C., Peng, C.W., Yeh, T. C., Lu, H. I., Hung, W. L., Weng, C. J., Yang, T. I. & Yeh, J. M. (2012). Novel anticorrosion coatings prepared from polyaniline/graphene composites. *Carbon*, 50, 5044–5051.

Chelladurai, S. J. S. & Arthanari, R. (2018). Effect of stir cast process parameters on wear behaviour of copper coated short steel fibers reinforced LM13 aluminium alloy composites, *Materials Research Express,* 5(6), 066550.

Chelladurai, S. J. S., Arthanari, R., Selvarajan, R., Ravichandran, T. P., Ravi, S. K. & Petchimuthu, S. R. C. (2019). Optimisation of dry sliding wear parameters of squeeze cast AA336 aluminium alloy: copper-coated steel wire-reinforced composites by response surface methodology. *International Journal of Metalcasting* 13(2), 354-366.

Chelladurai, S. J. S., Murugan, K., Ray, A. P., Upadhyaya, M., Narasimharaj, V. & Gnanasekaran, S. (2020). Optimization of process parameters using response surface methodology: A review. *Materials Today: Proceedings*, 37(2), 1301–1304.

Chen, G., Yang, J., Tang, J. & Zhou, X. (2015). Hierarchical $NiCo_2O_4$ nanowire arrays on Ni foam as an anode for lithium-ion batteries. *Royal Society of Chemistry Advances*, 5, 23067– 23072.

Chen, S., Zhao, W., Liu, W. & Zhang, S. (2009). Preparation, characterization and

activity evaluation of p–n junction photocatalyst p-NiO/n-ZnO. *Journal of Sol-Gel Science and Technology,* 50, 387-396.

Chen, W. & Gao, W. (2011). Microstructures and properties of sol-enhanced nanostructured metal-oxide composite coatings. *Progress in Natural Science: Materials International*, 21, 355–362.

Chen, W., He, Y. & Gao, W. (2010). Synthesis of Nanostructured Ni–TiO_2 Composite Coatings by Sol-Enhanced Electroplating. *Journal of Electrochemical Society*, 157(8), 122-8.

Chen, X. H., Chen, C. S., Xiao, H. N., Cheng, F. Q., Zhang, G. & Yi, G. J. (2005). Corrosion behavior of carbon nanotubes – Ni composite coating. *Surface and Coatings Technology*, 191 (2005), 351–356.

Chen, Y., Lu, X. & Gao, B. (2014). Ionic Liquid-Assisted Synthesis of a NiO/CNTs Composite and Its Electrochemical Capacitance. *Royal Society of Chemistry Advances*, 6, 1–9.

Chhetri, S., Ghosh, S., Samanta, P. & Murmu, C. (2019). Effect of Fe_3O_4 -decorated n-doped reduced graphene oxide nanohybrid on the anticorrosion performance of epoxy composite coating. *Chemistry Select*, 4, 13446–13454.

Chigondo, M. & Chigondo, F. (2016). Recent natural corrosion inhibitors for mild steel: An overview. *Journal of Chemistry*, Article ID 6208937, 1-7.

Chui, Z., Chen, S., Wang, L., Man, C., Liu, Z., Wu, J., Wang, X., Chen, S. & Li, X. (2017). Passivation behavior and surface chemistry of 2507 super duplex stainless steel in acidified artificial seawater containing thiosulfate. *Journal of Electrochemical Society*, 164, 856–868.

Ciubotariu, A-C., Benea, L., Lakatos, M. & Dragan, V. (2008). Electrochemical impedance spectroscopy and corrosion behaviour of Al_2O_3-Ni nano-composite coatings. *Electrochimica Acta*, 53, 4557–4563.

Clemente, F., Arpaia, P. & Manna, C. (2013). Characterisation of human skin impedance after electrical treatment for transdermal drug delivery, *Measurement*, 46, 3494–3501.

Coana, T. Barrosob, G. S., Motzb, G., Bolzána, A. & Machadoa, R. A. F. (2013). Preparation of PMMA/hBN composite coatings for metal surface protection. *Materials Research,* 16(6), 1366-137.

Coetzee, D., Venkataraman, M., Militky, J. & Petru, M. (2020). Influence of nanoparticles on thermal and electrical conductivity of composites. *Polymers*, 12(4).

Cole, I. & Marney, D. (2012). The science of pipe corrosion: A review of the literature on the corrosion of ferrous metals in soils. *Corrosion Science*. 56, 5-16. DOI: 10.1016/j.corsci.2011.12.

Contreras, A. & Quej-Ake, L. M., Lizárraga, C. R. & Pérez, T. (2015). The role of

Calcareous Soils in SCC of X52 Pipeline Steel. *Materials Research Society Symposium Proceeding,* 1766(3), 416-427.

Corrosion Costs and Preventive Strategies in the United States, (2013), retrieved from http://www.cctechnologies.com, 2nd August, 2019 .

Cummiings, F. R. (2012). *TiO_2 nanotube based dye-sensitised solar cells* (Doctorate dissertation). University of the Western Cape, Cape Town, South Africa.

Danafar, F., Razi, A. F., Salleh, M. A. M. & Biak, D. R. A. (2009). Fluidized bed catalytic chemical vapor deposition synthesis of carbon nanotubes: A review. *Chemical Engineering Journal*, 155, 37–48.

Daneshvar, F. (2016). Carbon nanotube/metal corrosion issues for nanotube coatings and inclusions in a matrix. *Applied Physics*, 1-17.

Das, A. K. & Dewanjee, S. (2018). Optimization of extraction using mathematical models and computation. In S. D. Sarker & L. Nahar (Eds.), *Computational Phytochemistry*, 75–106.

Das, R., Ali, E., Bee, S., Hamid, A., Ramakrishna, S. & Zaman, Z. (2014). Carbon nanotube membranes for water purification: A bright future in water desalination. *Desilination, 336*, 97–109.

Das, S., Banthia, S. Patra, A. Sengupta, S. & Singh, S. B. (2018). Novel bilayer Zn-Ni/Ni-CoSiC nanocomposite coating with exceptional corrosion and wear properties by pulse electrodeposition. *Journal of Alloys and Compounds*, 738, 394-404.

Dastjerdi, R. & Montazer, M. (2010). A review on the application of inorganic nano-structured materials in the modification of textiles: Focus on anti-microbial properties. *Colloids and Surfaces B: Biointerfaces*, 79, 5– 18.

Davis, J. R. (2001). *Surface engineering for corrosion and wear resistance*. Cleveland, OH USA: ASM International, ISBN 1615030727. 2.

Deepa, K., Venkatesha, T. V., Nagaraja, C. & Vinutha, M. R. (2017). Electrochemical corrosion studies of Zn-CuO and Zn-NiO-CuO composite coatings on mild steel. *Analytical & Bioanalytical Electrochemistry*, 9 (3), 374-389.

Deepa, K. & Venkatesha, T. V. (2018). Journal of science: Advanced materials and devices combustion synthesis of Ni doped SnO_2 nanoparticles for applications in Zn-composite coating on mild steel. *Journal of Science: Advanced Materials and Devices*, 3(4), 412–418.

De-Oliveira, P. F. M., Torresi, R. M., Emmerling, F. & Camargo, P. H. C. (2020). Challenges and opportunities in the bottom-up mechanochemical synthesis of noble metal nanoparticles. *Journal of Materials Chemistry A*, 8(32), 16114–16141.

Dervishi, E., Li, Z., Xu, Y., Saini, V., Biris, A. R., Lupu, D. & Biris, A. S. (2009). Carbon nanotubes: synthesis, properties, and applications. *Particulate Science Technology*, 27(2), 107-125.

Dong, D., Chen, X. H., Xiao, W. T., Yang, G. B. & Zhang, P. Y. (2009). Preparation and properties of electroless Ni-P-SiO_2 composite coatings. *Applied Surface Science*, 255, 7051-7055.

Dubois, N. A. (1913). Protection of iron and steel by paint films. *The journal of industrial and engineering chemistry,* 5 (12), 34-54.

Dumain, E. D, Agawa, T. & Goel, S. (1999). Cure behavior of polyesteracrylate hybrid powder coatings. *Journal of Coating Technolology,* 71, 69–75.

Dunens, O. M., MacKenzie, K. J. & Harris, A. T. (2009). Synthesis of multiwalled carbon nanotubes on fly ash derived catalysts. *Environmental Science Technology,* 43(20), 7889-7894.

Dupuis, A. C. (2005). The catalyst in the CCVD of carbon nanotubes: A review. *Progress in Material Sciences,* 50, 929–961.

Eatemadi, A., Daraee, H., Karimkhanloo, H., Kouhi, M. & Zarghami, N. (2014). Carbon nanotubes: Properties, synthesis, purification, and medical applications. *Research Letters,* 9, 393 1–13.

Elango, G., Manoj, S., Santhosh, S., Muthuraja, S. & Mohana, S. (2015). Green synthesis of SnO_2 nanoparticles and its photocatalytic activity of phenolsulfonphthalein dye. *Spectrochimica Acta Part A: Molecular and Biomolecular Spectroscopy*, 145, 176–180.

Eliyan, F. F. & Alfantazi, A. (2013). Corrosion of the Heat-Affected Zones (HAZs) of API-X100 pipeline steel in dilute bicarbonate solutions at 90^{o}C: An electrochemical evaluation. *Corrosion Science*, 74, 297–307.

Eliyan, F. F. & Alfantazi, A. (2014). Mechanisms of corrosion and electrochemical significance of metallurgy and environment with corrosion of iron and steel in bicarbonate and carbonate solutions—A review. *Corrosion*, 70, 880–898.

Elizabeth, I., Nair, A. K., Pratap, B. & Gopukumar, S. (2017). Electrochimica acta multifunctional Ni-NiO-CNT composite as high performing free standing anode for Li ion batteries and advanced electro catalyst for oxygen evolution reaction. *Electrochimica Acta*, *230*, 98–105.

EN 12501-2. (2003). *Protection of metallic materials against corrosion. corrosion likelihood in soil. part 2: Low alloyed and unalloyed ferrous materials*. Pilsen, Czech Republic: European Standard Store.

Escalante, E. (1995). Corrosion tests and standards: Application and interpretation. In R. Baboian (Ed.), *Soils* (pp.137-142). Philadelphia: ASTM Interational.

Eugene, A, L., Ugwu, M, O. & Aronimo, S. B. (2017). A review on synthetic methods of nanostructured materials. *Chemistry Research Journal,* 2(5), 97-123.

Ezhilarasi, A. J., Vijaya, J. K., Kaviyarasu, M., Maaza, A., Ayeshamariam, L. & Kennedy, J (2016). Green synthesis of NiO nanoparticles using *Moringa oleifera* extract and their biomedical applications: Cytotoxicity effect of nanoparticles against HT-29 cancer cells. *Journal of Photochemistry and Photobiology*, 164,

352-360.

Farag, A. A. (2020). Applications of nanomaterials in corrosion protection coatings and inhibitors *Corrosion Revision*. 1–20.

Farrukh, M. A., Heng, B. & Adnan, R. (2010). Surfactant-controlled aqueous synthesis of SnO_2 nanoparticles via the hydrothermal and conventional. *Turkish Journal of Chemistry*, 34:537-550.

Fayomi, O. S. I., Akande, I. G. & Odigie, S. (2019). Economic Impact of Corrosion in Oil Sectors and Prevention: An Overview. *Journal of Physics: Conference Series*, 1378(2).

Fayomi, O. S. I., Popoola, A. P. I. & Aigbodion, V. S. (2015). Investigation on microstructural, anti-corrosion and mechanical properties of doped Zn–Al – SnO_2 metal matrix composite coating on mild steel. *Journal of Alloys and Compounds, 623,* 328–334.

Feng, C., Li, L., Guo, Z. & Li, H. (2010). Synthesis and characterisation of tin dioxide / multiwall carbon nanotube composites. *Journal of Alloys and Compounds,* 504, 457–461.

Ferreira, C. A. M., Ponciano, J. A., Vaitsman, D. S. & Pérez, V. (2007). Evaluation of the corrosivity of the soil through its chemical composition. *Science of the Total Environment*, 388, 250–255.

Fiedler, S., Veparskas, M. & Richardson, J. L. (2007). *Soil redox potential: Importance, field measurements, and observations, in advances in agronomy*. In: D.L. Sparks, (Eds.). Cambridge, UK: Academic Press. 94, 1–54.

Forsyth, M. & Hinton, B. (2014). Rare Earth-Based Corrosion Inhibitors. OK, USA: Woodhead Publishing, ISBN 9780857093585.

Fu, Y., Ma, R., Shu, Y., Cao, Z. & Ma, X. (2009). Preparation and characterisation of SnO_2/ carbon nanotube composite for lithium ion battery applications. *Materials Letters, 63*(22), 1946–1948.

Fujimoto, S. & Tsuchiya, H. (2007). Semiconductor properties and protective role of passive films of iron base alloys, *Corrosion Science* number, 49, 195-202.

Gang, W. U., Xiao-yan, T., Gui-ying, L. I. & Chang-wei, H. U. (2013). Effect of molar ratio of citric acid to metal nitrate on the structure and catalytic activity of NiO nanoparticles. *Chemical Research China University,* 29, 154-158.

Gao, W. & Li, Z. (2004). Nano-structured alloy and composite coatings for high temperature applications. *Material Resources*, 7, 175–182.

Gao, W., Cui, T. T., Zhu, Y. F., Wen, Z., Zhao, M. & Li, J. C. (2015). Design principles of inert substrates for exploiting gold clusters' intrinsic catalytic reactivity. *Scientific Reports,* 5, 15095.

García, S. J., Fischer, H. R. & Van der Zwaag, S. (2011). A critical appraisal of the potential of self-healing polymeric coatings. *Progress in Organic Coatings*, 72, 211-221.

Garcia-Heras, M., Jimenez-Morales, A., Casal, B., Galvan, J. C., Radzki, S. & Villegas, M. A. (2004). Preparation and electrochemical study of cerium-silica sol-gel thin films. *Journal of Alloys and Compounds*, 380, 219–224.

Georgiou, E. P., Van der Donck, T. & Celis, J. P. (2017). Electrodeposition and structural characteristics of intermetallic nickel-tin based coatings. *International Journal of Surface Engineering and Coatings.* 95(6), 301-307.

Ger, M. D. & Hwang, B. J. (2002). Corrosion and wear resistance study of Ni-P and Ni-P-PTFE nanocomposites coatings. *Material Chemistry and Physics,* 76, 38– 45.

Gharegozloo, S. H., Ataie, A., Abdizadeh, H., Mostafavi, E. Parnianb, M. J. & Khodadadib, A. A. (2016). High performance Ni–CNTs catalyst: Synthesis and characterisation. *Royal Society of Chemistry Advances, 6*, 47072–47082.

Ghasemzadeh, A., Hawa, H. Z. E. & Rahmat, J. A. (2010). Antioxidant activities, total phenolics and flavonoids content in two varieties of Malaysia Young Ginger (*Zingiberofficinale Roscoe*). *Molecules*, 15, 4324-4333.

Ghosh, S. K., Dey, G. K., Dusane, R. O. & Grover, A. K. (2006). Improved pitting corrosion behavior of electrodeposited nanocrystalline Ni-Cu alloys in 3.0 wt.% NaCl solution. *Journal of Alloys and Compounds*, 426, 235–243.

Govindrao, P., Ghule, N. W., Haque, A. & Kalaskar, M. G. (2019). Journal of drug delivery science and technology metal nanoparticles synthesis: An overview on methods of preparation, advantages and disadvantages and applications. *Journal of Drug Delivery Science and Technology*, *53*(6), 101174.

Grigoriev, D., Shchukina, E. & Shchukin, D. G. (2017). Nanocontainers for self-healing coatings. *Advances in Material Interfaces*, 4, 1600318.

Grossi, M., Di Lecce, G., Gallina Toschi, T. & Riccò, B. (2014). Fast and accurate determination of olive oil acidity by Electrochemical Impedance Spectroscopy. *The Institute of Electrical and Electronics Engineers Sensors Journals,* 14, 2947–2954.

Groysman, A. (2017). Corrosion problems and solutions in oil, gas, refining and petrochemical industry. *Koronze a Ochrana materialu,* 61(3) 100-117.

Gupta, N., Gupta, S. M. & Sharma, S. K. (2019). Carbon nanotubes: synthesis, properties and engineering applications. *Carbon Letters*, *29*(5), 419–447.

Guan, S. W. (2003). External corrosion protection systems for flammable and combustible liquids underground storage tanks. *Anti-Corrosion Methods and Materials, 50*(2), 91–107.

Hamdy, A. S. (2010). Corrosion protection performance via nano-coatings technologies. *Recent Patent in Material Sciences*, 3, 258–267.

Hameed, R., M. A. & Fekry, A., M. (2010). Electrochemical impedance studies of modified Ni-P and Ni-Cu-P deposits in alkaline medium. *Electrochimica Acta*, 55, 5922.

Han, Y. D., Chen, L., Jing, H. Y., Nai, S. M. L., Wei, J. & Xu, L. Y. (2013). *Effect of Ni-Coated Carbon Nanotubes on the Corrosion Behavior of Sn-Ag-Cu Solder*. *Journal of Electronic Materials*, *42*(12), 3559–3566.

Hao, L., GuoweiLv, Zhou Y., Zhu, K., Dong, M., Liu Y. & Yu, D. (2018). High performance anti-corrosion coatings of poly (vinylbutyral) composites with polyn-(vinyl) pyrrole and carbon black nanoparticles. *Materials*, 11, 2307, 1-13, doi:10.3390/ma11112307.

Har, L. W. & Ismail, I. (2012). Antioxidant activity, total phenolics and total flavonoids of *Syzygiumpolyanthum* (Wight) Walp leaves. *International Journal of Medicinal and Aromatic Plants*, 2(2), 219-228.

Härkönen, E., Potts, S. E., Kessels, W. M. M., Díaz, B., Seyeux, A., Jolanta, ´S., Maurice, V., Marcus, P., Radnóczi, G. & Tóth, L. (2013). Hydrogen—Argon plasma pre-treatment for improving the anti-corrosion properties of thin Al_2O_3 films deposited using atomic layer deposition on steel. *Thin Solid Films*, 534, 384–393.

Hasnidawani, J. N., Hassan, N. A., Hassan, N. & Samat, N. (2017). ZnO nanoparticles for anti-corrosion nanocoating of carbon steel zno nanoparticles for anti-corrosion nanocoating of carbon steel. *Material Science Forum*.

He, Z. B., Maurice, J. L., Lee, C. S., Cojocaru, C. S. & Pribat, D. (2010). Nickel catalyst faceting in plasma enhanced direct current chemical vapor deposition of carbon nanofibers. *The Arabian Journal for Science and Engineering*, 35(1C), 11-19.

Hedayati, M., Salehi, M., Bagheri, R., Panjepour, M. & Naeimi, F. (2012). Progress inorganic coatings tribological and mechanical properties of amorphous and semi-crystalline PEEK/SiO_2 nanocomposite coatings deposited on the plain carbon steel by electrostatic powder spray technique. *Progress in Organic Coatings* 74, 50–58.

Hernandez, R. K. K. (2007). *Rail base corrosion detection and prevention*. Pueblo, CO, USA : Transportation Technology Centre, Inc.

Herrera, H. H., M. Ruiz Reynoso, A., C. Trinidad González, J., O. González Morán, C., G. Miranda Hernández, J., Mandujano Ruiz, A. & Orozco, O. R. (2020). Electrochemical Impedance Spectroscopy (EIS): A Review study of basic Aspects of the Corrosion Mechanism Applied to Steels. In: M. El-Azazy, M. Min and P. Annus (Eds.). *Electrochemical Impedance Spectroscopy* (pp.234-342). London, UK: IntechOpen Limited.

Hiromoto, S. (2010). Corrosion of metallic biomaterials. *Metals for Biomedical Devices*, 4, 99-121.

Hiromoto, S. & Mischler, S. (2006). The influence of proteins on the fretting-corrosion behaviour of a Ti–6Al–4V alloy, *Wear,* 261, 1002–1011.

Hibbard, G., Aust, K. T., Palumbo, G. & Erb, U. (2001). Thermal Stability of Electrodeposited Nanocrystalline Cobalt. *Scripta Materialia*, 44, 513–518.

Hintsho, N., Ahmed, S., Pranav, K., Tripathi, B. P. & Shane, D. (2015). The effect of CO_2 on the CVD synthesis of carbon nanomaterials using fly ash as a catalyst. *Royal Society of Chemistry,* 5, 53776–53781.

Hiromoto, S. (2010). Corrosion of metallic biomaterials. *Metals for Biomedical Devices*, 4, 99-121.

Hiromoto, S. & Mischler, S. (2006). The influence of proteins on the fretting-corrosion behaviour of a Ti–6Al–4V alloy, *Wear,* 261, 1002–1011.

Hone, J., Llaguno, M. C. & Biercuk, M. J. (2002). Thermal properties of carbon nanotubes and nanotube-based materials. *Applied Physics A: Materials Science and Processing* 74, 339-343.

Hu, Z. & Jie, X. (2015). Study of Polyacrylic Acid Dispersing Pb-Sn-CNTs Composite Plating Solution. *5th International Conference on Advanced Design and Manufacturing Engineering (ICADME 2015)* 542899, 2147–2151.

Huang, J., Zhu, N., Yang, T., Zhang, T. & Wu, P. (2015). Biosensors and Bioelectronics Nickel oxide and carbon nanotube composite (NiO /CNT) as a novel cathode non-precious metal catalyst in microbial fuel cells. *Biosensors and Bioelectronic*, *72*, 332–339.

Humberto, J., Linda, G., Mariana H. S., Eli, S. & Puchi-Cabrera, (2008). Effect of deposition parameters on adhesion, hardness and wear resistance of Sn–Ni electrolytic coatings. *Surface and Coatings Technology*, 202, 2072–2079.

Iijima, S., Ajayan, P. M. & Ichihashi, T. (1993). Growth model for carbon nanotubes. *Physics Revision Letters,* 69(21):3100.

Ismail, A. I. M. & El-Shamy, A. M. (2009). Engineering behaviour of soil materials on the corrosion of mild steel. *Applied Clay Sciences*, 42, 356–362.

Iyasara, A. C. & Ovri, J. E. O. (2013). Corrosion Inhibition of Stainless Steel (314l) using molasses. *The International Journal of Engineering and Science*, 2(1), 346-352.

Jafari, K. & Jabbarzade, M. (2016). Synthesis of NiO/CNTs Nanocomposite by direct chemical precipitation method for preparation of voltammetric sensor in acetaminophen analysis. *STEM Fellowship Journal*, 2 (1), 117–21.

Jagadeesan, A. K., Thangavelu, K. & Dhananjeyan, V. (2020). Carbon Nanotubes: Synthesis, Properties and Applications, 21st Century Surface Science - a Handbook, Phuong Pham, Pratibha Goel, Samir Kumar and Kavita Yadav, IntechOpen,

Jamkhande, P. G., Ghule, N. W., Bamer, A. H. & Kalaskar, M. G. (2019). Metal nanoparticles synthesis: An overview on methods of preparation, advantages and disadvantages, and applications. *Journal of Drug Delivery Science and*

Technology, 53, 101174.

Jeevanandam, S. (2018). Effective atmospheric corrosion management using coating condition inspection and maintenance programme. paper presented at the international petroleum technology conference, Kuala Lumpur, Malaysia. 2-14.

Jiang, C., Cao, Y., Xiao, G. & Zhu, R. (2017). A review on the application of inorganic nanoparticles in chemical surface coatings on metallic substrates. *Royal Society of Chemistry Advances*, 7, 7531 7531–7539.

Jing, M., Wang, C., Hou, H., Wu, Z., Zhu, Y., Yang, Y., Jia, X., Zhang, Y. & Ji, X. (2015). Ultrafine nickel oxide quantum dots enbedded with few-layer exfoliative graphene for an asymmetric supercapacitor: Enhanced capacitances by alternating voltage, *Journal of Power Sources,* 298, 241–248.

Kammona, O., Kotti, K., Kiparissides, C., Celis, J. P. & Fransaer. J. (2009). Synthesis of polymeric and hybrid nanoparticles for electroplating applications. *Electrochimica Acta*, 54, 2450-2457.

Kariim, I., Abdulkareem, A. S., Abubakre, O. K., Bankole, M. T., Tijani, J. O. & Mohammed, I. A. (2016). Studies on the suitability of alumina as metallic catalyst Support for MWCNTs in a CVD reactor. 296-305.

Kartal, M., Uysal, M., Gul, H., Alp, A., Akbulut, H., Kartal, M. & Akbulut, H. (2016). Pulse electrocodeposition of Ni/MWCNT nanocomposite coatings. *Surface Engineering*, 31(9), 659-665.

Katariya, M. N., Jana, A. K. & Parikh, P. A. (2013). Corrosion inhibition effectiveness of zeolite ZSM-5 coating on mild steel against various organic acids and its antimicrobial activity. *Journal of Industrial and Engineering Chemistry*, 19(1), 286-291.

Kausar, A. (2019). Performance of corrosion protective epoxy blend-based nanocomposite coatings: a review. *Polymer-Plastics Technology and Materials,* 2-16.

Kavitha, K. S., Baker, S., Rakshith, D., Kavitha, H. U., Harini, B. P. & Satish, S. (2013). Plants as Green Source towards Synthesis of Nanoparticles, *International Research Journal of Biological Science*, 2: 66- 67.

Kenneth, K. A., Tolulope, M. A. & Peter, A. O. (2014). Corrosion and wear behaviour of Al–Mg–Si alloy matrix hybrid composites reinforced with rice husk ash and siliconcarbide. *Journal of Material Research Technology*, 3, 9-16.

Khadija, M., Emran, Shimaa, M. A. & Hamedh A. A. (2018). Green methods for corrosion control. In: M. Aliofkhazraei (Eds.), *Corrosion Inhibitors, Principles and Recent Applications*, (pp. 61-72). London, SW7 2QJ, UK. IntechOpen Limited Publishers.

Khalil, M. W., Eldin, T. A. S., Hassan, H. B., El-Sayed, K., & Hamid, Z. A. (2016). Electrodeposition of Ni-GNS-TiO_2 nanocomposite coatings as anticorrosion film for mild steel in neutral environment. *Surface Coating Technology*, 275, 98-111.

Khan, I., Saeed, K. & Khan, I. (2017). Nanoparticles: Properties, applications and toxicities. *Arabian Journal of Chemistry,* 12(7), 908-931.

Khan, P. F., Shanthi, V., Babu, R. K., Muralidharan, S. & Barik R. C. (2015). Effect of benzotriazole on corrosion inhibition of copper under flow conditions. *Journal of Environmental Chemical Engineering*, 1-33.

Khodair, Z. T., Khadom, A. A. & Jasim, H. A. (2018). Corrosion protection of mild steel in different aqueous media via Epoxy/nanomaterial coating: Preparation, characterisation and mathematical views. *Journal of Materials Research and Technology*, http://Doi.org/10.1016/j.jmrt.2018.03.003

Khorrami, S. A. & Lofti, R. (2013). Influence of carrier gas flow rate on carbon nanotubes growth by TCVD with Cu catalyst. *Journal of Saudi Chemical Society* , 20, 432-436.

Khramov, A. N., Voevodin, N. N., Balbyshev, V. N. & Mantz, R. A. (2005). Sol-gel-derived corrosion-protective coatings with controllable release of incorporated organic corrosion inhibitors. *Thin Solid Films*, 483, 191–196.

Kim, S-K. & Oh, T-S. (2011). Electrodeposition behavior and characteristics of Ni-carbon nanotube composite coatings. *Transactions of Nonferrous Metals Society of China*, 21(1), 68−72.

Kleiner, Y. & Rajani, B. (2001). Comprehensive review of structural deterioration of water mains: Statistical models. *Urban Water*, 3, 131-150.

Kokilaramani, S., Al-Ansari, M. M., Rajasekar, A., Al-Khattaf, F. S., Hussain, A. M. R. & Govarthanan, M. (2021). Microbial influenced corrosion of processing industry by re-circulating waste water and its control measures - A review. *Chemosphere*, *265*, 129075.

Kolawole, F. O., Kolawole, S. K., Agunsoye, J. O., Adebisi, J. A., Bello, S. A. & Hassan, S. B. (2018). Mitigation of corrosion problems in API 5L steel pipeline – A review. *Journal of Materials and Environmental Sciences,* 9 (8), 2397-2410.

Kotsedi, L. (2010). *Fabrication and characterisation of a solar cell using an aluminium P-doped layer in the hot-wire chemical vapour deposition process*. (Doctoral dissertation). University of the Western Cape, Cape Town, Soth Africa.

Kumar, A. M. & Gasem, Z. M. (2015). In situ electrochemical synthesis of polyaniline/fMWCNT nanocomposite coatings on mild steel for corrosion protection in 3.5% NaCl solution, *Progress in Organic Coatings,* 78, 387-394.

Kumar, M. & Yoshinori, A. (2010). Chemical Vapor Deposition of Carbon Nanotubes: A Review on Growth Mechanism and Mass Production Department of Materials Science and Engineering. *Journal of Nanoscience and Nanotechnology, 10,* 3739–3758.

Kumar, N. & Kumbhat, S. (2016). Essentials in Nanoscience and Nanotechnology Published 2016 by John Wily & Sons, Inc, 31-74.

Kuwana, K., Endo, H., Saito, K., Qian, D., Andrews, R. & Grulke, E. A. (2005).

Catalyst deactivation in CVD synthesis of carbon nanotubes. *Carbon,* 43, 253 – 260.

Kwon, S., Shinoda, K., Suzuki, S. & Waseda, Y. (2007). Influence of silicon on local structure and morphology of c-FeOOH and a-FeOOH particles. *Corrosion Science*, 49, 1513-1526.

Laoui, T. (2010). Corrosion performance of copper coated with carbon nanotubes. *The Arabian Journal for Science and Engineering,* 35, (1), 57-63.

Lee, C. K. (2008). Corrosion and wear-corrosion resistance properties of electroless Ni-P coatings on GERP composite in wind turbine blades. *Surface and Coatings Technology,* 202, 48-68.

Lee, C. K. (2012). Electroless Ni–Cu–P/nano-graphite composite coatings for bipolar plates of proton exchange membrane fuel cells. *Journal of Power Sources,* 220, 130–137.

Lee, H., Singh, J. K., Ismail, M. A. & Bhattacharya, C. (2019). Corrosion mechanism and kinetics of Al-Zn coating deposited by arc thermal spraying process in saline solution at prolong exposure periods. *Scientific Reports*, 1–17.

Lee, W. & Characklis, W.G (1993). Corrosion of mild steel under anaerobic biofilm. *Corrosion*, 49, 186–199.

Lefojane, R., Direko, P., Mfengwana, P., Mashele, S., Matinise, N., Maaza, M. & Sekhoacha, M. (2020). Green Synthesis of Nickel Oxide (NiO) Nanoparticles Using Spirostachys africana Bark Extract. *Asian Journal of Scientific Research*, 13(4), 284–291.

Li, D. G., Bai, Z. Q., Zhu, J. W. & Zheng, M. S. (2007). Influence of temperature, chloride ions and chromium element on the electronic property of passive film formed on carbon steel in bicarbonate/carbonate buffer solution. *Electrochimica Acta,* 52, 7877–7884.

Li, Q., Yan, H., Zhang, J. & Liu, Z. (2004). Effect of hydrocarbons precursors on the formation of carbon nanotubes in chemical vapor deposition. *Carbon,* 42, 829–835.

Li, X. L., Zhang, J. H., Xu, W. Q., Jia, H. Y., Wang, X., Yang, B., Zhao, B., Li, B. F. & Ozaki, Y. (2003). Mercaptoacetic acid-capped silver nanoparticles colloid: Formation, morphology, and SERs activity. *Langmuir*, 2003, 19, 4285–4290.

Li, Y., Li, L. & Yu, J. (2017). Applications of zeolites in sustainable chemistry. *Chemistry*, 3, 928–949.

Lim, K. S., Yahaya, N., Othman, S. R. & Fariza, S. N. (2013). The relationship between soil resistivity and corrosion growth in tropical region. *Journal of Corrosion Science and Engineering*, 16 (54) 1-10.

Lin, L., Xing, H., Shu, R., Wang, L., Ji, X., Tan, D. & Gan, Y. (2015). Preparation and microwave absorption properties of multi-walled carbon nanotubes decorated with Ni-doped SnO_2 nanocrystals. *RSC Advances, 5*(115), 94539–94550.

Liu, D., Liu Y., Zong, R., Bai, X. & Zhu, Y. (2014). Controlled synthesis of 1D ZnO nanostructures via hydrothermal process. *Material Research Bulletin*, 49(1), 665-671.

Liu, D., Zhao, W., Wu, F., Cen, Q., Zeng, Z., Wu, X. & Xue, Q. (2015). Effect of curing agent molecular structures on the tribological and corrosion behaviors of epoxy resin coatings. *Colloids and Surfcae a Physicochemcal and Engineering Aspect*, 472, 85-91.

Lowe, A. M. (2002). *Estimation of electrochemical noise impedance and corrosion rates from electrochemical noise measurements* (Doctoral dissertation), Curtin University of technology, Australia.

Lu, X., Wang, S., Xiong, T., Wen, D., Wang, G. & Du, H. (2019). Anticorrosion properties of Zn–Al composite coating prepared by cold spraying. *Coatings*, 9, 210, 1-10.

Luiz, E. V. J., Keila, C. K., João, B. R. N., Aloísio N. K., Dachamir, H. & Rodrigo M. (2016). Dip coating of a carbon steel sheet with Ni reinforced TiO_2 nanoparticles. *Materials Research*. 19(3), 648-653.

Ma, J., Xu, J., Jiang, S., Munroe, P. & Xie, Z. (2016). Effects of pH value and temperature on the corrosion behavior of a Ta_2N nanoceramic coating in simulated polymer electrolyte membrane fuel cell environment. *Ceramic International,* 42, 16833–16851.

MacDiarmid, A. G. (2000). Nobel lecture: Synthetic metals: A novel role for organic polymers. *Reviews of Modern Physics*, 73, 701.

Madhankumar, A., Nagarajan, S. & Rajendran, N. (2012). EIS evaluation of protective performance and surface characterization of epoxy coating with aluminum nanoparticles after wet and dry corrosion test. *Journal of Solid State Electrochemistry*, 16, 2085–2093.

Mahalingm, S., Abdullah, H., Shaari, S., Muchtar, A. & Asshari, I. (2015). Structural, morphological, and electron transport studies of annealing dependent In_2O_3 dye-sensitized solar cell. *Scientific World Journals,* 1–11.

Malik, M. A., Hashim, M. A., Nabi, F., Al-Thabaiti, S. A. & Khan Z. (2011). Anti-corrosion ability of surfactants: A review. *International Journal of Electrochemical Science*, 6, 927-1948.

Mariam, A. A., Kashif, M., Arokiyaraj, S., Bououdina, M., Sankaracharyulu, M. G. V. & Hashim, U. (2014). Bio-synthesis of NiO and Ni nanoparticles and their characterisation. *Digest Journal of Nanomaterials and Biostructures*, *9*(3), 1007–1019.

Marx, W. & Barth, A. (2010). Carbon nanotubes: a scientometric study. *Carbon Nanotubes*, 1–17.

McGee, J. D., Thomas, S. S., Bammel, B. D. & Bryden, T. R. (2012). *Release on demand corrosion inhibitor composition.* U.S. Patent No. 8241524.

Merlin, C., Vedhi, K., Muthu, A. & Mohamed, S. (2018). Influence of pH and temperature on the structure and size of tin oxide nanoparticles. *Journal of Nanoscience and Technology*, 4 (5), 564–566.

Moghadam, L. N. & Salavati-Niasari, M. (2017). Facile synthesis and characterisation of NiO-SnO_2 ceramic nanocomposite and its unique performance in organic pollutants degradation. *Journal of Molecular Structure,* 1146, 629-634.

Mohamed, R. M. & Aazam, E. S. (2012). Photocatalytic oxidation of carbon monoxide over NiO-SnO_2 nanocomposites under UV irradiation. *Journal of Nanotechnology*, 794874, 1-9.

Mohammed, I. A., Bankole, M. T., Abdulkareem, A. S., Ochigbo, S. S., Afolabi, A. S. & Abubakre, O. K. (2017). Full factorial design approach to carbon nanotubes synthesis by CVD method in argon environment. *South African Journal of Chemical Engineering*, 24(1), 17-42.

Møller, P., Rasmussen, J. B., Köhler, S. & Elplatek, L. P. N. (2013). Electroplated Tin-Nickel Coatings as a Replacement for Nickel to Eliminate Nickel Dermatitis. *National Association of State Foresters Surface Technology White Papers* 78 (3), 15-24.

Monshi, A., Foroughi, M. R. & Monshi, M. R. (2012). Modified Scherrer equation to estimate more accurately nano-crystallite size using XRD. *World Journal of Nano Science and Engineering*, 2, 154–160.

Montemor, M. F. (2014). Functional and smart coatings for corrosion protection: A review of recent advances. *Surface Coating Technology*, 258, 17–37.

Montgomery, D.C. (2014). Design and analysis of experiments. 8th ed. New York: John Wiley and Sons.

Munnings, C., Badwal, S. P. S. & Fini, D. (2014). Spontaneous stress-induced oxidation of Ce ions in Gd-doped ceria at room temperature, *Ionics*, 20 (8), 1117–1126.

Naderi, R., Fedel, M., Deflorian, F., Poelman, M. & Olivier, M. (2013). Synergistic effect of clay nanoparticles and cerium component on the corrosion behavior of eco-friendly silane sol-gel layer applied on pure aluminum. *Surface and Coatings Technology.* 224:93-100. DOI: 10.1016/j.surfcoat.2013.03.005.

Nagham, M. A., Nawfel, M. B. M. & Noorhan, A. H. (2019). Review on corrosion and rust inhibition of machines in chemical engineering field, *International Journal of Thermodynamics and Chemical Kinetics*, 5(1), 15-24.

Narayanan, T. S. N. S. (2005). Surface pretreatment by phosphate conversion coatings a review *Reviews on Advances in Material Sciences*, 9, 130–177.

Natalia, L., Pacioni, C. D., Borsarelli, V. R. & Alicia, V. V. (2015). Synthetic Routes for the Preparation of Silver Nanoparticles. A Mechanistic Perspective. *Silver*

Nanoparticle Applications, Engineering Materials, DOI 10.1007/978-3-319-11262-6-2.

Nawfel, M. B. (2015). Hydrodynamic and thermal flows of fluids. *Chemical Process Engineering Resources*. 32, 22– 35.

Neacşu, I. A., Nicoară, A. I., Vasile, O. R. & Vasile, B. Ş. (2016). *Inorganic micro- and nanostructured implants for tissue engineering. Nanobiomaterials in Hard Tissue Engineering,* 271–295.

Nernst, W. (1894). Methode zur Bestimmung von Dielektrizitatskonstan- ten. *Zeitschrijtfur Elektrochemie*, 14, 622–663.

Nesterova, T., Dam-Johansen, K., Pedersen, L. T. & Kiil, S. (2012). Microcapsule-based self-healing anticorrosive coatings: Capsule size, coating formulation, and exposure testing. *Progress in Organic Coatings,* 75, 309–318.

Nie, J., Wang, F., Chen, Y., Mao, Q., Yang, H. & Song, Z. (2019). Results in Physics Microstructure and corrosion behavior of Al-TiB_2 /TiC composites processed by hot rolling. *Results in Physics*, 14, 102471, 2211-3797.

Nie, X., Li, X., Du, C., Huang, Y. & Du, H. (2009). Characterization of corrosion products formed on the surface of carbon steel by Raman spectroscopy. *Journal of Raman Spectroscopy*. 40, 76-79.

Noor, E. A. (2009). Evaluation of inhibitive action of some quaternary N-heterocyclic compounds on the corrosion of Al–Cu alloy in hydrochloric acid. *Material Chemistry and Physics,* 114, 533–541.

Novakovic, J. & Vassiliou, P. (2009). Vacuum thermal treated electroless NiP–TiO_2 composite coatings. *Electrochimica Acta,* 2009, 54, 2499-2503.

Nowicka-Nowak, M., Zubielewicz, M., Kania, H., Liberski, P. & Sozanka, M. (2018). Influence of hot-dip galvanised organic coatings depending on the zinc bath Pb content and the postgalvanising cooling method. *International Journal of Corrosion*, 1-8, 2102086.

Obasi, N. A., Joy, U., Eberechukwu, E., Akubumo. E. I. & Okorie, U. C. (2012). Proximate composition, extraction, characterisation and comparative assessment of coconut and melon seeds and seed oils. *Pakistian Journal of Biological Sciences*, 15, 1-9.

Oladele, S. K. & Okoro, H. K. (2011). Investigation of corrosion effect of mild steel on orange juice. *African Journal of Biotechnology*, 10(16), 3152-3156.

Olivares, O., Likhanova, N., Gomez, B., Navarrete, J., Llanos-Serrano, M., Arce, E. & Hallen, J. (2006). Electrochemical and XPS studies of decylamides of α-amino acids adsorption on carbon steel in acidic environment. *Applied Surface Sciences,* 252, 2894–2909.

Olivares-Xometl, O., Likhanova, N., Martínez-Palou, R. & Domínguez-Aguilar, M. (2009). Electrochemistry and XPS study of an imidazoline as corrosion inhibitor

of mild steel in an acidic environment. *Material Corrosion*, 60, 14–21.

Oliver, W. C. (2004). Measurement of hardness and elastic modulus by instrumented indentation: Advances in understanding and refinements to methodology. *Journal of Materials Research*, 19(1), 3-20.

Orazem, M. E. & Tribollet, B. (2008). *Electrochemical impedance spectroscopy*. Hoboken.: USA. John Wiley & Sons, 523 S., hardcover, 82.90 E.-ISBN 978-0470041406.

Parashar, M., Shukla, V. K. & Singh, R. (2020). Metal oxides nanoparticles via sol–gel method: a review on synthesis, characterization and applications. *Journal of Materials Science: Materials in Electronics*, 31(5), 3729–3749.

Patil, G. E., Kajale, D. D., Gaikwad, V. B. & Jain, G. H. (2012). Preparation and characterization of SnO_2 nanoparticles by hydrothermal route. *International Nano Letters*, 17, 2–6.

Patil, R. C. & Radhakrishnan, S. (2006). Conducting polymer based hybrid nanocomposites for enhanced corrosion protective coatings. *Progress in Organic Coatings,* 57, 332–336.

Payne, A. S. (1999). Control of Underground Corrosion. Washington, DC, USA: US Department of agriculture: 23-18.

Pearson, P. & Cousins, A. (2016). *Assessment of corrosion in amine-based post-combustion capture of carbon dioxide systems.* Absorption-based post-combustion capture of carbon dioxide. Royston Road, Duxford, CB22 4QH, UK: Woodhead Publishing is an imprint of Elsevier. The Officers' Mess Business Centre. 439-463.

Pereira, R. F. C., Oliveira, E. S. D., Lima, M. A. G. A. & Brazil, S. L. D. (2015). Corrosion of Galvanized Steel under Different Soil Moisture Contents. *Material Resources*, 18, 563–568.

Phil, S., Yong, M. & Chul, H. (2015). Applied Surface Science Characterisation and photocatalytic performance of SnO_2-CNT nanocomposites. *Applied Surface Science*, 357, 302–308.

Popoola, A. P. I., Daniyan, A. A., Umoru, L. E. & Fayomi, O. S. I. (2017). Effect of WO_3 nanoparticles loading on the microstructural, mechanical and corrosion resistance of Zn matrix/TiO_2-WO_3 nanocomposite coatings for marine application. *Journal of Marine Science and Application,* 16: 1389-1387.

Popov, B. V. (2015). Corrosion engineering; Basics of corrosion measurement, Elsevier B.V, 2-16,

Popova, A., Christov, M. & Zwetanova, A. (2007). Effect of the molecular structure on the inhibitor properties of azoles on mild steel corrosion in 1mhydrochloric acid. *Corrosion Science*, 49, 2131–2143.

Prabakaran, M., Kim, S. H., Hemapriya, V., Kim, I. S. & Chung, I. M. (2016). *Rhus verniciflua* as a green corrosion inhibitor for mild steel in 1 M H_2SO_4, *Royal Society of Chemistry Advances,* 6(62), 57144-57153.

Prasannakumar, R. S., Chukwuike, V. I., Bhakyaraj, K., Mohan, S. & Barik, R. C. (2020). Applied Surface Science Electrochemical and hydrodynamic flow characterization of corrosion protection persistence of nickel/multiwalled carbon nanotubes composite coating. *Applied Surface Science*, 507, 145073.

Praveen, B. M. & Venkatesha, T. V. (2009). Electrodeposition and properties of Zn-Ni-CNT composite coatings. *Journal of Alloys and Compounds*, 482, 53–57.

Pritchard, O., Hallett, S. H. & Farewell, T. S. (2013). *Soil corrosivity in the UK: Impacts on critical infrastructure*; Infrastructure Transitions Research Consortium: Oxford, UK, 1–55.

Pusawale, S. N., Deshmukh, P. R. & Lokhande, C. D. (2011). Chemical synthesis of nanocrystalline SnO_2 thin films for super-capacitor application. *Applied Surface Science* (257) 9498–9502.

Qin, F., Jiang, C., Cui, X., Wang, Q., Wang, J. & Huang, R., (2018). Effect of soil moisture content on corrosion behavior of X70 steel. *International Journal of Electrochemical Science*, 3, 1603-1613.

Qin, L.Y., Lian, J. S. & Jiang. Q. (2010). Effect of grain size on corrosion behavior of electrodeposited bulk nanocrystalline Ni. *Transactions of Nonferrous Metals Society of China*, 2010. 20(1), 82-89.

Qu, Z., Wang, L., Tang, H., Ye, H. & Li, M. (2019). Effect of nano-SnS and nano-MoS_2 on the corrosion protection performance of the polyvinylbutyral and zinc-rich polyvinylbutyral coatings. *Nanomaterials*, 9, 956.

Quej-Aké, L., Marin-Cruz, J., Galvan-Martínez, R. & Contreras, A. (2014). Corrosion behavior of low carbon steel exposed to different soils. *Materials Science Forum,* 793(22), 169-179.

Quej-Ake, L., Mireles, M., Galván-Martinez, Pérez-Campos, R., Contreras-Cuevas, A., Esparza-Muñoz, R. & Contreras, A. (2015). Electrochemical characterisation of X60 steel exposed to different soils from south of México. *Materials Characterisation*, 101-116.

Radhakrishnan, S., Siju, C. R., Mahanta, D., Patil, S. & Madras, G. (2009). Conducting polyaniline-nano-TiO_2 composites for smart corrosion resistant coatings. *Electrochimica. Acta*, 54, 1249-1254.

Radushkevich L.V. & Lukyanovich V. M. (1952). The Structure of carbon forming in thermal decomposition of carbon monoxide on an iron catalyst. *Soviet Journal of Physical Chemistry*, 26, 88-95.

Rafiuddin, M. Z. I. (2016). Preparation, characterisation, electrical conductivity and dielectric studies of Na_2SO_4 and V_2O_5 composite solid electrolytes. *Measurement,* 81, 102–112.

Raghav, G. R., Selvakumar, N. & Thansekhar, K. J. M. R. (2014). Corrosion analysis of copper -TiO_2 nanocomposite coatings on steel using sputtering, *International Journal of Innovative Research in Science, Engineering and Technology*, 3(3), 1105–1110.

Rahman, G., Najaf, Z., Mehmood, A., Bilal, S. & Ali, H. (2019). An Overview of the Recent Progress in the Synthesis and Applications of Carbon Nanotubes. *Carbon*, 5 (3), 2-31.

Rahmani, K., Jadidian, R. & Haghtalab, S. (2015). Evaluation of inhibitors and biocides on the corrosion, scaling and biofouling control of carbon steel and copper-nickel alloys in a power plant cooling water system. *Desalination*, 393, 174–185.

Raj, V., Palanisamy, K., Arthanareeswari, M. & Devikala, S. (2014). Surface modification of mild steel using Ag doped SnO_2 nanoparticles for corrosion inhibition. *International Journal of Advanced Chemical Science and Applications,* 1 (2), 16-20.

Rajeev, S., Pawan K. V. & Gagandeep, S. (2012). Total phenolic, flavonoids and tannin contents in different extracts of Artemisia absinthium. *Journalof Intercultural Ethnopharmacology,* 1 (2), 101-104.

Rajendran, R. V. S. (2012). *Nanoparticle-based corrosion inhibitors and self-assembled monolayers*. Dindigul, India: Woodhead Publishing Limited. 283-303.

Rajput, N. (2015). Methods of preparation of nanoparticles: A review. *International Journal of Advances in Engineering & Technology*, 7 (4), 1806-1811.

Ramirez, N., Regueiro, A., Arias, O. & Contreras, R. (2008). Electro-chemical impedance spectroscopy: An effective tool for a fast microbiological diagnosis. *Biotecnologia Aplicada,* 26, 72–78.

Rane, A. V., Kanny, K., Abitha, V. K. & Thomas, S. (2018). Methods for Synthesis of Nanoparticles and Fabrication of Nanocomposites. In *Synthesis of Inorganic Nanomaterials*, 121–139.

Rani, B. E. A. & Basu, B. B. J. (2012). Green inhibitors for corrosion protection of metals and alloys: An overview. *International Journal of Corrosion*, (4), Article Id 380217, 15.

Rathi, P., Trikha, S. & Kumar, S. (2017). Plant extracts as green corrosion inhibitors in various corrosive media- a review, *World Journal of Pharmacy and Pharmaceutical Sciences*, 6 (4), 482-514.

Rauf, M. A., Marzouki, N. & Korbahti, B. K. (2008). Photolytic decolorization of Rose Bengal by UV/H_2O_2 and data optimization using response surface method. *Journal of Hazardous Materials*, 159, 602-609.

Rebak, R. B. (2013). Corrosion of Non-Ferrous Alloys and Titanium-Based Alloys. *In: Materials Science and Technology,* 2, 104-108.

Reddy, B. R., Harish, G. S. & Reddy, P. S. (2014). Preparation and characterisation of Cu doped NiO nanoparticles: Effect of pH. *International Journal of Advanced Research,* 2(11), 272–275.

Reilly, P. T. A. & Whitten, W. B. (2006). The role of free radical condensates in the production of carbon nanotubes during the hydrocarbon CVD process. *Carbon,* 44, 1653–1660.

Reimer, L. (1998). Scanning electron microscopy: physics of image formation and microanalysis. *Springer*, 527.

Rezaeiolum, A., Aliofkhazraei, M., Karimzadeh, A., Rouhaghdam A. S. & Miresmaeili, R. (2017). Electrodeposition of Ni–Mo and Ni–Mo-(nano Al_2O_3) multilayer coatings, *Surface Engineering,* 34(6),423-432.

Roberge, P. R. (2008). *Corrosion Engineering: Principles and Practice*. Columbus, OH, USA: McGraw-Hill.

Romer, A. E. & Bell, G. E. (2001). Causes of external corrosion on buried water mains. *In: Pipelines: Advances in Pipelines Engineering & Construction*,1-9.

Sadeghi, E., Markocsan, N., Hussain, A. T. & Huhtakangas, M. (2018). Effect of $Si0_2$ Dispersion on Chlorine- Induced High-Temperature Corrosion of High-Velocity Air-Fuel Sprayed NiCrMo Coating. *Corrosion*, 74(9), 984-1000.

Sadek, R. F., Farrag, H. A., Abdelsalam, S. M. & Keiralla, Z. M. H. (2019). A powerful nanocomposite polymer prepared from metal oxide nanoparticles synthesized via brown algae as anti-corrosion and anti-biofil. *Frontier in Material*. 6,140, 1–17.

Saji, V. S. (2012). The impact of nanotechnology on reducing corrosion cost in corrosion protection and control using nanomaterials. In (eds) V. S., Saji, and R., Cook. *Nanomaterials*. (pp 3-15). Philadelphia, PA, USA: Woodhead Publishing Limited: ISBN 9781845699499.

Saji, V. S. (2010). A review on recent patents in corrosion inhibitors. *Recent Patent on Corrosion Sciences*, 2, 6–12.

Sakhare, R. D., Khuspe, G. D., Navale, S. T., Mulik. R. N., Chougule, M. A., Pawar, R. C., Lee C. S., Sen, S. & Patil, V. B. (2013). Nanocrystalline SnO_2 thin films: structural, morphological, electrical transport and optical studies. *Journal of Alloys Compounds,* (563), 300–306.

Salem, S. S. & Fouda, A. (2021). Green Synthesis of Metallic Nanoparticles and Their Prospective Biotechnological Applications: An Overview. *Biological Trace Element Research*, *199*(1), 344–370.

Salimon, J., Abdullah B. M. & Salih, N. (2012). Selectively increasing of polyunsaturated (18:2) and monounsaturated (18:1) fatty acids in Jatropha curcas seed oil by crystallization using D-optimal design. *Chemistry Central Journal*, 6, 65-80.

Saputri, D. D., Jan'ah, A. M. & Saraswati, T. E. (2020). Synthesis of carbon nanotubes (CNT) by chemical vapor deposition (CVD) using a biogas-based carbon precursor: A review. *IOP Conference Series: Materials Science and Engineering*, 959, 012019, 3-8.

Sarmiento, H., Natalia, K. & Raul, S. Z. (2017). Localized corrosion characteristics of nickel alloys: A Review. *Acta Metallurgica Sinica (English Letters)*, 1-10.

Schoolcraft, T. A. &. Garrison, B. J. (1991). Initial Stages of Etching of the Silicon Si110 2x1 Surfaces by 3.0-eV Normal Incident Fluorine Atoms: A Molecular Dynamics Study. *Journal of the American Chemical Society*, 113 (22), 8221.

Schuh, C. A., Nieh, T. G. & Iwasaki, H. (2003). The effect of solid solution W additions on the mechanical properties of nanocrystalline Ni. *Acta Materialia,* 51, 431–443.

Selvakumari, J. C., Ahila, M., Malligavathy, M. & Padiyan, D. P. (2017). Structural, morphological, and optical properties of tin (IV) oxide nanoparticles synthesized using *Camellia sinensis* extract: a green approach. *International Journal of Minerals, Metallurgy and Materials*. 24(9), 1043–1051.

Senthilkumar S. & Rajendran, A. (2017). Eco-friendly synthesis and characterisation of nanostructure sno_2 thin films using citrus aurantifolia peel extract by spin coating method. *Journal of Nanomedicine Resources,* 6(4), 00164.

Senthilkumar, S., Perumalsamy, M., Prabhu, H. J., Basha, C. A. & Swaminathan, G. (2013). Box behnken design based optimization of solar induced photo catalytic decolourization of textile dye effluent. *Central European Journal of Engineering*, 3, 135-144.

Shahid, N., Saira H. & Rashid, A. (2013). Synthesis of multi-walled carbon nanotubes and their application in resin based nanocomposites. *Journal of Physics: Conference Series,* 439 (2013) 012009.

Shahzad, F., Ettinger, K., Letofsky-Papst, I., Weber, J. & Knoll, P. (2015). Preparation and characterisation of NiO nanoparticles. *Journal of Nano Research*, 31, 93-102.

Shajudheen, M. V. P., Rani, A. K., Kumar, S. V., Maheswari, U. A., Sivakumar, M. & Kumar, S. S. (2017). Comparison of anticorrosion studies of titanium dioxide and nickel oxide thin films fabricated by spray coating technique. *International Conference on Recent Advances in Material Chemistry,* 5 (2018), 8889–8898.

Sharma, G., Kumar, D., Kumar, A., Al-Muhtaseb, A. H., Pathania, D., Naushad, M. & Mola, G. T. (2017). Revolution from monometallic to trimetallic nanoparticle composites, various synthesis methods and their applications: A review. *Materials Science and Engineering C*, *71*, 1216–1230.

Shchukin, D. G., Zheludkevich, M., Yasakau, K., Lamaka, S., Ferreira, M. G. S. & Möhwald, H. (2006). Layer-by-layer assembled nanocontainers for self-healing corrosion protection. *Advances in Material Sciences*, 18, 1672–1678.

Sheng, M., Wang, Y., Zhong, Q., Wu, H., Zhou, Q. & Lin, H. (2011). The effects of nano-SiO_2 additive on the zinc phosphating of carbon steel. *Surface Coatings and Technology*. 20, 3455-3460.

Shi, H., Liu, F. & Han, E. (2010). Corrosion behaviour of sol–gel coatings doped with

cerium salts on 2024-T3 aluminum alloy. *Materials Chemistry and Physics*. 124(1), 291-297.

Shi, L., Sun, C. F., Gao, P., Zhou, F. & Liu, W.M. (2006). Electrodeposition and characterization of Ni–Co–carbon nanotubes composite coatings. *Surface Coating Technology*, 200, 4870-4875.

Shi, Y. L., Yang, Z. & Xu, H. (2004). Preparation of electroplated Ni-P-ultrafine diamond, Ni-P-carbon nanotubes composite coatings and their corrosion properties. *Journal of Materials Science,* 39**,** 5809–5815.

Shoaib, S., Srinophakun, T. R. & Palsson, N. S. (2018). Influence of Soil Conditions on corrosion behavior of buried coated and uncoated carbon steels. *IEEE International Conference on Innovative Research and Development (ICIRD)*, (20), 1–6.

Shreir L. L., Jarman, R. A. & Burstein, G. T. (2010). *Metal environment reactions*. Oxford UK: Publishers, 1, 1-43.

Shrgeshty, M., Aliofkhazraei M. & Karimzadeh, A. (2018). Study on functionally graded Zn–Ni–Al_2O_3 coatings fabricated by pulse-electrodeposition, *Surface Engineering*, 35(2), 167-176.

.

Shuaib-Babata, Y. L., Ibrahim, H. K., Ambali, I. O., Yahya, R. A., Ajao, K. S., Aremu, N. I. & Pelumi, A. A. (2019). Inhibitive Potential of Prosopis Africana on Corrosion of Low Carbon Steel in 1 M Hydrochloric Acid Medium. *International Journal of Engineering Materials and Manufacture*, 4(2), 66-76.

Siavash, J., Z., Chen, J. Z. & Florin, B. (2019). Pitting, lacy covers, and pit merger in stainless steel: 3D peridynamic models. *Corrosion Science,* 150, 17-31.

Singh, A., Gautam, P. K., Verma, A., Singh, V., Shivapriya, P. M., Shivalkar, S. & Samanta, S. K. (2020). Green synthesis of metallic nanoparticles as effective alternatives to treat antibiotics resistant bacterial infections: A review. *Biotechnology Reports*, 25, 427.

Slepski, P., Gerengi, H., Jazdzewska, A., Orlikowski, J. & Darowicki, K. (2014). Simultaneous impedance and volumetric studies and additionally potentiodynamic polarization measurements of molasses as a carbon steel corrosion inhibitor in 1 M hydrochloric acid solution. *Construction and Building Materials*, 52, 482–487.

Solomon, M. M., Umoren, S. A., Udosoro, I. I. & Udoh, A. P. (2010). Inhibitive and adsorption behaviour of carboxymethyl cellulose on mild steel corrosion in sulphuric acid solution. *Corrosion Science*, 52, 1317-1325.

Sonia, K. & Nazmul, I. (2018). Carbon Nanotubes-Properties and Applications. *Organic & Medicinal Chemistry: International Journal*, 7(1), 555705.

Soriano, L., Preda, I., Gutier´rez, A. & Palacin, S. (2007). Surface effects in the Ni 2p x-

ray photoemission spectra of NiO. *Physical Review B,* 75, 233417.

Sosa, E. & Alvarez-Ramirez, J. (2009). Time-correlations in the dynamics of hazardous material pipelines incidents. *Journal of Hazard Materials*, 1204-1209.

Sreeya, S. (2009). *Carbon nanotube electronic structures as anti-corrosion coatings* (Doctoral dissertation). New Jersey Institute of Technology and Rutgers, The State University of New Jersey, Newark, USA.

Sriraman, K. R., Strauss, H. W., Brahimi, S., Chromik, R. R., Szpunar, J. A., Osborne, J. H. & Yue, S. (2012). Tribological behavior of electrodeposited Zn, Zn–Ni, Cd and Cd–Ti coatings on low carbon steel substrates. *Tribiology International*, 56, 107–120.

Stansbury, E. E. & Buchanan, R. A. (2000). *Fundamentals of Electrochemical Corrosion.* West Conshohocken, PA, USA: ASM International.

Stromberg, C. Thissen, P. Klueppel, I. Fink, N. & Grundmeier, G. (2006). Synthesis and characterisation of surface gradient thin conversion films on zinc coated steel. *Electrochimica. Acta,* 52, 804–815.

Su, D., Ford, M. & Wang, G. (2012). Mesoporous NiO crystals with dominantly exposed {110} reactive facets for ultrafast lithium storage. *Scientific Reports*, *2*, 1-7.

Subramaniam, M. P., Arunachalam, G., Kandasamy, R., Veluswamy, P. & Hiroya, I. (2017). Effect of pH and annealing temperature on the properties of tin oxide nanoparticles prepared by sol–gel method. *Journal of Material Science and Material Electronics*.

Sudrabin, L. P. & Marks, H. C. (1952). Cathodic protection of steel in contact with water. *The Journal of Industrial and Engineering Chemistry*, 44 (8), 1-24.

Sugimoto, K. (2009). Kinzoku-Fushoku-Kogaku (Corrosion Engineering of Metals), Tokyo: Uchida Rokakuho Publishing, 1-32.

Sui, Y., Fu, W. & Yang, H. (2010). Low temperature synthesis of Cu_2O crystals: Shape evolution and growth mechanism. *Crystal growth Design*, 10(1), 99-108.

Suk, J. H., Hong, S. C., Jang, G. S. & Hwang, N. M. (2021). Two-step deposition of silicon oxide films using the gas phase generation of nanoparticles in the chemical vapor deposition process. *Coatings*,11, 365, 18-22.

Suleiman, I. Y., Abdulwahab, M. & Awe, F. E. (2016). Influence of particulate loading on the mechanical properties of al-4.5 Cu/GSA composite. *Nigerian Journal of Engineering,* 23, 86–97.

Suleiman, I. Y., Aigbodion, V. S., Obayi, C. O. & Mu'azu, K. (2018). Surface characterisation, corrosion and mechanical properties of polyester-polyester/snail shell powder coatings of steel pipeline for naval applications. *The International Journal of Advanced Manufacturing Technology*, 2-16.

Suresh, K. C., Surendhiran, S., Manoj Kumar, P., Ranjth Kumar, E., Khadar, Y. A. S. &

Balamurugan, A. (2020). Green synthesis of SnO_2 nanoparticles using Delonix elata leaf extract: Evaluation of its structural, optical, morphological and photocatalytic properties. *SN Applied Sciences*, 2(10), 1-12.

Tabatabaei, M., Davoudi, M., Ramezanzadeh, M. & Ghasemi, E. (2020). Construction of a smart active/barrier anti-corrosion system based on epoxy-ester/zinc intercalated kaolin nanocontainer for steel substrate. *Construction and Building Materials*, 247, 118555.

Tallman, D. E., Spinks, G., Dominis, A. & Wallace, G. G. (2002). Electroactive conducting polymers for corrosion control. *Journal of Solid State Electrochemistry*, 6, 73–84.

Tang, X. & Yan, X. (2016). Dip-coating for fibrous materials: mechanism, methods and applications. *Journal of Sol-Gel Science and Technology*, 12–14.

Tavandashti, N. P. & Sanjabi, S. (2010). Corrosion study of hybrid sol–gel coatings containing boehmite nanoparticles loaded with cerium nitrate corrosion inhibitor. *Progress in Organic Coatings.* 69(4), 384-391.

Tavandashti, N. P., Ghorbani, M., Shojaei, A., Mol, J. M. C., Terryn, H., Baert, K. & Gonzalez-Garcia, Y. (2016). Inhibitor-loaded conducting polymer capsules for active corrosion protection of coating defects. *Corrosion Sciences*, 112, 138–149.

Teoh, L. G. & Li, K. (2012). Synthesis and Characterization of NiO Nanoparticles by Sol Gel Method. *Materials Transactions*, 53(12), 2135–2140.

Tiba, T. & Oliveira, E. M. (2012). Utilization of cathodic protection for transmission towers through photovoltaic generation. *Renewable Energy*, 40, 150–156.

Tudela, I., Zhang, Y., Pal, M., Kerr, I. & Cobley, A. J. (2014). Ultrasound-assisted electrodeposition of composite coatings with particles. *Surface and Coatings Technology,* 259, 363-373.

Umbreen, A. & Bushra, K. (2013). Synthesis and characterisation of NiOnanopowder by sol-gel method. *International Journal of Science and Research*, 4(5), 2405-2408.

Umoren, S. A., Obot, I. B., Ebenso, E. E. & Obi-Egbedi, N. O. (2008). *International Journal of Electrochemical Science*, 3, 1029-1035.

Usman, A.I., Aziz, A.A. & Noqta, O.A. (2019) Green sonochemical syn- thesis of gold nanoparticles using palm oil leaves extracts. *Materials Today Proceedings* 7, 803–807.

Vander Wal, R. L., Berger, G. M. & Ticich, T. M. (2003). Carbon nanotube synthesis in a flame using laser ablation for in situ catalyst generation. *Applied Physics A,* 77(7), 885–889.

Veleva, L. (2005). *Soils corrosion tests and Standards: Application and Interpretation*. (2^{nd} ed.). West Conshohocken, PA, USA: ASM International.

Venkataraman, A., Amadi, E.V., Chen, Y. & Papadopoulos C. (2019). Carbon nanotube assembly and integration for applications. *Nanoscale Research Letters,* 14**,** 220.

Wahab, R., Kim, Y. S. & Shin, H. S. (2009). Synthesis, characterisation and effect of pH variation on zinc oxide nanostructures. *Materials Transactions*. 50(8), 2092–2097.

Wang, S., Dun, C., Li, X., Liunn, Z., Zhu, M. & Zhang, D. (2015). Field corrosion characterisation of soil corrosion of X70 pipeline steel in a red clay soil. *Progress in Natural Science, Material International*, 25, 242–250.

Wang, X. D., Vinodgopal, K. & Dai, G. P. (2019). Synthesis of carbon nanotubes by catalytic chemical vapor deposition. In: H. E. Saleh and S. M. M. El-Sheikh, (Eds.), *Perspective of Carbon Nanotubes*, (pp. 1-19). London, IntechOpen Limited.

Wang, X. S., Liu, X., Wen, L., Zhou, Y., Jiang, Y. & Li, Z. (2008) Comparison of basic dye crystal violet removal from aqueous solution by low-cost biosorbents, *Separation Science and Technology*, 43, 3712-3731.

Wang, Y., Zhang, L., Hu, Y. & Li, C. (2016). Comparative study on optical properties and scratch resistance of nanocomposite coatings incorporated with flame spray pyrolyzed silica modified via in-situ route and ex-situ route. *Journal of Material Science and Technology,* 32, 251–258.

Wang, Y., Zhou, X., Liang, Z. & Jin, H. (2018). Characterisation of ultrasonic-assisted electrochemical deposition of Ni-Co-ZrO_2. *Coatings*, 8, 211.

Wang, Z., Li, Z., Sun, J., Zhang, H., Wang, W., Zheng, W. & Wang, C. (2010). Improved hydrogen monitoring properties based on p-NiO/n-SnO_2 heterojunction composite nanofibers. *Journal of Physical Chemistry: C,* 114, 6100–6105.

Wansah, J. F., Udounwa, A. E., Ahmed, A. D., Essiett, A. A. & Jackson, E. U. (2014). Application of nanotechnology in the corrosion. *Proceedings of the first African International Conference/Workshop on Applications of Nanotechnology to Energy, Health and Environment, UNN,* 103–110.

Wasim, M. & Shoaib, S. (2019). Influence of Chemical Properties of Soil on the Corrosion Morphology of Carbon Steel Pipes. *Metals in Soil - Contamination and Remediation*. 1-15.

Wei, H., Heidarshenas, B., Zhou, L., Hussain, G., Li, Q. & Ostrikov, K. (2020). Green inhibitors for steel corrosion in acidic environment: state of art. *Materials Today Sustainability*, 10, 100044.

Wei, Y., Qiu, J., Xu, L. & Zhang, F. (2009). Corrosion behaviors of TiO_2 nanotube layers on titanium in Hank's solution. *Biomedical Materials*, 4 (6), 1-13.

Wunderlich, W. (2014). The Atomistic Structure of metal/ceramic interfaces is the key issue for developing better properties. *Metals*, 4, 410–427.

Xie, J. & Varadan, V. K. (2005). Synthesis and characterisation of high surface area tin oxide / functionalized carbon nanotubes composite as anode materials. *Materials Chemistry and Physics*, 91, 274–280.

Xin, S. S. & Li, M. C. (2014). Electrochemical corrosion characteristics of type 316L stainless steel in hot concentrated seawater. *Corrosion Science,* 81, 96–101.

Xu, J. M., Sun, W. C., Wang, Y., Jia, Z W. & Guo. F. (2017). Influences of MWCNTS concentration on the friction and anti-wear behavior of Ni-P coating influences of MWCNTS. *3rd International Conference on Advanced Materials Research and Applications (AMRA),* 170, 2–6.

Xu, L., Zheng, R., Liu, S., Song, J., Chen, J., Dong, B. & Song, H. (2012). NiO@ZnO heterostructured nanotubes: coelectrospinning fabrication, characterization, and highly enhanced gas sensing properties. *Inorganic Chemistry*, 2012, 51, 7733-7740.

Xue Y. J., Jia, X. Z., Zhou, Y. W., Ma, W. & Li, J. S. (2006). Tribological performance of Ni−CeO_2 composite coatings by electrodeposition. *Surface Coating Technology*, 200, 5677−5681.

Yahaya, N., Noor, N. M., Othman, S. R., Sing, L. K. & Din, M. M. (2011). New Technique for Studying Soil-Corrosion of Underground Pipeline. *Journal of Applied Science*, 11, 1510–1518.

Yan, M., Wang, J., Han, E. & Ke, W. (2008a). Local environment under simulated disbanded coating on steel pipelines in soil solution, *Corrosion Science,* 50 (1), 1331-1339.

Yan, T. J., Wang, X. X., Long, J. L., Liu, P., Fu, X. L., Zhang, G. Y. & Fu, X. Z. (2008b). Urea-based hydrothermal growth, optical and photocatalytic properties of single-crystalline $In(OH)_3$ nanocubes, *Journal of Colloidial Interface Science*, 325, 425-431.

Yang, Z., Xu, H., Li, M. K., Shi, Y. L. Huang, Y. & Li. H. L. (2004) Preparation and properties of Ni/P/single-walled carbon nanotubes composite coatings by means of electroless plating. *Thin Solid Films*, 466(1-2) 81- 86.

Yaro, A. S., Khadom, A. A. & Wael, R. K. (2013). Apricot juice as green corrosion inhibitor of mild steel in phosphoric acid. *Alexandria Engineering Journals*, 52, 129–135.

Yasakau, K. A., Zheludkevich, M. L., Lamaka, S. V. & Ferreira, M. G. (2006). Mechanism of corrosion inhibition of AA2024 by rare-earth compounds. *Journal of Physical Chemistry B*, 110, 5515–5528.

Yu, L., Wang, G., Wan, G., Wang, G., Lin, S., Li, X. & Xiang, Y. (2016). Highly effective synthesis of NiO/CNT nanohybrids by atomic layer deposition for high-rate and long-life supercapacitors. *Dalton Transactions,* 2016, 45, 13779–13786.

Yuliarto, B., Zulhendry, D. W., Luh, N., Septiani, W. & Fahmi, M. Z. (2019). Synthesis and Characterisation of Tin Oxide-MultiWalled Carbon Nanotube Composite Material as Carbon Monoxide Gas Sensor. *Nano Engineering and Materials Technologies III: Materials Science Forum,* 947, 35–39.

Zainudin, S. N. F., Abdullah, H., Markom, M. & Ahmad, M. (2018). Temperature dependency of SnO_2 -NiO-MWCNT nanocomposite thin film for dye-sensitised solar cells. *Ionics,* 1-7.

Zeng, R.C., Zhang, F., Lan, Z. D., Cui, H. Z. & Han, E. H. (2014). Corrosion resistance of calcium-modified zinc phosphate conversion coatings on magnesium-aluminum alloys. *Corrosion Science*, 88, 452–459.

Zhan, Y., Shao, Y., Shi, Q. & Li, P. (2017). Effect of polyaniline/montmorillonite content on the corrosion protection of epoxy coating. *Anti-Corrosion Methods and Materials*, 64 (1), 75-82.

Zhang, D. E., Ni, X. M., Zheng, H. G., Li, Y., Zhang, X. J. & Yang, Z. P. (2005). Synthesis of needlelike nickel nanoparticles in water-in-oil microemulsion, *Material Letter,* 59, 2011-2014.

Zhang, D., Zhang, H., Zhao, S., Li, Z. & Hou, S. (2019). Electrochemical impedance spectroscopy evaluation of corrosion protection of X65 carbon steel by halloysite nanotube-filled epoxy composite coatings in 3.5% NaCl Solution. *International Journal of Electrochemical Science*, 14, 4659–4667.

Zhang, H., Ding, Y., Wu, C., Chen, Y., Zhu, Y. & Zhong, S. (2003). The effect of laser power on the formation of carbon nanotubes prepared in CO_2 continuous wave laser ablation at room temperature. *Physics B,* 325, 224-229.

Zhang, J., Zeng, D., Zhu, Q., Wu, J., Huang, Q., Zhang, W. & Xie, C. (2016). Enhanced room-temperature NO_2 response of NiO-SnO_2 nanocomposites induced by interface bonds at p-n heterojunction. *Physical Chemistry Chemical Physics,* 1-12.

Zhang, Y. L., Yang, Y., Zhao, J. H., Tan, R. Q, Cui, P. & Song, W. J. (2009). Preparation of ZnO Nanoparticles by a Surfactant-Assisted Complex Sol-gel Method Using Zinc Nitrate. *Journal of Sol-Gel Science and Technology*, 51, 198-203.

Zhao, X. C., Xiao, G. Y., Zhang, X., Wang, H. Y. & Lu, Y. P. (2014). Ultrasonic induced rapid formation and crystal refinement of chemical conversed hopeite coating on titanium. *Journal of Physics and Chemistry C,* 118, 1910–1918.

Zhao, X., Qi, Y., Zhang, Z., Li, K. & Li, Z. (2019). Electrochemical Impedance Spectroscopy investigation on the corrosive behaviour of waterborne silicate micaceous iron oxide coatings in seawater. *Coatings,* 9, 415, 1-17.

Zhao, Y., Seko, K. & Saito, Y. (2006). Effects of process parameters and substrate structures on growth of SWCNTs by catalytic decomposition of ethanol. *Journal of Applied Physics,* 45(8A), 6508-6512.

Zheng, H., Shao, Y., Wang, Y., Meng, G. & Liu, B. (2017). Reinforcing the corrosion protection property of epoxy coating by using graphene oxide-poly (urea-formaldehyde) composites. *Corrosion Sciences*, 123, 267–277.

Zhu, H., Luo, H., Ai, D. & Wang, C. (2016). Mechanical impedance based technique for steel structural corrosion damage detection. *Measurement,* 88, 353–359.

Zhu, Q. J., Cao, A., Wang, Z. F., Song, J. W. & Chen, S. L. (2011). Fundamental Aspects of Stray Current Corrosion on Buried Pipeline. *Advanced Material. Resources*, 146–147, 70–74.

APPENDICES

APPENDIX A

XRD Graphs for Calculating the Crystallite Sizes of NiO during the Experimental Runs

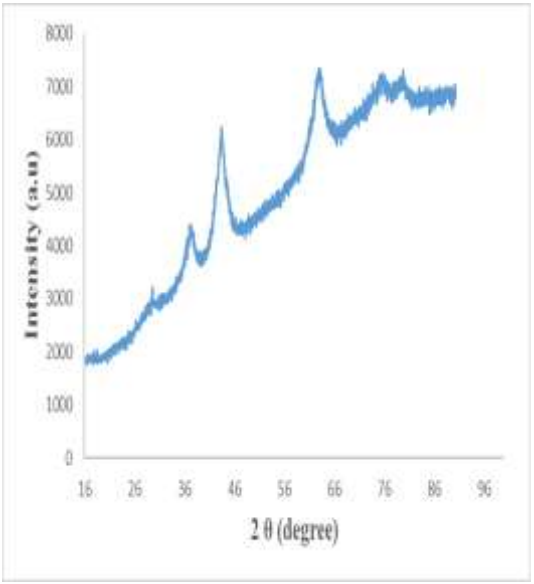

C_1=Run 1

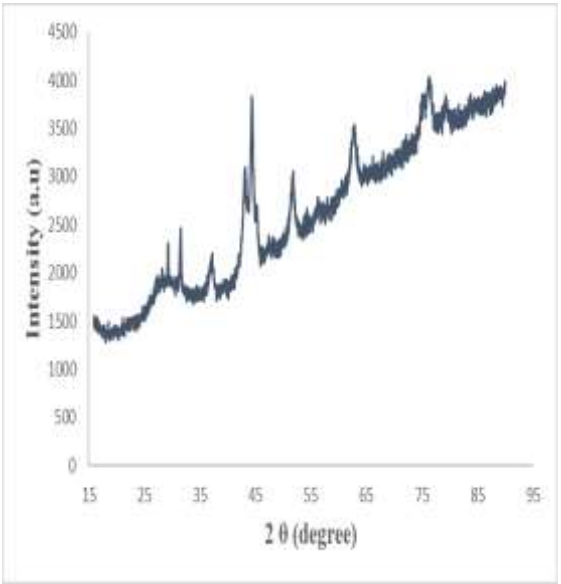

C_2=Run 2

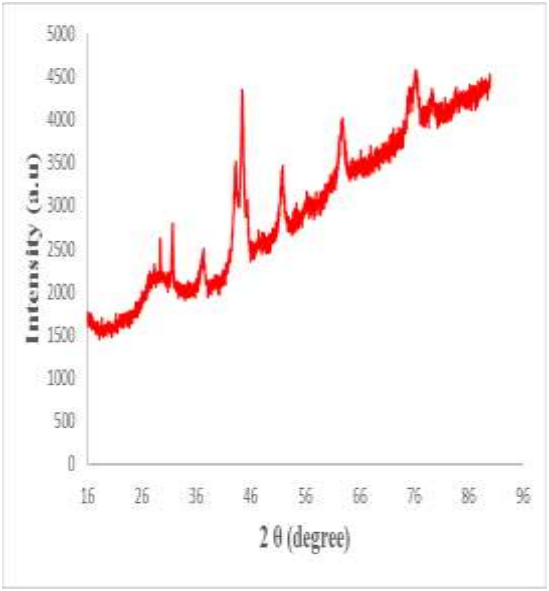

C_3=Run 3

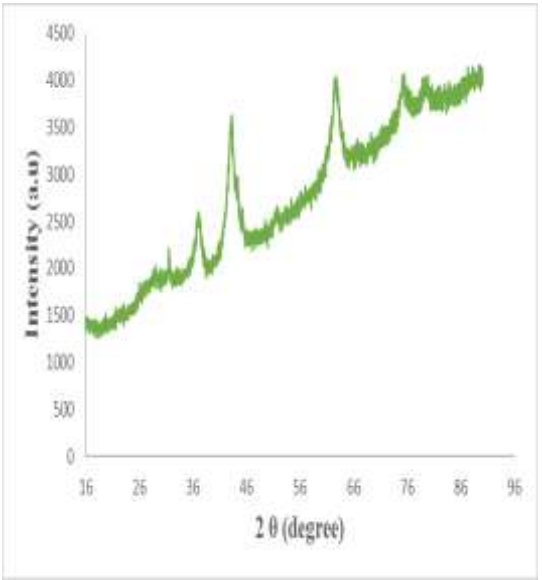

C_4=Run 4

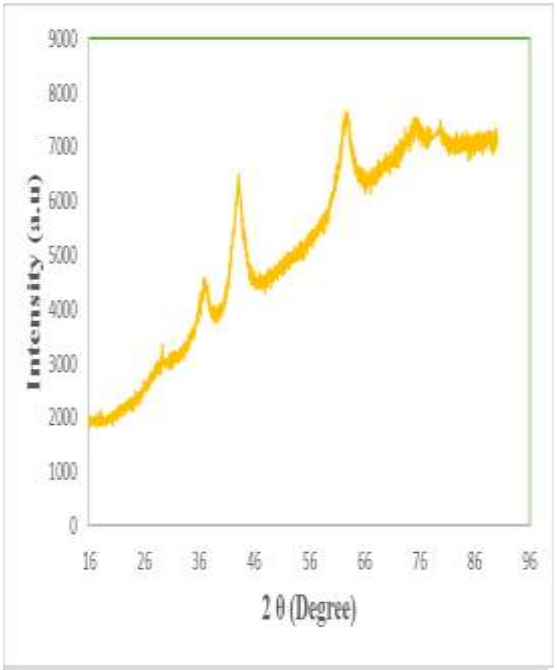

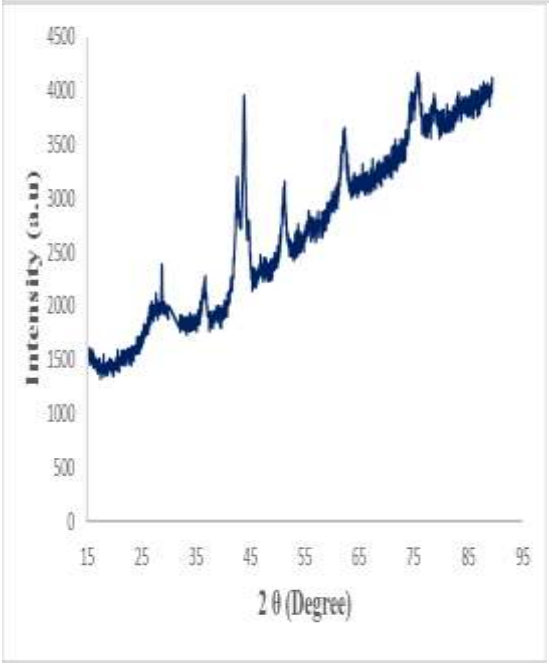

C_5=Run 5 **C_6=Run 6**

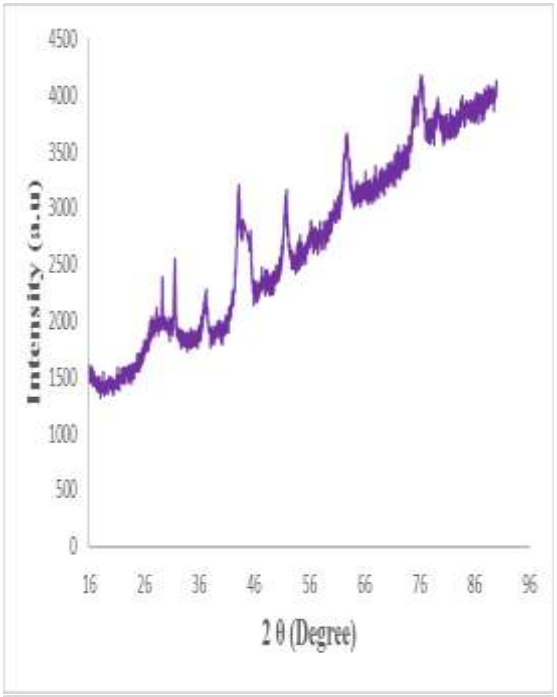

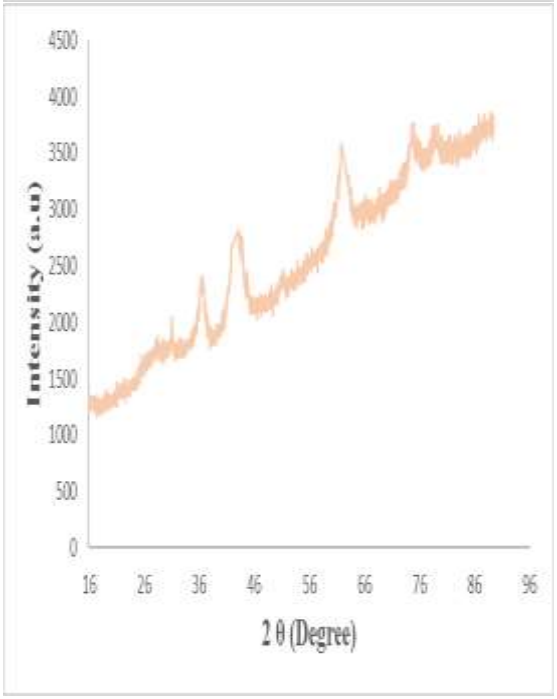

C_7=Run 7 **C_8=Run 8**

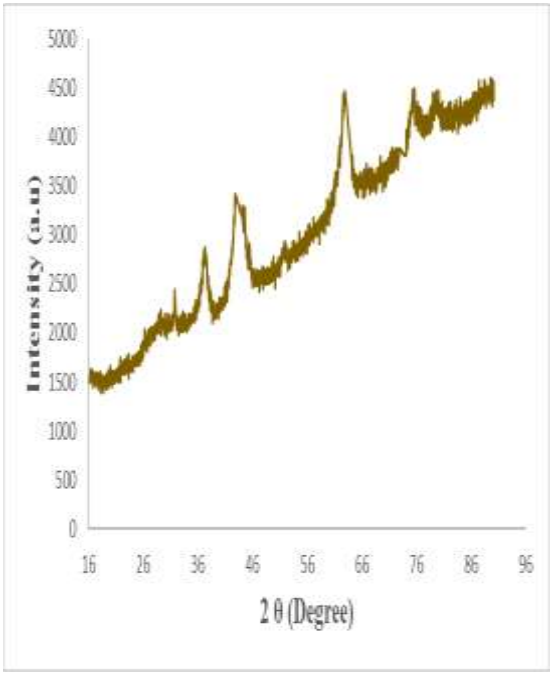

C_9=Run 9

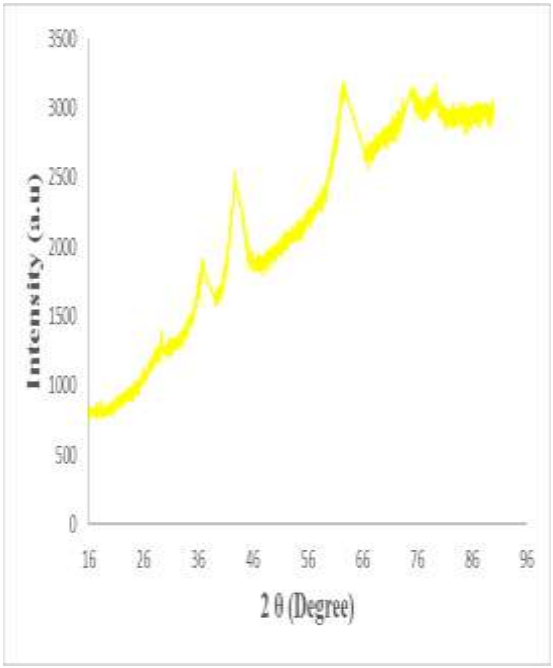

C_{10}=Run 10

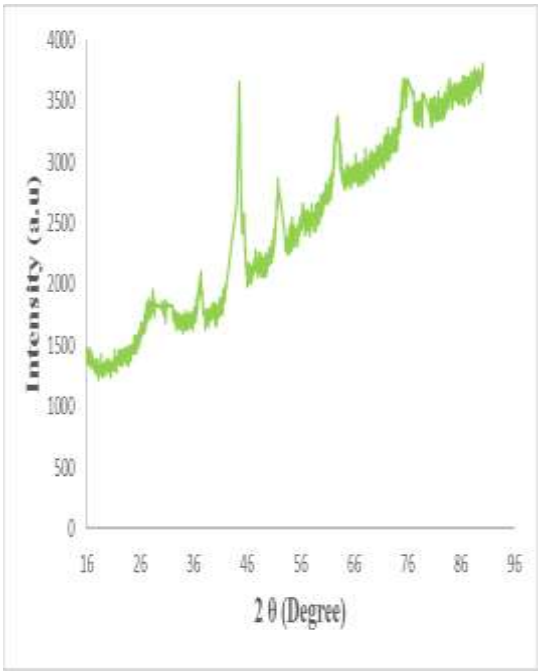

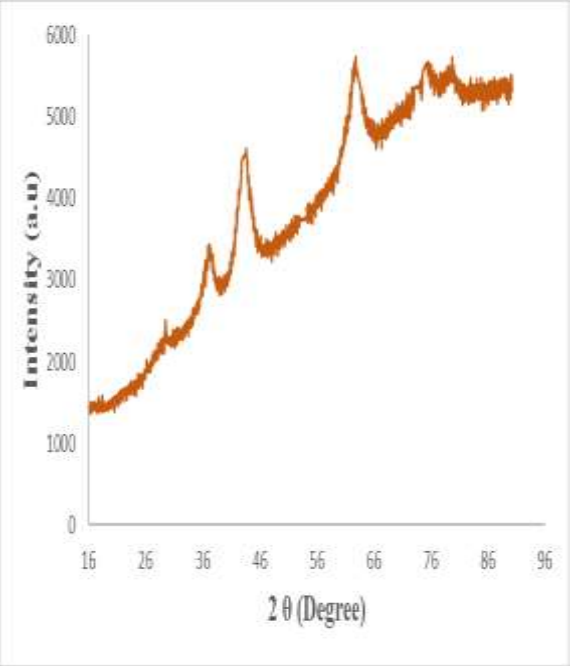

C_{11}=Run 11

C_{12}=Run 12

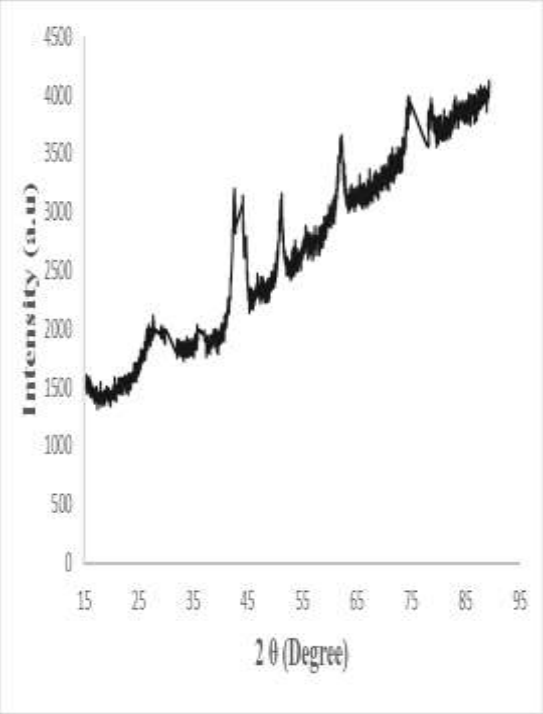

C_{13}=Run 13

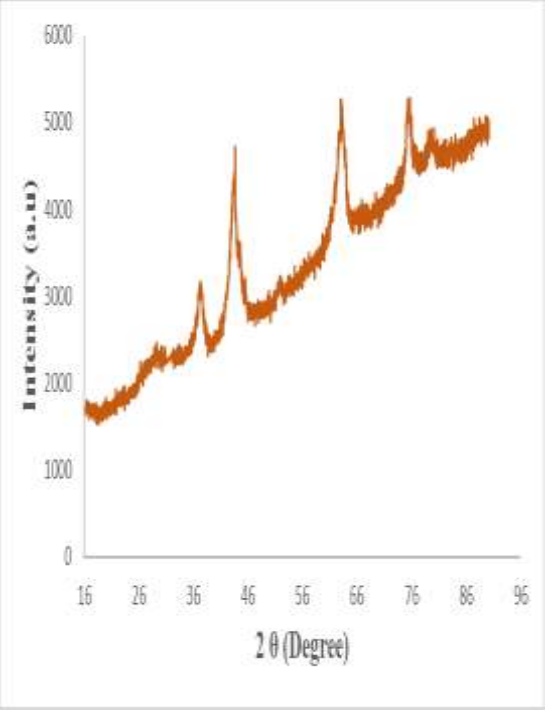

C_{14}=Run 14

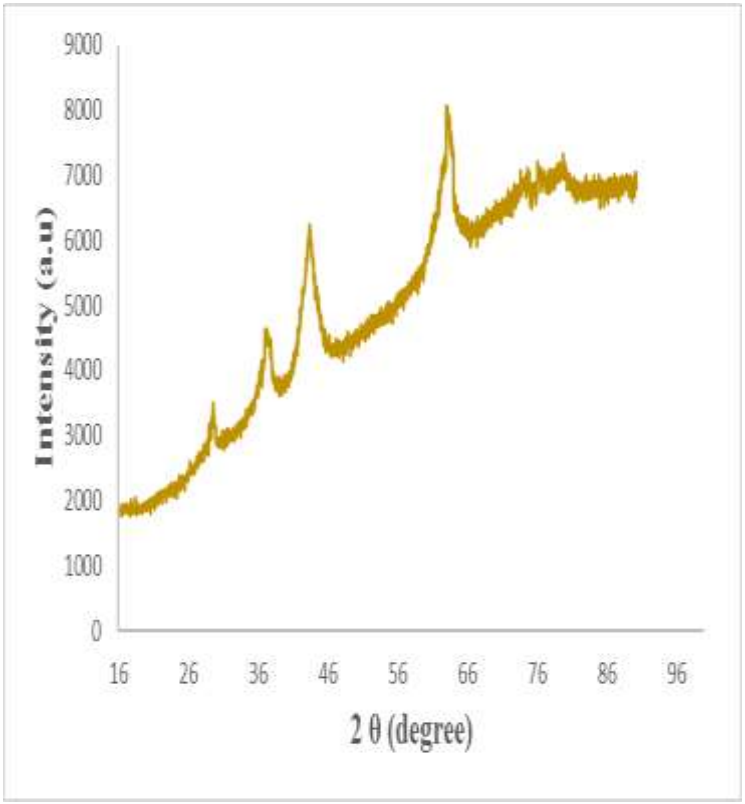

C_{15}=Run 15

APPENDIX B

XRD Graphs for Calculating the Crystallite Sizes of SnO_2 during the Experimental Runs

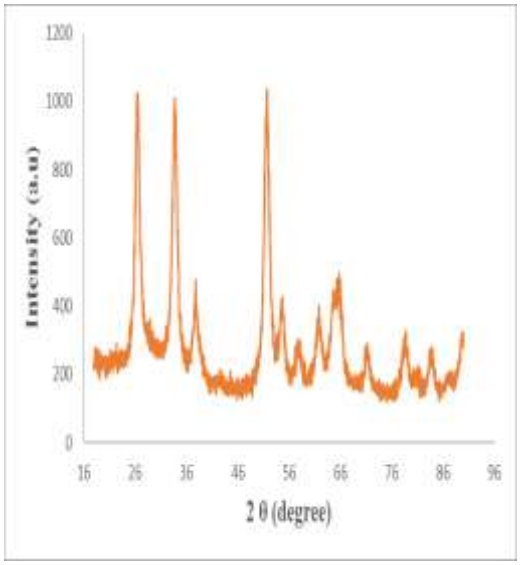

D_1=Run 1

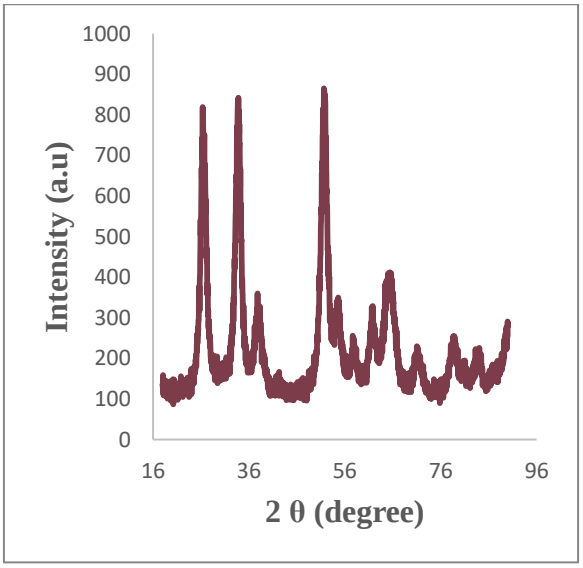

D_2=Run 2

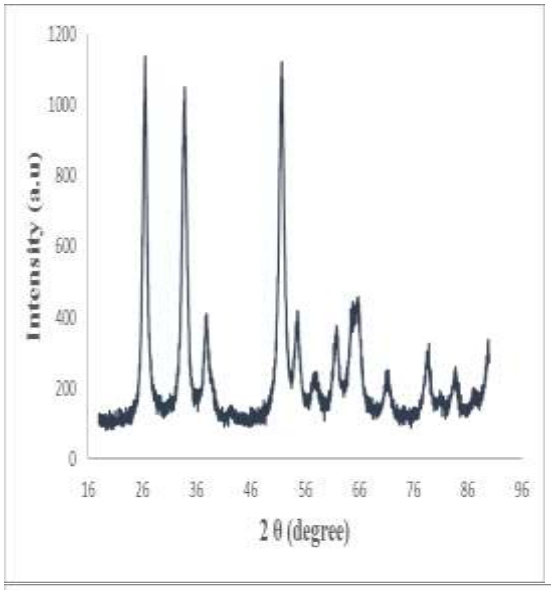

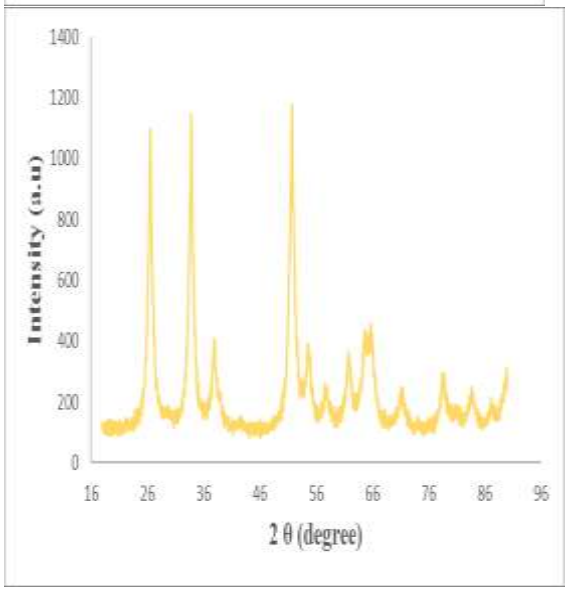

D_3=Run 3 **D_4=Run 4**

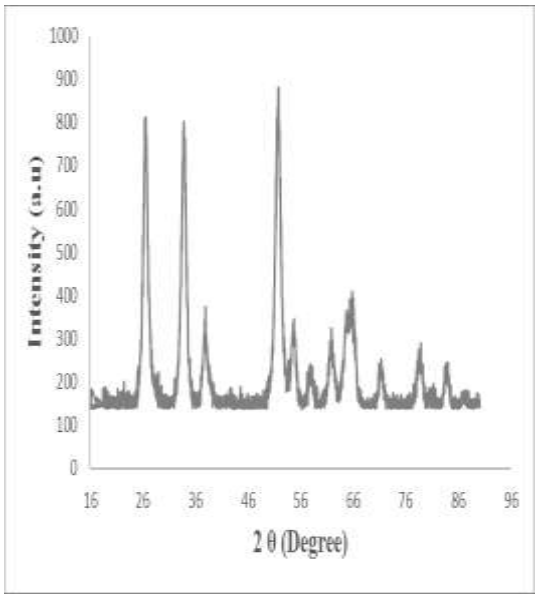

D_5=Run 5

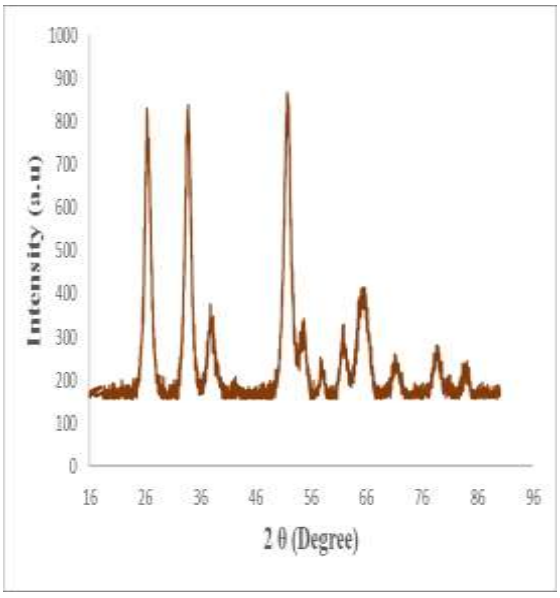

D_6=Run 6

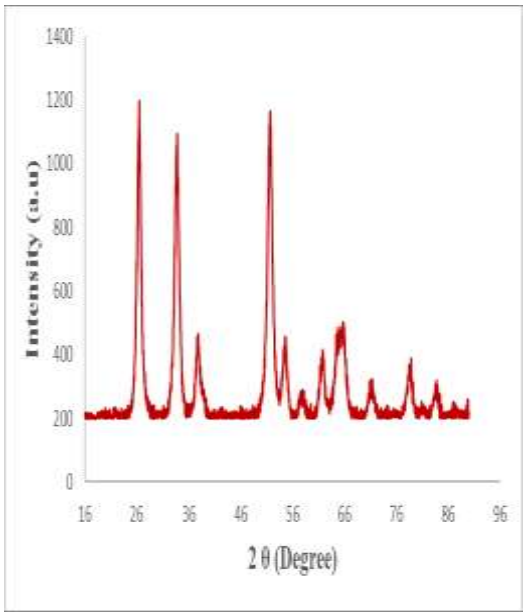

D_7=Run 7

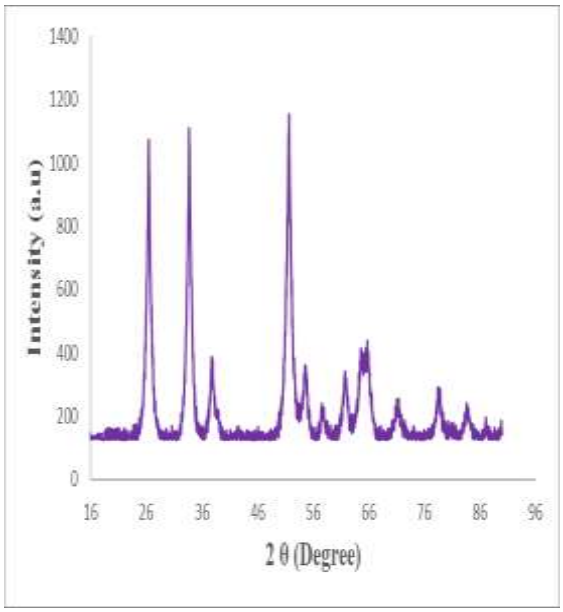

D_8=Run 8

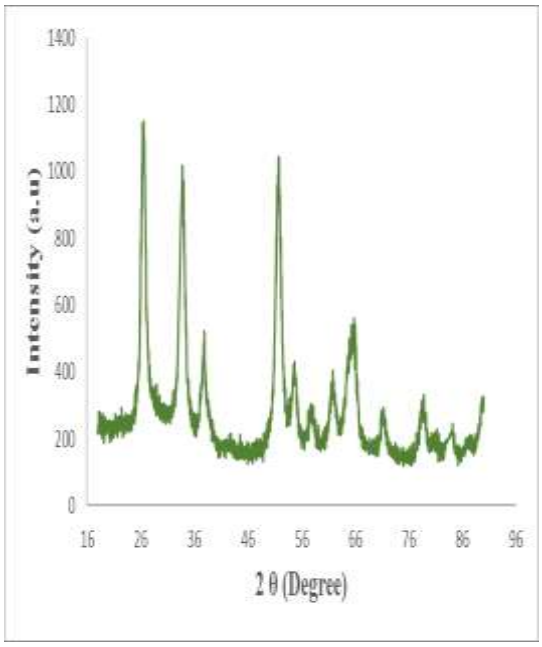

D_9=Run 9

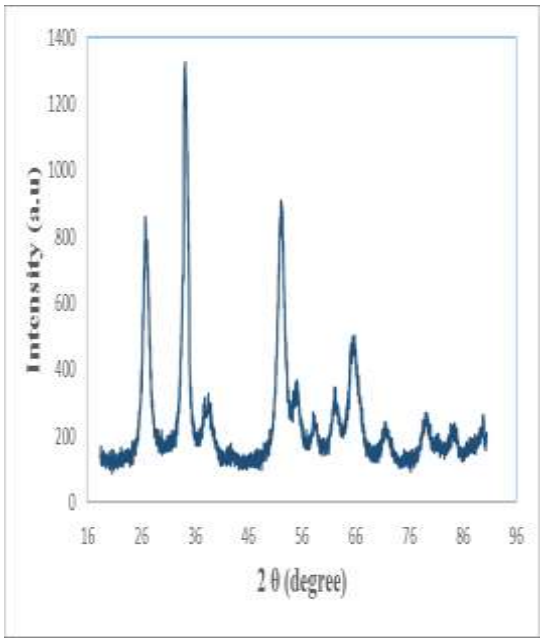

D_{10}=Run 10

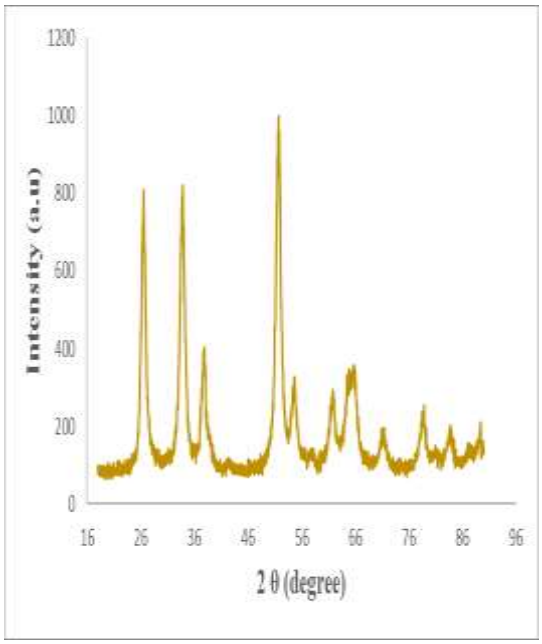

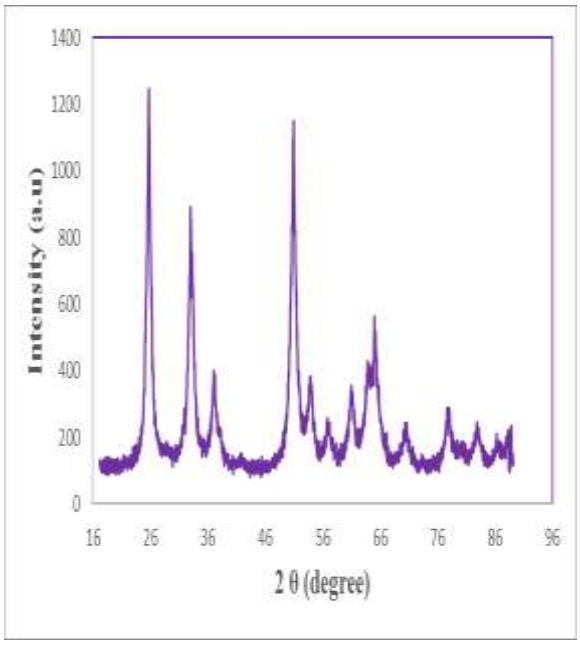

D_{11}=Run 11

D_{12}=Run 12

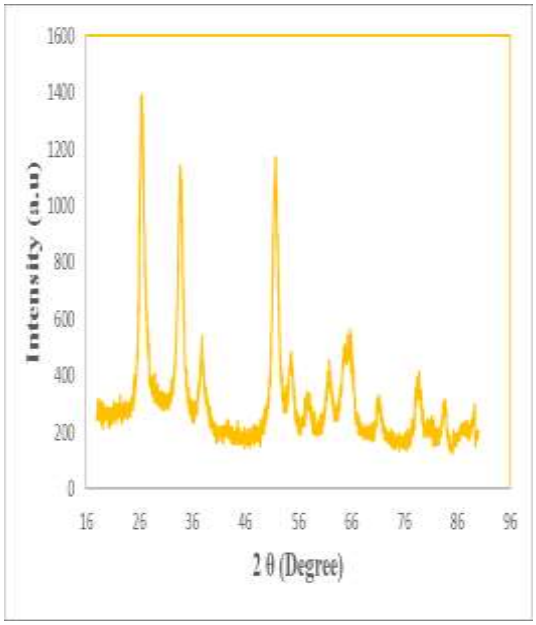

D_{13}=Run 13

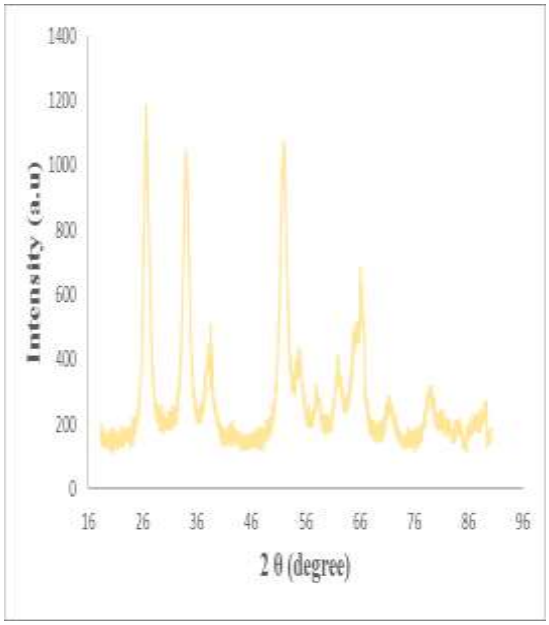

D_{14}=Run 14

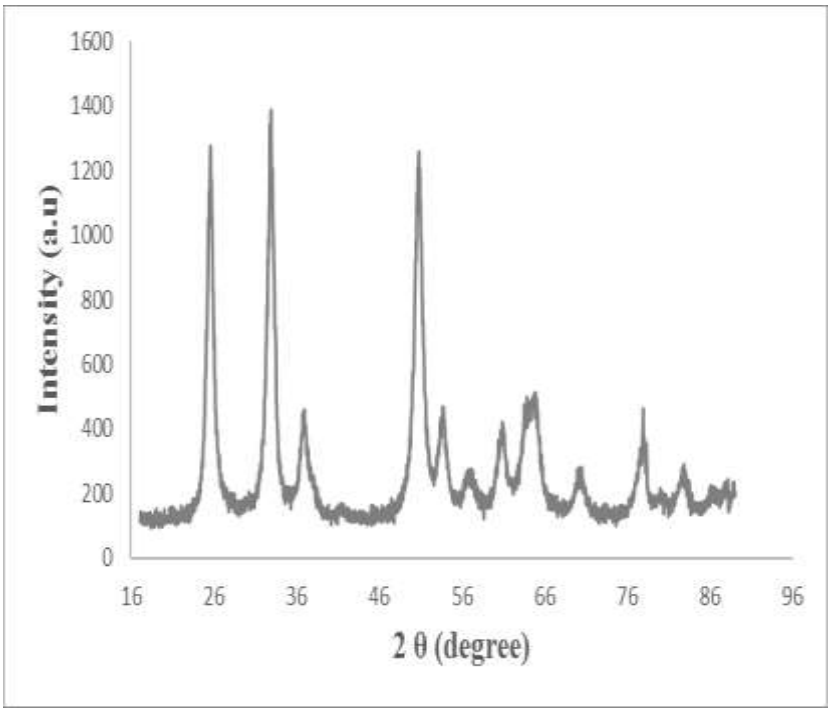
1600
1400
1200
1000
800
600
400
200
0
Intensity (a.u)
16
26
36
46
56
66
76
86
96
2 θ (degree)

D_{15}=Run 15